Experimental study of variability and defects in vacuum-bag-only corner laminates

Nicolas Krumenacker

A thesis submitted in partial satisfaction of the requirements for

the degree of Doctor of Philosophy

Department of Mechanical Engineering

McGill University

May 16, 2018

To Anne, mom and dad

Abstract

Vacuum-bag-only (VBO) semipreg processing can now produce flat panels and complex-shape parts at the coupon-level that rival the laminate quality and mechanical performance of similar parts produced via autoclave prepreg processing. Still, the primary aim for the development of out-of-autoclave technologies remains the robust manufacturing of large, integrated parts such as primary aero-structures. To this end, the high-level of variability and defects present in VBO semipregs and processed complex-shape parts poses a key challenge, notably in terms of in-service reliability. In turn, load cases have become correspondingly complex resulting in critical out-of-plane components. To this end, improving the accuracy of through-the-thickness experimental test methods is vital to the determination of representative interlaminar strength allowables for structural design and to the development of new and comprehensive, multiaxial failure criteria.

The aim of this thesis is to investigate variability and defects in VBO complex-shape laminates and offer technical recommendations. The work is divided into two parts: first, novel improvements are proposed for current characterization and testing methods utilized in R&D, and second, the key factors that affect laminate quality and mechanical performance are investigated. An L-bracket corner geometry (curved beam) is selected as the simplest representative case for sharply-curved details in existing aero-structures.

Three notable improvements are proposed for the characterization and mechanical testing of corner specimens. First, a semi-automated thickness-measurement method is implemented in Matlab that determines the thickness profile of specimens as a function of location along the tool-side edge. The method is shown to be more accurate, precise and powerful than the direct methods currently in use. Second, mechanical stiffening-sleeves are developed to eliminate the error in applied bending moment engendered by excessive flexure of the specimen's moment arms when tested under the four-point bending, curved beam strength configuration (ASTM D6415). This modification further allows for the correction of the corner opening during testing via a simple geometric factor. The effect of sleeve-offset distance is investigated, and the proposed improvements are validated via finite element modelling, mechanical testing and fractographic inspection of failed sections viewed via scanning electron microscopy. Third, a novel method is developed to characterize the extent, magnitude and morphology of fibre waviness in tape corners

based on the digital image analysis of optical micrographs and 3D data from X-ray computed micro-tomography.

The experimental work considers a number of factors that are determined to significantly affect the laminate quality and interlaminar mechanical performance of corner specimens, namely: consolidation pressure loss, tool-shape, reinforcement type, ply-stacking sequence and pertinent industrial cases. The laminate quality is assessed in terms of corner thickness deviation, porosity and fibre contents, and fibre waviness in the case of convex tape corners. In turn, the mechanical performance is assessed in terms of curved beam and interlaminar tensile strengths, energy-to-failure and fractographic inspection of failed sections via optical microscopy. Lastly, a statistical analysis is conducted to establish the repeatability of the research environment and the reliability of its empirical findings.

Overall, this thesis contributes to the characterization methods and the understanding of VBO semipreg processing with respect to the manufacturing of large and integrated parts. In particular, practical improvements are made to the curved beam strength test method that increase the accuracy of experimentally-determined measurements and properties. In turn, the experimental investigation of variability and defects in corners and their effect on mechanical performance builds on existing research conducted on flat laminates and, to a lesser extent, complex-shape coupons. The research findings are ultimately distilled in a set of design principles for industrial processing.

Abrégé

La fabrication de pièces composites en tissus semi-imprégnés par simple sac à vide produit d'ores et déjà des panneaux et des pièces complexes à l'échelle d'échantillons qui rivalisent avec la qualité finale et la performance mécanique de pièces similaires produites par autoclave et tissus pré-imprégnés. Cependant, la motivation principale derrière le développement des technologies hors-autoclave demeure la fabrication de larges pièces intégrées tel que les structures aérospatiales primaires. Cependant, les hauts taux de variabilité et de défauts présents dans les tissus semi-imprégnés et les pièces à forme complexe produits par cette méthode représentent un défi technique important notamment en ce qui concerne la fiabilité opérationnelle de ces pièces. De plus, les cas de charges deviennent eux aussi de plus en plus complexes avec des composants hors plan critique. À cette fin, il est essentiel d'améliorer la précision des méthodes d'essais mécaniques hors plan afin de déterminer les contraintes interlaminaires admissibles pour la conception structurelle, et le développent de nouveaux critères exhaustifs de défaillance multiaxiales.

L'objectif de cette thèse est d'étudier la variabilité et les défauts présents dans les pièces composites stratifiés de formes complexes produites par simple sac à vide, et de proposer des recommandations techniques pour l'industrie. Ce travail de recherche comprend deux parties : dans un premier temps sont présentées des améliorations novatrices pour les méthodes de caractérisation et d'essais mécaniques actuellement utilisées en recherche et développement, et dans un deuxième temps sont étudiés les facteurs clés influençant la qualité finale des pièces ainsi que leurs performances mécaniques. Une géométrie en angle en forme de « L » est sélectionnée, car elle représente le cas le plus simple représentant les parties à fortes courbures présentes dans les structures aérospatiales.

Trois avancées importantes sont proposées pour la caractérisation et l'essai mécanique des coins en composites stratifiés. Premièrement, une méthode semi-automatisée de mesure d'épaisseur est implémentée avec Matlab afin de déterminer le profil d'épaisseur du spécimen en fonction de la position le long du bord coté moule. Il est démontré que cette méthode est plus exacte, précise et puissante comparée aux méthodes de mesures directes actuellement utilisées. Deuxièmement, des raidisseurs mécaniques sont développés pour la configuration d'essai de flexion en quatre points sur poutres courbées (ASTM D6415) afin d'éliminer l'erreur dans le calcul du moment appliqué qui est engendrée par la déformation excessive des brides du spécimen. Cette modification permet ensuite de corriger l'ouverture du rayon pendant l'essai avec l'application d'un simple facteur géométrique. L'effet du décalage des raidisseurs par rapport au coin est par la suite étudié, et l'amélioration apportée par leur usage est validée via une modélisation par éléments finis, et par des essais mécaniques et une inspection fractographique de sections fracturées via microscopie électronique à balayage. Troisièmement, une nouvelle approche est développée pour caractériser l'étendue, l'amplitude et la morphologie de l'ondulation des fibres dans les coins à base de plis unidirectionnels. Cette approche est basée sur l'analyse digitale de données en 2D et 3D provenant de balayages en micrographie optique ainsi qu'en micro-tomographie à rayons-X informatisée.

Ces travaux expérimentaux examinent un certain nombre de facteurs jugés importants en ce qui concerne la qualité finale et les propriétés interlaminaires des coins en composites stratifiés produits par simple sac à vide, à savoir : la perte de pression de consolidation, la forme du moule, l'architecture des renforcements primaires, la séquence d'orientation des plis de tissus semi-empreignés, et les cas industriels pertinents. La qualité résultante est évaluée en fonction de déviations locales d'épaisseur, de taux de porosité, de contenu en fibres et d'ondulation des fibres dans le cas de coins à base de plis unidirectionnels. À son tour, la performance mécanique est évaluée en fonction de résistances à la flexion et à la traction interlaminaire, d'énergie au point de fracture et d'inspection fractographique de sections fracturées via microscopie optique. Enfin, une analyse statistique est menée afin d'établir la répétabilité de l'environnement de recherche et la fiabilité de ces résultats empiriques.

Globalement, cette thèse contribue aux méthodes de caractérisations et à la compréhension du procédé hors autoclave par simple sac à vide en ce qui concerne la production de pièces larges et intégrées. En particulier, les méthodes de caractérisation et d'essai sur coin en composites stratifiés sont améliorées de façon pratique tout en augmentant la précision des mesures et propriétés déterminées expérimentalement. De plus, l'étude expérimentale de la variabilité et des défauts sur les coins ainsi que leur effet sur la performance mécanique supplémente les connaissances actuelles qui sont principalement basé sur des expériences sur panneau plat, et dans une moindre mesure sur des formes complexes à l'échelle de l'échantillon. Ces résultats expérimentaux sont finalement distillés en un ensemble de directives de conception pour les procédés industriels.

Acknowledgements

First and foremost, I wish to acknowledge my fiancée, parents and four siblings, for their unwavering and treasured love and support. I am equally grateful to Pascal Hubert, my research supervisor, for providing me with the opportunity to complete my doctoral research at a world-renowned university in Canada and in a composites research group known for its excellence. I am particularly beholden to him for his steadfast support in the face of certain adversarial circumstances. I wish to additionally acknowledge Isabelle Paris at Bombardier Aerospace for lending her vast expertise in the mechanical testing of composite materials.

Second, I wish to acknowledge the support of my research colleagues and peers: Anna Madra for lending her vast expertise in micro-CT data analysis, Kobyé Bodjona for his FE modelling and Matlab coding advice, Swaroop Visweswaraiah and Valentin Romanov for their intellectual feedback, and Mostfa Yourdkhani, Tim Centea and Cyril Cattin for their formative advice early on. I am forever grateful to have met so many exceptional people over my years spent in the Structures and Composite Materials Laboratory and more generally at McGill.

Third, I wish to acknowledge the vital in-kind contributions made by Bombardier Aerospace and financial support from the National Science and Engineering Research Council of Canada (NSERC) and the Research Center for High Performance Polymer and Composite Systems (CREPEC). My studies at McGill were also made possible by personal financial support from the Lorne Trottier Engineering Graduate Fellowship, NSERC and the Consortium for Research and Innovation in Aerospace in Quebec. I wish to finally thank the thesis advisory and evaluation committee members for their time and valued input in reviewing my work.

Finally, I wish to acknowledge two mentors, who offered invaluable advice and imparted on me the importance of professionalism early in my academic research journey, namely LeRoy Alaways at Villanova University and Dan Price at the adidas Innovation Team.

Declaration of authorship

The doctoral research presented in this thesis and its write-up is entirely the work of the author with the only exceptions being the following experimental activities.

§ 3.7.2 – Mr. Nicolas Brodusch, a technician in the Department of Mining, Metals and Materials at McGill University, prepared and imaged the scanning electron microscopy samples in consultation with the author.

§ 5.5.3 – Dr. Rui Tahara, a postdoctoral fellow in the Department of Biology at McGill University, performed the X-ray computed micro-tomography (micro-CT) scans per the requirements of the author. In turn, Dr. Anna Madra, a postdoctoral associate in the Department of Aeronautics and Astronautics at the Massachusetts Institute of Technology, treated and analyzed the micro-CT data in consultation with the author.

Contents

Figures

1 Introduction

2 Materials and general methods

3 Development of stiffening-sleeves for curved beam strength testing

Appendices

Tables

5 Mechanical performance of corners

1
Introduction

1.1 Framing the research

The post-World War II economic expansion prompted an abundance of engineering innovation in the aerospace industry starting with the Jet Age and followed by the Space and Arms Races. A wealth of novel engineering materials was concurrently developed to advance aero-structural design, which could no longer solely be accommodated by incremental improvements in existing engineering materials, namely metal alloys. Of particular note are the commercial advent of engineering plastics (polymers) such as epoxy resins in the mid 1940s in Europe and the USA [1], and the later development of fine, synthetic fibres such as carbon fibre in the early 1960s in the UK [2]. The combination of these novel materials led to the swift development of fibre-reinforced plastics, which are commonly referred to as *polymer matrix composites* (PMCs) or, more plainly, *advanced composites*. Ever since their conception, PMCs have been the predominant subclass of *synthetic composites*, which now include highly specialized—albeit less well established—*metal* and *ceramic matrix composites* (MMCs and CMCs, resp.) [3, 4]. PMCs and especially *carbon fibre-reinforced polymers* (CFRPs) are projected to continue their market dominance across industries for the foreseeable future [5-7].

What are synthetic composites?

Composite materials are mixtures of two (or more) constituents present in reasonable proportions (> 5%), consisting of chemically-distinct phases at the microscale with discrete interfaces and possessing significantly different thermo-mechanical, chemical or electrical properties. They consist of a *primary-reinforcing phase* encased in and reinforcing a continuous *matrix* to achieve an end-product with new or significantly superior properties compared to those of the individual constituents. In particular, *synthetic composites*, which consist of PMCs, MMCs and CMCs, use synthetic fibres as the primary-reinforcement for engineering materials.

Introductory textbooks such as *Composites materials: Engineering and science* by Matthews and Rawlings [3] and *An introduction to composite materials* by Hull and Clyne [8] may be perused for a comprehensive and multidisciplinary overview of these materials.

The trend towards lighter integrated aero-structures

The defence and civil sectors of the aerospace industry have historically been the early-adopters of synthetic composites. Nonetheless, aero-structures such as aircraft frames have traditionally been comprised since the late 1930s of vast quantities of mechanically-fastened, metallic parts, whose lengthy assembly can account for up to half of the total airframe cost [4]. Aero-structural design has thus generally evolved towards lighter and more integrated structures (i.e. large-scale and complex-shape) that are cheaper to produce, assemble and maintain [9]. To this end, conventional aerospace-grade alloys such as 7000-series aluminum alloys have generally reached the limit of their potential on account primarily of their relatively low specific stiffness and strength properties, and poor fracture toughness and corrosion resistance [7, 9-11]. The sole exception are titanium alloys, which partly overcome these limitations and, as a result, have seen a moderate uptick in use on novel airframes such as that of the Boeing 787 Dreamliner airliner (~15 wt.%) [4, 12]. Fig. 1-1 presents Ashby-plots comparing engineering materials with respect to mechanical properties that are key to aero-structural design.

The aerospace industry has leaned heavily on PMCs containing high loading fractions (> 50 vol.%) of continuously-aligned fibres (e.g. carbon, glass and aramid) to replace and integrate metal parts given tailorable and superior specific mechanical properties and processing methods developed specifically to manufacture larger and more complex parts [2, 4, 7, 9, 13-15]. It is accepted that PMCs should not merely replace metal alloys but rather ought to revolutionize aero-structural design [2]. In particular, CFRPs possess superior specific mechanical properties, fatigue life, fracture toughness and corrosion resistance compared to aluminum alloys [2, 4, 7, 10]. The superior mechanical performance is owed to the development of high-modulus and -strength carbon fibres [2, 15], as illustrated in Fig. 1-1.B. Several examples of novel, large-scale and complex-shape aero-structures are presented in Fig. 1-2 that mostly consist of CFRPs. It should be noted that complex-shape laminates not only consist of sharply-curved regions with single and double curvatures but also include complex features such as ply-drops and metal inserts.

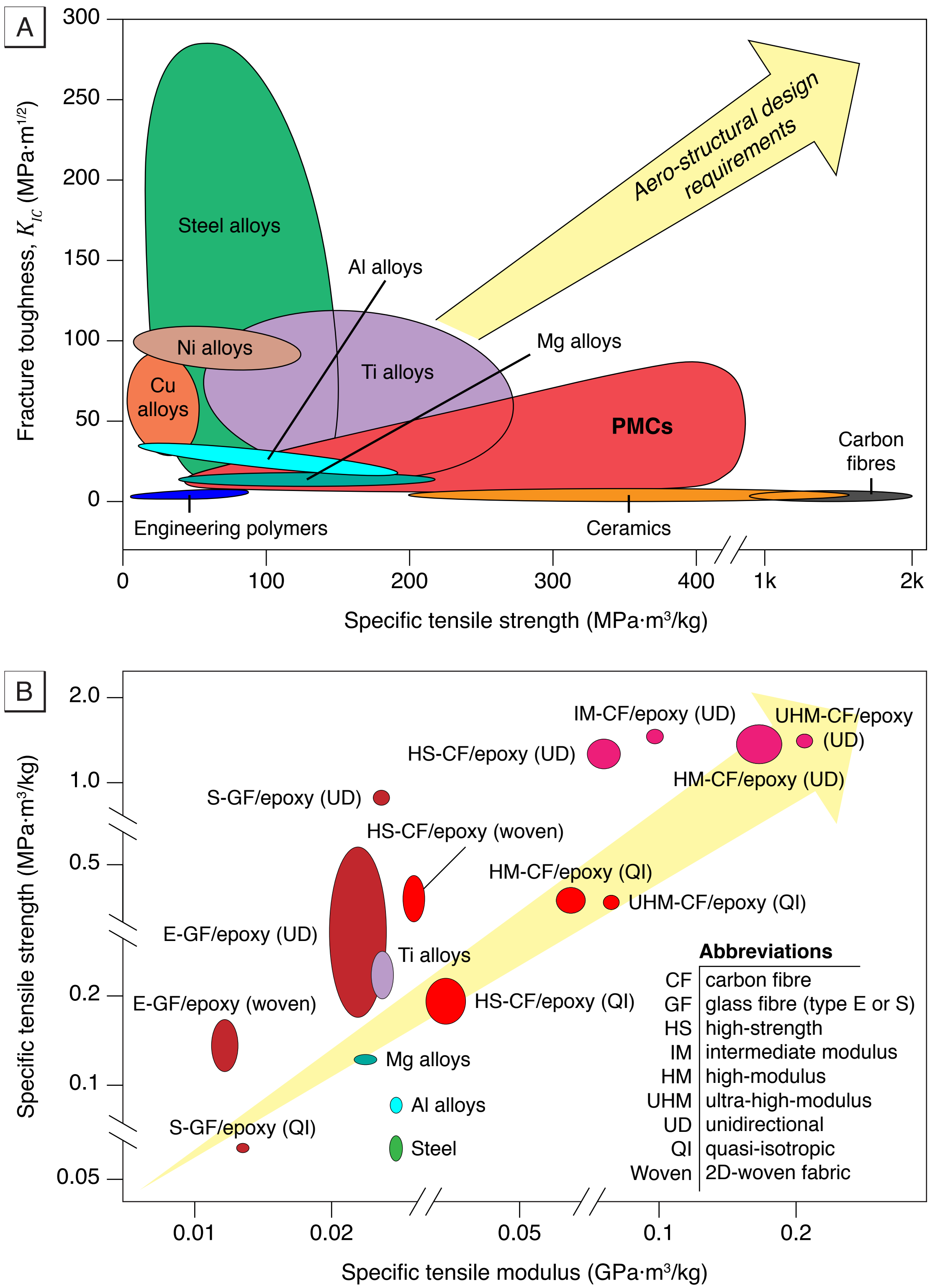

Fig. 1-1. Comparison of engineering materials used in aero-structures: A) specific tensile strength vs. fracture toughness (adapted from [10, 16], resp.); B) specific tensile modulus vs. the specific tensile strength (~60 vol.% fibre loading fractions; adapted from [17]).

Composite fuselage section assembly of the Airbus A350 XWB long-distance airliner [18]

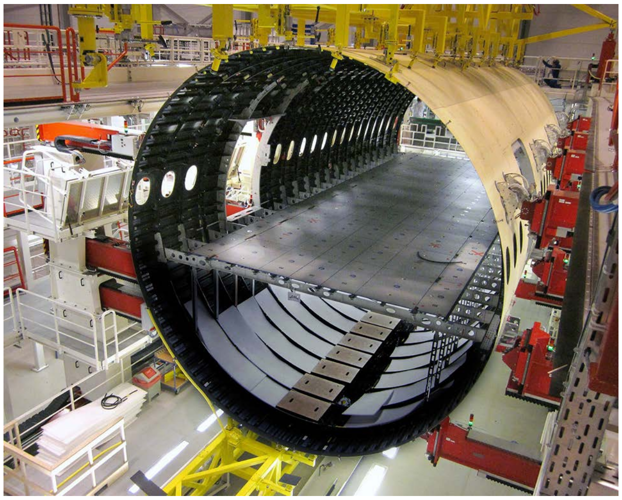

Fully-assembled composite airframe of the Sikorsky S-97 Raider helicopter prototype [19]

NASA Composite Crew Module demonstrator [20]

NASA-Boeing composite cryogenic propellant tank (cryotank) demonstrator (5.5 m dia.) [21]

Fig. 1-2. Examples of novel, large-scale and integrated aero-structures made of CFRPs [18-21].

In turn, the majority of PMCs currently used in industry consist of thermosetting matrices (irreversible cure), epoxy resins being the most common subclass given a potent combination of cost-efficiency, thermo-mechanical properties, chemical and environmental resistance and practicality of use and storage [1, 3]. Aero-structural parts typically consist of laminated stacks of prepreg plies that can be oriented to address specific load cases. *Prepregs* are beds of primary fibre reinforcement (unidirectional beds—tape—or fibre tows woven into a fabric) that are “pre”-impregnated with *b-stage resin* (catalyzed but effectively uncured). Once cured, the resin matrix fully encapsulates the fibres and acts as an environmental shield. In addition, it serves to maintain the part geometry, transfer loads between fibres and resist interlaminar stresses [2, 3, 15].

The mechanical and chemical attributes of PMCs render them highly-desirable for aero-structural applications given the cyclical and hygrothermal loading typically experienced by aircraft frames among other conditions such as exposure to jet fuel. Their advantageous properties and design versatility ultimately translate into improved aircraft fuel efficiency, maneuverability, range, payload capacity and service life, in addition to reduced scheduled maintenance and operating costs [2, 7, 13, 14].

At first, the use of PMCs was limited to secondary structures such as flaps, engine nacelles and fairings. The development in the 1980s of the Bell-Boeing V-22 Osprey military tiltrotor aircraft as part of the US Army's Advanced Composites Airframe Program (ACAP) and the Airbus A320 short-to-medium range airliner as a response to the 1970s energy crises marked the first extensive use of PMCs in primary structures such as the fuselage, wings and empennage: > 43 and 28 wt.% of the airframe for the V-22 and A320, resp. [2, 13]. It should be noted that a few highly-covert, military programs such as the Northrup Grumman B-2 Spirit stealth bomber made far more extensive use of state-of-the-art PMCs years prior to civil aviation and more visible defence programs—though information about the true extent of their composite usage remains classified.

The adoption of PMCs for primary structural applications has soared in the 2000s thanks in part to automation of "on-wing" repairs and the development of non-destructive inspection/evaluation (NDI/NDE) techniques, which have greatly improved trust in the flight worthiness of composite structures and thus facilitated their certification [7, 22]. The airframe of the Boeing 787 Dreamliner long-range airliner, which made its maiden flight in December 2009, consists of 50 wt.% of PMCs with the majority being CFRPs [23]. Aluminum alloys account for only 20 wt.%, which is up to a four-fold reduction compared to the airframe of a typical airliner. In turn, its direct competitor is the Airbus A350 XWB, which made its maiden flight in June 2014, and contains 52 wt.% of PMCs [24]. Propelled by Boeing's radical design, both manufacturers eventually adopted an all-composite fuselage—not seen before in civil aviation for a large airliner [25]. The manufacturing, operation and maintenance cost-savings of this new generation of integrated, composite-airframe airliners is highly lucrative for manufacturers, airlines and ultimately passengers—not to overlook, eco-friendlier given the significant, in-service reduction in greenhouse emissions [26]. This trend towards larger and more integrated composite structures is currently rapidly permeating the other transportation industries, namely the automotive [27] and marine [28] sectors.

Enduring challenges

Despite recent trends, composite aero-structures remain limited to mostly shell-like parts with relatively simple geometries that still rely on mechanical fastening as a primary means of assembly. To this end, recent developments are underway to replace metallic assembly components. Hybrid bolted-bonded joining represent a stepping stone to complete co-bonding of integrated aero-structures [29], which is still in early development [30]. In turn, randomly oriented strand (ROS) composite moulding aim to replace complex-shape metallic parts such as brackets [31]. Still, load cases have become correspondingly complex and often include critical out-of-plane components. Stress engineers rely on through-thickness (T-T) mechanical test methods to generate representative interlaminar strength allowables for structural design. Improving the reliability of these test methods continues to be of critical importance notably as they can play an important role in the development of next-generation, multiaxial failure criteria [32]. It should be noted that the terms "T-T" and "out-of-plane" are used interchangeably throughout this thesis.

In turn, the relatively low fracture toughness of thermosetting resins remains their Achilles Heel (Fig. 1-1.A). Prepreg laminates with thermosetting matrices typically exhibit brittle damage initiation modes (or failure mechanisms) that can engender catastrophic failure. The most prevalent modes are matrix micro-cracking, interply delamination and fibre fracture—the first two being matrix-dominated mechanisms [33-35]. A fourth, matrix-dominated mechanism appears in compression, namely the formation of "kink-bands" caused by fibre micro-buckling [36, 37]. The synergistic presence of these failure mechanisms engenders relatively weak in-plane compressive properties [37] and weaker-still transverse and interlaminar properties [36, 38] due to the presence of fibres and processing defects acting as stress concentrators [35].

In particular, delamination is especially detrimental to the overall structural integrity of laminates rendering resin toughness a key property [3, 33, 35, 38, 39]. Fig. 1-3 illustrates the delamination failure of a laminated T-joint coupon, which is representative of sharply-curved details in aero-structures (stiffeners, ribs and spars). Furthermore, damage initiation modes greatly depend on reinforcement type (fibre architecture). For instance, woven composites are riddled with matrix-rich interstices in-between woven yarns, where matrix micro-cracking can initiate, and which are very difficult to conventionally reinforce [40]. Lastly, sharply-curved details that are subjected to T-T loads in the plane of curvature are especially vulnerable to delamination due to the presence of critical interlaminar stresses [41].

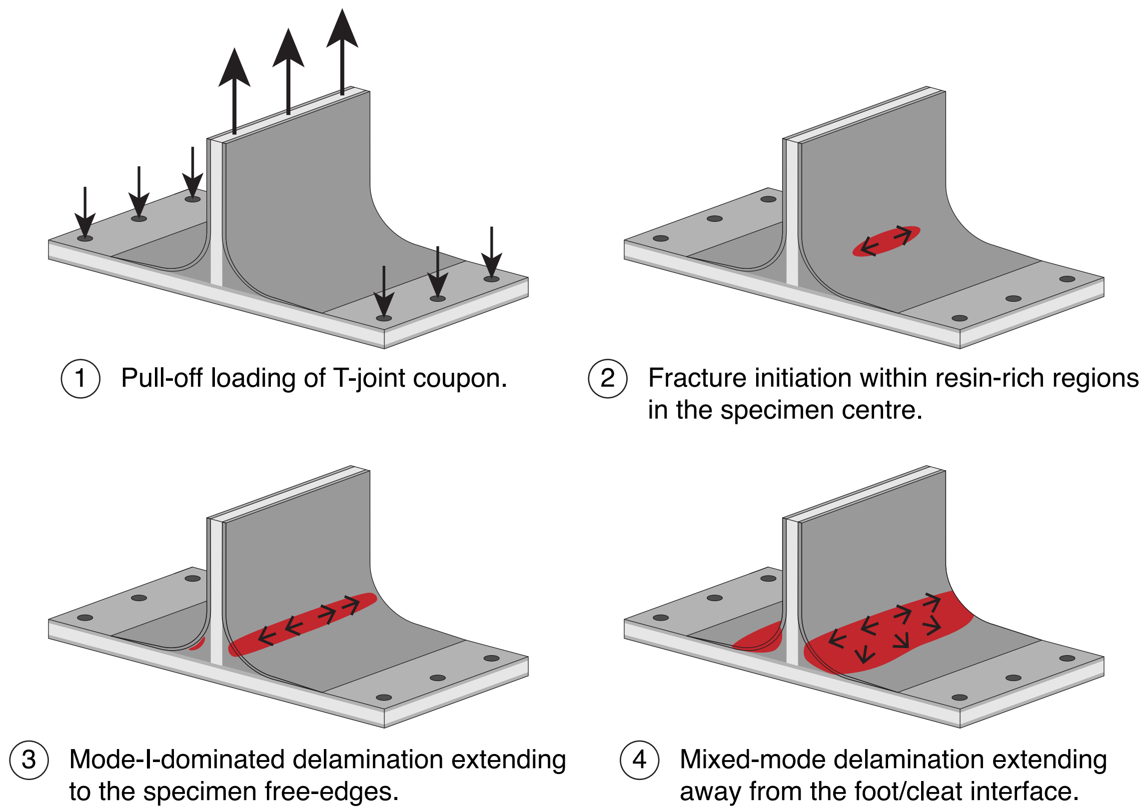

Fig. 1-3. Example of delamination initiation and growth in a laminated T-joint coupon (adapted from [42]).

With respect to prepreg laminate processing, industrial autoclaves remain the preferred means of curing for the majority of high-performance, thermoset-based composite applications. An autoclave is essentially a large pressure vessel and a convection oven combined into a single unit to regulate both ambient pressure and temperature during the cure. For one, primary aero-structures require excellent laminate consolidation that can currently only be reliably achieved via autoclave curing (e.g. all examples given in Fig. 1-2 except for the NASA cryotank). High consolidation pressure (up to 7 atm) translates into high hydrostatic resin pressure during resin impregnation and gelation, which effectively suppresses void formation—one of the most consequential types of defects affecting the mechanical strength and delamination resistance of composite laminates. Autoclave curing thus remains the benchmark process against which other processes are evaluated [15, 43-46].

The adoption of PMCs has historically been solely performance-driven [45]. Nonetheless, the demand for ever larger and integrated structures across industries is rapidly exacerbating the capacity of current autoclave infrastructure and equipment thereby imposing a new economic paradigm. Upfront capital investment and operating costs are rising steeply as autoclaves increase in scale to keep up with demand. Meanwhile, production is adversely affected, and the rates of composite insertion and innovation in industry may in turn suffer. One incentive across industries to circumvent these impediments is to shift away from autoclave processing towards more energy-efficient, low pressure (< 1 atm), out-of-autoclave (OOA) processes such as vacuum-bag-only (VBO) processing of dedicated prepregs. These technologies aim to deliver the same level of quality and performance, while significantly lowering equipment acquisition and operating costs, improving energy efficiency and streamlining production [6, 47-49]. Fig. 1-4 showcases the difference in the infrastructure required for conventional autoclave processing of large, integrated composite structures compared to VBO processing in a more readily scalable convection oven.

Large autoclave used to cure the wing shells of the Airbus A350 XWB airliner [60]

Scalable industrial convection oven for VBO processing of large composite parts [61]

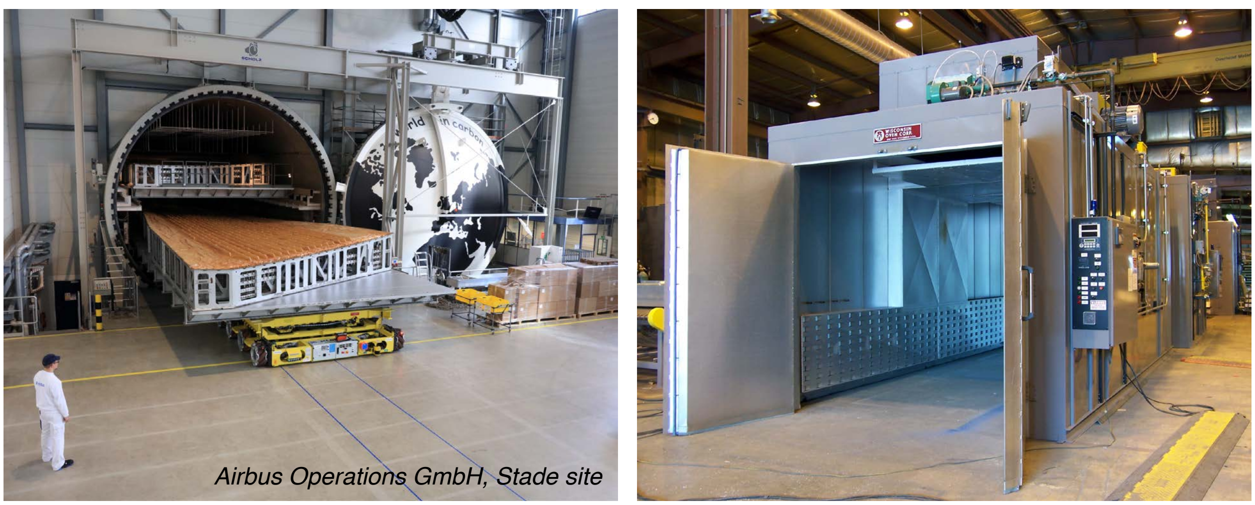

Fig. 1-4. Typical industrial equipment used to cure advanced composite aero-structures (from: [50, 51]).

High-quality, flat laminates can already be readily achieved via VBO processing thanks to advances in dedicated prepregs that feature improved air evacuation and optimized resin chemistry [49, 52-58]. More recently, such processes have been used to cure a select few aero-structural parts of increasing size, complexity and structural importance [6, 49, 52, 57, 59-61]. In particular, the

NASA-Boeing cryotank demonstrator (Fig. 1-2) is one such successful example of the novel application of OOA and VBO technologies to replace an existing large-scale, complex-shape and critical aero-structure previously consisting of an all-metal design.

Despite this recent progress, the key challenge for OOA and, more specifically, VBO technologies remains the inherent variability observed in cured complex-shape regions (e.g. corners) that primarily exhibit significant local thickness deviation and porosity, in addition to in- and out-of-plane fibre waviness. The accelerated insertion of these technologies in high-end industries hinges on a deeper understanding of the influence of processing parameters on laminate consolidation and mechanical performance in complex-shape laminates. In addition, the development of robust predictive tools and design guidelines that can accurately predict thickness deviation, porosity and their combined effect on mechanical performance will further help to bolster industry confidence in and acceptance of these maturing technologies.

1.2 Chapter outline

The remainder of this chapter delves deeper into the aforementioned challenges to underscore the motivation for this thesis. First, prepreg laminate processing is presented in § 1.3 comparing VBO processing to conventional autoclave processing. Then, T-T mechanical test methods are discussed in § 1.4 with regards specifically to the most recent development in ILT-testing and representative coupon selection for sharply-curved, aero-structural details. Next, the state of research on variability and defects and the mechanical performance of VBO laminates are discussed in § 1.5 in terms of both flat and complex-shape laminates. Finally, the findings of the surveyed literature and the thesis objectives and structure are presented in §§ 1.6 and 0, resp.

1.3 Prepreg laminate processing

1.3.1 Overview

The vast majority of advanced composite aero-structures consist of thermoset prepreg laminates that require a carefully selected application of temperature and pressure to achieve the high quality required for high-performance structural applications—effectively defect-free parts.

To this end, autoclave processing has been the customary route since the late 1940s, and VBO processing has been gaining traction since the Nineties and maturing out of the R&D phase. Both processing routes employ a vacuum-bagging arrangement enclosing the laminate onto a processing tool and consist of four overall stages: 1) prepregging (production of dedicated prepregs), 2) ply collation (layup), 3) vacuum-bagging (assembly of processing consumables) and 4) processing (laminate consolidation and cure). This section provides an overview of both processing routes focusing on of their key differences at each of the four processing stages (§§ 1.3.2 and 1.3.3), as well as an outlook on the future of VBO processing (§ 1.3.4).

1.3.2 Autoclave prepreg processing

Autoclave processing predictably and repeatedly produces laminated parts of the highest quality, and thus remains the benchmark-process for aero-structures. Autoclave prepregs are typically fabricated via hot-melt impregnation, which consists of the following steps: 1) coating siliconized release paper with a film of b-stage resin (catalyzed but effectively uncured), 2) sandwiching one or both sides of a dry fibre-bed with coated release paper in a prepegging unit, 3) impregnating the dry fibre-bed by passing the sandwiched sheet through heated compaction rollers, and 4) rolling the continuous prepreg feed onto a spool [45, 62]. The applied heat is carefully controlled to fully wet-out the dry fibre-bed by lowering the resin viscosity—autoclave prepregs are widely assumed in the literature to be fully impregnated. Importantly, the resin is only negligibly-cured (short heat exposure) to retain optimal flow potential while achieving a moderately self-adhesive tack at room-temperature to aid with later ply collation [63]. Lastly, prepreg rolls are stored in refrigerators until parts are ready for layup and processing to stall the resin polymerization reaction.

Standard tape and 2D-woven prepregs contain 34-45 wt.% and 30-60 wt.% of resin, resp., and are 0.05-3 mm- and 0.1-0.5 mm-thick, resp. Importantly, autoclave prepregs are designed to contain a surplus of resin that will be bled out of the part during the cure to achieve a desired fibre volume fraction (60-65%). Prepreg are generally conceived with a 1:1 fibre-to-resin weight ratio, which results in roughly 10 wt.% of resin loss via bleeding [62].

The second phase, ply collation (layup), consist of assembling the part by laying up and collating precut prepreg plies according to a specific stacking sequence (set of ply orientations) onto a processing tool surface. Layup for small-scale production is often manual; however, the process can be automated for large parts and production lines using automated tape laying or fibre placement (ATL/AFP) [44, 64]. It should be further noted that a typical aero-structure will consist of freshly-laminated prepreg plies in addition to other components such as honeycomb core inserts and pre-cured composite stiffeners, which are co-bonded with structural adhesives and added during the layup stage or during secondary processing operations [43, 45].

A critical aspect of layup is the potential entrapment of air between plies [45], which may result in undesirable levels of porosity in the finished part that will affect interlaminar strength properties. Care must be taken by the operator to properly lay down plies with a hand-roller and proper "squeegeeing" technique [65, 66]. In addition, complex tool-shapes may impede ply collation and may require intermediary debulking, which is the process of compacting the laminate after the addition of each new ply or group of plies by temporarily covering the laminate with a vacuum-bag and pulling vacuum (up to 30 min) [67]. This process encourages prepreg draping and laminate consolidation while also aiding with the removal of entrapped air. Finally, the layup duration may be extensive on the order of hours for small parts to weeks for large integrated parts (e.g. airliner wing shells). The resin may polymerize to an undesirable degree-of-cure during this time, which will adversely alter its thermo-viscous properties. To this end, optimizing the resin chemistry has played a key role in extending the RT out-time of prepregs, during which the thermo-mechanical properties remain stable and optimal for resin-flow [45].

The third phase, vacuum-bagging, consists of enclosing the laminate with an impermeable seal onto the tool surface prior to curing. A standard vacuum-bagging arrangement and an autoclave system are illustrated in Fig. 1-5. First, the tool surface is coated with a release agent or simply covered with a release-film, on top of which the laminate is typically directly assembled. An edge-dam (edge-bleeder) and a perforated release-film and bleeder-cloth are then placed around and atop of the laminate, resp., to allow for the removal of surplus resin and bubbles of entrapped air and cure volatiles. A textured peel-ply may alternatively be used in place of the perforated release-film to leave a fine imprint onto the laminate surface and improve the later adherence of coatings. Next, the part is covered with a breather-cloth layer to create a pathway between the laminate and vacuum-ports and to ensure that an even vacuum pressure is exerted over the entire part. Lastly, an impermeable vacuum-bag is placed atop the assembly and sealed around all edges with a gummy sealant-tape to create a pressure differential between the laminate and the positive inert gas pressure inside the autoclave chamber. Operator experience and strict adherence to best practices and the order of processing consumables is key to achieving high-quality parts. The typical issue arising during vacuum-bagging is the presence of air leaks that result in suboptimal void suppression—it is imperative to check the bagging under vacuum prior to starting the curing process [44, 45, 52, 66]. Some leaking is however unavoidable. To this end, the acceptable leakage rate in industry is ≤ 0.7 kPa/min.

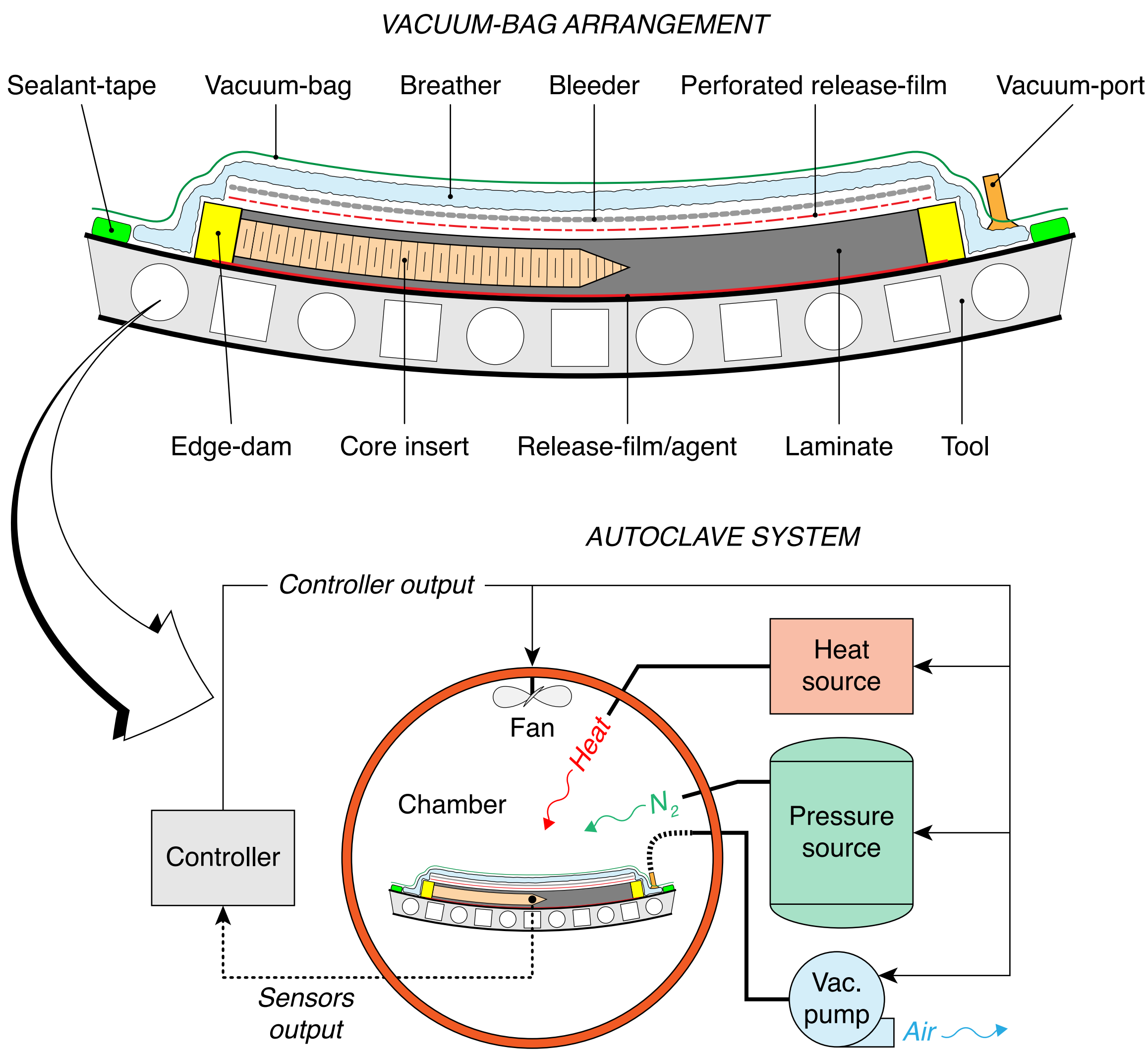

Fig. 1-5. Standard vacuum-bag arrangement and autoclave system (adapted from [43]).

The fourth and final stage, processing, consists of carefully selected temperature and pressure cycles applied in concert to the vacuum-bagged laminate inside of the autoclave chamber (Fig. 1-5) to essentially form the finished part (barring secondary and finishing operations). In the case of thermoset-matrix composites, the processing phase is critical given that the material and part geometry are created simultaneously: the thermo-mechanical properties of the resin matrix and the consolidated laminate quality are thereafter permanent. A standard autoclave processing cycle for a thermoset prepreg laminate is presented in Fig. 1-6 and consists of three phases: resin-flow, curing and part cooling.

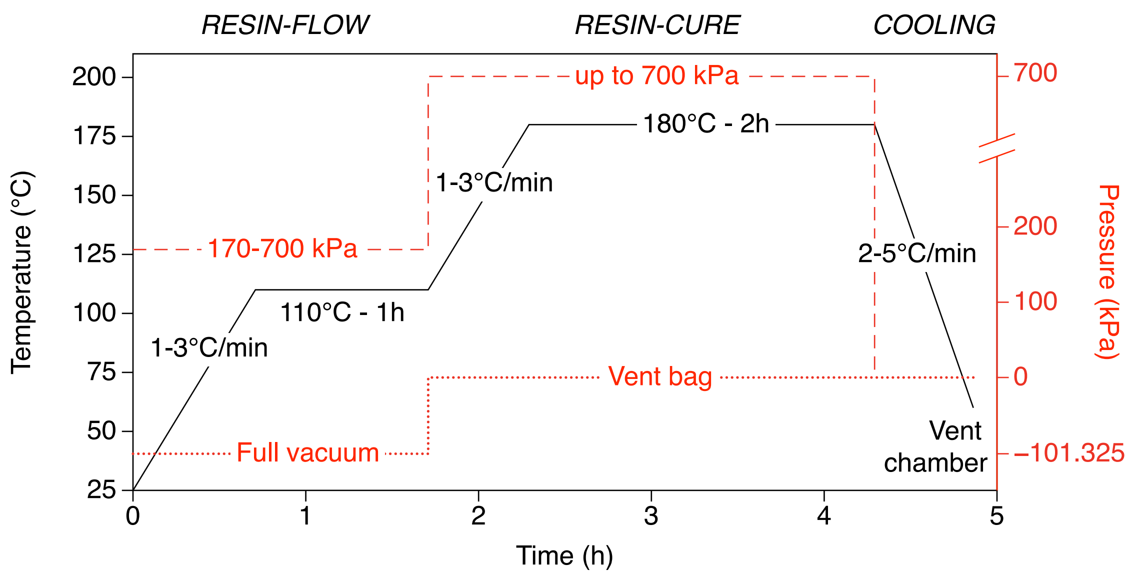

Fig. 1-6. Standard autoclave processing cycle for a monolithic prepreg laminate (data from [46, 68]).

With respect first to the resin-flow phase, the application of a thermal ramp (typically 1-3°C/min) allows the resin to melt and flow. Importantly, temperature activates the exothermic polymerization reaction of the resin (crosslinking of polymer chains). In turn, resin viscosity is a function of the degree-of-cure (extent of crosslinking) and temperature. This first ramp causes the viscosity to initially plunge to a minimum value, after which it rapidly increases as the reaction progresses. A short isothermal dwell (~1h; temperature depends on resin system) thus follows the initial ramp to maintain a low-enough viscosity and extend the resin-flow phase. Meanwhile, full vacuum is pulled inside of the vacuum-bag (ideally up to 101.3 kPa), and the autoclave chamber is simultaneously pressurized (170-700 kPa depending on the prepreg system). Importantly, the bag pressure must be less than the chamber pressure to guarantee fibre-bed compaction. It may further be noted, as an aside, that autoclave chambers are filled with purified nitrogen (N_2), an abundant and relatively cheap inert gas to avoid oxidation reactions and the hazard of potential combustion.

The careful application of temperature and pressure promotes the removal of entrapped air and curing volatiles (bubble migration) via resin bleeding, which is a function of fibre-bed permeability and resin viscosity. The fibre-bed permeability decreases as resin bleeds and the laminate compacts. In turn, the bleeding rate abates as the resin cures and its viscosity increases exponentially. The aim of the resin-flow phase is thus to control resin bleeding such as to maximize bubble migration while preventing the formation of resin-rich or -starved regions [43-46].

With respect then to the resin-cure phase, the application of a second thermal ramp up to a longer, elevated isothermal dwell (~2h; temperature depends on resin system) allows the resin to gel, vitrify and reach a very high degree-of-cure for optimal thermo-mechanical properties. *Gelation* is the point at which the viscosity reaches an infinite value, flow ceases and the resin attains a non-zero modulus of elastic (may sustain non-hydrostatic stresses); in turn, *vitrification* is the point at which the resin's instantaneous glass-transition temperature surpasses its local temperature and the thermo-mechanical behaviour becomes highly-elastic. A standard autoclave cure cycle is designed for both of these transitions to occur during the second, resin-cure isothermal dwell rather than during a thermal ramp such as to minimize thermal gradients and limit the formation of residual stresses [43].

Meanwhile, immediately before the second ramp, the vacuum-bag is allowed to vent to atmospheric pressure, and the chamber pressure is increased to a maximum value (up to 700 kPa) to fully consolidate the laminate and collapse remaining voids. Venting before the start of the curing phase is critical for void suppression. Whereas vacuum helps to remove volatiles during the resin-flow phase, it can have the reverse effect and trap volatiles during gelation in the event that the resin continues to outgas. This issue is compounded by the fact that the hydrostatic resin pressure reaches a minimum value during the second ramp. Understanding and predicting void formation is a key yet complex aspect of the process cycle design. Finally, the third and final processing phase involves part-cooling with a thermal ramp (2-5°C/min) to 50-60°C, beyond which the autoclave chamber may be safely vented. Importantly, the cooling ramp may impart additional residual stresses and must not, therefore, be overlooked [43-46].

Autoclave processing has evolved into a well-understood and dependable process for curing prepreg laminates requiring optimal mechanical properties. Table 1-1 lists the main advantages and disadvantages of this process. The application of high-pressure bearing down onto the laminate is the primary attribute of autoclave processing and results in effectively defect-free parts by crushing voids and consolidating the laminate up to high fibre volume fractions. Furthermore, a state-of-the-art process modelling approach has been developed over the past three decades to tackle lingering performance issues such as part distortion (residual stresses) and sandwich core effects (e.g. skin-dimpling and core-crushing). Beyond predicting part defects, these modelling advances can optimize tooling, autoclave thermal efficiency and control systems and, in turn, significantly decrease equipment and operating costs. Though important work remains to streamline process design, autoclave prepreg processing may be considered to be a mature and proven processing route [43-45, 48].

Table 1-1. Attributes of autoclave prepreg processing (adapted from [43, 48]).

Advantages	Disadvantages
- Optimal laminate quality and properties	- Massive upfront investment
- Compatible for large, integrated parts	- Production line bottleneck (limited capacity)
- Robust, repeatable process	- Long processing turnaround time
- Well-understood, predictable process	- Excessive energy consumption
	- High pressure
	- Difficult temperature control (thermal latency)
	- Substantial cost for lost nitrogen
	- Costly tooling
	- Large footprint and elaborate infrastructure

Despite these clear benefits, autoclave processing is not without important shortcomings as listed in Table 1-1, which are mostly economic in nature. In particular, the system is not very thermally efficient as it takes an inordinate amount of time to heat up and cool down the tooling and all-nitrogen atmosphere inside the chamber. In turn, the finite capacity of even the largest autoclaves represents a bottleneck in production lines, which is compounded by a long processing turnaround-time. Next, the processing equipment and associated operating costs all rise at once as autoclaves increase in scale to keep up with the demand for ever larger, integrated structures such as entire airliner fuselage sections. Autoclave processing remains economical only for high-end, low-volume and slow-production applications. Meanwhile its massive cost, among other shortcomings, is a significant deterrent against the continued adoption of structural PMCs across industries. Whereas the adoption of PMCs has historically been performance-driven, their democratization has elevated cost-efficiency to be the principal driver behind the push to develop cheaper OOA technologies such as VBO processing of dedicated prepregs with increasing parity in laminate quality and mechanical performance [43-45, 48].

1.3.3 VBO semipreg processing

OOA processing is an umbrella-term describing the family of processes developed, in part, to address the economic shortcomings of autoclave processing. These processes can be grouped into two subclasses: liquid composite moulding (LCM) such as vacuum-assisted resin infusion (VARI) and prepreg-based processes such as VBO processing of dedicated prepregs in a regular convection oven. Though compression moulding of thermoplastic-based PMCs (heat-pliable and re-mouldable) is technically an OOA process, the majority of OOA applications are aimed at thermosetting systems. In particular, LCM processes replace the conventional autoclave prepregging, layup and vacuum-bagging stages with a single, closed-mould application. This route is more versatile (high variety of heating methods), faster (high level of automation, fewer operations and near net-shape parts) and cheaper in terms of material costs (no-prepregging and less scrap). However, two-sided, pressurized tooling is prohibitively expensive—similarly to autoclave processing, and single-sided, vacuum-only processing results in lower quality and performance parts due in part to lower fibre volume fractions. Still, LCM is a good candidate for higher volume, faster production and less critical applications. Meanwhile, VBO processing of dedicated prepregs represents the best, low-pressure candidate-process to replace autoclave processing in many structural applications given a desirable combination of cost-effectiveness, sustainability and improving performance [48, 49, 52].

With respect first to prepregging, early attempts at VBO processing with autoclave prepregs resulted in unacceptable levels of porosity due to low applied pressure and inconsistent resin bleeding, particularly in the case of high fibre volume fraction prepregs. In turn, the high-porosity had a detrimental effect on laminate fracture toughness (resistance to delamination) [49]. As the fibre-bed compacts, it takes on an increasing portion of the applied consolidation pressure at the detriment of the resin hydrostatic pressure. The combination of resin bleeding and less-than-ideal vacuum-bag pressure due, for instance, to vacuum-bag leaks further lowers the resin pressure below that of entrapped gases and effectively inhibits the collapse of voids, which may in fact expand in volume [44, 52].

The current, second-generation VBO prepregs are uniquely different from their autoclave predecessors in that they incorporate air evacuation pathways directly into the prepreg, as illustrated in Fig. 1-7. These pathways are created by controlling the degree of impregnation during prepregging. Whereas autoclave prepregs are effectively fully-impregnated, VBO prepregs are only semi-impregnated on both major surfaces, allowing the midplane of tape prepregs and the tow-cores of 2D-woven prepregs to remain resin-free [49, 52]. VBO prepregs are henceforth referred to as *semipregs* to distinguish them from conventional autoclave prepregs. The two most prevalent semipreg resin systems are currently MTM45-1 and CYCOM® 5320 epoxy resins, both of which are manufactured by Cytec, USA [48, 49, 52].

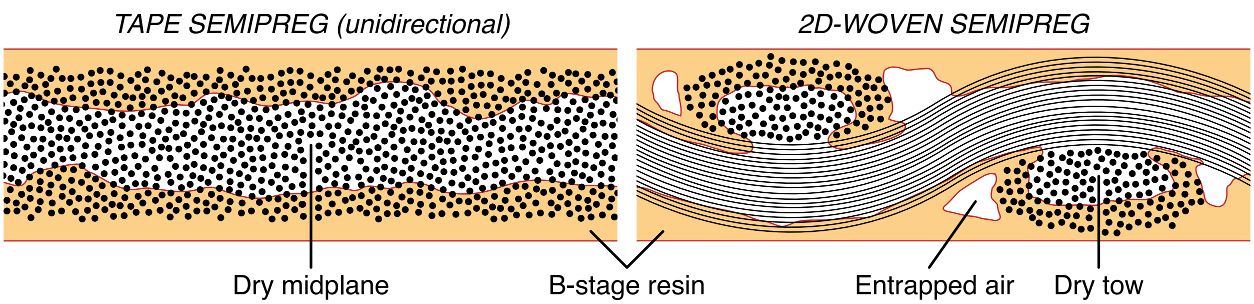

Fig. 1-7. In-plane air evacuation strategies of current-generation semipregs (cross-sectional view).

Physical air evacuation pathways are much more effective at evacuating entrapped air than bubble migration via resin-bleed in conventional prepregs, which is only acceptable given the ability to subsequently crush remaining voids. Semipregs are not typically designed to bleed resin and thus only contain the desired, final weight-fraction of resin. In addition, the resin chemistry has been optimized to minimize the release of curing volatiles. However, the presence of dry-fibre regions renders semipregs more delicate to handle, notably in the case of tapes, even though the application of resin to both sides helps to keep their integrity. Once the ply is collated, it cannot be removed without tearing it apart, rendering mistakes during layup very costly. Importantly, semipregs also possess significantly higher bulk-factors than conventional prepregs, which is the ratio of the uncured-to-cured ply thicknesses [49, 52]. This attribute is undesirable yet unavoidable and will be later discussed in the context of laminate thickness variation in complex-shape parts.

With respect then to ply collation, the process of laying down plies is identical to that of autoclave prepreg processing, although particular attention ought to be given to intermediary debulking for complex-shape laminates given the higher bulk-factors of semipregs. The main differences with autoclave processing as far as part-assembly is concerned arise in the sequence of vacuum-bagging consumables. To avoid resin-bleed, the perforated release-film and bleeder-cloth placed directly atop of the laminate are replaced by a single sheet of non-perforated release-film. In turn, the edge-bleeder dam is replaced by an edge-breather dam, which only allows entrapped gases to escape while effectively sealing the resin in the laminate. Edge-breather strips typically consist of lengths of gummy sealant-tape (or cork noodles) that are partly-wrapped in dry fibreglass tape of the kind typically used in the boating industry, as illustrated in Fig. 1-8. The bottom of the strip is free of tape such as to form a tight seal with the tool surface. Meanwhile, the fibreglass tape is directly pressed against the edge of the laminate on one side and allowed to freely drape on the other side such as to contact the breather layer and form an air permeable bridge. Importantly, the strip must be at least as tall as the debulked laminate [52, 56, 69].

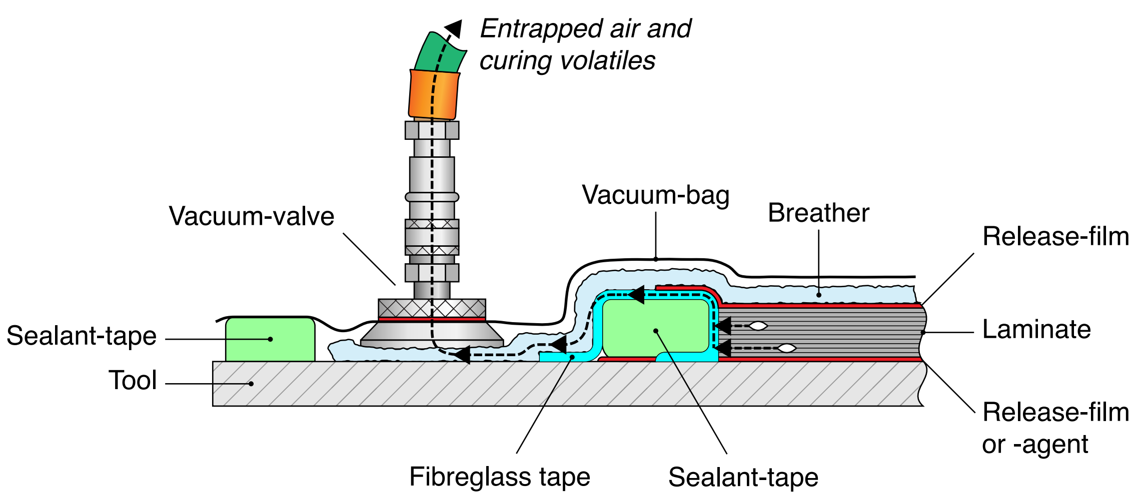

Fig. 1-8. Edge-breathing strategy.

With respect finally to processing, the cure cycle is notably different from autoclave processing in that it is preceded by a crucial step, air evacuation, and takes place outside of the high-pressure environment of an autoclave chamber. Fig. 1-9 illustrates the typical cure cycle and semipreg laminate consolidation during VBO processing. First, air evacuation is achieved via the application of a vacuum-hold (Fig. 1-9.B), which consists of drawing vacuum in the bag at room-temperature. The maximum amount of entrapped air must be removed during this critical step. In addition to evacuating entrapped air, the applied pressure compacts the fibre-bed and thus increases the fibre volume fraction while reducing the laminate thickness. It should be noted that negligible resin-flow occurs given that the operation takes place at room-temperature (high resin viscosity). Lastly, the length of the vacuum-hold is a function of the part-size and semipreg permeability and can take well in excess of 15h for large parts given the mediocre in-plane and very poor out-of-plane air permeability of current-generation semipregs [48, 49, 52, 70].

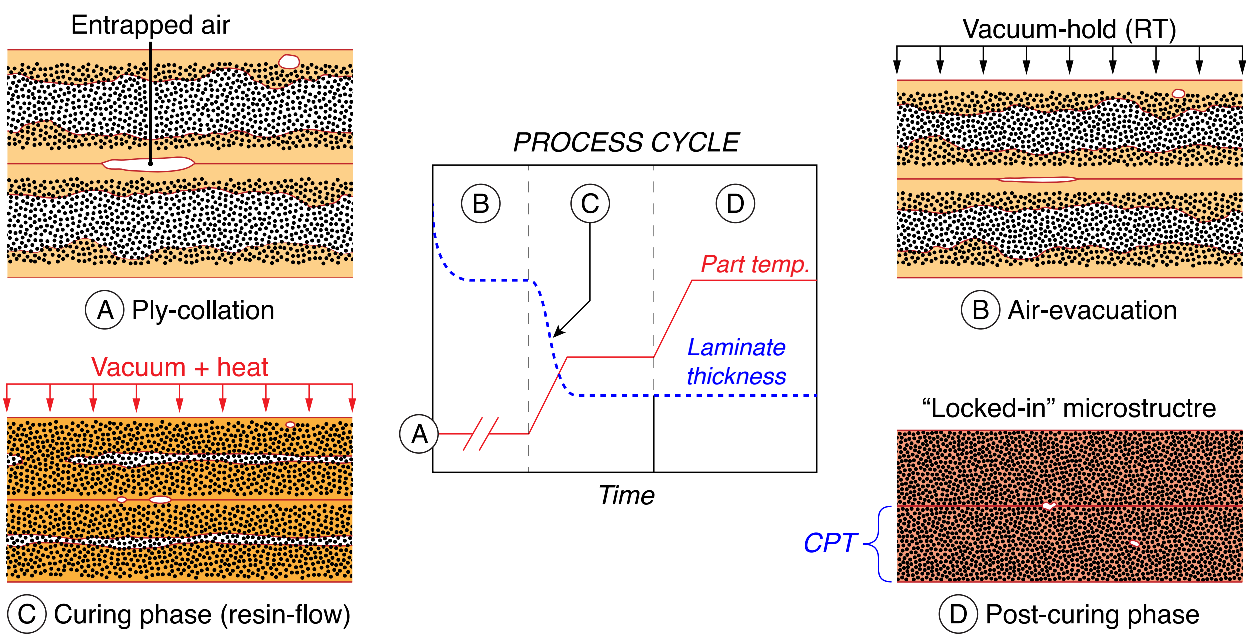

Fig. 1-9. VBO semipreg laminate consolidation during the processing and curing (adapted from [49, 52]).

In turn, the cure cycle typically takes place in a regular convection oven (Fig. 1-4)—although emerging heating technologies such as heated tooling (electric or fluid systems) are now under development. It should first be noted that the cure cycle terminology varies somewhat from that of an autoclave cure cycle. The resin-flow phase is commonly referred to as the *curing* phase (Fig. 1-9.C) for many VBO resin systems such as Cytec CYCOM® 5320, because gelation occurs during the first isothermal dwell. This first dwell is also longer than that of the standard autoclave cycle (~2h vs. ~1h, resp.). The second phase is then referred to as the *post-curing* phase (Fig. 1-9.D) as vitrification still occurs during the second isothermal dwell. Importantly, the oven chamber is under atmospheric pressure with the sole source of consolidation pressure being the vacuum pulled inside of the vacuum-bag. The consolidation pressure is thus vulnerable to altitude and atmospheric effects. The processing cycle is no longer truly a time-temperature-pressure cycle from a system control aspect, but rather more simply a time-temperature cycle [49, 52].

During the curing phase, resin flows and wets-out the dry-fibre regions used for air evacuation. Full resin impregnation typically occurs during the first thermal ramp. In turn, the fibre-bed further compacts and the laminate experiences a second thickness-drop that effectively reaches the cured ply thickness (CPT). Though the air evacuation channels are now blocked, bubble migration may still be possible while the local resin viscosity remains low enough. Importantly, there no longer is a need to vent the vacuum-bag prior to gelation given resin chemistries optimized for negligible outgassing. Full laminate consolidation and void collapse must occur during the resin-flow phase given the limited consolidation pressure, which is why the air evacuation step and a strong vacuum source are quintessential (> 95 kPa). The vacuum-bag may in fact be removed for the post-curing phase and the laminate allowed to free-stand for the remainder of the cycle—provided it can sustain its own weight. A free-standing post-cure can help to mitigate the effects of cure shrinkage such as residual stresses and "spring-in" of complex-shape features due to thermal gradients in the part and the local mismatch in the coefficient of thermal expansion (CTE) between the tool and the laminate [49, 52].

Specific considerations with respect to processing complex-shape, semipreg laminates are presented in-depth in Chapter 2, which deals with the materials and general methods of this thesis. Of particular note are the vacuum-bagging strategies over sharply-curved details and the vacuum-hold and thermal cycle design. The following works are otherwise recommended for a more general overview of OOA and, in particular, VBO processing. First, Schlimbach and Ogale present a practical overview of OOA processes, including semipreg processing via a variety of heating technologies in terms of their positive and negative attributes, economic considerations and future trends [48]. In turn, a literature review by Centea *et al.* offers a comprehensive overview of semipreg processing, notably on the topics of air evacuation, resin flow, laminate compaction and void formation, in addition to giving an overview of important academic and industrial demonstrator parts and discussing the economics of prepreg processing [49]. Lastly, Hubert *et al.* most recently authored a seminal chapter on VBO processing advances in *Comprehensive composite materials II* that notably presents the state-of-the-art of VBO process modelling and design tools and highlights the next areas of progress [52].

Advances in VBO processing and semipregs over the past three decades are rapidly closing the gap in laminate quality and performance with conventional autoclave processing. Table 1-2 summarizes the main advantages and disadvantages of VBO semipreg processing in a convection oven compared to autoclave prepreg processing. As indicated in the previous section, current OOA resins, semipregs and process modelling and design tools are already capable of achieving flat laminated parts that rival the quality and performance of similar parts cured in an autoclave under very high pressure [49, 52-57]. Furthermore, the jump to large, integrated structures is well-underway in the aerospace industry [6, 49, 52, 57, 59-61]. The cost-effectiveness of VBO semipreg processing is bound to improve as market-demand increases, technological democratization improves and material, tooling and manufacturing costs drop [48, 49].

Still, important performance and economic hurdles remain to be cleared. One such hurdle is the need for a better understanding of variability and defects in sharply-curved details and large-scale structures that are engendered by locally-deficient air evacuation and compaction, and undesirable semipreg properties (e.g. low permeability and high bulk-factor)—among other key factors. This particular hurdle is the primary motivation for this work.

Table 1-2. Attributes of semipreg oven curing compared to autoclave processing (adapted from [48, 52]).

Advantages	Disadvantages
- High-quality and -performance flat laminates* - Increasingly compatible for large, integrated parts - Lower upfront investment - Larger production volume - Simpler process control (ease-of-use) - Relatively well-understood process (recent advances in process modelling and design tools)	- Higher variability and defects in complex-shape laminates (thickening, voids and fibre waviness) - Very long processing turnaround time (additional air evacuation step) - Batch-production* - Relatively high energy consumption (futile thermal mass heating*) - Lower heat transfer rate^ - Still-limited capacity^ - Costly tooling*

*Similar to autoclave processing; ^addressed by emerging heating technologies (e.g. heated tooling).

1.3.4 Outlook on the future of VBO semipreg processing

It will take a decade or more to ascertain whether VBO semipreg processing lives up to the current hype or whether progress stagnates as was the case with the nanocomposite research craze of the past two decades. If the current rates of progress and industrial insertion are any indication, it stands a good chance of becoming the viable alternative to autoclave prepreg processing. Already, the interest surrounding OOA technologies has created an industry-wide paradigm shift towards more cost-effective and sustainable manufacturing.

Three areas of progress are worth briefly mentioning: next-generation semipregs, novel processing technologies and industrial insertion. First, work on the next-generation of semipregs features notable advances in air evacuation strategies. Optimizing the pattern of resin deposition (continuous vs. discontinuous) and the degree of impregnation during prepregging can drastically improve the air permeability of semipregs, thereby improving the robustness of the process and laminate quality while shortening the vacuum-hold required for air evacuation. Notable examples of next-generation semipregs are "USCpreg" [71] developed at the University of Southern California, USA, and Cytec's third-generation of CYCOM® 5320 2D-woven semipregs [72], which both feature resin-gap patterns that expose dry surface-fibres and create a 3D-network of air evacuation channels throughout the ply thickness. Fig. 1-10 illustrates some of the novel T-T air evacuation strategies of this next-generation of semipregs.

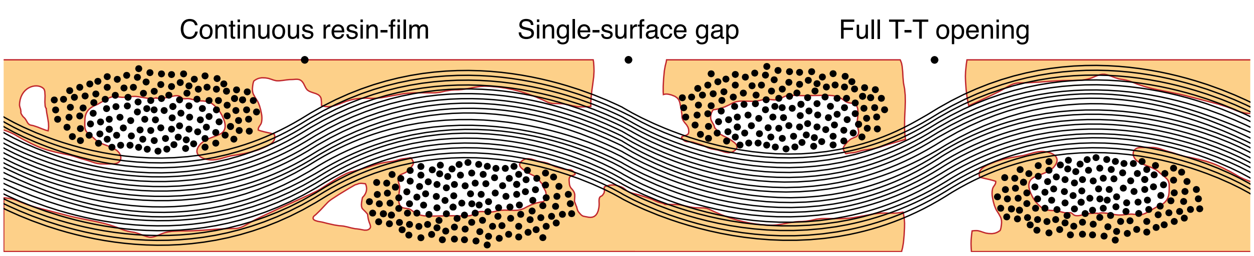

Fig. 1-10. Novel T-T air evacuation strategies of next-generation semipregs (cross-sectional view).

Second, work on process automation is ongoing to minimize layup time and labor cost. To this end, primary suppliers of semipregs and OOA resins such as Cytec and Hexcel are working with end-users such as NASA on new OOA tapes for ATL [61]. Going one step further, NASA demonstrated the potential of combining ATL with the local application of heat and vacuum to cure laminates to a high laminate quality directly during layup [73]. In this same vein, work on alternative heating methods aim to dispense with convection ovens altogether, as they are costly, thermally-inefficient and limited in capacity. To this end, electrical and liquid heated tooling technologies are under development that drastically reduce infrastructural footprints and costs—albeit at an elevated tooling cost, while improving thermal control, reducing heating and cooling durations and optimizing heat distribution (multi-zone heating of complex-shape parts). In addition, breakthroughs in other manufacturing fields such as additive manufacturing can further bolster novel tool-design and, in turn, lower the cost of tool-manufacturing [52].

Last but not least, industrial insertion necessitates improvements in NDI techniques at the various stages of production, in addition to the curation of comprehensive material databases. VBO semipreg processing is more sensitive to material variability, which arises during prepregging in the form of degree and consistency of resin impregnation. To this end, NDI technologies that could characterize the prepreg *in-situ* and perform quality control would greatly improve the robustness of the process [52, 74]. In turn, monitoring part quality post-cure is similarly critical. To this end, the correlation of standardized porosity panels to ultrasound attenuation measurements has been demonstrated for several semipreg systems [49]. This work is being further extended to other invisible defects such as fibre waviness [75].

With respect to material databases, the certification of new material systems and processes in the aerospace industry is very expensive (upwards of US$ 5M for the US Federal Aviation Agency [47]). The National Center for Advanced Material Performance (NCAMP), which is part of the National Institute for Aviation Research (NIAR) at Wichita State University, USA, was setup to work with civil aviation agencies in the US and Europe and address this specific issue [76]. It currently curates a growing database of autoclave prepregs and semipregs such as Cytec's MTM45-1 and CYCOM® 5320 resin systems. Manufacturers only need to prove equivalency with a material in the database to gain certification, while material suppliers can certify new materials independently of aircraft certification programs. Such initiatives will serve to further democratize access to VBO semipregs and OOA technologies and bolster their rate of insertion in structural applications across industries.

1.4 Through-thickness mechanical test methods

1.4.1 Overview

Sharply-curved laminated details in aero-structures that are subjected to T-T loads and, most notably, flexure in the plane of curvature are especially vulnerable to mode-I delamination due to the presence of critical interlaminar tensile (ILT) stresses [41] and given the relatively poor fracture toughness of PMC laminates [3, 33, 35, 38, 39]. Improving the reliability of T-T test methods is thus critically important for the design of integrated aero-structures *vis-à-vis* the determination of representative, interlaminar strength allowables (maximum permissible values for a given design application). In addition, better experimental data will play an important role in the development of future, multiaxial failure criteria [32, 77].

The following section first reviews the evolution of ILT test methods with a focus on representative L-shape specimens (a.k.a. curved beams, corners, angles or brackets) and the limitation of current test methods and standards (§ 1.4.2). In turn, the data reduction is presented for *curved beam strength* (CBS) testing via pure bending along with the determination of *interlaminar tensile strength* (ILTS; i.e. the maximum radial stress) in a curved anisotropic beam experiencing uniform bending (§ 1.4.3). Finally, notable design considerations are discussed regarding the closed-form analytical methods used as part of development processes and the current status of failure criteria aiming to predict delamination in sharply-curved details (§ 1.4.4).

1.4.2 Evolution and status of interlaminar tensile test methods

Kedward *et al.* first surveyed ILT delamination failure of "generic curved regions" in composite aero-structural components due to T-T flexural loads [41]. In turn, they offered a pivotal evaluation of candidate test methods to characterize this critical failure mode. ILT test methods have come a long way since then. Cui *et al.* [78], Broughton [36] and, more recently, Olsson [32] surveyed ILT test methods at different stages of their development. T-T test methods for the determination of ILTS can generally be sorted chronologically into two specimen types and four loading configurations, as illustrated in Fig. 1-11: A) "flatwise" testing of thick laminate coupons via T-T tension and waisted gauge sections (1986 [79]); and L-shape specimens tested under B) single-cantilever tension via a frictionless link (1991 [80]), C) tensile end-loading via a double hinged-clamp mechanism (1991-3 [81, 82]) and D) four-point bending (1994 [83]).

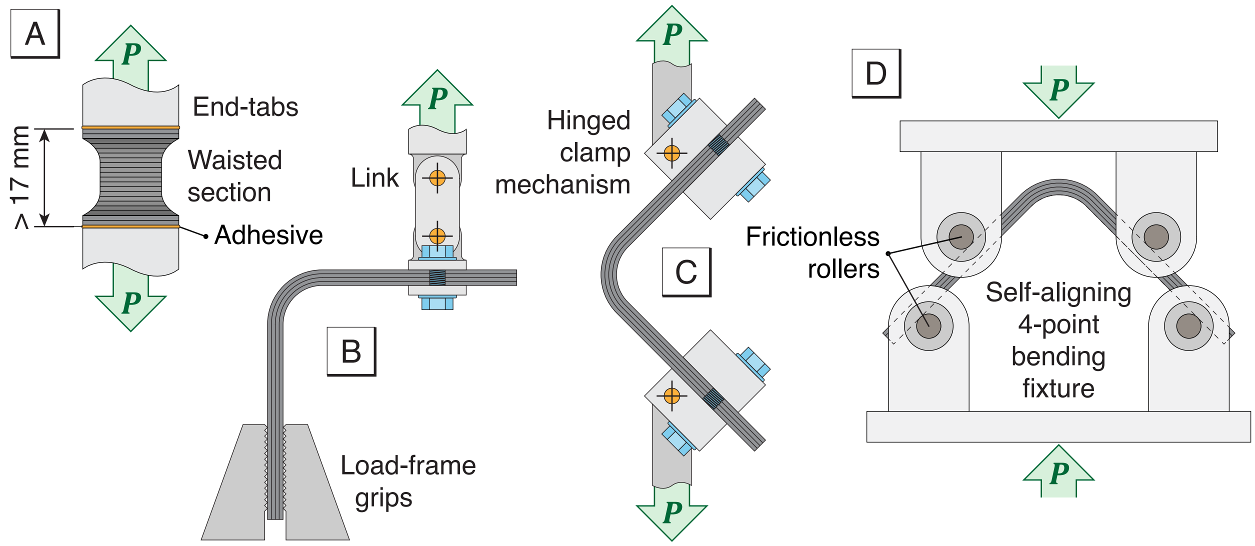

Fig. 1-11. Evolution of ILT test methods: A) T-T "flatwise" thick waisted coupons (1986 [79]); L-shape specimens tested under: B) single-cantilever tension via a frictionless link (1991 [80]), C) tensile end-loading via a double hinged-clamp mechanism (1991-3 [81, 82]) and D) four-point bending (1994 [83]).

Flatwise tensile specimens with waisted sections (Fig. 1-11.A) are generally acceptable for the determination of T-T elastic constants and strengths [36, 84-86], but important limitations hinder their use for structural design. Thick, waisted specimens are required to constrain failure within the gauge section [36, 84, 86]. The primary limitation is that thick laminates are unrepresentative of typical composite structural details owing to size effects [87, 88], and differences in microstructure [32] and final residual stress-state [41]. In addition, flatwise specimens are difficult and expensive to manufacture [32, 36, 41] and require painstaking alignment in mechanical testing load frames to reduce the likelihood of premature failure on account, in part, of their fragility [36, 84]. In fact, several laminates must typically be sandwiched together and co-bonded to obtain sufficiently-thick specimens, which can introduce undesirable stress variations in the vicinity of bond-lines [32, 36]. Lastly the strength characteristics of the end-tab bond-line can result in premature failure during environmental and fatigue testing [82].

The need for specimens that are more representative of curved details than flatwise specimens has been the principal motivator for the development of curved beam strength test methods [32, 41, 78, 80, 82, 85, 88], in addition to the need for simpler—and cheaper—methods [32, 78, 81, 83]. NASA researchers first proposed the use of a bolted C-shape specimen subjected to tensile end-loading in order to obtain the desired ILT failure [41, 82]. The tensile end-loading method was subsequently refined with the introduction of an L-shape specimen akin to a flange-to-web transition with a rounded corner that would be simpler to manufacture (Fig. 1-11.B-C) [80, 81]. NASA concurrently developed a hinged-loading mechanism (HLM) to introduce the tensile end-loads into the specimen flanges (legs or arms). Though simpler, the primary drawback of the HLM method is that it still requires painstaking specimen alignment [83].

An alternative loading configuration had previously been proposed whereby a four-point bending (4PB) fixture subjects C-shape specimens to a constant, pure bending moment in the plane of curvature [89]. This configuration greatly simplifies specimen installation and eliminates interlaminar shear stresses in the curved region. NASA further refined this method by utilizing its L-shape specimen and designing a self-aligning 4PB-fixture with loading rollers mounted with frictionless ball-bearings (Fig. 1-11.c) [83]. The new 4PB-method was shown to produce identical failures and nearly identical stresses as the HLM method and was subsequently adopted by ASTM as the D6415b test standard [90]. Industry variations were also implemented by private manufacturers such as the Airbus AITM1-0069 standard, which uses an adjustable 4PB-fixture that varies roller diameter and loading span with specimen thickness [91].

Three noteworthy improvements were published since the adoption of the ASTM standard that address several key limitations. First, the standard strictly restricts the specimen geometry that may be used for the determination of ILTS to a relatively thick and narrow geometry (4.2 and 25 mm, resp.) [90]. However, a narrow specimen width produces overtly conservative ILTS design allowables for wide parts owing to free edge effects. To this end a novel resin edge-treatment that eliminates this effect has been shown to greatly increase the measured ILTS values [92].

Second, the presence of manufacturing defects in the specimen corner region produces large data scatters [90, 93, 94]. The test is particularly sensitive to porosity [93, 94], which results in the measurement of "apparent" ILTS rather than a true material property. To this end an intricate method was proposed to eliminate the effect of porosity on the determination of ILTS by integrating load-curve test data and X-ray computed micro-tomography (micro-CT) measurements of individual specimens into a high-fidelity 3D finite element (FE) model and utilizing the latter to subsequently obtain more accurate ILTS values [93, 94]. This method succeeds in markedly reducing data scatter; however, its authors acknowledge that the method is far too involved to be standardized.

Third, the ASTM standard does not account for the complex specimen deformation, which is a combination of corner opening and flange flexure. The standard does warn that for crosshead displacements greater than 5 mm a significant error in the applied moment calculation arises from excessive flange flexure. The working assumption is that flanges remain straight throughout the test [90]. However, the 5 mm threshold is often exceeded as demonstrated in the literature [95-98] and per the experience of the author [99]. This error may be significant as the standard suggests, though its true magnitude is importantly not given.

Furthermore, ASTM does not adjust the corner radius value used to calculate the ILTS despite the visible opening of the corner. An analytical solution was derived to account for the combined corner opening and flange flexure of thin specimens loaded via the HLM method [100]. A similar analytical solution has yet to be derived to account for the deformation of specimens subjected to four-point bending. An alternative, semi-empirical approach was proposed to determine flange deflection via experimental measurements or the use of a high-fidelity FE-analysis, and to subsequently converge upon the correct angle of curvature of the corner via a custom MathWorks Matlab algorithm [95]. Though this method shows a very good agreement with the FE results, it renders the data reduction markedly more complex and, once again, difficult to standardize.

ASTM instead suggests the use of bonded doublers to support the specimen flanges during the test and directly eliminate flange flexure [90]. Such modifications however fall outside of the scope of the current standard, and no published studies were found that directly eliminate flange flexure for the 4PB-CBS method. The primary merit of using rigid flange supports lies in the simplicity of the solution, whereas the other aforementioned developments are all intricate and thus impractical for standard use. Nonetheless, the co-curing or -bonding of doublers complicates the specimen manufacturing process and will substantially add to the preparation time and cost.

Meanwhile, recent efforts by Makeev *et al.* are revisiting thick-laminate coupons using novel characterization techniques such as digital image correlation (DIC) and alternative loading configurations such as short-beam strength via three-point bending [93]. Such methods offer promising results in terms of determining true material properties; however, the aforementioned drawbacks of flatwise tensile testing remain, most notably, the fact that specimens are not representative of sharply-curved details in terms of both manufacturing and loading. Olsson ascertains that relatively thin, L-shape specimens employed by the various CBS loading configurations are ideally suited to test the performance of actual complex-shape components [32]. Efforts should therefore be focused on improving the reliability of the current 4PB-CBS standards.

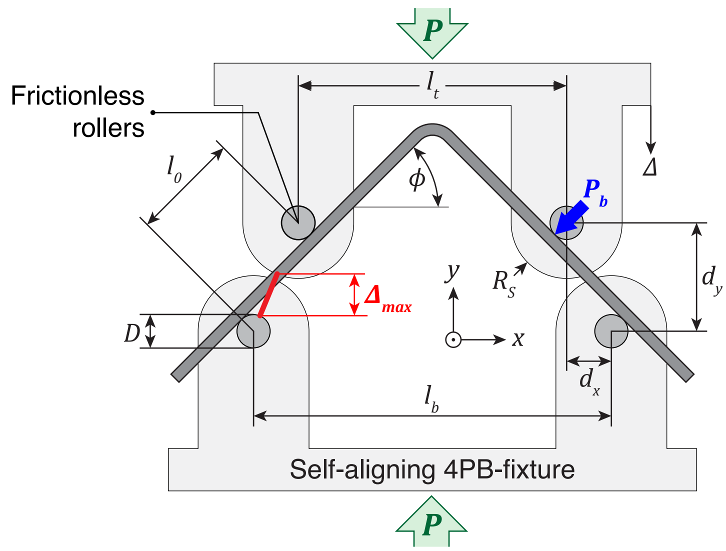

Fig. 1-12. Schematic of the four-point bending fixture and geometric variables (adapted from [90]).

1.4.3 Radial stress in a curved anisotropic beam under uniform bending

This section covers the pertinent theory associated with the 4PB-CBS method as established in the ASTM D6415 test standard [90]. The calculations are used to reduce the FE modelling (FEM) and experimental data in the results chapters of this thesis. Two properties are to be determined that are critical for aero-structural design: 1) *the curved beam strength* (CBS), which is the applied, pure bending moment per unit width at failure; and 2) the ILTS. It should be noted that CBS is a structural property, whereas ILTS is ideally a material property. Fig. 1-12 provides a schematic of the 4PB-CBS fixture and the important geometric variables used in the data reduction.

First, the CBS is determined with Eq. (1-1), where: M is the applied moment, P is the total force applied on the fixture by the load frame, P_b is the force exerted by each loading roller, l_0 is the distance between rollers along the flange axis, d_x is the horizontal distance between adjacent top and bottom rollers, ϕ is the flange angle from the horizontal, D is the roller diameter, and t is the nominal flange thickness [90].

$$CBS = \frac{\mathrm{M}}{\mathrm{w}} = \frac{\mathrm{P_b l_0}}{w} = \frac{P}{2w cos(\phi)}\left(\frac{d_x}{\cos(\phi)} + (D+t)\tan(\phi)\right) \tag{1-1}$$

The angle ϕ changes significantly during the test and must therefore be adjusted in order to correctly calculate the applied moment at failure. It is given by Eq. (1-2), where: d_y is the vertical distance between the top and bottom rollers, ϕ_i is the initial flange angle from the horizontal, and Δ is relative displacement between the two fixture halves. Blanchfield and Allegri have since proposed a more accurate trigonometric relationship for ϕ given by Eq. (1-3) [95]. They estimate the error of the Eq. (1-2) to be about 2.0% for the ILTS specimen that is prescribed by the ASTM standard.

$$\phi = \ sin^{-1}\left(\frac{-d_x(D+t) + d_y\left[d_x^2 + d_y^2 - D^2 - 2Dt - t^2\right]^{0.5}}{d_x^2 + d_y^2}\right) \tag{1-2}$$

where: $d_y = d_x tan(\phi_i) + (D+t)/\ cos(\phi_i) - \Delta$

$$\phi = tan^{-1}\left(\frac{d_y}{d_x}\right) - sin^{-1}\left(\frac{D+t}{\left[d_x^2 + d_y^2\right]^{0.5}}\right) \tag{1-3}$$

With respect then to the ILTS determination, Lekhnitskii authored the seminal work on the classical elasticity theory of anisotropic plates and curved beams [101]. The 4PB-CBS method relies on this elasticity solution for the maximum radial stress in a curved beam section with cylindrical anisotropy and experiencing a pure bending moment [41, 83, 90]. A schematic of a curved laminate section experiencing a pure bending moment is presented in Fig. 1-13 along with representations of the T-T stress distributions. It should be noted that 2D plane-stress is assumed. Interestingly, Lekhnitskii's solution predicts a T-T shear stress ($\tau_{\theta r}$; i.e. interlaminar shear—ILS) of zero throughout the curved section and a non-linear tangential stress distribution (σ_θ ; a.k.a circumferential or "hoop" stress). It should further be noted that the solution is based on the plane-stress assumption. The maximum radial stress ($\sigma_{r,max}$; i.e. interlaminar tension—ILT) is given by Eq. (1-4), where: r_i and r_o are the inner and outer surface radii, and r_{max} is the radial position, at which the maximum stress occurs—not to be confused with the mean radius, r_m. The moduli of elasticity in the tangential and radial directions (E_r and E_θ , resp.) can be estimated with the elastic moduli of a unidirectional laminate (E_1 and $E_2 = E_3$, resp.) [90].

$$\sigma_r^{max} = \frac{-M}{r_o^2 w g}\left(1 - \frac{1-c^{k+1}}{1-c^{2k}}\left(\frac{r_{max}}{r_o}\right)^{k-1} - \frac{1-c^{k-1}}{1-c^{2k}}c^{k+1}\left(\frac{r_o}{r_{max}}\right)^{k+1}\right)$$

$$\text{where:} \quad c = r_i/r_o, \quad k = (E_\theta/E_r)^{0.5}$$

$$g = \frac{1-c^2}{2} - \frac{k}{k+1}\cdot\frac{(1-c^{k+1})^2}{1-c^{2k}} + \frac{kc^2}{k-1}\cdot\frac{(1-c^{k-1})^2}{1-c^{2k}} \qquad (1\text{-}4)$$

$$r_{max} = \left[\frac{(1-c^{k-1})(k+1)(cr_o)^{k+1}}{(1-c^{k+1})(k-1)r_o^{1-k}}\right]^{1/2k}$$

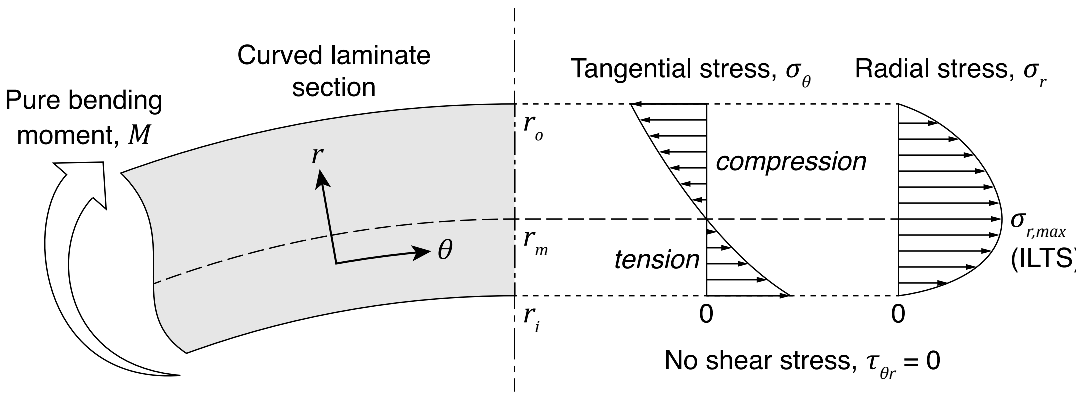

Fig. 1-13. Schematic of T-T stresses in a curved anisotropic beam under pure bending.

The complexity of Lekhnitskii's classical elasticity solution lengthens the analysis and increases the potential for typing errors. Attempts have thus been undertaken to derive simpler expressions based on simple bending theory (SBT), which assumes a linear tangential stress distribution. To this end, Ko derived an expression for $\sigma_{\theta r,max}$ in the case of relatively thin curved laminates ($r_0 \longrightarrow r_i$) by assuming that the maximum value occurs at the midplane ($r = r_m$) [102]. In turn, Mabson and Neall derived a more accurate equation that importantly solves for the correct radial location ($r_{max} = (r_i\ r_o)^{0.5}$) [103]. It should be noted, as an aside, that Mabson and Neall's work allowed for the investigation of interlaminar stresses in the corners of curved, C-section structural beams, which experienced secondary, T-T bending moments caused by a primary, out-of-plane moment applied to the entire beam.

Kedward *et al.* found Ko and Mabson and Neall's expressions to be adequate for the analysis of isotropic materials—albeit somewhat "unconservative"; however, they demonstrated that both expressions rapidly loose accuracy in the case of sharply-curved details [41]. Instead, Kedward *et al.* substituted the correct radial location solved by Mabson and Neall into the expression derived by Ko as given in Eq. (1-5). Compared to previous efforts, this simple approximation only yields a small error of less than 2.0 % given relatively low degrees of anisotropy and large radius-to-thickness ratios ($E_\theta/E_r \leq 20$, i.e. $k \leq 4.47$, and $r_m/t \leq 2$, resp.) [90]. Fig. 1-14 illustrates the design space, within which the "Kedward approximation"—as it will henceforth be referred to as—works best.

$$\sigma_r^{max} = ILTS = \frac{3 \cdot CBS}{2t(r_i r_o)^{0.5}} \tag{1-5}$$

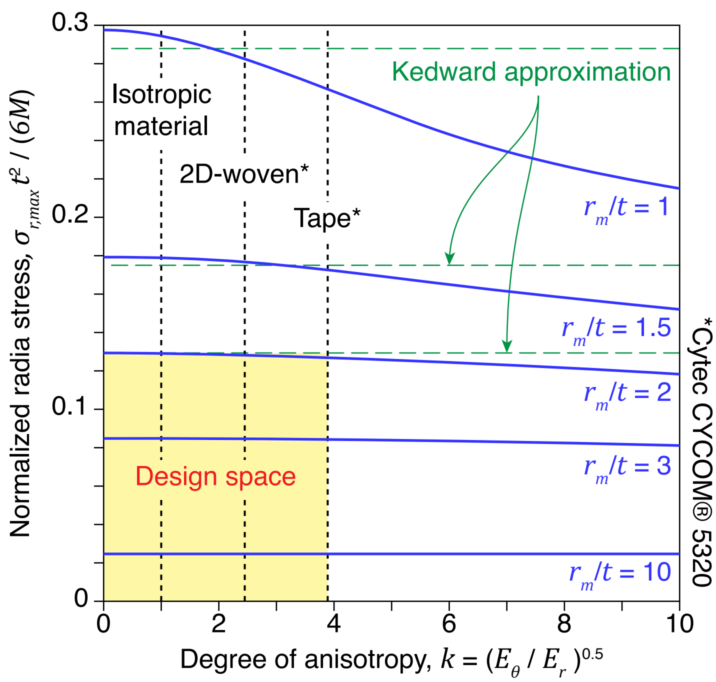

Fig. 1-14. Plot of the normalized radial (ILT) stress vs. degree of anisotropy (adapted from [90]).

1.4.4 Design considerations

Lekhnitskii's classical elasticity solution and simple bending theory approximations form the basis of current experimental and analytical methods used in the determination of ILTS design allowables and the certification of aero-structures, resp. These methods place a focus on pure bending as the critical T-T loading component in singly-curved details given that it is primarily responsible for engendering mode-I delamination. Nevertheless, other loading components merit attention such as radial and tangential (end-) loads given the complexity of load cases and failures observed in actual, integrated structures. To this end, Most *et al.* offer an overview and comparison of simple, closed-form analytical expressions and high-fidelity (full-scale) FEM approaches for interlaminar stress prediction in curved details [104]. Importantly, they investigate the more complex case of doubly-curved details subjected to more complex load cases, namely double-bending and distributed loading.

High-fidelity FE models utilize 3D-brick elements to compute both in- and out-of-plane stresses. Though highly-accurate, such models are time-consuming to construct, computationally-expensive to run and, ultimately, impractical for the early dimensioning stage of an aero-structural development program, which relies primarily on the prediction of in-plane stresses. Instead, integrated structures such as fuselage skin and stringer assemblies are idealized with 2D/3D-shell and 1D-beam elements to simulate the skin and stringers, resp. These elements are more computationally efficient for predicting in-plane-stresses. It should also be noted that 3D-shell elements are specifically designed to estimate T-T normal stresses [105, 106] but are not yet suited to the task of predicting delamination. Secondary analytical tools are thus necessary to estimate the T-T stress-state in sharply-curved details based on the internal loads and moments obtained from FEM. The T-T stress can subsequently be used with appropriate failure criteria to predict the failure point and mode. Table 1-3 compares the closed-form analytical expressions and methods typically used as part of aerospace development processes.

A key aspect of these closed-form, analytical expressions is the trade-off between ease-of-use and accuracy compared to more exact, higher-order solutions that are much more involved to implement. To this end, the Kedward approximation performs rather well, particularly in the case of singly-curved details (conservative in the case of double curvature), while being notably independent of the degree of anisotropy and the stacking sequence [104]. For cases falling outside of the design space highlighted in Fig. 1-14, it is recommended to employ the more exact expressions based on Lekhnitskii's classical elasticity solution.

The expressions and methods that have so far been discussed are independent of the stacking sequence, which is a limitation for more complex sequences such as ones that are highly-grouped, unbalanced or asymmetric. Modern aerospace development programs therefore opt for highly-capable, layer-wise methods that are developed in-house and implemented as stand-alone software. Two such methods were developed by the Engineering Sciences Data Unit (ESDU) in

Table 1-3. Comparison of closed-form analytical expressions used as part of aerospace development processes for the prediction of interlaminar stresses.

Expression(s)	Theory	Inputs			T-T outputs			$\sigma_{r,max}$	Ease-of-use	Software	Failure criterion
		M	P_r	P_θ	σ_r	σ_θ	$\tau_{\theta r}$				
Lekhnitskii [101]	CET; plane-stress	✓	✓	✓	✓	✓	✓	Exact			Quadratic
*ESDU 94019 [107]	CET / CLT; plane-strain	✓	✓	✓	✓	✓	✓	Exact		✓	Quadratic
*^Airbus A400 Spar [108]	CET / CLT; plane-strain	✓	✓	✓	✓	✓	✓	Exact		✓	Quadratic
Ko [102]	CET; plane-stress	✓	✓		✓			Exact	✓		Max stress
Ko (simplified) [102]	CET / SBT; plane-stress	✓	✓		✓			Approx.	✓		Max stress
Kedward *et al.* [41]	SBT; plane-stress	✓			✓			Approx.	✓		Max stress
Mabson and Neall [103]	SBT; plane-stress	✓			✓			[x]Approx.	✓	✓	Max stress

*Layer-wise method; ^ internal development process document used by Fletcher [110]; [x] exact solution in software; CET: classical elasticity theory; CLT: classical laminate theory; SBT: simple bending theory.

the UK in the early-Nineties [107] and, more recently, by Airbus UK Ltd. as part of the development program of the A400 Atlas military transport aircraft [108]. Both methods follow from Lekhnitskii's classical elasticity solution for a "composite" curved anisotropic beam consisting of concentric anisotropic layers [101] and make use of classical laminate theory (CLT) [109]. In turn, both are based on the 2D plane-strain assumption, which Jackson and Martin demonstrated to yield effectively identical results to the 2D plane-stress assumption used by the other expressions [81]. Finally, both methods output near-exact ILT, ILS and tangential stress distributions and make use of quadratic failure criteria to predict the failure point and T-T laminate location. Despite these additional capabilities, such methods are more challenging to implement.

As a final design consideration, it is important to note the current status of failure criteria that are used in conjunction with the T-T stress analysis of sharply-curved details. Failure prediction in composite laminates experiencing complex load cases is very difficult given multiple failure mechanisms acting at different scales and often interacting with one another. Indeed, the general outcome of the World Wide Failure Exercise (WWFE) is that failure prediction in composite laminates is far from maturity [111]. As trivial as it may seem, one of the key challenges is to better define what constitutes "failure", to which end improved T-T test methods and better experimental data are required [32, 77]. In turn, though there currently exists a panoply of failure criteria used in industry, they are often bound to specific load cases and failure mechanisms, and their specific usage varies among aerospace manufacturers [112]. Importantly, confidence in delamination prediction is especially poor [111]. While work on new, comprehensive failure criteria continues, Most *et al.* [104] recommend using the quadratic failure criteria developed by Wisnom *et al.* [113] for ILT and ILS failures, for which mode-I delamination is the primary failure mode.

1.5 Variability and defects in VBO semipreg laminates

1.5.1 Overview

Current semipregs can yield flat laminates that rival the laminate quality readily achieved via autoclave processing in terms of both fibre volume fraction (> 60%) and void content (<< 1% for tapes). Still, scaling up remains problematic as VBO processing does not reliably yield high-quality, complex-shape laminates. Variability in semipreg quality and processing conditions such as locally-varying degrees of resin impregnation during prepregging and suboptimal vacuum-bag pressure, resp., engender deficient local consolidation of the laminate, i.e. poor fibre-bed compaction, air evacuation or resin-flow (incomplete impregnation). Material and processing properties are therefore critical to the presence of variability and the formation of defects in cured semipreg laminates, which, in turn, are detrimental to their mechanical performance and reliability for aero-structural applications.

The following sections review the state of research into the three, most prevalent types of variability and defects commonly observed in semipreg laminates, namely: porosity (§ 1.5.2), local thickness deviation (§ 1.5.3) and fibre waviness (§ 1.5.4). In turn, key parametric studies are highlighted in § 1.5.5. Lastly, the sparse research investigating the relationship between these defects and mechanical performance is reviewed in § 1.5.6. It should be noted that defects induced by ATL/AFP layup such as tow-gaps and overlaps and pertaining to the VBO processing of sandwich structures are beyond the scope of this particular review. Reviews by Dirk *et al.* [64] and Centea *et al.* [49] may instead be perused for overviews of the defects specific to these applications.

1.5.2 Porosity

Porosity generally refers to the presence of *voids* (gas bubbles entrapped in the laminate) and dry-fibre regions (resin starvation). Voids are arguably the most prevalent type of defect found in both flat and complex-shape (sharply-curved or variable thickness) semipreg laminates given the limited, available consolidation pressure of VBO processing. Fig. 1-15 illustrates the general void species and their location within tape and 2D-woven mesostructures. The presence of voids critically degrades the fracture toughness and strength properties of laminates by acting as local stress concentrators [35]. Two independent phenomena are responsible for void formation: the entrapment of gases in the resin (air, water vapor and curing volatiles) and incomplete resin impregnation due to deficient resin-flow [49, 52]. The factors influencing both phenomena are briefly enumerated herein. A review by Centea *et al.* may be perused for a more in-depth overview of the state of the research into void formation in VBO processing.

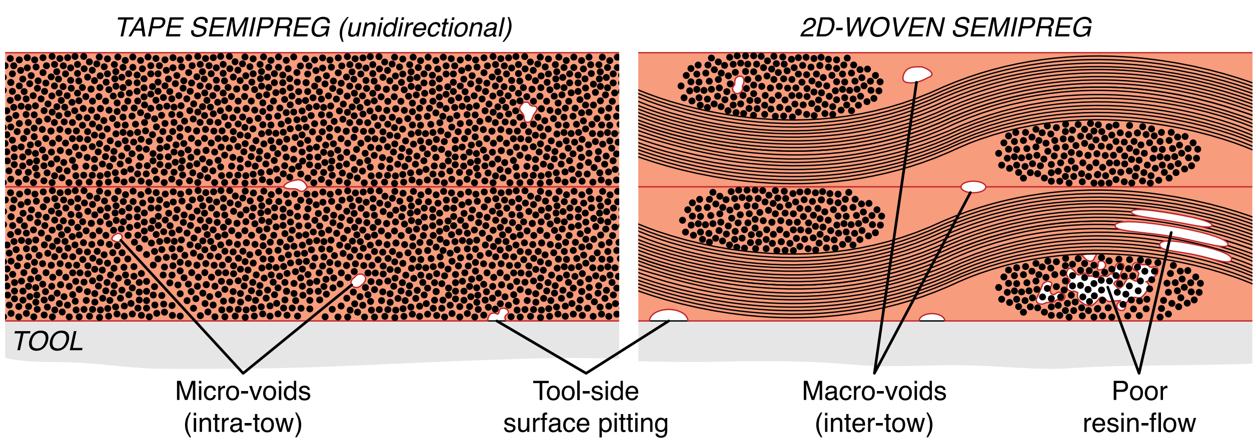

Fig. 1-15. General void species found in consolidated and cured VBO semipreg laminates.

With respect first to gas-induced porosity, voids nucleate during the resin-flow/curing phase prior to gelation. In particular, a void grows when its internal gas pressure exceeds the local hydrostatic resin pressure acting on its surface. Gas-induced voids are typically highly-ellipsoidal in shape, varied in size (micro- to- macro-scale) and are most often found in resin-rich regions, namely ply interfaces and 2D-weave interstices; for this reason, they are further denoted as *macro-*

or *inter-tow voids*. They may also be found within fibre-dense regions—albeit less frequently, in which case they are further denoted as *micro-* or *intra-tow voids* (Fig. 1-15) [114].

The theory of void formation and dissolution is well understood in the context of autoclave prepreg processing [115, 116]. Important research has been carried out over the past decade to better understand the notable susceptibility of VBO processing to porosity. The key factors to affect gas-induced porosity have been methodically investigated in the literature and importantly include: 1) insufficient air evacuation and relatively long air evacuation distances (air evacuation is not restricted) [117-119]; 2) water vapor from absorbed moisture due to improper prepreg storage or ambient conditions during layup [117-119]; and 3) deficient consolidation pressure due to deficient vacuum-bag pressure [99, 114, 118, 119], reduced ambient pressure (elevation and weather) [114, 120] and restricted air evacuation (simulating large, integrated parts) [99, 114, 121]. A common takeaway from the cited research is that the limited, available consolidation pressure undermines void suppression due, primarily, to internal void pressure from entrapped gases and, to a lesser extent, decreased hydrostatic resin-pressure. As Centea *et al.* emphasize, the tendency of VBO processing for gas-induced porosity requires a strict adherence to proper semipreg storage, ambient condition control during handling and layup, and robust processing tools and equipment [49].

Importantly from a process design standpoint, Grunenfelder *et al.* adapted a diffusion-based, semi-empirical model to predict the level of absorbed water, beyond which entrapped vapor pressure inside of voids will overtake the available hydrostatic resin pressure during the cure resulting in void growth [117]. They further observed that conventional autoclave prepregs are far less susceptible to developing vapor-induced porosity upon exposure to moisture than semipregs. This finding is most likely owed to the presence of air evacuation channels in semipregs, which imparts a substantially larger surface area for water absorption.

Whereas most studies focus on factors rather than location, Hamill *et al.* specifically investigated gas-induced porosity on the tool-side surface of laminates, which is commonly referred to as *surface pitting* [122]. Though this type of porosity is not as detrimental to mechanical performance, it compromises part finish, which is an important factor for the subsequent application of coatings, and lowers the general part aesthetic, which is an important factor in consumer-driven markets such as that of high-end sporting goods. In turn, Helmus *et al.* devised a novel experimental approach to investigate the formation of macro-voids at ply interfaces due to air entrapment during ply collation [123]. Interestingly, they found the surface roughness of semipreg tapes to play a critical role in establishing a temporary air evacuation network, which explains the negligible macro-porosity levels typically observed in flat, semipreg-tape laminates.

With respect then to flow-induced porosity, this phenomenon is conceivably simpler to explain from a phenomenological standpoint in that it stems from incomplete resin impregnation of the dry air evacuation channels: resin-flow is hindered by either an insufficient time-window or more often by deficient properties such as high resin viscosity and poor fibre-bed permeability. Flow-induced porosity may occur independently of gas-induced porosity and will typically manifest itself in the form of micro-voids within fibre-dense regions that are highly-irregular in shape due to adjacent fibres, and which are often on the scale of individual carbon fibres (Fig. 1-15). In cases of particularly poor resin-flow, large portions of air evacuation channels may remain resin-free as nearby choke-points block the evacuation of remaining gases and eventually enclose the region (Fig. 1-15).

The key factors to affect flow-induced porosity have also been methodically investigated in the literature and importantly include: 1) resin out-time, which will affect the initial degree-of-cure and, in turn, the resin viscosity [58, 120, 124-126]; 2) intermediary debulking during layup, which importantly may partly collapse air evacuation channels [114]—notably in the case of sharply-curved details [121, 127]; 3) fibre-bed architecture and air evacuation strategies, which evidently affect the in- and out-of-plane air permeability of semipregs [99, 114, 121]; and 4) stacking sequence [120]. A common takeaway from the cited research is that partial resin-impregnation is disastrous to laminate quality and, in turn, mechanical performance. High fibre-bed permeability and low resin viscosity are vital for optimal resin-flow. To this end, adherence to proper ply collation, vacuum-bagging and air evacuation protocols (intermediary debulking and out-time) and robust cure-cycle design are critical to ensuring full resin impregnation.

Importantly from a process design standpoint, Centea and Hubert developed a representative 2D model for the resin impregnation of a dry tow and subsequently performed a parametric study [128]. They demonstrate that the time required to complete resin impregnation is principally affected by the initial degree-of-cure of the resin and the cure cycle temperature, i.e. the resin viscosity. In particular, they determine that faster thermal ramps and elevated isothermal dwells can safeguard against concerns over incomplete resin impregnation by sufficiently lowering the viscosity. This finding was further substantiated with experimental work by Centea *et al.* [126].

In addition, Grunenfelder *et al.* demonstrated that second-generation, OOA resin systems such as Cytec CYCOM® 5320 develop a substantial amount of micro-porosity beyond a typical out-time of 20 days [124]. To this end, Cytec has significantly increased the out-time of its leading resin system with the introduction of CYCOM® 5320-1. Lucas *et al.* demonstrated that semipregs utilizing the new formulation yield acceptable levels of micro-porosity beyond the 30-day mark (< 1%) [58]—albeit at the cost of a longer cure cycle.

Lastly, the local degree of resin impregnation varies significantly in current-generation semipregs as was eluded to in § 1.3.4. Work is underway to improve the accuracy and ease of use of methods to determine the degree of impregnation [74], all-the-while more robust, next-generation prepregging processes are also under development. In terms of modelling, Helmus *et al.* developed a stochastic 2D model for resin impregnation that captures the effect of a variable degree of impregnation and subsequently predicts more representative levels of micro-porosity within flat, semipreg-tape laminates. This stochastic approach is currently being adapted via FEM to predict porosity in complex-shape laminates [129].

1.5.3 Local thickness deviation

Local deviations from nominal part thickness is common in sharply-curved semipreg laminates. This second type of defect was first investigated experimentally and numerically in the context of autoclave prepreg processing [130-136] resulting in a relatively good understanding of the problem. The more recent introduction of semipregs in complex-shape applications and the large thickness deviations that ensued highlighted remaining gaps in the understanding of the underlying mechanisms. In particular, the limited, available consolidation pressure and the high-bulk-factor of semipregs has been experimentally shown to exacerbate thickness deviation over sharply-curved tool features. Research has thus far been carried out on singly-curved specimens [69, 99, 127, 137], more complex part geometries with multiple sharply-curved features in close succession [138] and methods to control the problem, namely the use of pressure intensifier strips [69, 121, 138] and intermediary debulking [121]—including an investigation into the potential of heat-assisted debulking [127]. The principle mechanisms affecting thickness deviations are illustrated in Fig. 1-16. Local "corner thickening" is the expected outcome in the majority of cases except in the special case of layups containing a majority of transverse plies (90°; aligned in the 2-dir.), which instead yields local "corner thinning". Two phenomena have thus far been established in the literature to govern thickness deviation in curved regions: pressure-differentials and resistance to interplay slippage [130, 137].

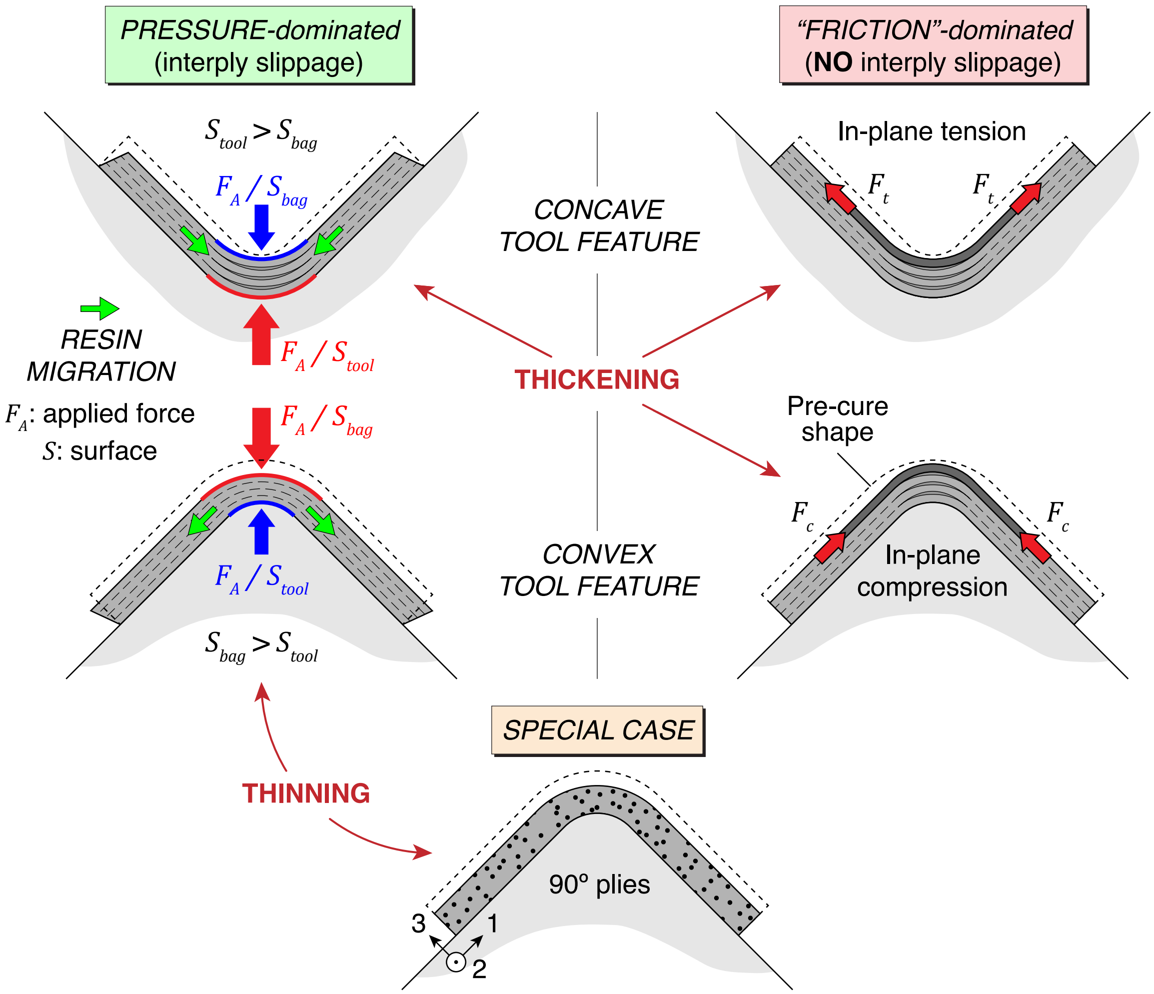

Fig. 1-16. Thickness deviation in singly-curved laminates (adapted from [69, 137]).

With respect first to pressure-dominated mechanisms, Hubert and Poursartip first advanced the presence of significant pressure differentials between sharply-curved regions and adjacent, flat regions as a key mechanism [130]. In the case of convex tool features under static equilibrium, the consolidation pressure acting on the laminate's bag-side is larger than the tool-side reaction pressure due to a mismatch in surface area; the reverse holds true in the case of concave tool features (Fig. 1-16). The resultant consolidation pressure gradients over convex and concave tool features results in local corner thinning and thickening, resp.

In addition to investigating fibre-bed compaction, Hubert and Poursartip performed 2D FEM resin-flow simulations and demonstrated that resin migrates away from and towards convex and concave regions, resp. [136]. Differentials in consolidation pressure acting on the laminate produce local gradients in hydrostatic resin pressure within the laminate during the resin-flow phase. This secondary effect may result in resin-rich regions appearing on the tool-side of laminates processed over concave tool features and severe local porosity due to suboptimal hydrostatic resin pressure [99, 121]. Lastly, when coupled with very deficient consolidation pressure of the kind discussed with respect to flow-induced porosity, very large radial voids eventually form across concave regions as plies and consumable layers bridge the tool feature during compaction [99, 129]. Fig. 1-17 presents an example of local thickening and severe porosity in a sharply-curved, concave semipreg laminate that experienced restricted air evacuation during processing.

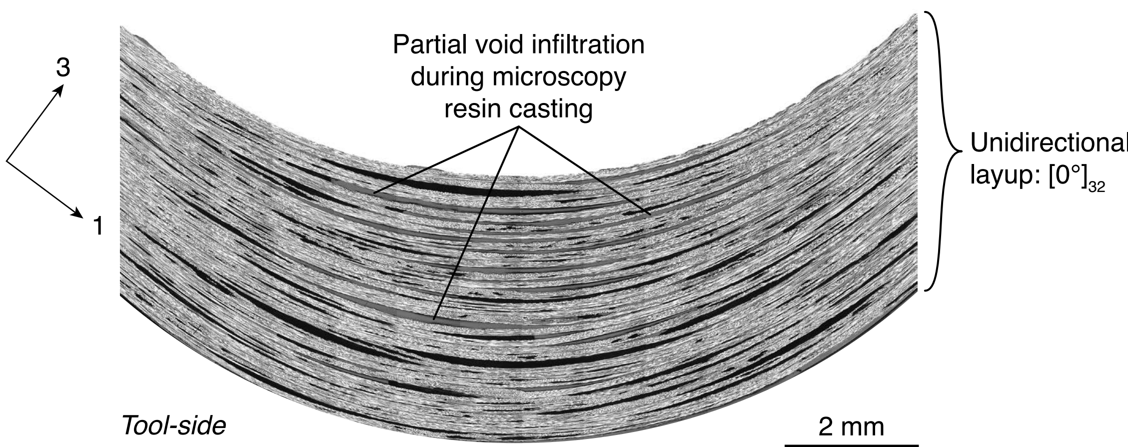

Fig. 1-17. Example of severe porosity in a sharply-curved concave semipreg laminate due to restricted air evacuation (cross-sectional view; brightfield illumination micrograph; 5x objective).

The pressure-dominated mechanism advanced by Hubert and Poursartip [130] forms the basis of a model developed by Brillant and Hubert [139] to predict the extent of thickness deviation in cured semipreg laminates. A key assumption of this model is unimpeded interply slippage. In most cases, however, ply conformation is constrained by interply friction (Fig. 1-16) [137] and, to a lesser extent, the presence of proximal curved regions and physical obstacles such as inserts and edge-dams [69]. The pressure-differential model thus under-predicts the extent of thickness deviation. Instead, Levy *et al.* followed an earlier attempt by Cauberghs [138] to describe the compaction kinematic of friction-dominated consolidation in terms of geometrical considerations [137]. Importantly, interply friction prohibits ply conformation beyond a critical, adjacent flange length [135]. Levy *et al.* subsequently collected thickness deviation data from experimental studies using L-shape specimens with various flange lengths and radius-to-thickness ratios. They demonstrated that the friction- and pressure-differential models complimented each other by providing upper- and lower-bound thickness deviation estimates, resp.—albeit quite extreme ones.

It would be remiss not to emphasize the critical role that ply orientation and stacking sequence play on local thickness deviation. In general, laminates containing large quantities of either 0°-plies or transverse plies (90°) display the largest thickness deviations, compared to quasi-isotropic and cross-ply laminates ($[45°/0°/-45°/90°]_{ns}$ and $[0°/90°]_{ns}$, resp.) [69, 131]. In particular, the fibre-bed of mostly-transverse laminates ($[90°]_n$) has very low resistance to interlaminar shear-flow during compaction, which allows fibres to migrate with the resin in the case of a concave tool feature. This special case is the only instance to result in local corner thinning (Fig. 1-16) [69, 130].

Finally, experimental data from L-shape semipreg laminates is generally characterized by a high degree of variability owing to multiple effects interacting with one another [69, 121, 127]. The friction-model proposed by Levy *et al.* provides an initial estimate—albeit a very unconservative one. To this end Hubert *et al.* have extracted experimental thickness data from several studies that used multiple L-shape specimen configurations (tool-shape, radius, thickness, primary-reinforcement architecture and layup). They subsequently present semi-empirical correction factors for the friction-model to address the four principal cases: convex and concave, pressure- and friction-dominated [52].

Important work remains to be done in the development of design tools that can capture the high-variability and stochasticity of local thickness deviations and, in turn, provide more accurate estimates. Meanwhile, current thickness measurement methods typically fall into the category of direct, hand-measurements of L-shape specimens via a Vernier caliper or a micrometer ([81, 88, 140] or indirect, manual measurements (cursor-operated) of scanned specimen profiles in image analysis software [69, 121, 137, 138]. The case is made in § 2.4.1 that both categories offer limited precision, accuracy and practicality, and that thus improved, semi/fully automated methods are required to provide better data for modelling.

1.5.4 Fibre waviness

Fibre waviness is a third and somewhat less-prevalent type of defect that is closely related to thickness deviations found over sharply-curved tool features. Potter *et al.* make the important distinction that waviness and thickness deviations may be thought of as "irregularities" rather than defects [141]. Defects such as porosity are generally considered to be process-induced and can be remedied by a strict adherence to a robust processing cycle. In contrast, the fibre waviness and thickness deviations typically found in complex-shape laminates are unavoidable consequences of design choices rather than the sole product of deficient processing parameters. Indeed, as will be demonstrated in this thesis, near-optimal processing parameters do not completely remove either irregularity. Potter *et al.* argue that it is in fact flat, uniform laminates that ought to be deemed a special case when considering the quality and mechanical performance of generic composite laminate structures.

Fibre waviness has been shown to have disastrous consequences notably on in-plane compressive strength, as well as fatigue endurance, interlaminar shear strength and fracture toughness [141-144]. It generally occurs either in-plane [142, 143, 145] or out-of-plane [130, 145, 146] over complex-shape features such as sharply-curved tool features [130, 141, 146] and ply-drops [141, 147]. In addition, fibre waviness can be further categorized into two regimes: *marcelling* and *wrinkling*. With respect first to *marcelling*, the term is often used to describe locally-periodic, in- and out-of-plane waviness [148] given its resemblance to the hair style bearing the same name. In turn, sudden, severe in- and out-of-plane waviness is often referred to as *wrinkling* [141]. Typical regimes of fibre waviness observed in autoclave-processed, curved laminates are presented in Fig. 1-18. It should finally be noted that a certain degree of fibre misalignment is to be expected owing to intrinsic prepreg and semipreg variability as received from the manufacturer (in-plane waviness and stray fibres, and out-of-plane dimpling) [141] in addition to small-angle ply misalignment during ply collation [64, 149]. Material-induced misalignment is ubiquitous in generic composite parts and may thus be considered to be the "far-field" degree of misalignment.

As with porosity and thickness deviation, fibre waviness has been the subject of numerous experimental and numerical studies that have generally focused on autoclave prepreg laminates and hand-layup [130, 141, 144, 146, 150] as well as special layup processes such as filament winding [144, 148] and ATL/AFP [64]. In particular, Kugler and Moon discussed the underlying mechanisms of process-induced, in-plane waviness in flat laminates [150]. In turn, Hubert and Poursartip discussed the role of fibre-bed compaction behaviour on the formation of out-of-plane wrinkling in corner laminates [130], and Lightfoot *et al.* discussed the effect of interply shear due to tool-part interaction (mismatch in coefficients of thermal expansion—CTE) [146]. With respect then to OOA processes, research has by-and-large focused on LCM processes, namely RTM [141, 151, 152]. In particular, Potter *et al.* reviewed the effect that ply draping has on the formation of fibre waviness and wrinkling in RTM-processed laminates [141], which is a prime concern in the design and manufacturing of wind-turbine blades (vacuum-assisted RTM).

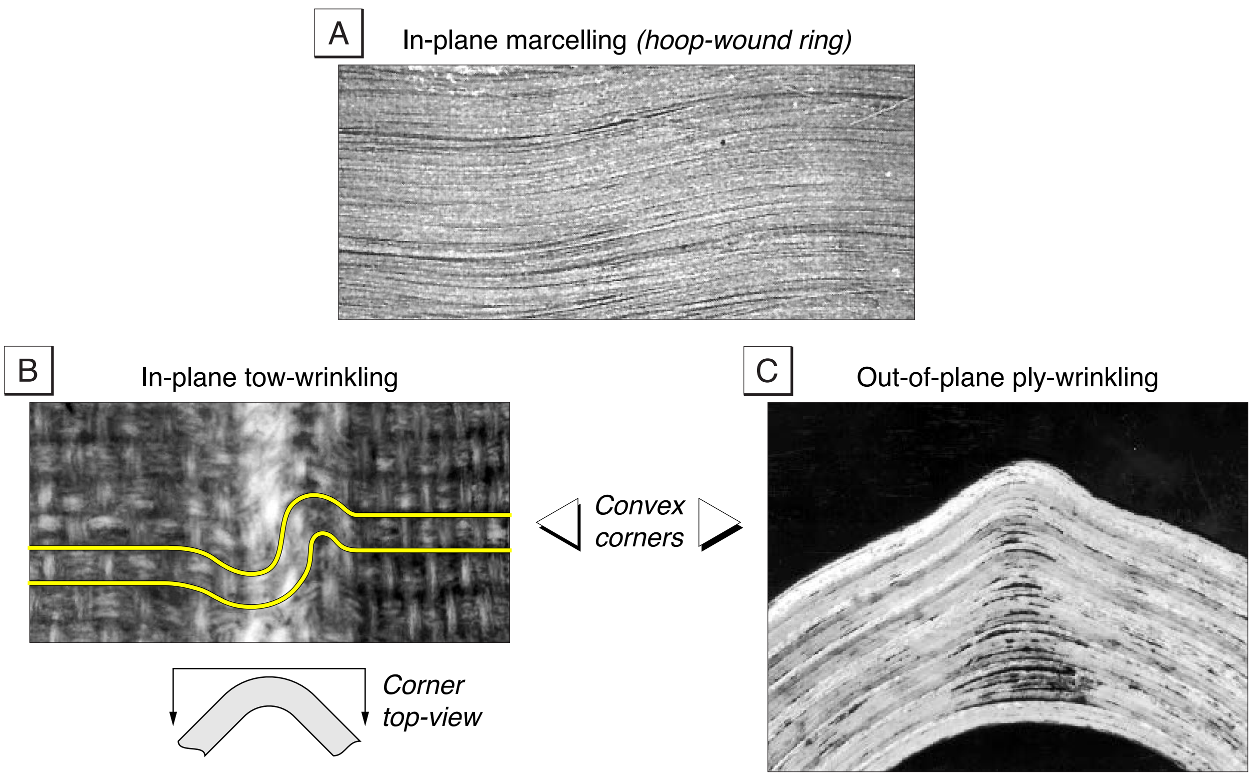

Fig. 1-18. Examples of fibre waviness: A) in-plane marcelling in unidirectional laminate; B) in-plane PW tow-wrinkling in convex corner; and C) out-of-plane ply wrinkling in convex corner (reproduced from [148], [141] and [130], resp.).

Comparatively little research has been dedicated to material- and process-induced fibre waviness in semipreg laminates. Farnand *et al.* conducted the only study that could be found to specifically investigate fibre waviness in current semipreg tape laminates (Cytec CYCOM® 5320/T650 tape) [153]; however, they investigated vacuum-assisted, hot-drape-forming rather than VBO processing with hand-layup. They discuss two notable mechanisms, as illustrated in Fig. 1-19: 1) compaction-induced micro-buckling of fibres (marcelling) in 0° plies (hoop-dir.) and 2) rolling-shear-induced wrinkling of 90° (transverse) plies. Importantly, they allude to the potential role that air evacuation channels may play in the formation of in-plane waviness over sharply-curved tool features—though they stop short of further characterizing this particular regime of waviness. This specific case and the effect of semipreg architecture thus merits further investigation.

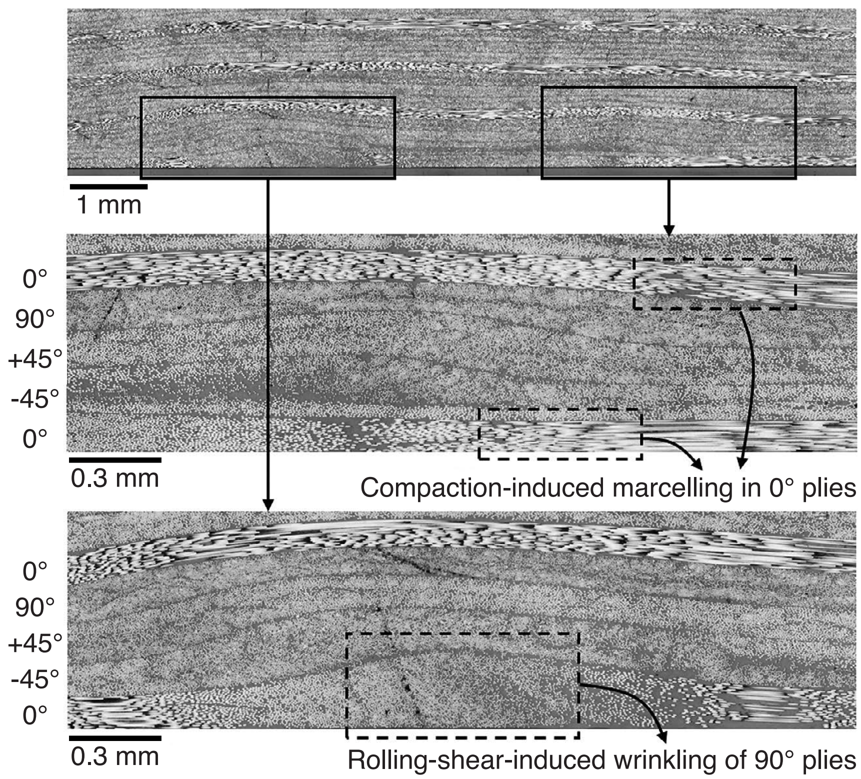

Fig. 1-19. Fibre waviness mechanisms in semipreg tape laminates (reproduced from [153]).

A final noteworthy aspect of fibre waviness research is the development of experimental characterization methods. The bulk of current methods are destructive in nature as they rely on the optical microscopy imaging or micro-CT scanning of small laminate samples. Despite this key drawback, these methods yield the most accurate and precise results for R&D. Meanwhile, NDI techniques such as the ultrasonic method developed by Smith *et al.* can yield high-resolution measurements [75] but are generally better suited for quality inspection during manufacturing.

The precursor to many of the current methods available in the literature is the straightforward, optical microscopy technique developed by Yurgartis in the late 1980s for the measurement of small-angle fibre misalignment in single-sections containing unidirectional and mostly-orthogonal fibres [154]. This method has proven to be very popular but has since been replaced by a slew of adaptations such as the pseudo-3D method developed by Clarke in the mid 1990s, which correlates 2D-planar measurements between multiple, parallel and tightly-spaced microscopy-slices [155]. Nonetheless, pseudo-3D methods based on 2D micrographs are very demanding and are only applicable for the analysis of small laminate regions.

Instead, the future of fibre-bed characterization methods lies in the analysis of fully-3D, micro-CT scanning data with spatial resolutions that extend well below a single-micron—albeit with currently significant scan times and cost, and limited scanning volumes. Of note is the improvement by Sutcliffe *et al.* [156] of a 2D-method developed by Creighton *et al.* [157], which determines local fibre alignment based on the presence of elongated contrast-features in low-magnification images. Sutcliffe *et al.* importantly upgraded the method to treat stacks of reconstructed micro-slices by implementing an automated correlation function approach between micro-slices. This approach is particularly useful for the analysis of CFRP laminates, which contain densely-packed and very thin fibres (< 60 vol.%; ~5-10 μm). Of further note is the more recent method developed by Nikishkov *et al.* for the creation of FE-meshes from reconstructed micro-CT data. This method can also determine waviness from tomograms with suboptimal resolution and contrast by instead interpolating available fibre slope data with radial basis functions.

These novel 3D-scanning and digital image analysis methods have the potential of drastically cutting down on sample preparation and characterization time, all the while micro-CT equipment is becoming more widely accessible and powerful. These methods are however currently poorly suited to handle complex-shape laminates. To this end, further work is especially needed in the following areas beyond general improvements in computational efficiency: 1) tomogram segmentation given the very close and variable X-ray attenuation thresholds of carbon fibres and epoxy matrices; 2) registration (re-orientation) of misoriented scanned volumes; and 3) warping techniques to measure the magnitude of fibre waviness measurements in curved regions with respect to pre-determined reference planes.

1.5.5 Key parametric studies

Three key types of variability and defects have thus far been discussed, namely porosity, local thickness deviations and fibre waviness. A fourth type of process- and design-induced defects that has not been discussed is out-of-plane distortion locked-in during the cure cycle. Soltani *et al.* have performed a couple of parametric studies that linked distortion and, in particular, warping to layup symmetry, and to lesser extents ply orientation and reinforcement type [158, 159]. In turn, Luner and Bond investigated the effect of tool radius, isothermal dwell temperature and reinforcement type on “spring-in” of convex corner laminates [160]. That being the case, this type of defect is not nearly as prevalent and pronounced in the relatively thick (> 3 mm) and balanced laminates that are generally used in CBS/ILTS testing.

It is important to specifically mention a couple of parametric studies that highlight the important factors that have thus far been investigated and linked to the quality of flat and corner semipreg laminates. With respect first to flat laminates, Centea *et al.* investigated the effect of deficient consolidation pressure (vacuum-bag and ambient) and important process considerations (intermediary debulking and restricted air evacuation) on the void content and thickness reduction of laminates with two reinforcement types (UD and 8HS) [114]. Three important findings of this study are as follows: 1) 2D-woven semipregs were more susceptible to defects than unidirectional tapes; 2) restricted air evacuation is a worst-case scenario that is representative of attempting to evacuate entrapped air from very large parts; and 3) monitoring of the rate of thickness change of the laminate during the cure highlighted the formation of macro-porosity during the initial heat ramp.

In turn, Ma *et al.* conducted a similar type of study on corner laminates [121]. The multiple sample configurations included variations in the following parameters: laminate thickness and corner radii (varied independently), corner angle (35, 45 and 60°), tool-shape (convex or concave), and reinforcement type (5HS and 8HS). In addition, the efficacy of pressure intensifier strips was investigated to abate thickening in concave sample in addition to increasing corner radius and performing intermediary debulking. The important findings of this study are as follows: 1) concave corners exhibit the worst quality in terms of both thickness deviation and void content given significant resin accumulation, as illustrated in Fig. 1-20.A; 2) conversely, convex corners manifest corner thinning, as illustrated in Fig. 1-20.B; and 3) increasing the corner radii improved ply conformation and lowering porosity, while intermediary debulking is best suited for lowering porosity and the use of pressure intensifier strips for improving ply conformation.

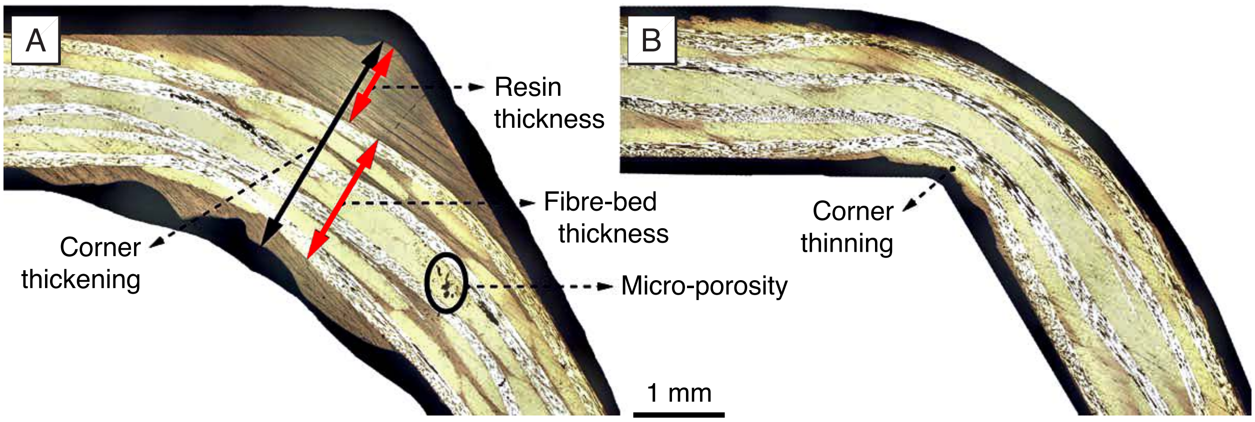

Fig. 1-20. Laminate quality in sub-90° VBO corner laminates: A) concave and B) convex (source: [121]).

Both parametric studies employed a systematic approach to investigating key design and processing factors (e.g. reinforcement type and consolidation pressure, resp.). Still, empirical work remains to be done in the investigation of new factors and factors that have thus far only been investigated in the context of flat laminates or only party in the context of corner laminates. Such factors will be fully discussed in § 5.4.1 and can, for the time being, be classified into three general categories: design consideration, deficient processing conditions and noteworthy industrial cases.

1.5.6 Mechanical performance

As discussed in § 1.3, the impetus for VBO semipreg processing is to offer a cheaper and more versatile processing route that yields large, integrated structures with the same high quality and performance readily achieved by autoclave prepreg processing [52]. Three decades of academic and industry-led research has resulted in an improved understanding of the variability and defects induced or affected by processing parameters and an overall maturation of the technologies involved, namely the development of semipregs with improved air evacuation strategies. Indeed, semipregs laminates have reached parity in coupon-level mechanical performance with autoclave prepregs laminates, as illustrated in Fig. 1-21, which gathers data from resin manufacturers and NCAMP to compare the relative performance for the two most common primary-reinforcement architectures: unidirectional tape and PW. Importantly, no major differences are evident between in- and out-of-plane, and fibre- and matrix-dominated properties, except for the ILTS value of the semipreg-PW, which stems from a single-plate test that may not be representative of the true ILT-performance of this material. It should be further noted that these tests were not performed under strict repeatability conditions [161]. On a more general note, the soundness of research findings is an important issue in composite research and notably in the case of VBO semipreg processing given the intrinsic variability of cured parts and the typically low number of sample repeats per tested corner configuration. This aspect of composite research will be discussed in greater depth in § 4.4.1, which deals specifically with the repeatability of experiments and the statistical relevance of corresponding research findings.

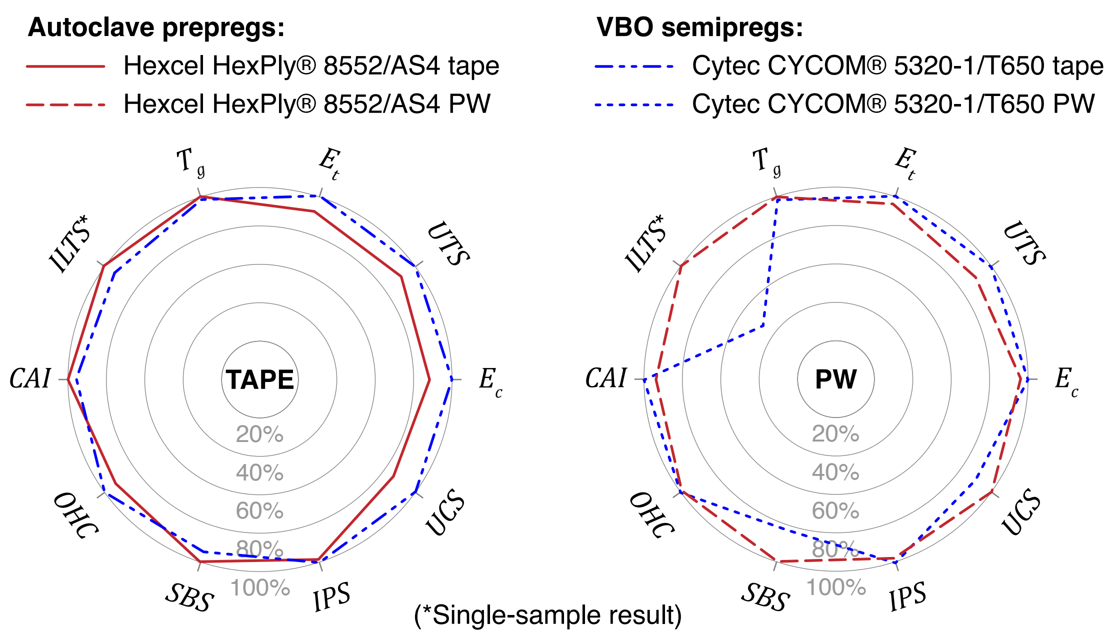

Fig. 1-21. Parity in coupon-level mechanical performance between autoclave prepregs and current-generation VBO semipregs (data from [68, 162-166]).

Despite the parity in mechanical properties of near-optimal, labscale flat laminates, VBO semipreg processing is less robust given the limited, available consolidation pressure, and is thus more susceptible to variability and defects, which will be increasingly prevalent in larger integrated parts. With respect to generic composite structures, it can therefore be expected that mechanical performance will be locally affected and deviate from coupon-level performance. A handful of studies have investigated the effect of process deficiencies on mechanical properties. Of note, Sutter *et al.* at NASA performed a preliminary study to compare the effect of out-time and ply collation technique (manual vs. automated) on standard autoclave prepregs and second-generation semipregs [167]. They observed a substantial drop in matrix-dominated properties for the semipreg laminates processed beyond a certain out-time owing to the presence of severe micro-porosity. In turn, Vo *et al.* [168] and Walker *et al.* investigated the effect of key VBO process parameters on matrix-dominated mechanical properties, namely combined-loading compression (CLC) strength and short-beam strength (SBS), resp. They both demonstrated strong correlations between the predicted glass-transition temperature of the epoxy matrices and matrix-dominated strength properties and resin-fibre adhesion (failure mode), and thus proved the need for an adequate, isothermal post-cure dwell to reach a near-optimal glass-transition temperature.

Current reference works on semipreg processing reflect the sparseness of the research that has thus far been conducted into the effect of variability and defects on mechanical performance [49, 52]. Considerably more research has comparatively been undertaken to establish relationships between processing parameters and variability and defects. In addition, the handful of aforementioned experimental studies have focused on lab-scale, flat laminates. As pointed out by Potter *et al.*, however, the quality and performance of coupon-level, flat laminates is not wholly representative of generic composite structures but rather represent a special, simplified case [141]. Further work ought to therefore be conducted on establishing the VBO processing factors that most affect the interlaminar performance of complex-shape laminates, starting with that of sharply-curved corners.

1.6 Summary

The literature survey covers the important aspects of VBO semipreg processing and more specifically the issues pertaining to sharply-curved details in current aero-structures. A number of research areas that require further empirical work have been uncovered. The particular gaps in knowledge can be divided into experimental methodology and understanding of materials and processing as presented in Table 1-4.

With respect first to experimental methodology, three areas for improvement have been highlighted. First, there is a need to estimate and reduce the error in the applied bending moment determination and its effect on the CBS and ILTS determination for current 4PB-CBS standards, namely ASTM D6415 (§ 1.4.2). A particular emphasis is placed on the need for modifications that may be standardized. In turn, there is a need for thickness measurement methods for complex-shape laminates with improved accuracy, precision and ease-of-use (§§ 1.5.3 and 2.4.1). Lastly, there is a need to adapt fibre-bed characterization methods to investigate fibre waviness in curved regions such as corners (§ 1.5.4).

Table 1-4. Gaps in experimental methods for and understanding of VBO complex-shape laminates.

Experimental methodology	Materials and processing
- Error in applied bending moment in current 4PB-CBS test standards - Limited accuracy and precision of thickness measurement methods for complex-shape laminates - Fibre waviness characterization in corners	- Factors affecting laminate quality of sharply-curved details - Factors affecting the mechanical performance of corners - Corner design and processing guidelines - Repeatability of research findings given high degree of variability

With respect then to improving the understanding of material and processing knowledge, four areas for improvement have been highlighted. First, additional experimental work is required to select and investigate the design, processing and industrial factors that affect laminate quality in sharply-curved details (§ 1.5.5). In turn, there is a need to investigate the effect of these factors and the reliability of VBO processing in general on the mechanical performance of sharply-curved details (§§ 1.5.6 and 1.5.6, resp.). Next, this empirical work should build on the work of Centea *et al.* [114] and Ma *et al.* [121] and add to current design and processing guidelines for parts that include sharply curved details. Lastly, there is a need to investigate the repeatability of experiments and the corresponding research findings given the intrinsic variability observed in cured, current-generation semipreg laminates (§§ 1.5.6 and 4.4.1). A more general consideration is the statistically-unrepresentative nature of findings in composite research given insufficient repeated observations.

1.7 Thesis objectives and structure

In light of the gaps in methodology and of knowledge highlighted in the previous section, two overarching aims and corresponding objectives are proposed. **The first aim (I) is to improve the current state of methodology for the experimental characterization of corners**. The objectives proposed to this effect are as follow:

i. Estimate the effect on the CBS and ILTS determination of the error in the applied bending moment calculation for current 4PB-CBS test standards, namely ASTM D6415;
ii. Develop a direct, practical and cost-effective modification that may be standardized to reduce the magnitude of these errors;
iii. Develop a versatile, semi-automated thickness measurement method for corners and validate its accuracy and precision against existing norms;
iv. Develop a characterization approach to assess the extent, magnitude and morphology of fibre waviness in corners.

In turn, **the second aim (II) is to advance the understanding of relationship between design and processing, and laminate quality and mechanical performance in VBO corners**. The objectives proposed to this effect are as follow:

i. Investigate the soundness of the research findings in terms of the statistical repeatability of the experiments and the intrinsic variability of measurements;
ii. Systematically assess the effect of select design factors, deficient consolidation pressure and noteworthy industrial processing cases on laminate quality;
iii. Systematically assess the effect that these same factors have on mechanical performance and, in particular, ILT properties;
iv. Consolidate the empirical findings into concise design and processing guidelines;
v. Investigate the extent, magnitude and morphology of fibre waviness in unidirectional-tape corners.

Thesis structure

The work contained in this thesis follows the structure illustrated in Fig. 1-22 and is broken down into the following body chapters:

Chapter 2 covers the materials and general experimental methods, including: material selection and general processing cycle design, specimen preparation, the corner thickness profile acquisition (profiling) method (Obj. I.iii), and the optical microscopy methods for the determination of constituent volume fractions.

Chapter 3 is the first results chapter and focuses on estimation of the CBS and ILTS error due to the error in applied bending moment as calculated in ASTM D6415 (Obj. I.i). In turn, a novel solution is developed to directly eliminate flange flexure in the form of cost-effective, mechanically-assembled and adjustable stiffening-sleeves (Obj. I.ii). The work is performed via 2D and 3D FEM and validated via mechanical testing and a subsequent fractographic inspection.

Chapter 4 is the second results chapter and focuses on the selection of and effect that key design, processing and industrial factors have on laminate quality in terms, primarily, of void and fibre content, and thickness deviation (Obj. II.ii), from which design and processing guidelines are extracted (Obj. II.iv). In turn, a method for the determination of experimental repeatability is developed and the soundness of the research findings is assessed in terms of the three aforementioned laminate quality measurements (Obj. II.i).

Chapter 5 is the third and final results chapter and focuses on the effect that the factors selected in chapter 4 have on mechanical performance as determined via CBS testing (Obj. II.iii). The findings are subsequently used to extract further design and processing guidelines (Obj. II.iv). In turn, the soundness of the research findings is assessed in terms of CBS and ILTS measurements (Obj. II.i). Finally, a characterization approach is developed to investigate fibre waviness in corners via image analysis of both 2D micrographs and reconstructed 3D-data from micro-CT scans (Obj. I.iv). This approach is subsequently used to characterize the extent, magnitude and morphology of the fibre waviness occurring in unidirectional-tape, convex-corner (Obj. II.v).

Finally, **Chapter 6** closes this thesis by enumerating and discussing its principal research contributions in terms of the stated research aims and objectives. In addition, notable recommendations for future work are offered.

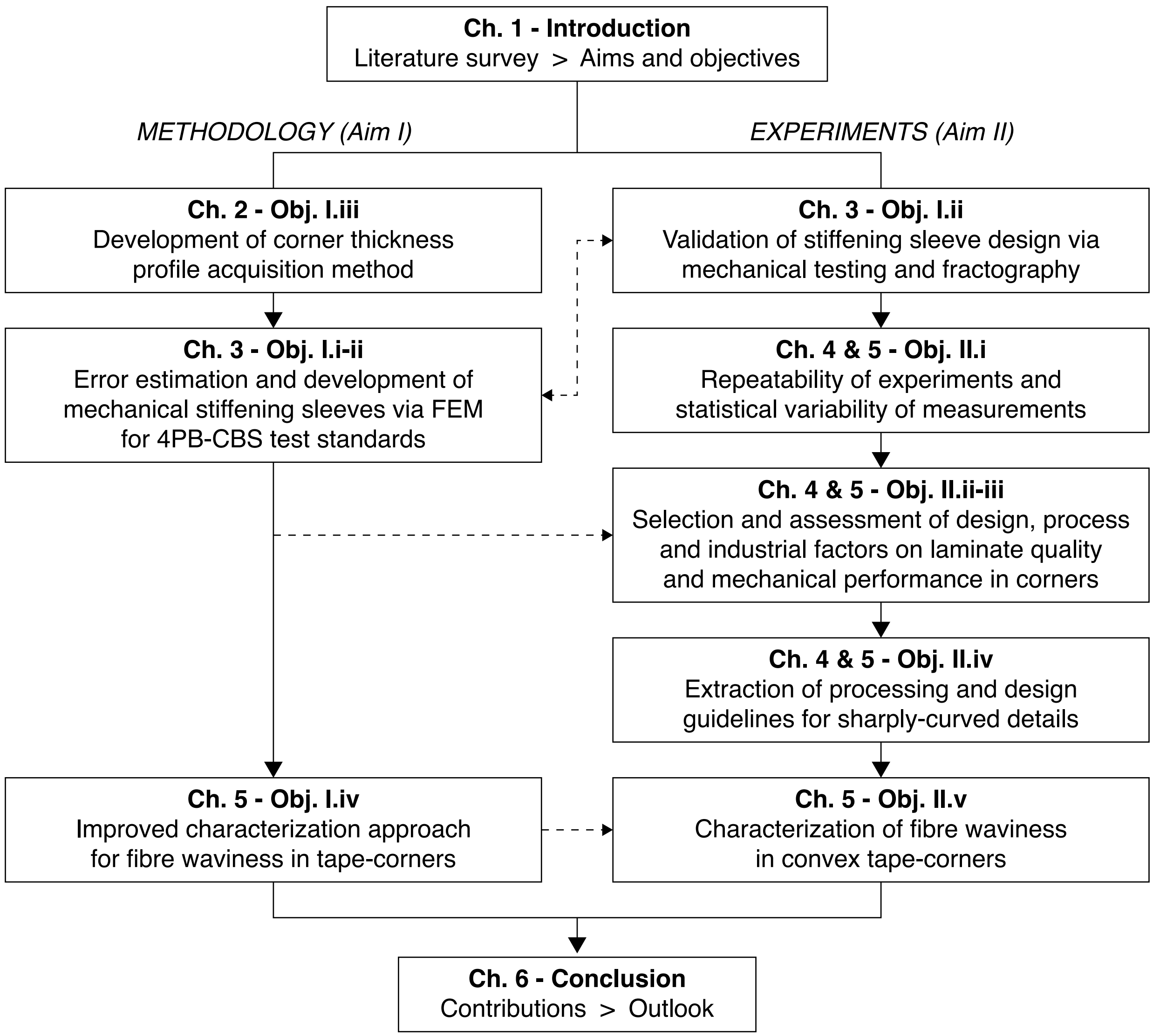

Fig. 1-22. Thesis structure with objectives.

2

Materials and general methods

2.1 Chapter overview and outline

The experimental work presented in this thesis centers around a single curved beam (corner) specimen geometry that is manufactured, conditioned and tested from a single set of VBO semipregs and utilizing a consistent set of experimental methods and measurements. The singly-curved corner specimen configuration is deemed to be the simplest case to represent the behaviour of more complex-shape laminates. The only experimental conditions to change are the factors under investigation at the sample-level, e.g. deficient consolidation pressure. The material selection and general methods are thus combined in this chapter for conciseness. They include the most advanced OOA resin systems and the best academic and industrial research practices.

It should be noted that methods that pertain to only part of the experimental work such as finite element modelling (FEM), scanning electron microscopy (SEM) and X-ray computed micro-tomography (micro-CT) are presented alongside the respective experimental results in the subsequent results chapters. In addition, the following terminology is henceforth employed: each corner beam that is manufactured and tested represents a singular *sample* of the overall population for a given set of experimental conditions; samples are in turn comprised of multiple *specimens* that correspond to a single *observation* per measurement type.

The chapter outline is as follows. The first section (§ 2.2) introduces the materials selected for the experimental work, their physical and mechanical properties, and the associated cure cycle design. The subsequent sections describe in detail the methodical preparation of corner specimens (§ 2.3), and the image analysis methods used to assess laminate quality in corner regions, namely: 1) the acquisition of the full specimen thickness profile from scanned sample profiles to assess thickness deviation (§ 2.4), and 2) the analysis of resin-mounted laminate cross-sections via optical microscopy to assess fibre and void contents, and corresponding T-T distributions (§ 2.5). The mechanical testing methodology is presented in Chapter 3 alongside proposed modifications aimed at improving the accuracy of measured, ILT mechanical properties.

2.2 Material selection and general processing cycle design

2.2.1 Material selection and physical properties

The experimental work is conducted on semipregs specifically designed for VBO processing. As noted in Chapter 1, there have now been several generations of semipregs, the latest and most advanced of which are expensive and challenging to procure for academic research. They are solely produced in cooperation with and used by key aerospace industrial partners for specific aircraft development projects. The semipregs that were obtained for this thesis were generously provided by Bombardier Aerospace and represent some of the most advanced semipregs currently used in industry. Resin formulation and associated properties are a critical component where intellectual property is concerned. For this reason, only a general description of these materials and their properties is provided in a manner that is concurrent with published studies that have thus far made use of them and technical data published by the manufacturers [106, 169, 170].

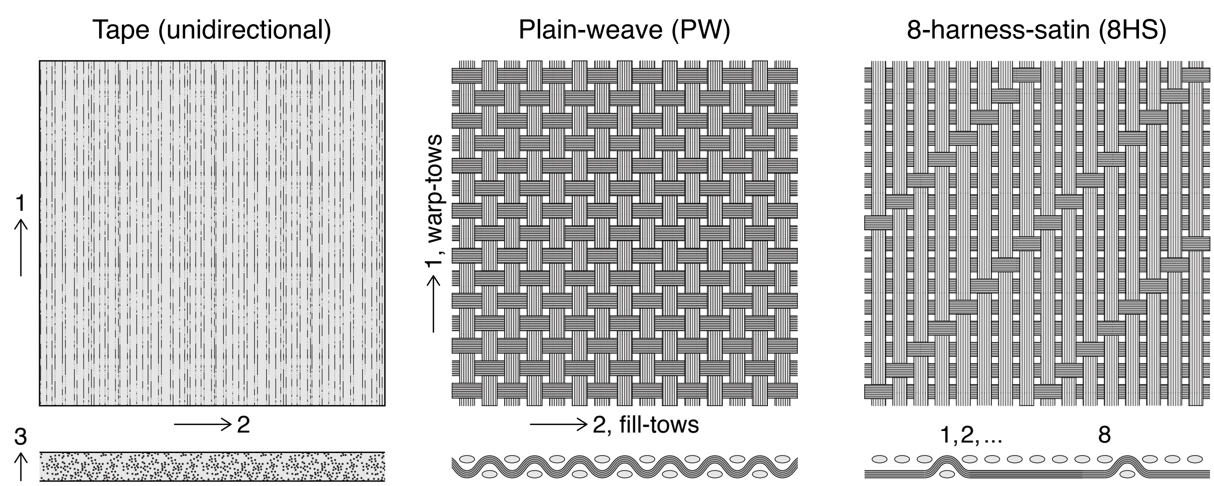

Fig. 2-1. Primary-reinforcement architectures of the selected semipregs.

Three semipregs with different primary-reinforcement architectures are selected, as illustrated in Fig. 2-1: a unidirectional tape (tape), a plain weave (PW) and an 8-harness-satin weave (8HS). All three were manufactured by Cytec Engineered Materials Inc., USA. They contain similar formulations of Cytec's proprietary CYCOM® 5320 toughened resin [170], an epoxy resin, and utilize Cytec's THORNEL® T650/35 pan-based carbon fibres [171], which have a nominal diameter of 6.8 µm. The semipregs are henceforth referred to as *tape* (or simply *T*), *PW* and *8HS* given the common resin system. Their physical properties are presented in Table 2-1. The aim of this selection is to vary fibre-reinforcement architecture in order to study its effects on the quality and mechanical performance of corner laminates. They also differ significantly in terms of degree of resin impregnation, air evacuation strategy, bulk-factor and tow structure.

Table 2-1. Physical properties of the three selected Cytec CYCOM® 5320 semipregs.

Property	Tape	PW	8HS
Resin	CYCOM® 5320*	CYCOM® 5320*	CYCOM® 5320
Resin content by weight	33%	36%	36%
Out-life	> 21 days	> 21 days	21 days
Carbon fibre	T650/35 pan	T650/35 pan	T650/35 pan
Tow fibre count	6k	3k	3k
Prepreg areal weight	145 $g \cdot cm^{-3}$	196 $g \cdot cm^{-3}$	370 $g \cdot cm^{-3}$
Bulk-factor†	1.21	1.33	1.53
Air evacuation network	Dry mid-plane [114]	Dry tow cores and surface openings [72, 172]	Dry tow cores [114]

*Extended out-life formulation resulting in negligible differences in cure and mechanical properties.
†Experimentally measured.

Centea and Hubert presented a methodology to study resin-flow in dry-fibre regions, which involves the image analysis of microstructural 3D-data of partially cured semipreg laminates obtained via micro-CT scanning [173]. This technique was used to investigate the air evacuation networks of the tape and 8HS [114], and of the PW [172]. Cytec employs the traditional hot-melt process to partially impregnate the tape and 8HS, and makes use of a newly patented resin deposition strategy to partially impregnate the PW [72]. The tape is fully impregnated on both major surfaces, but only partially impregnated through-the-thickness. Air evacuates through the dry unidirectional fibre mid-plane (Fig. 1-7). In contrast, the PW and the 8HS have only superficially impregnated fibre tows. Air is evacuated through the dry tow cores. The key difference between the PW and 8HS is that the major surfaces of the 8HS, like the tape, are fully coated in resin, whereas the PW has surface openings (resin-free) at tow crossovers on one major surface to improve T-T permeability (Fig. 1-10) [72, 172].

Looking at the other physical properties, the tape has the lowest areal weight and bulk-factor compared to the two fabrics. In turn, the PW and 8HS share the same tow count and similar air evacuation networks, but the areal weight and bulk-factor of the 8HS are significantly greater than the values of the PW, which are more comparable to the values of the tape. Centea observed that the 8HS has a tighter and thicker weave with more circular and fibre-dense tow cross-sections, whereas the PW has a looser and thinner weave with more elliptical tow cross-sections [63].

The reinforcement type, degree of impregnation and air evacuation network dictate the initial laminate thickness and the practicality of conforming plies to a given tool radius—especially a concave one. In turn, air evacuation, inter- and intra-ply fibre nesting, and resin impregnation during the cure cycle influence the final laminate thickness. The *bulk-factor*, which is the dimensionless ratio of the before and after thickness measurements, strongly influences thickness deviations in complex-shape parts. The physical properties of the semipregs will also influence the void content, fibre waviness and interlaminar mechanical properties of corner laminates.

It should be noted that there is no inter-batch variability on account that the selected semipregs come from single batches, i.e. identical rolls. In addition, the out-life—or tack-life—of the CYCOM® 5320 resin system is at least 21 days. The out-time up to the moment of cure of all semipregs used in experiments are estimated to be no more than 5 days—less than a fourth of the resin out-life. This estimate is conservative and accounts for the shipping and handling time of semipreg rolls prior to arrival and storage in laboratory freezers, as well as the cumulative out-time of all subsequent experimental steps. No effect due to ageing is expected at the 5-day mark based on the product information [170] and research findings for this resin system [58, 63, 124].

2.2.2 General processing cycle design

Processing of semipregs typically involves three stages: a room-temperature (RT) hold, and a two-part cure cycle comprising of a cure dwell and a post-cure dwell performed in a regular mechanical convection oven (Blue M Oven equipped with an Omega PID controller). The RT-hold is the first and crucial step regarding air evacuation. It consists of leaving the assembled semipreg laminate and vacuum-bag on the tool under vacuum pressure at RT until a satisfactory degree of air evacuation has been reached. The duration is primarily dictated by the in-plane air permeability of the semipreg laminate. T-T air permeability is generally orders of magnitude smaller and is therefore omitted from the process design [70]. It should be noted that no published data could be found to corroborate the improvements in T-T air permeability reported by Cytec for its patented PW.

A model developed by Arafath *et al.* [70] is used to estimate the requisite hold time, t_{hold}, needed to evacuate a desired mass fraction of air for a given semipreg laminate,

$$t_{hold} = \frac{\eta_{air} L^2}{p_0 K}\left[-\frac{1}{0.9} ln\left(\frac{m}{m_0}\right)\right]^{\frac{1}{0.6}} \tag{2-1}$$

where: η_{air} is the dynamic viscosity of air; L is the equivalent laminate radius (17.8 cm); p_0 is the ambient pressure; K is the in-plane air permeability of the laminate; and m/m_0 is the desired mass fraction of remaining gas—in this case, air. The hold is performed at an expected standard laboratory RT of 23 ± 2°/C [174]. The Sutherland equation is widely used to estimate the effect of temperature on the dynamic viscosity of standard air. For the chosen temperature range, the viscosity varies negligibly, an average value of 1.85×10^{-5} Pa·s is therefore used. Montreal being at sea-level, the ambient pressure is set at 101.325 kPa. That being the case, fluctuations in ambient pressure can be shown to minimally affect the requisite debulk time.

In-plane permeability values are presented in Table 2-2. and are estimated from published values for the same or similar semipregs. Three common layups (stacking sequences) are considered: 1) unidirectional or *UD* ($[0°]_{n,s}$); 2) cross-ply or *XP* ($[0°/90°]_{n,s}$); and 3) quasi-isotropic or *QI* ($[45°/0°/-45°/90°]_{n,s}$). Intermediary debulking is found to significantly decrease the in-plane permeability of the referenced woven semipreg laminates by a factor of 1.58-2. The decrease is due to the collapsing of air evacuation pathways, itself the product of inter and intra-ply fibre nesting. It is unclear to what extent intermediary debulking during the layup decreases the in-plane permeability of tapes given a lack of empirical data. It should also be noted that an increase in the number of plies has been shown to significantly decrease the in-plane permeability of a laminate. Measurements are often made on layups that consist of fewer plies than desirable for actual parts. Given the relatively low confidence in published permeability found in the literature, a knock-down factor of at least 2 is applied to all the estimated RT-hold times as a conservative measure. The last column of Table 2-2 presents the selected RT-hold times.

Table 2-2. Published in-plane permeability measurements and estimated RT-hold times.

Semipreg (layup)	K (m²)	Referenced material	Ref.	t_{hold}	$> 2 \cdot t_{hold}$
Tape (UD, QI†)	2.04×10^{-15}	Toray T800SC / 3900	[70]	7.37h	15h
Tape (XP, QI*)	9.6×10^{-15}			1.57h	4h
PW (UD, QI†)	1.2×10^{-13}	Cytec PW / 5320^	[175]	7.52m	0.5h
Debulked PW (UD, QI†)	6×10^{-14}			15.04m	
8HS (UD, QI†)	5.04×10^{-14}	Cytec 5HS / MTM45-1	[176]	17.90m	1h
Debulked 8HS (UD, QI†)	3.18×10^{-14}			28.38m	

*Assumed to be similar to the XP layup; †assumed to be similar the UD layup; ^predecessor prepreg to the selected PW without the patented surface openings

Intermediary debulking at room-temperature is shown to have a mediocre effect on air evacuation in corner laminates [67, 137]. Thermally-assisted compaction (hot-debulk) shows more potential [127], but it is not further considered given that it is still far from becoming a standard practice in academic research and industry. The primary reason for employing a debulk step in the case of corner laminates is to promote interply collation, which reduces the likelihood of fibre-bridging and wrinkling for concave and convex corners, resp. [121, 127]. The post-cure benefits are reduced corner thickening and void content. The lack of ply slippage during cure given the relatively long flange length [137] is partly overcome by allowing plies to nest, partially compact and therefore better conform to the desired corner geometry during layup.

The second stage of the process is the cure cycle. Kratz *et al.* have characterized the cure kinetics (the degree-of-cure), viscosity and glass-transition temperature of the CYCOM® 5320 resin with semi-empirical models [169] following the first steps of the characterization methodology presented by Khoun *et al.* [177]. The models were experimentally validated using one-dimensional heat transfer analysis on very thick semipreg laminates. Modelling these three properties as a function of temperature and time is a crucial step in the design of a suitable cure cycle. The physical constants and fitted parameters of the three models are presented in Table 2-3.

The cure kinetics model assumes that the exothermic reaction rate of the thermoset resin ($d\alpha / dt$) is proportional to the experimentally measured heat flow rate (dH / dt). The *degree-of-cure* (α) is a dimensionless unit ratio that is proportional to the degree of polymerization (cross-linking) of polymer chains as they form permanent covalent bonds. The model therefore predicts the degree-of-cure achieved by a given cure cycle as well as the thermal evolution for a given part geometry. The latter accounts for exothermal peaks in thicker parts that can result in temperatures and temperature gradients that exceed allowable limits. In turn, the viscosity model accounts for the evolution of the viscosity and the ability of the resin to flow and impregnate the fibre-bed during the cure cycle. It is imperative that air evacuation and full resin impregnation of the dry reinforcement regions occur prior to gelation of the resin, which will otherwise entrap any remaining voids. Lastly, the glass-transition temperature model predicts the final glass-transition temperature, which is an important predictor of mechanical properties and directly related to the degree-of-cure. A part must be dimensionally stable and strong enough to be removed from a processing tool and perform as intended. Studies performed by Kratz *et al.* [169] and Khoun *et al.* [177] can be perused to gain a more detailed understanding of the characterization methodology and the implications of these models with regard to cure cycle design.

Table 2-3. Characterization modelling constants for the Cytec CYCOM® 5320 resin (adapted from [169]).

Model	Constant	Value	Physical significance
Cure kinetics	E_1, E_2 (J·mol^{-1})	82,375, 62,355	Activation energies
	D	40.4	Diffusion constant
	α_{C0}	-1.22	Degree-of-cure at absolute zero
	α_{CT} (K^{-1})	4.53×10^{-3}	Accounts for the critical degree-of-cure increase with temperature
	R (J·mol^{-1}·K^{-1})	8.314	Universal gas constant
	A_1, A_2 (s^{-1})	8.23×10^{4}, 1.04×10^{5}	Fitted parameters
	m_1, m_2	0.75, 0.90	
	n_1, n_2	12.46, 2.07	
Viscosity	$E_{\eta 1}$, $E_{\eta 2}$ (J·mol^{-1})	93,931, 83,400	Viscosity activation energies
	α_{gel}	0.48	Degree-of-cure at gelation
	$A_{\eta 1}$, $A_{\eta 2}$ (Pa·s)	8×10^{-13}, 2.9×10^{-11}	Fitted parameters
	A, B and C	3.2, 12.7, -29.6	
Glass-transition temperature	T_{g0} (°C)	-8.4	T_g of the uncured resin
	$T_{g\infty}$ (°C)	212	T_g of the fully cured resin
	λ	0.66	Fitted parameter

The cure kinetics model ($d\alpha/dt$) is fitted to temperature-ramp and isothermal dwell data from dynamic scanning calorimetry (DSC) experiments, and the viscosity model (η) is fitted to similar data from rheology experiments.

$$\frac{d\alpha}{dt} = K_1\alpha^{m_1}(1-\alpha)^{n_1} + \frac{K_2\alpha^{m_2}(1-\alpha)^{n_2}}{1+exp^{D(\alpha-(\alpha_{C0}+\alpha_{CT}T))}} \tag{2-2}$$

$$\text{where: } K_i = A_i\ exp^{E_{Ai}/R\cdot T}, i = 1, 2$$

$$\eta = \eta_1 + \eta_2\left(\frac{\alpha_{gel}}{\alpha_{gel}-\alpha}\right)^{A+B\alpha+C\alpha^2} \tag{2-3}$$

$$\text{where: } \eta_i = A_{\eta i}\ exp^{E_{\eta i}/R\cdot T}, i = 1, 2$$

K_i and η_i given are Arrhenius temperature dependencies. The glass-transition temperature model (T_g) is fitted to dynamic mechanical analysis (DMA) experiments performed on semipreg laminates cured at different temperatures,

$$T_g = \frac{(T_{g\infty}-T_{g0})\lambda\alpha}{1-(1-\lambda)\alpha} + T_{g0} \tag{2-4}$$

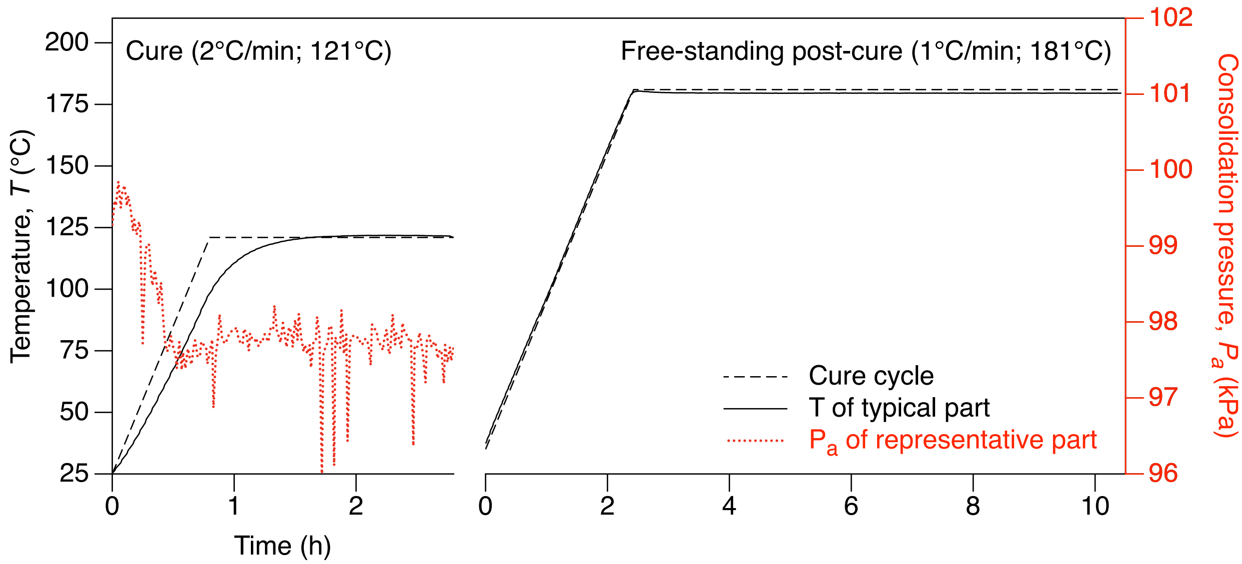

Fig. 2-2. Selected cure and post-cure cycles for the Cytec CYCOM® 5320 resin.

The cure kinetics and viscosity model predictions are employed to design a single cure cycle to process all three selected semipregs. The cure cycle is presented in Fig. 2-2 and is split into two stages: 1) the cure itself consists of a 2 °C/min ramp and a 2 h dwell at 121 °C, both performed in a vacuum-bag; and 2) the post-cure consists of a 1 °C/min ramp and an 8 h dwell at 181 °C, both performed free-standing, i.e. with the laminate demoulded. Parts are left to cool via natural, RT air convection after each stage. The cure ramp follows industrial practices in addition to Cytec's recommendations [170]. The ramping rate is halved for the post-cure as a precaution in order to slow the exothermic reaction and thus limit the temperature spike at the beginning of the post-cure dwell. A free-standing post-cure is selected to relieve any cure-induced stresses. Finally, the post-cure dwell has been extended to 8h in order to achieve a more optimal, final degree-of-cure and glass-transition temperature (α_{max} = 0.98, $T_{g,max}$ = 205 °C). The consolidation pressure being plotted is the effective pressure acting down on the laminate, i.e. the difference between the ambient and vacuum-bag pressures (§ 2.3.2). The model predictions for the evolution of the degree-of-cure, viscosity and glass-transition temperature are presented in Fig. 2-3.

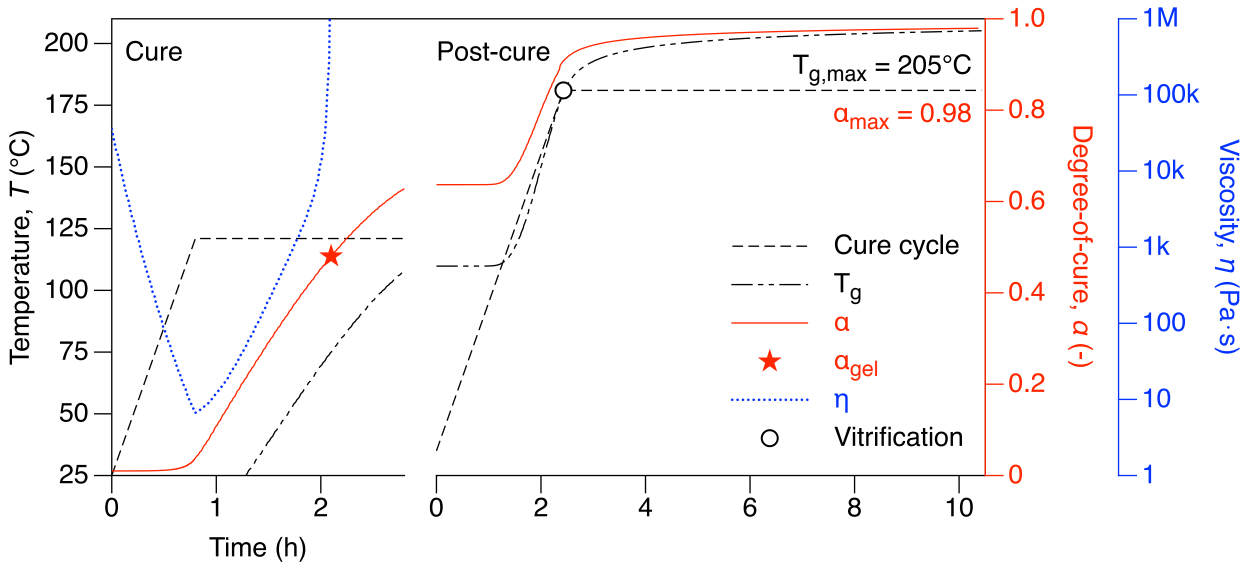

Fig. 2-3. Predicted evolution of the degree-of-cure, viscosity and glass-transition temperature for the selected cure and post-cure cycles.

2.2.3 Mechanical properties

Select mechanical properties of the three selected semipregs are presented in Table 2-4 and were determined by the manufacturer via the relevant ASTM mechanical test standards. Test coupons were pre-conditioned to meet room-temperature-dry specification (RTD; ASTM D5229, procedure D; 48h at 70 ± 3 °C in a regular mechanical convection oven). The symbols that are utilized are consistent with the relevant ASTM standards.

Table 2-4. Mechanical properties of the three selected Cytec CYCOM® 5320 semipregs.

Property	Units	Tape	PW	8HS	ASTM method
$E_{11} = E_\theta$*	GPa	134	64.5	63.1	D3039 / SRM-1^
E_{22}*	GPa	9.93	E_{11}†	E_{11}†	D3039 / D6641
$E_{33,t} = E_r$*	GPa	$E_{22,t}$**	10.8	10.9	D6641
ν_{12}	-	0.33*	0.057	0.048	D3039
ν_{13}	-	ν_{12}**	0.5‡	0.5‡	n/a
ν_{23}	-	0.5‡	ν_{13}†	ν_{13}†	n/a
G_{12}	GPa	5.41	5.74	5.87	D5379
G_{13}	GPa	G_{13}**	3.00‡	3.00‡	n/a
G_{23}	GPa	3.11**	G_{13}†	G_{13}†	n/a
$F^{sbs} \approx S_{13}$ = ILSS	MPa	117	93.8	82.0	D2344
$F_{33,tu} = \sigma_{r,max}$ = ILTS	MPa	80.2"	34.7"	38.7"	D6415
$k = (E_\theta / E_r)^{0.5}$	-	3.89	2.45	2.41	n/a

*Average of E_t and E_c ; **transverse isotropy; †warp-fill symmetry assumption; ‡estimated property; "property determined for QI layup; ^SACMA test method. (Coupon conditioning: RTD; ASTM D5229 procedure D; 48h at 70 ±3 °C in a regular convection oven.)

Certain assumptions are made in order to calculate missing properties. Transverse isotropy is assumed for the tape and the warp (1-dir.) and fill (2-dir.) are assumed to be symmetrical for the PW and 8HS. Values for the out-of-plane Poisson's ratios, ν_{13} and ν_{23} are simply estimated as is often the norm in modelling work [92, 178] and can be shown to have minimal impact on results. Lastly, the tangential and radial properties in the corner region (denoted by θ and r, resp.) are estimated from the properties of a flat laminate, except for the ILTS, which is determined from mechanical tests performed on corner specimens (ASTM D6415). It should be noted that the in-plane elastic constants, E_{11} and E_{22}, are averages of the respective compression and tension moduli, and that the ILTS properties were determined for quasi-isotropic laminates and are therefore conservative compared to the expected values for unidirectional layups. The mechanical properties of the tape are further discussed in Chapter 3 with regards to populating finite element models.

2.3 Specimen preparation

2.3.1 Curved beam strength specimen design

The curved beam strength—or corner—specimen that was proposed by Jackson and Ifju [83] is used for all experiments and is illustrated in Fig. 2-4. The specimen consists of two equal flanges, also called moment arms or legs, that form a right-angle and are joined by a curved bend of constant radius, i.e. the corner region. The ASTM D6415 test standard recommends specific dimensions to be used when determining the ILTS—in addition to limiting the material and layup to unidirectional tape with the fibres oriented in the hoop (tangential) direction [90]. In particular, the standard recommends a laminate thickness to 4.2 ± 0.2 mm irrespective of the UD-tape being tested. Based on preliminary experimental work [99, 127] and limited material availability, a smaller specimen is considered in order to create one consistent specimen geometry for all three selected semipregs. Table 2-5 summarizes the key specimen dimensions. The new specimen is roughly 20% smaller in width, thickness and radius but importantly maintains the same proportions. It is henceforth referred to as the *custom specimen* or simply the *specimen*.

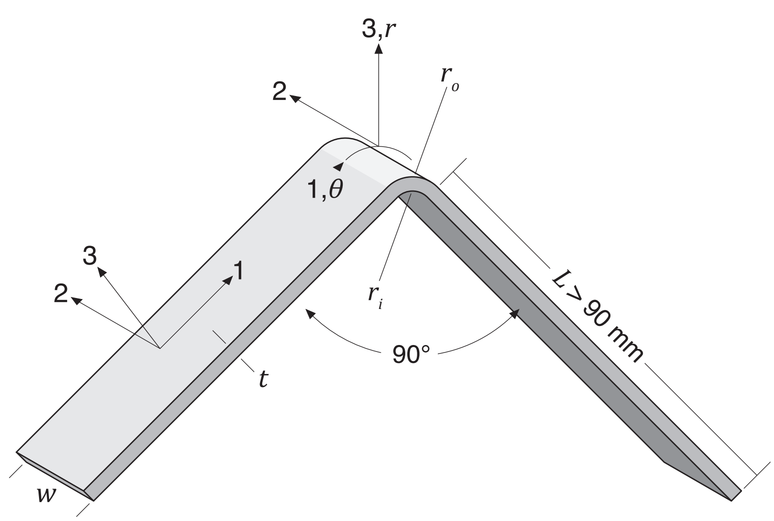

Fig. 2-4. Curved beam strength specimen schematic.

A single specimen geometry allows for only one tool-plate to be manufactured and thus reduces experimental costs significantly. It is of critical importance, however, that a corner ratio (r_m / t) of approximately 2 be maintained as is the case with the ASTM specimen. Respecting this

Table 2-5. Curved beam strength specimen dimensions.

Dimension / ratio	ASTM D6415 sp.	Tape custom sp.	PW custom sp.	8HS custom sp.
w (mm)	25 ± 1	20	20	20
t_{ply} [cv (%)] (mm)	n/a	0.135 [1.13]	0.197 [0.419]	0.373 [0.617]
n_{plies}	n/a	24	16	8
t (mm)	4.2 ± 0.2	3.24	3.15	2.98
w/t	5.95	6.17	6.35	6.71
Convex corner				
r_i (mm)	6.4 ± 0.2	4.5	4.5	4.5
r_m/t*	2.02	1.89	1.93	2.01
Concave corner				
r_o (mm)	10.6 ± 0.2	7.8	7.8	7.8
r_m/t*	2.02	1.91	1.98	2.12

*$r_m = (r_i + r_o) / 2$

ratio ensures that the Kedward approximation for the ILTS can be utilized with minimal error during modelling (§ 1.4.3) and mechanical testing data reduction given the heterogeneity of the selected semipregs [41]. In addition, the typical, balanced quasi-isotropic layup, $[45°/0°/-45°/90°]_{ns}$, has a basic ply count unit of 8, meaning that the laminate thickness can only be increased in 8-ply increments. By happenstance, the selected tape, PW and 8HS semipregs allow for an approximate thickness of 3 mm with ply counts of 24, 16 and 8, resp. Inner and outer radii of 4.5 and 7.8 mm are selected for specimens made on convex and concave tool surfaces, resp., in order to preserve the original corner ratio. It should be noted that the specimen width is also reduced to 20 mm in order to maintain a less critical width-to-thickness ratio of roughly 6.

Of secondary importance, the test frame and load cell used for the experimental work have an upper working limit of 4.5 kN, which was deemed to be close to the peak load of preliminary specimens that were tested. In addition, the custom four-point bending (4PB) fixture used in experiments has relatively long stainless-steel loading rollers that deflect considerably under a higher peak load (> 104 mm long compared to ≤ 25 mm specimen width). This unaccounted-for deformation increases the already significant error in the applied bending moment calculations [90]. Fig. 2-5 compares the degree of roller deflection between the standard and custom specimens for the longest rollers. This data is the result of finite element modelling work performed with Abaqus/Standard, which will be described in depth in Chapter 3. The reduction in specimen size yields a substantial reduction in roller deflection of nearly 60%. A final source of motivation for reducing the specimen size was to more judiciously utilize the finite quantities of semipreg that were generously provided by Bombardier Aerospace for the experimental presented in this thesis.

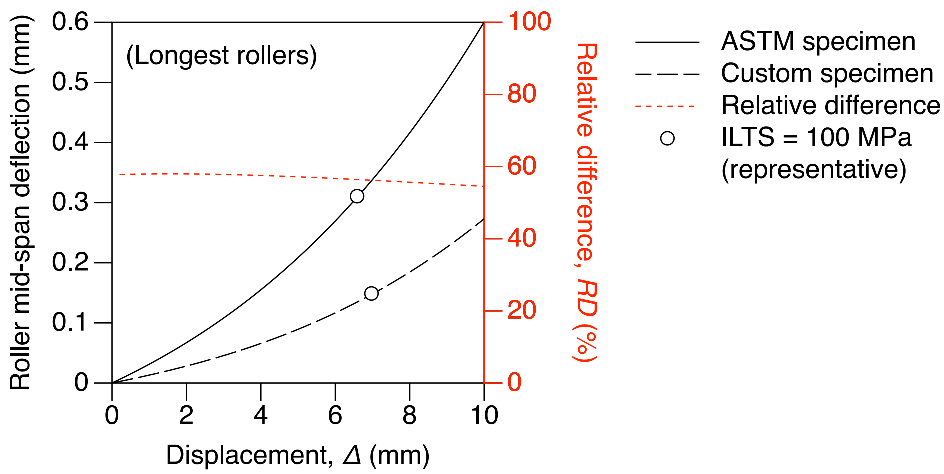

Fig. 2-5. Reduction in loading roller mid-span deflection of the custom ASTM D6415 fixture.

2.3.2 Curved beam tool design and experimental processing setup

Corner specimens are manufactured on a single curved beam tool, which is double-sided (concave and convex tool surfaces) and specifically designed for the specimen dimensions that are determined in the previous section. Fig. 2-6 depicts the tool with the corresponding vacuum-bagging consumables sequence in its convex and concave configurations. Fig. B-1 and B-2 in Appendix B detail the machined features and associated dimensions. The tool is machined from aluminum 6061-T6, which offers a good compromise between thermos-mechanical properties, corrosion resistance, machinability and cost given the relatively low quantities of plates that it was designed to process (< 100 corner beams per side). The tool is 11.4 mm thick with a working surface that is 610 mm long between vacuum-ports and flanges that are 190 mm wide. The work surface accommodates prepreg plies that are 280 × 450 mm on the convex side and 250 × 450 mm on the concave side. These dimensions allow for up to 15 specimens (20 mm wide) to be cut from each manufactured corner beam.

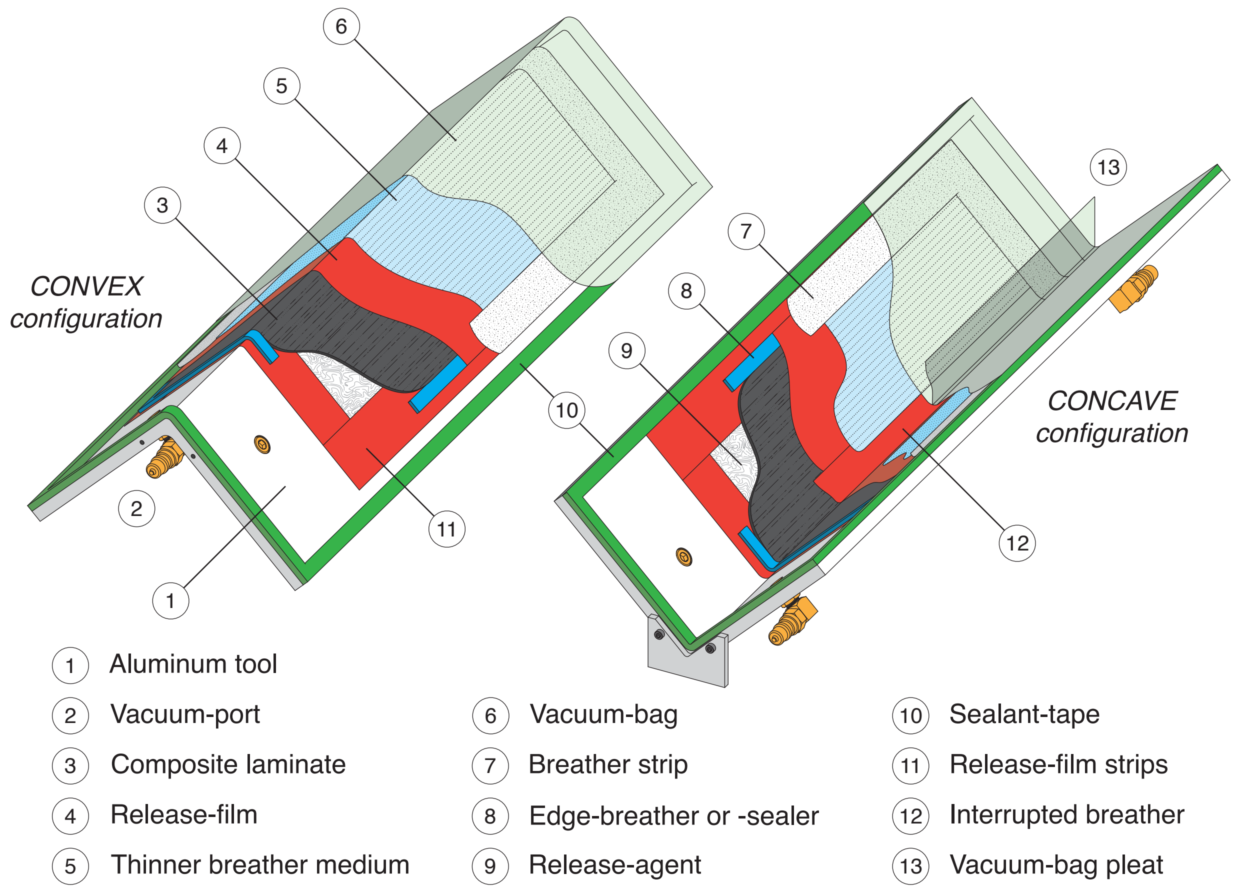

Fig. 2-6. Two-sided curved beam tool and vacuum-bagging consumable sequence (reproduced in [52]).

Both major tool surfaces are manually polished and sealed using a solvent-based mould sealer. The areas directly below the laminates are further treated with a solvent-free, semi-permanent release-agent instead of release-film to prevent wrinkling [146]. Vacuum is pulled and monitored through the tool via two industry-standard quick disconnect vacuum-ports. This feature reduces the chance of air leaks and vacuum-bag wrinkles compared to the use of a bulky, standard through-bag vacuum-valve. The tool is rotated between the convex and concave configurations by simply substituting the vacuum-ports on one surface with the plugs found in identical NPT-holes on the other surface. The tool materials and vacuum-bagging consumables are listed in Table 2-6 and consist of commercially available products that are widely used in industry for autoclave and various OOA processes such as VBO semipreg processing.

The ASTM D5687 test standard covers the preparation of flat composite test panels and offers a thorough description of the conventional layup process and the processing consumables that are involved [66]. Deviations from the standard layup arrangement are necessary in the case of convex and concave tool features in order to reduce the bulk and bridging, resp., of processing consumables. The layup over convex features is the simpler of the two cases. A thinner breather layer is recommended in order to reduce consumable bulk and the likelihood of wrinkles transferring onto the laminate surface. A released peel-ply is used to replace the typical breather given that it is considerably thinner and only slightly less air permeable. Regular edge-breather strips are laid around the laminate perimeter to create a continuous air pathway between the edge-breather strips and the vacuum-ports (Fig. 1-8).

Table 2-6. Summary of curved beam tool materials and vacuum-bagging consumables.

Materials and consumables	Commercial product	Fig. 2-6 callout
Tool material / mould sealer	Aluminum 6061-T6 / Zyvax® Sealer GP	1
Vacuum-port	Airtech AQD500TF quick disconnect	2
Release-film	Airtech A4000	4, 11
Released peel-ply	Airtech Econolease	5
Vacuum-bag	Airtech Wrightlon® 6400	6
Breather	Airtech Airweave® N4	7
Edge-breather cloth	West Marine fibreglass tape (2”-wide)	8
Release-agent	Zyvax® EnviroShield™	9
Sealant-tape	Airtech GS-213-3 synthetic rubber	10

The layup over concave features represents the more challenging case on account of consumable bridging. Certain steps can be taken to alleviate corner defects [138]. The top release-film is cut and overlapped at the corner to avoid bridging while still covering the entire laminate surface. In turn, the peel-ply breather layer is interrupted over the corner surface. The vacuum-bag cannot however be overlapped or interrupted. A pleat is therefore created over the corner region to release any tension. Lastly, release-film strips are placed under the laminate edges for both the convex and concave configurations to reduce abrasion of the release-agent during debulk steps and the subsequent likelihood of a corner beam locally adhering to the tool surface.

The laminate temperature, T, is monitored throughout the RT-hold, and the cure and post-cure cycles via a K-type thermocouple wire sensor fixed with pressure-sensitive tape to the outside of the vacuum-bag over the corner region. In turn, the ambient atmospheric and vacuum-bag air pressures, P_0 and P_b, are only monitored throughout the RT-hold and cure cycle given that the post-cure is performed free-standing. Pressures are measured via Wika A10 pressure transmitters. The sensor signals are picked up via an experimental setup that is comprised of a National Instruments' C-Series DAQ system (modules 9213 and 9219 mounted on a 9219 chassis) and an external DC power supply. This setup is controlled with the LabVIEW SignalExpress software. The measurements are performed in order to first ascertain the strict adherence to the selected process. The pressure data is of subsequent importance in establishing the applied consolidation pressure, P_a, during the RT-hold and cure cycle,

$$P_a = P_0 - P_b \qquad (2\text{-}5)$$

Consolidation pressure is a critical process variable that is of later interest with regard to the experimental results presented in Chapter 4. It is represented as the *consolidation pressure level* (CPL) acting on the laminate as a percentage of atmospheric pressure at sea-level (P_{atm}),

$$CPL = \left(1 + \frac{P_a - P_{atm}}{P_{atm}}\right) \cdot 100 \qquad (2\text{-}6)$$

where $P_{atm} = 1 \text{ atm} = 101.325 \text{ kPa}$

2.3.3 Specimen machining, conditioning and naming

The machining and preparation of corner beams and specimens follow general best practices for the preparation of test coupons from flat composite panels [65, 66] as well as the specimen preparation guidelines laid out in the ASTM D6415 test standard for CBS specimens [90]. The standard stresses the vital importance of edge-surface quality when mechanically loading corner specimens to observe failure [90, 94]. Fletcher demonstrated that the mechanical properties determined by this standard are innately conservative due to the presence of free edges [92]. Great care is therefore taken in preparing specimen edge-surfaces that are free of machining-induced damage.

Corner beam trimming and specimen cutting are both performed using a manually operated, industrial tile saw equipped with water cooling (Rubi DX-350 model; 2,800 rpm), and a custom diamond cut-off blade manufactured by Ukam Industrial Superhard Tools, USA. The blade features a very rigid, stainless-steel body and a proprietary, nickel-bonded alloy rim (1.8 mm wide) that holds a single diamond layer with a mesh size of 180/200 (meshes per inch) and a C100 concentration (4.4 ct/cm^3). The beam is first trimmed and squared to create the requisite flange length before specimens are individually sliced from the beam. The specimen width is initially set at 21 ± 1 mm to provide a 1 mm margin for the final machining step, namely grinding.

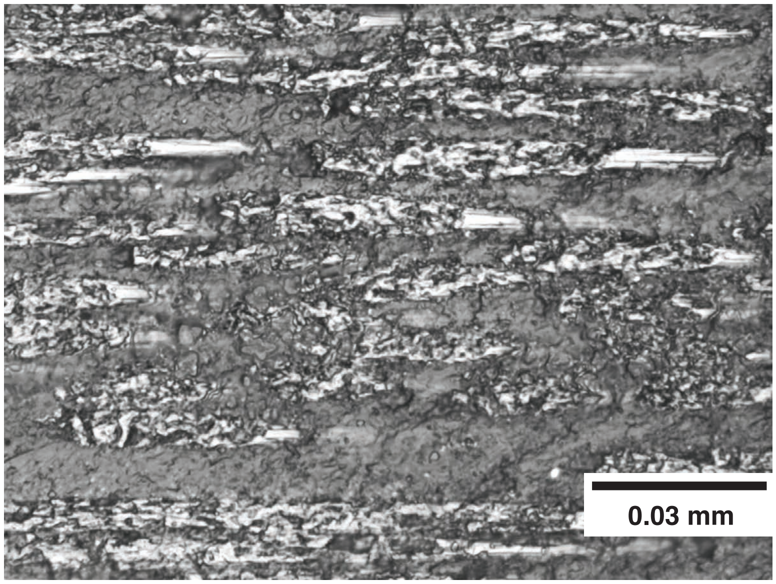

Fig. 2-7. Bright-field illumination (50x objective) of a specimen edge-surface after fine-grinding.

Manual plane-grinding and fine-grinding are performed on a lab-scale polisher (Metlab Forcimat) in order to obtain surfaces that are free of notches caused by the blade wobble during specimen slicing. Plane-grinding typically removes upwards of 0.25 mm of material from each specimen edge-surface to erase any evidence of notches and to even the surface. An interrupted diamond grinding disk with a grit of 220-P (Struers MD-Piano) is used in concert with water cooling and a platen speed of 400 rpm. The final machining step is fine-grinding, which utilizes a similar grinding disk with a finer diamond grit of 1,200-P, water cooling, and the same platen speed in the reverse direction. This step removes a minimal amount of material (< 0.1 mm per edge-surface) in order to erase the roughness left-over from plane-grinding. Fig. 2-7 provides an example of the typical surface quality after fine-grinding: some surface-fibre damage is present and is to be expected; there is however no evidence of further machining-induced damage such as matrix micro-cracking, interply delamination and fibre pullout. A mean specimen width of 20.22 mm with a standard deviation and coefficient of variation of 0.438 mm and 2.13% is achieved for the combined 175 corner specimens prepared for the experimental work presented in Chapters 3, 4 and 5. The measurements are made with a digital Vernier caliper with a precision of ± 10 μm.

Every specimen is thoroughly washed prior to conditioning in order to remove surface contaminants that remain after the machining operations. This step is first performed with mild soapy water and a gentle cleaning action using a soft bristle brush. It is then repeated with diluted isopropanol (approximately 1:5 by volume) to remove the soap while leaving negligible residue. Lastly, surface moisture is dried off with compressed air before proceeding to conditioning.

Hygrothermal environmental effects are not a subject of investigation in this thesis and are therefore undesirable. In order to achieve a standard and reproducible conditioning state across samples, specimens are typically stored over long durations in a controlled environment to achieve equilibrium in terms of relative humidity (RH). The chosen environment in comparative studies is often the standard laboratory atmosphere in which future tests are to be performed (23 ± 2 °C with a RH of 50 ± 10% [174]). In the present case, the RTD condition is instead selected as the more appropriate condition on account of a lack of control over the laboratory atmosphere, in which specimen are stored and tested. The conditioning is performed in accordance with Procedure D of the ASTM D5229 test standard [174]: specimens are kept for 48h inside a vacuum-bag placed in a regular mechanical convection oven set to 70 ± 3 °C (Blue M Oven equipped with an Omega PID controller) and subsequently air cooled and stored in a desiccator until final use (Multisorb Technologies MiniPax® Sorbent silica gel packets).

A clear advantage of RTD conditioning is the significant reduction in the duration that is required to reach equilibrium compared to laboratory conditioning. In addition, it is preferable to remain consistent with the material properties provided in Table 2-4, which were obtained for the RTD condition. It should be noted that water absorption occurs over a much longer time-scale than that of a single mechanical test lasting than 15 min. Any change that occurs after specimens are removed from desiccation storage and prior to testing are therefore deemed to be negligible.

Lastly, every specimen and sample are uniquely labelled for later tracking. A fine-tip, permanent silver ink marker works best on the specimen's shiny black surface. The naming scheme combines the essential experimental details into a single alphanumeric string segmented by hyphens. This same scheme is later used for computer filenames such as those of scanned images. The segments are detailed in Table 2-7. A full sample name could for instance read: "CBS-T24UD-M-B-1-1,2,3,4,5". It should be noted that only sample-level results are presented and discussed in

Chapters 4 and 5. A simplified scheme is therefore utilized therein for clarity, which only includes segments 2-5) with the ply count in segment 2) being replaced by a hyphen and segment 5) being only included in the case of multiple samples for a given test condition, i.e. repeated baselines.

Table 2-7. Sample naming scheme segments.

	Segment	Format	Example	Simplified scheme
1.	Experiment	Letter code	"CBS"	×
2.a.	Material	"T", "PW" or "8HS" (§ 2.2.1)	"T24UD"	✓
2.b.	No. of plies	24/16/8 for tape/PW/8HS (§ 2.3.1)		×
2.c.	Stacking sequence	"UD", "XP" or "QI" (§ 2.2.2)		✓
3.	Tool-shape	"M" or "F" for "convex"/"concave"	n/a	✓
4.	Processing condition	Sample conditioning code (§ 4.3)	"B" for "baseline"	✓
5.	Sample ref.	Single integer	1	Only if applicable
6.	Specimen(s) ref.	Integer(s) separated by commas	1,2,3,4,5	×
7.	Image resolution (Only if applicable)	Scan: ####dpi (§ 2.4.2); Micrograph: ##x (§ 2.5.2)	"3000dpi" "10x"	×

2.4 Corner thickness profile acquisition

2.4.1 Motivation for improved thickness measurement method

Measurement of the corner specimen thickness is required for the calculation of experimentally-determined mechanical properties, namely the CBS and ILTS. In turn, improved data will aid the development of more accurate local thickness deviation models. To this end, the measurement method must meet a satisfactory degree of precision and accuracy. Corner specimens are especially prone to thickness deviations in the corner region, hence special care must be given to the measurement method. Thickness measurements are also key in assessing the laminate quality where thickness deviation and T-T phenomena are concerned.

The thickness of corner specimens has traditionally been measured by hand, i.e. *direct* means, with the aid of precision measurement devices such as a Vernier caliper [81] or a micrometer [88]. The *Mil-Handbook-17* provides comprehensive guidelines for such direct measurements [140]. However, image analysis—an *indirect* method—is fast becoming the method of choice to measure thickness over complex-shape laminates [69, 121, 137, 138]. The approach consists of first scanning specimen profiles and then making manual measurements on the scanned images with the aid of computer software such as ImageJ, an open-source Java code (imagej.nih.gov). Measurement tools that are native to the software interface and that are cursor-operated are used in a manner that is analogous to the physical use of a caliper or micrometer. For its part, the ASTM D6415 standard recommends the use of direct physical methods to measure thickness [90]: a knife-edge caliper is preferred for the curved surfaces of a corner region; in turn, a micrometer is preferred for flat flange surfaces: ball (4-6 mm dia.) and flat-anvil interfaces are to be used for the rougher bag-side surface and the smoother tool-side surface, resp. The accuracy of both instruments should be suitable for a reading within 1% of the measured thickness, to which end a precision of ± 25 μm is typically suitable. It should be noted that the standard limits the acceptable amount of thickness deviation at the corner to 5% of the nominal flange thickness in order for this mean value to be used in subsequent data reduction.

Even though the aforementioned manual measurement methods—physical and digital (cursor-operated)—can be very practical, they share certain key drawbacks. For one, the geometry of the probing interface can interact with the specimen's surface roughness and result in a systematic error or bias in the measured, nominal specimen thickness. For instance, a micrometer with a large ball-interface diameter compared to the distance between the peaks and valleys of the surface roughness will tend to overestimate the specimen's mean thickness irrespective of the number of measurements made [140]. Whether this error is of practical significance can be argued on a case by case basis. Secondly and more importantly, setting and reporting an exact location for a given thickness measurement (the position on the respective specimen surface or edge) is vital when investigating thickness deviation. However, making repeatable, location-dependent measurements is difficult and inaccurate in the case of traditional hand measurement methods and—to a lesser degree—cursor-operated, digital methods. Manual methods generally rely on visual-determination of the measurement location. Lastly, such methods are most practical when a low measurement count per specimen is required. In contrast, a significantly higher measurement count is required to adequately capture thickness deviation over the entirety of a complex-shape specimen.

Given the aforementioned drawbacks of manual thickness measurement methods and the large quantity of specimens to be tested (175), a semi-automated method was developed to analyze scanned specimen profiles via a MathWorks Matlab (R2015b) m-script. Fig. 2-8.A) illustrates the core process of the m-script whereby the bag-side and tool-side edges of a scanned specimen profile are fitted with functions, and the laminate thickness normal to the tool-side edge is then determined as a function of the location along that edge for an arbitrary amount of points. The method allows for all the measurements required by the ASTM D6415 standard to be made with improved accuracy and precision, and it provides a complete 2D representation of the thickness deviation for the entire specimen as a function of location, i.e. the specimen's *thickness profile*.

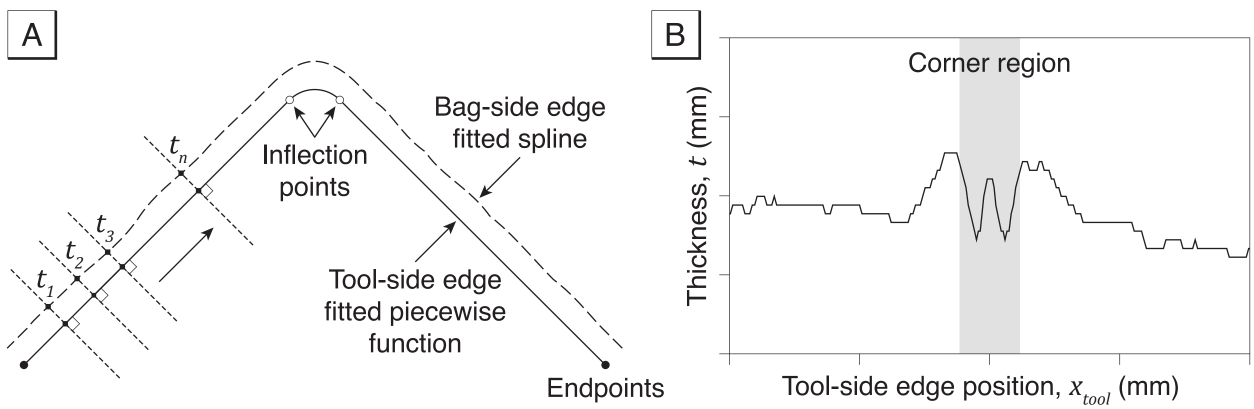

Fig. 2-8. Illustration of the proposed corner thickness profiling method at work: A) determination of the local specimen thickness as a function of location on the tool-side edge; B) typical thickness profile result.

It should be noted the method further allows for the determination of the tool-side radius and the angle between the flanges. These two additional measurements are used in the data reduction to determine the CBS and ILTS, yet procedures for making them on the specimens are absent from the standard [90]. As an example of the utility of the proposed method, Fig. 2-8.B) illustrates the thickness deviation of a unidirectional, semipreg-tape specimen with local thickening at the shoulders—or inflection points—of the corner region. This effect is colloquially referred to as the "Mickey Mouse [ears]" effect on shop floors and may otherwise be thought of as *convex corner shoulder-thickening*. It would be much more difficult to detect, measure and assess without resorting to a similar method that outputs the entire thickness profile of a given corner specimen. Krumenacker *et al.* have utilized this method in two conference papers that study the effect of processing parameters on VBO corners [99, 127].

2.4.2 Specimen scanning

The efficacy of the proposed corner thickness profile acquisition (simply *profiling*) method is contingent on three sources of edge detection error that all affect specimen edge detection: 1) cleanliness of specimen edge-surfaces and the scanning environment, 2) specimen edge quality, and to a lesser extent 3) the specimen layup. Fig. 2-9 presents the typical scanning artifacts that are associated with each error source. Edge detection is the most critical step in the method given that edge-fitting with functions and every subsequent measurement depend on its accuracy.

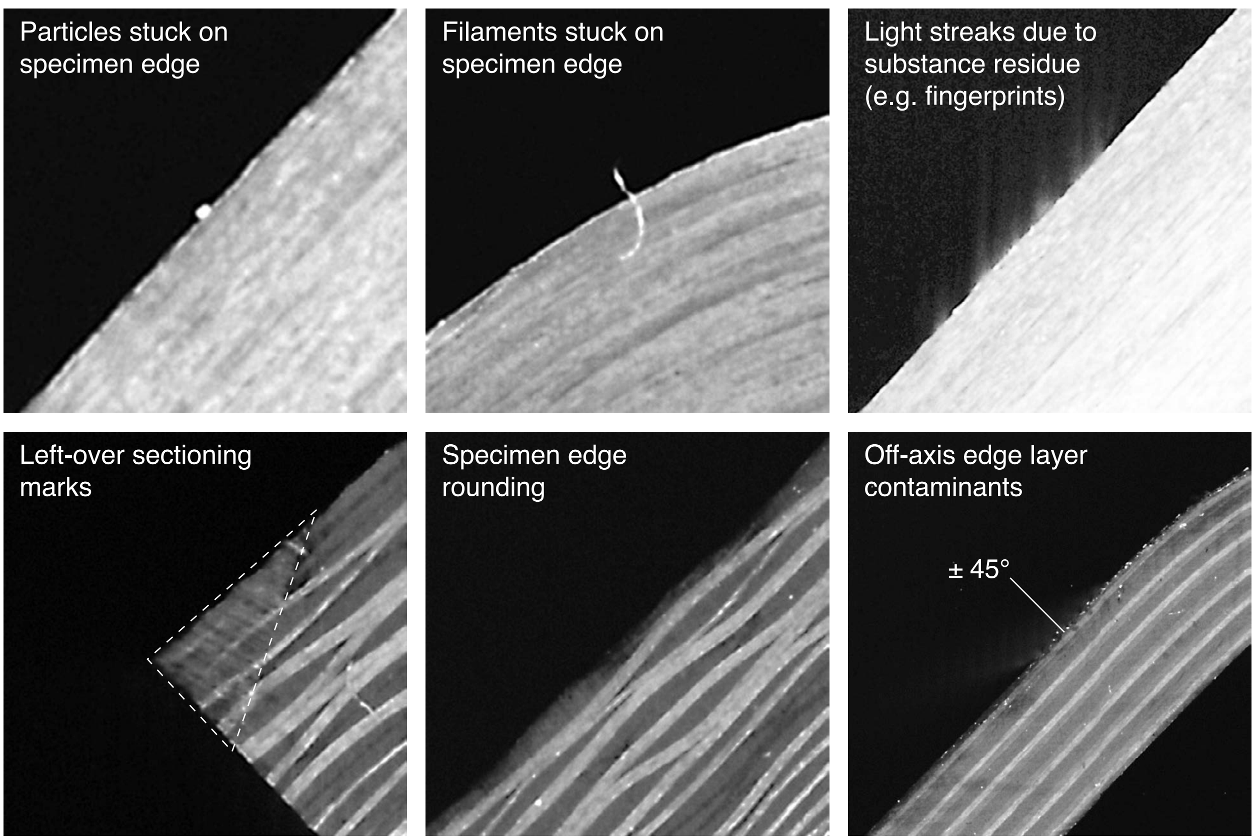

Fig. 2-9. Representative scanning artifacts of corner specimens.

The most common artifacts associated with cleanliness of the work space are the presence of dust particles and filaments that are stuck on specimen edges. These contaminants result in inaccurate local edge detection. Whereas some contaminants are to be expected and negligibly effect the overall edge detection and subsequent measurements, care must be taken to limit their presence. In contrast, the presence of substance residue such as smudge marks left by fingerprints or dirty specimen surfaces is of much greater concern as it can affect large edge portions and result in significant detection error. Issues of cleanliness are remedied by first wiping clean the scanning surface with an appropriately mild solvent applied to a lint free cloth prior to scanning, e.g. isopropanol applied to a lint-free cheesecloth. A compressed air canister is then used between scans to remove new contaminants. Specimens have previously been manually ground, washed and conditioned, and stored in clean sample plastic bags along with desiccant packets. They must be handled with nitrile gloves in order to ensure that no fingerprints and skin oils contaminate the interply s or the scanning surface.

A second source of edge detection error is poor specimen edge quality, which is a fully avoidable source of scanning artifacts that can be corrected by repeating the necessary specimen machining and conditioning steps as described in § 2.2.3. The two main artifacts in this category are the presence of leftover sectioning marks and rounded specimen edges that are caused by insufficient surface grinding and poor technique, resp. (Fig. 2-9). They affect the local edge contrast and result in inaccurate edge detection over large edge portions. The third and final error source, stacking sequence, concerns only specimens that contain off-axis surface plies such as a standard quasi-isotropic sequence: $[45°/0°/-45°/90°]_{ns}$. Off-axis surface fibres are much more prone to damage and pullout during machining operations, which renders them much more likely to trap edge contaminants. Little can be done to remedy this problem beyond taking additional precautions during machining, conditioning and scanning to keep edge-surfaces clean.

In cases with minimal edge artifacts, sample scans are treated directly by the first part of the m-script, which consists of removing background objects and transforming the scan into a binary image. In cases with excessive edge artifacts, it is strongly recommended that the source of the artifact be addressed and that affected specimens be rescanned. It is very difficult to write a script that will account for most types of artifact and instances without delving into advance machine learning methods. In some cases, it is possible to salvage certain scans by manually removing artifacts via advanced techniques in a program such as Adobe Photoshop; however, such an approach is time consuming, imperfect, and requires additional operator skills.

Beyond what has thus far been described, specimen scanning is straightforward and does not require specialty equipment. The specimens for a given corner beam sample are all scanned at once with a consumer-grade scanner (Canon LiDE 220) at a resolution of 3,000 dpi (~118 dot/mm). All image correction setting options are turned off, and scanned images are saved as 8-bit, grayscale TIFF files (256 colors). It should be noted that specimens are scanned on both side (edge-surfaces), resulting in two separate scanned images per sample, an a-side and a b-side scan. This information is stored in the scanned image filename according to the sample naming scheme (§ 2.2.3). All dimensions outputted by the m-script are averages of identical measurements made on a- and b-side scans of a given sample; the accompanying descriptive statistics are pooled.

2.4.3 Method implementation and validation

Execution of the corner thickness profiling method in Matlab consists of transferring correctly named sample scans into the same directory as that of the m-script, updating the general inputs specific to the samples being processed (e.g. initial guess for the tool-side corner radius and the nominal laminate thickness), and running the m-script. Fig. 2-10 illustrates the method's implementation and the structure of the m-script.

The script consists of four parts and two loops, the specimen-level loop (part 2) being nested inside of the sample-level loop (parts 1-3). Sample scans are processed sequentially in the order that they are accessed in the directory. In part 1, the current scanned image is treated, and the specimens contained in it are subsequently detected and separated into individual binary images. In part 2, the specimen subloop, each detected specimen is analyzed sequentially from first to last. The analysis consists of detecting and fitting tool- and bag-side specimen edges with functions, and subsequently making all measurements and acquiring the specimen's thickness profile based on these functions. Part 3 computes the descriptive statistics of the current sample scan for each type of measurement made in part 2. It should be noted once more that all the specimens for a given sample are scanned together on both side edges resulting in two scans per sample. Part 4 combines the respective a- and b-side measurements, the respective descriptive statistics, which are pooled, and the thickness profiles for each sample. The data is finally outputted for all samples processed during the current script run to a master Microsoft Excel workbook.

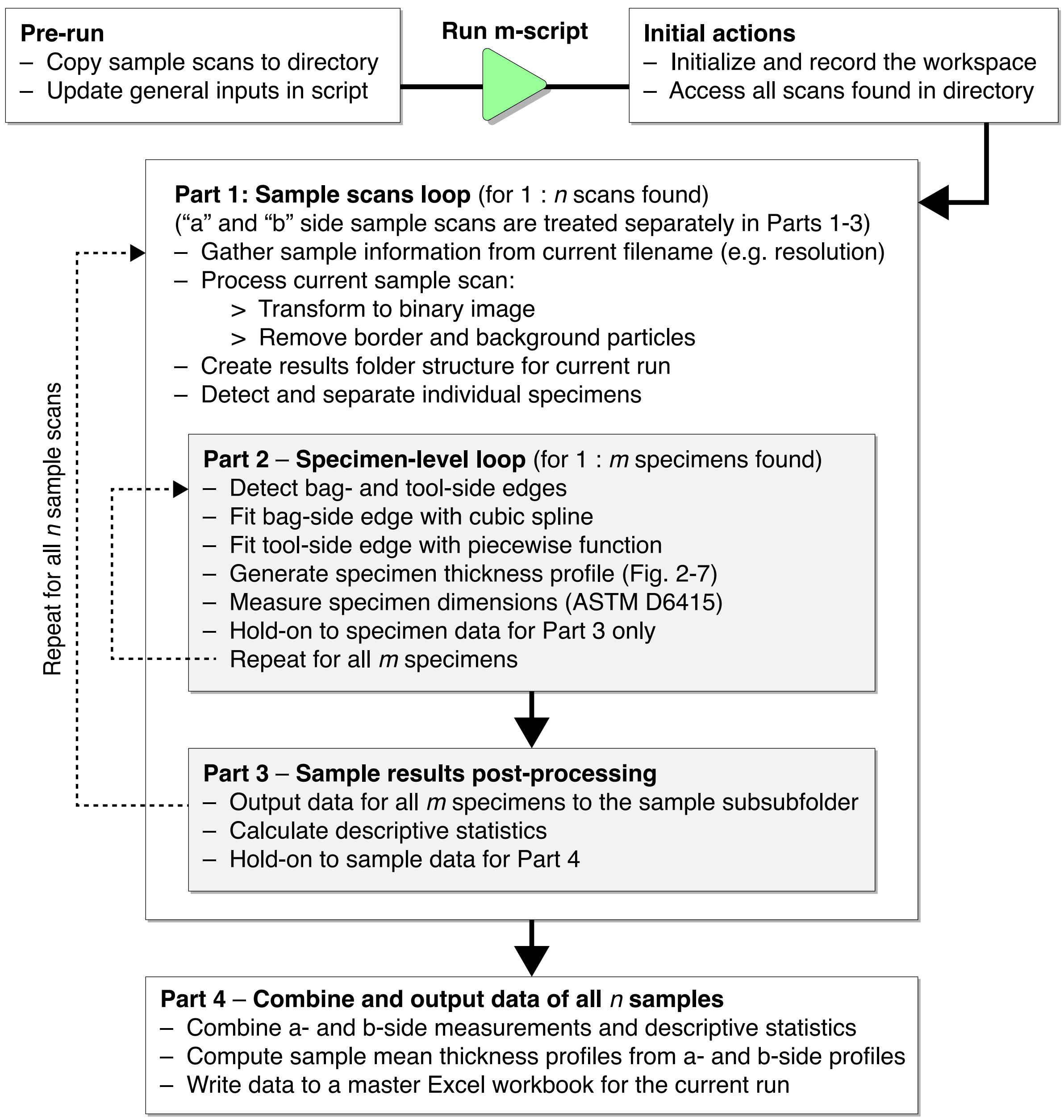

Fig. 2-10. Flowchart of the corner thickness profiling method.

The proposed method is validated experimentally by comparing its results to those obtained by direct and digital measurement methods. Direct measurements are made on sample scans in accordance with the ASTM D6415 test standard, and digital measurements are made via cursor-operated tools in ImageJ. The experimental data used in the comparison comes from two sets of 5 specimens from two convex corner beams, one tape (32 plies) and one PW (16 plies), both having unidirectional layups (all-0°-plies oriented in the hoop-direction). Four types of measurements are taken on each specimen: the flange thickness, the corner thickness, the inner corner radius, and the corner angle. Table 2-8 summarizes the experimental results.

Table 2-8. Comparison of dimensional measurement methods for corner specimens.

Measurement (mm; °)	Physical method (ASTM D6415)	ImageJ digital approach^	Thickness profile method in Matlab^
Tape			
Flange thickness	*4.12 ± 0.0284 (0.689); 30	4.11 ± 0.0438 (1.07); 30	4.10 ± 0.0238 (0.560); 16,342
Corner thickness	**4.41 ± 0.127 (2.89); 15	4.32 ± 0.171 (3.97); 15	4.24 ± 0.0469 (1.11); 3,286
Inner radius	n/a	5.84 ± 0.0584 (1.00); 5	5.86 ± 0.0661 (1.13); 5
Corner angle	n/a	89.3 ± 0.0259 (0.0290); 5	89.3 ± 0.0366 (0.0410); 5
PW			
Flange thickness	*4.19 ± 0.0198 (0.473); 30	4.14 ± 0.0230 (0.555); 30	4.11 ± 0.0127 (0.309); 16,315
Corner thickness	**4.39 ± 0.0356 (0.810); 15	4.33 ± 0.0408 (0.943); 15	4.25 ± 0.0254 (0.596); 3,262
Inner radius	n/a	5.93 ± 0.0709 (1.19); 5	5.97 ± 0.0592 (0.989); 5
Corner angle	n/a	89.0 ± 0.0207 0.0233); 5	89.0 ± 0.0423 (0.0475); 5

Number format: mean ± standard deviation (variation coefficient in %); number of measurements
*Micrometer measurement with ball-anvil interfaces (±1 µm)
**Vernier caliper with knife-edge interfaces (±10 µm)
^ Precision = ±8.5 µm (pixel size)

Digital calipers and micrometers are used to make the direct measurements with precisions of ±10 µm and ±1 µm, resp. Six thickness measurements are made on flanges and three on corner regions. The specimen sets are then scanned, one image per specimen set on one side only, in order to make digital measurements in ImageJ and automated measurements via the m-script. The guidelines presented in the previous section are used to obtain scans that are practically free of artifacts. The precision of both methods is estimated to be the image pixel size, i.e. 8.5 µm for a resolution of 3,000 dpi. The same number of digital measurements are taken via ImageJ on the flanges and corner regions as are taken physically. In contrast, the m-script automatically takes more than 3,000 measurements on flanges and 600 on corner regions (the number of data points is a function of the specimen size and image resolution). In turn, the corner radius and angle are only measured once per specimen. That being the case, nine points are used to fit a circle to the radius in ImageJ compared to over 550 points in Matlab. Finally, the descriptive statistics for each specimen set and measurement method are calculated, i.e. the mean, the standard deviation and the coefficient of variation. It should be noted that the data is deemed to be unstructured within each set on the basis that a given specimen set comes from the same corner beam. Measurement populations are therefore pooled for each set. In addition, it can be shown that populations are normally distributed, which is why the standard deviation is reported. Lastly, the corner radius and angle are not measured directly on specimens as the ASTM D6415 test standard does not provide guidelines for these dimensions.

First with regards to the two thickness measurements, the proposed method yields the lowest flange and corner mean values given the lack of probing interface bias, and the lowest coefficient of variation given the much larger datasets. In addition, the proposed method samples nearly the entire corner region to calculate the corner mean value. A lower mean value than is calculated by the other methods is therefore expected in the case of corner thickening. Digital measurements made in ImageJ are slightly less accurate and precise on account of the smaller number of measurements. The probing interface bias is removed; however, a second source of bias exists, which is the difficulty in obtaining thickness measurements that are normal to the tool-side—or reference—edge. The normal distance between the two edges should be the smallest distance, and therefore the means determined via ImageJ are slightly larger than those determined via the proposed method. With regards then to corner inner radius and angle measurements, there is little difference between the ImageJ and Matlab results, despite the much larger vector of points used to fit a circle by the m-script. It should be noted once more that beyond preparing and scanning specimens, the proposed method also benefits from being fully automated compared to the ImageJ approach. The proposed method for acquiring the thickness profile of corner specimens as implemented in an m-script is therefore deemed the most precise and accurate of the three investigated methods, as well as the most practical for the purposes of the experimental work.

2.5 Optical microscopy

2.5.1 Overview

Laminate quality extends beyond quantifying the thickness deviation in the corner region. It also includes fibre and void content measurements and the corresponding T-T distributions, as well as characteristics of the mesostructure such as interlaminar spacing between plies and verification of the stacking sequence. These measurements and observations are made via image analysis of polished specimen cross-sections that are prepared following a similar approach to that traditionally applied to metallographic sections.

Guidelines for specimen section preparation, casting, polishing and viewing via optical microscopy are derived from the consultation of several works that are specific to the selected materials. In *Failure analysis and fractography of polymer composites*, Greenhalgh presents overviews of optical microscopy techniques, section preparation and dissection, and quality assessment [179]. In *Optical microscopy of fiber reinforced composites*, Hayes and Gammon offer the most extensive guidelines found for the preparation and mounting of specimen sections into resin castings, and the requisite surface grinding and polishing steps to create adequate surface quality for subsequent optical microscopy and image analysis [180]. And finally, the image analysis approach is largely taken from §§ 6.6.6.5-7.3 of the *Mil-Handbook-17* [140]. These three reference-works should be perused to gain a more detailed understanding of the methods described in the following two sections (§§ 2.5.2-2.5.3).

It should be noted that optical microscopy is employed in two other aspects of the experimental work: the fractographic analysis of failed specimen cross-sections after curved beam strength testing via four-point bending; and the measurement of the in- and out-of-plane fibre misalignment—or waviness—in UD-tape corner regions. Deviations from the methods described in this chapter are fully detailed in the pertinent sections of Chapters 4 and 5.

2.5.2 Sample preparation, mounting and imaging

Three types of specimen sections are prepared for the laminate quality assessment of each corner beam sample and are regrouped and mounted in three different resin casting mounts. The sections are dissected from 5 randomly selected corner specimens per corner beam sample, and regrouped and mounted into 3 resin castings, one for each section type. Castings are limited to a surface area of 25 × 50 mm and a depth of 20 mm. Fig. 2-11 illustrates A) the location of the sections in a corner specimen and B) the mounting arrangement of the three-sample castings. The mesostructure of the flange, shoulder and corner regions is captured in a frontal plane section that consists of the entire corner region and ~17 mm of flange (Fig. 2-11 #1). The frontal plane is defined as the plane formed by the 1,θ-axis and the 3,r-axis. Only two such sections are included per casting for a given corner beam sample as they are only used qualitatively rather than quantitatively. In turn, the fibre and void contents of the corner and flanges are captured by 5 sagittal-plane sections taken in the middle of the corner region and one of the flanges, resp. (Fig. 2-11 No. 2 and 3, resp.). The sagittal plane is defined as the plane formed by the 2-axis and the 3,r-axis. These sections are ~15 mm wide and selected in order to increase the surface area under review in the corner, and to be normal to the hoop-direction, which is the principal fibre orientation, such as to intersect a majority of fibres. It should be noted that two additional laminate sections from unused specimen flanges are placed on both sides of the sections in each casting. This technique helps to achieve a flat and uniform polished surface [180].

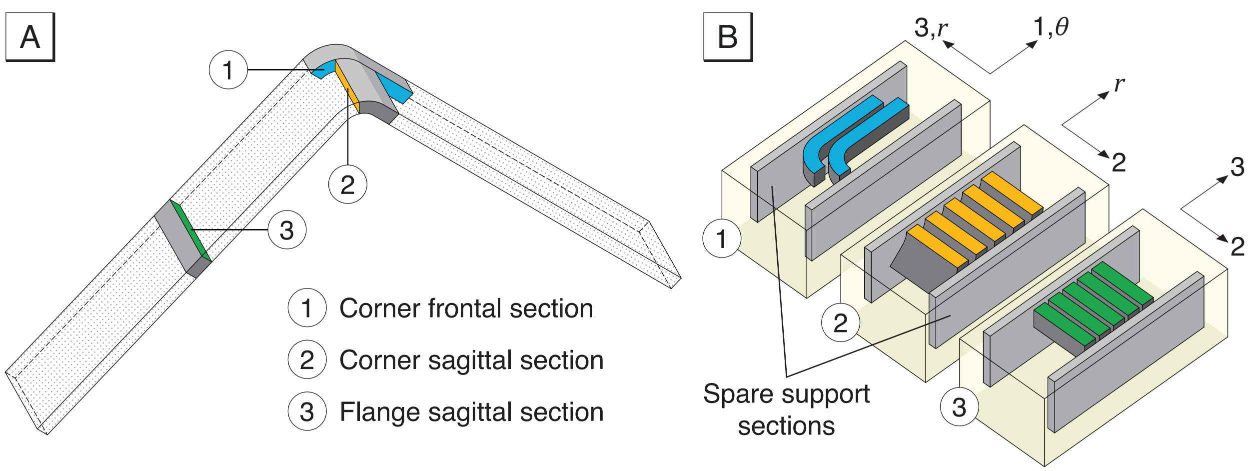

Fig. 2-11. Schematic of the three types of corner specimen cross-section for optical microscopy. A) location of the sections in the corner specimen; B) three cast resin mounting arrangements, one per section type, for a given corner beam sample.

Sections are dissected from corner specimens using an automated labscale cut-off saw (Struers Accutom-5) and a diamond wafer-blade designed for general polymer composite use (Struers 430CA, 0.4 mm thick, 152 mm dia.). The cutting parameters are 2,700 rpm at a feed rate of 0.020 mm/s. Specimens are then carefully cleaned and labeled before being mounted in a clear, two-part epoxy resin (Alumilite Amazing Clear Cast Epoxy; 1:1 mixing ratio by volume; 80 Shore D hardness) and left to cure at RT for 72 h (demoulded after 18 h). Soft or sticky castings are cured a further 1-2 h at 50-60 °C to ensure full cure.

Casting surface preparation is performed with the aid of an automated, labscale polisher equipped with an automated head (MetLab Forcimat). The process consists of five steps: plane- and fine-grinding, and rough-, intermediate- and fine-polishing. The process parameters are as follows: platen and head speeds of > 300 and 150 rpm and maximum cycle duration of 5 min for all steps, and piston force per specimen of > 30 N and > 50 N for grinding and polishing steps, resp. The platen and head run in counter directions and are reversed between steps. Great care must be taken to clean the castings and the polisher head between steps to reduce the chance of presence of contaminants from the previous step that can contaminate the consumables discs and thus scratch the casting surface. To this end, the castings are cleaned in an ultrasonic bath (Branson 2510) and the polisher head with lint-free cheese cloth, diluted isopropanol and compressed air.

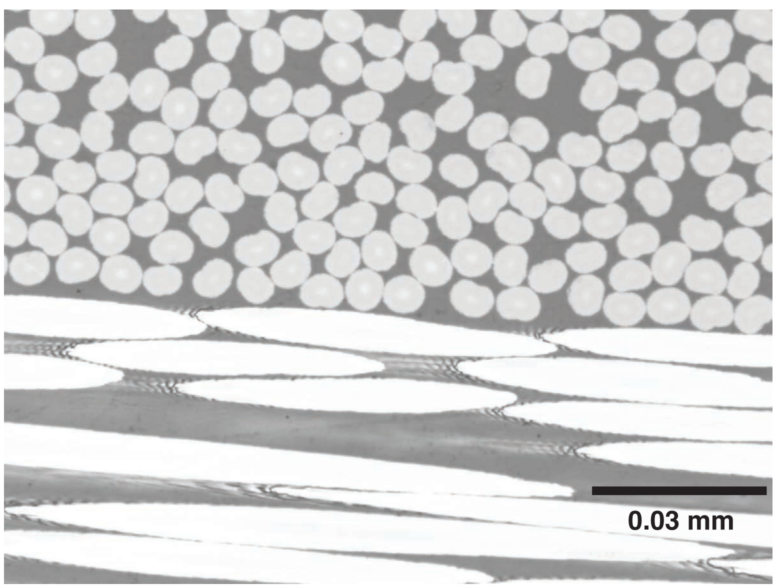

Fig. 2-12. Bright-field illumination (50x objective) of a polished tape laminate cross-section with the presence of interferometer bands at the ends of the angled fibres (~45°).

Plane-grinding exposes the cast section and creates a flat surface to work from using a 220-P grit interrupted diamond disc (Struers MD-Piano) with tap water. All subsequent steps aim to remove the surface scratches left by the preceding step. Fine grinding uses a finer diamond disc with a grit of 1,200-P and tap water. The rough, intermediate and fine polishing steps use de-agglomerated alumina suspensions that are diluted in distilled water with the following particle size and mixing ratios: 12.5, 5 and 0.3 µm, and 10 g/L, 10 g/L and 5 g/L, resp. Silk cloth discs with tightly woven plain-weave (Struers MD-Dur) are utilized on the platen to trap the suspended particles, reduce the erosion caused by the particles rolling and resist polishing-induced shear forces. The drip rate of suspension onto the spinning platen is roughly 1 drop per second as a rule of thumb. It should be noted that the 5-min cycle duration limit can be disregarded for the final polishing step as more time is often required. Fig. 2-12 presents a typical bright-field illumination view of a polished cross-section with normal and angled carbon fibres (0 and 45°). The presence of interferometer bands at the ends of angled fibres indicates a uniform polishing plane [180].

Polished sections are viewed under bright-field illumination with a 10x objective on a standard compound microscope (Nikon Eclipse L150) equipped with an automated stage. The microscopy software allows for automated mosaic stitching of entire polished cross-sections with auto-focusing and a 20% overlap. This feature enables the single capture of several thousand fibres at a sufficiently high magnification. Individual grayscale micrographs have a resolution of 1,920 × 1,200 px with an equivalent resolution of 0.581 µm/px. Lastly, the exposure, gain and gamma correction values are arbitrarily selected based on operator experience and are fixed for all micrographs taken as part of the experimental work. These values are evidently unique to the microscope setup used and thus not reported here.

2.5.3 Image treatment and analysis

The primary aim of the optical microscopy work is to assess laminate quality in terms of fibre and void content, which are representative markers of quality widely-used in academic circles and industry [63, 140, 172, 179, 180]. Once resin-mounted samples are prepared and stitched micrographs—or section mosaics—are captured, the image analysis is automated via a custom m-script in MathWorks Matlab (R2015b) that is largely derived from the approach detailed in §§ 6.6.6.5-6 of the *Mil-Handbook-17* [140]—no industry standard test method exists beyond this general procedure. The approach determines the fibre and void content as the respective mean percent areas for a number of sufficiently large laminate cross-sections per corner beam sample (>100 fibres per cross-section). The T-T fibre and void distributions can also be obtained, which is a unique feature of 2D and 3D image analysis.

Chemical matrix digestion and ignition loss are two alternative methods that are used in both academic circles and industry to determine the constituent volume fractions of polymer matrix composites [140, 179]. These methods are standardized in the ASTM D3171 and D2584 test standards, resp. Every method has benefits and drawbacks: matrix digestion, for one, is regarded by some as more accurate than conventional, thresholding-based image analysis methods [179]. Matrix digestion is however rejected here on account that carbon fibres are susceptible to oxidative degradation, and ignition loss is rejected on account that special temperature controls are required for carbon fibres [140]. Moreover, access to speciality equipment and concern over safety regulations render both methods impractical for general academic use. In contrast, indirect methods such as image analysis do not create harmful chemical waste.

Image analysis is not without its drawbacks. First and foremost, a large sample population of at least 20 specimen sections, each containing at least 100 fibres, is required to infer sound statistical estimates of overall populations [140]. Such a large number of specimens per corner beam is unfeasible on account of the relatively small beam size, large number of beams tested (> 30), required preparation time per sample, limited material availability and microscopy consumable costs. That being the case, the 5 section mosaics (stitched micrographs) used to determine mean sample estimates each contain several thousand fibres; this approach emulates the *large-area high-resolution* approach proposed by Davidson *et al.* in the late-Nineties [181]. The additional fact that these sections come from randomly selected specimens adds further credence to the representative nature of the overall cross-sectional area being sampled.

The determination of void and fibre aerial fractions for grayscale micrographs is based on widely-used image segmentation techniques. Fig. 2-13 presents an example of a stitched micrograph input and segmented image output processed by the m-script. The corresponding *histogram*, which is a plot of the distribution of image pixels as a function of tonal intensity, consists of three major peaks that correspond with the tonal values of voids (dark tones), matrix (mid-tones) and fibres (light tones)—carbon fibres appear to be lightest under bright-field illumination, i.e. direct lighting. The *threshold* (delineation point) between two peaks corresponds to the color intensity that separates neighboring constituents. Thresholds are calculated using a native Matlab function that employs Otsu's thresholding algorithm [182] and can compute up to 20 thresholds per histogram, i.e. *multithresh.m*. Use of this algorithm removes the operator error that is otherwise involved with visual inspection of the histogram—the more conventional approach [140]. Computed thresholds are used to create binary images that contain either only fibres or only voids, and the respective aerial factions are then simply computed by counting black or white pixels. The output image in Fig. 2-13 is a composite of binary images superimposed over the original micrograph. By extension, constituent distributions through-the-thickness are simply computed by counting black or white pixels for each pixel row of the image. It should first be noted that pixels distances are easily converted to millimeters given the known image resolution, and secondly that Matlab treats grayscale images as simple 2D matrices containing pixel tonal intensity values.

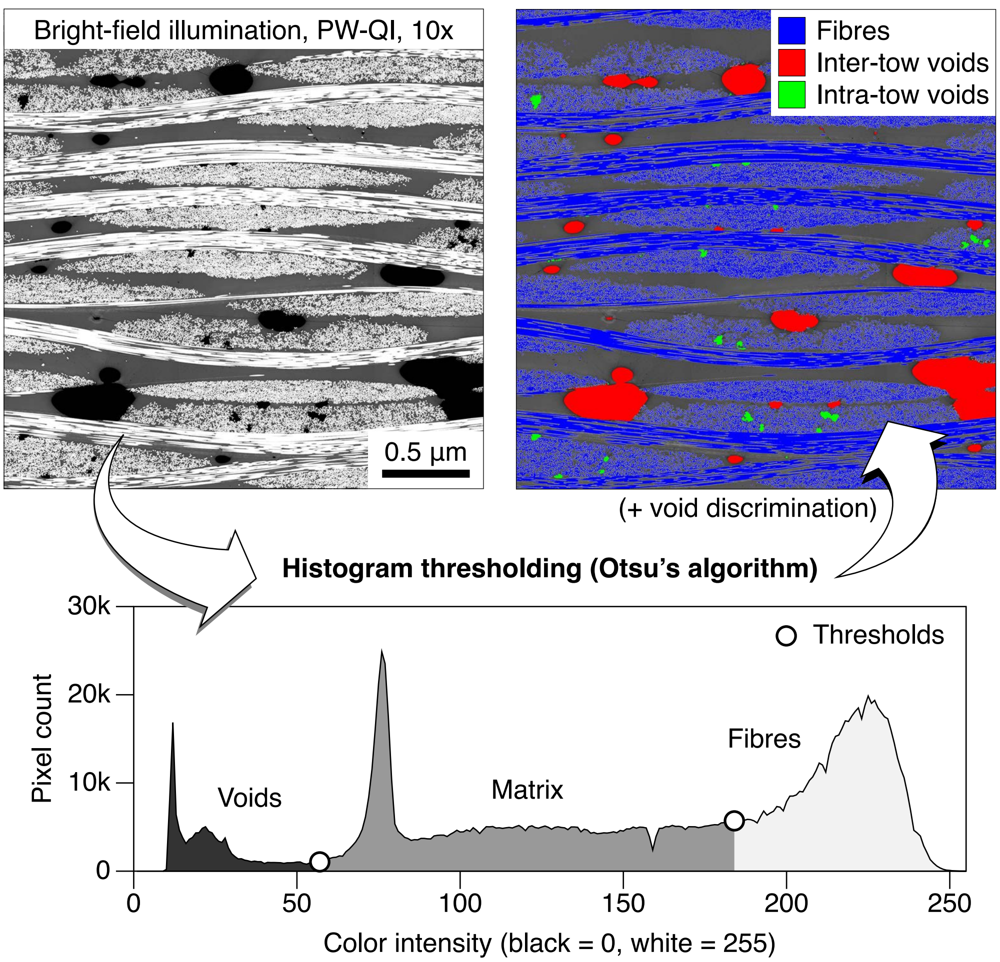

Fig. 2-13. Segmentation of laminate cross-section micrographs via histogram thresholding.

The present image analysis extends beyond the approach covered in the *Mil-Handbook-17* to discriminate between inter- and intra-tow voids, as showcased in Fig. 2-13. These two species of voids are pertinent in cases where clear resin interlayers exist between fibre tows and between plies. In the case of a UD-tape specimen of generally good quality, plies essentially nest and merge to form a single, thick unidirectional layer, and thus no clear distinction can be made between void species. The m-script makes a rudimentary guess as to which voids fall into the inter-tow category. This problem is a very complicated one to solve via conventional image analysis techniques without resorting to advanced machine learning methods. For the present application, the option to manually correct the initial guess is coded into the script: wrongfully selected inter-tow voids may thus be manually switched to intra-two voids and vice versa via a simple click of the cursor. What this solution lacks in elegance and practicality, it makes up for in implementation time.

As in the case of the thickness profile image analysis, important sources of error must be considered when segmenting images via thresholding techniques and making subsequent aerial fraction measurements. Errors are attributed to three sources: 1) poor mounted sample preparation technique, 2) poor micrograph capture and 3) morphology of the selected laminate cross-section. It should be noted that a majority of errors affect the perimeter edge of constituents, e.g. void edge erosion and insufficient resolution for fibre detection. This broad type of error disproportionally affects fibre thresholding on account of the much larger combined perimeter length of all fibres compared to that of all voids in a typical section.

First, poor mounted sample preparation technique results in polishing artifacts such as void edge erosion, broken fibre surfaces and resin scratches, which erroneously increase the aerial fraction of voids to the detriment of that of fibres. The inverse is true in the particular case of voids containing polishing debris, which can be nearly impossible to fully remove. Large voids that are affected by stubborn debris can be manually treated via Adobe Photoshop or similar software. In turn, poor image capture manifests itself in the following forms: blurriness from poor focus; inappropriate gamma and gain correction settings; insufficient magnification—or resolution; non-uniform lighting across the camera frame that engenders a systematic tonal gradient across micrographs; and stitching error. Image capture errors generally stem from the lack of operator experience and inadequate microscope and camera calibration. Third, some errors depend on the morphology of the laminate cross-section, which is unavoidable for some applications and represents one of the most significant drawbacks of micrographic image analysis. The heterogeneous graphite structure of carbon fibres is such that longitudinal fibres (< 30° with the micrograph plane) are much more reflective than fibres normal to the polished surface. Some cases make it impossible not to include longitudinal fibres, i.e. QI layups, and corner regions, which lack the adequate volume to prepare angled cross-sections in the first place. Ultimately, 2D image analysis methods rely on the assumption that the cross-section is representative of the volumetric fibre distribution, which is problematic for woven laminates.

Hayes and Gammon [180] and the *Mil-Handbook-17* [140] offer solutions and discuss alternative methods for the majority of the listed errors. The relative inaccuracy of image segmentation via thresholding has been a concern for several decades [183], and much more elaborate methods have been developed since [184]. Nevertheless, image thresholding via segmentation remains the norm in the aerospace industry [140] and is deemed adequate for the purpose of this work, which is to simply compare samples rather than determine statistically determined design- and certification-level properties.

2.6 Summary

The selected materials and general experimental methods presented in this chapter are used for the bulk of the experimental work presented in Chapters 3, 4 and 5. The selected semipregs are some of the most advanced systems currently used in VBO aerospace applications and include novel and patented air evacuation strategies. In turn, the selected processing and laminate layup methodology represents the cutting edge of academic research, and the specimen preparation follows the most current industrial guidelines. Lastly, the image analysis methods used to assess laminate quality extend beyond the current industry norms.

The proposed, semi-automated corner thickness profiling method is a novel approach to determine the thickness profile of sharply-curved details as a function of the position along the reference, tool-side edge—no other current published studies were found that used a similar approach to investigate complex-shape laminates. The analysis is implemented in Matlab and can be readily adapted to treat complex geometries other than L-shape corners and data other than 2D scans. In turn, the approach is validated against the more direct measurement methods that are currently used in the literature and prescribed by testing standards for sharply-curved laminates. Sets of measurements made on tape and 2D-woven corner laminates demonstrate that the new method is more accurate, precise and insightful. This method has thus far directly contributed to two conference papers that study the effect of processing parameters on VBO corners [99, 127] and generated data used for modelling thickness deviation in corners [52].

In turn, the analysis of laminate cross-section micrographs via thresholding extends beyond the general approach detailed in the *Mil-Hanbook-17*—a primary reference work for the North American aerospace industry. In particular, the method is semi-automated, the thresholds used to segment images are computed rather than visually set and void species are recognized.

Cutting edge image analysis techniques that employ machine learning algorithms and the overall transition from 2D optical microscopy images to 3D micro-CT data are revolutionizing composite research. Such methods are however still in their infancy and fall outside of the research scope and available resources for the experimental work. The proposed image analysis is deemed to be perfectly adequate for the purpose of comparative studies. The next chapter presents the curved beam strength mechanical testing methodology and the important modifications made to the ASTM D6415 test standard.

3

Development of stiffening-sleeves for curved beam strength testing

3.1 Introduction

ILT testing of composite laminates requires specimens that are representative of curved details in industrial parts, e.g. aircraft fuselage stringers, and standardized methods that are cost-effective, i.e. practical to setup and rapid to implement. Jackson and Ifju [83] proposed a refined method whereby a four-point bending (4PB) fixture with frictionless loading rollers subjects a corner specimen (§ 2.3.1) to a constant, pure bending moment in the plane of curvature. This test configuration greatly simplifies specimen installation and eliminates interlaminar shear stresses in the corner region compared to the previously proposed test configuration, i.e. tensile end-loading via a hinged-loading mechanism (HLM) [41, 82]. The CBS and ILTS are subsequently calculated from the resultant load-displacement data and geometric constants of the specimen-fixture assembly. The proposed method was formally adopted as the ASTM D6415 test standard [90].

An important shortcoming of this standard is that the data reduction does not account for the complex deformation of the corner specimen, which is a combination of flange flexure and opening of the corner region. The CBS calculation simply assumes that the specimen flanges remain straight and the radius constant during the test. Excessive flange flexure causes the CBS to be overestimated resulting in a potentially significant error. The standard does warn of the significance of this error beyond a general crosshead displacement of 5 mm [90]—though no analytical or semi-empirical corrections are offered in its current version. This error is akin to the significant error in bending stress in the case of flexural testing of flat laminates, for which corrections do exist [185].

The 5-mm threshold is often surpassed as demonstrated in the literature [95-98] and per the experience of the author [99] when testing laminates of intermediate stiffness and higher toughness. The error may then be significant as the standard suggests, though its true magnitude is unknown. Experimentally-determined strength properties can be compared to the results of the other interlaminar tensile test methods, namely the tensile-HLM test configuration [81] and flatwise tensile testing [87]. However, these methods are known to produce results that depend on the loading configuration and the specimen geometry, scale and quality [81, 83, 88, 96].

Finally, the ASTM D6415 test standard suggests the use of "bonded doublers" similar to specimen end-tabbing to support the specimen flanges during the test thereby directly eliminating flange flexure [90]. Such a modification however falls outside the scope of the standard, and no published studies were found that offer practical solutions to remedy this error. In addition, the bonding of doublers via co-curing or -bonding is deemed to be impractical as it complicates the specimen manufacturing and significantly increases preparation time and cost. In turn, the opening of the corner region is not considered in the ILTS calculation, which is affected by the aforementioned CBS error (Eq. (1-4)). An analytical solution was derived for the relatively simpler corner deformation of the tensile-HLM test configuration [100]; however, no simple-to-implement analytical solution yet exists for the 4PB test configuration. Only one accurate semi-empirical method was proposed for this test configuration [95]—though it is complicated and convoluted. This method relies on *in situ* measurements or FEM predictions of the specimen deformation and an iterative algorithm implemented in Mathworks Matlab to converge on the corrected flange angle to the horizontal (ϕ). Such an approach does not lend itself well to standardization.

3.2 Chapter objectives and outline

The first objective is to estimate the CBS and ILTS calculation errors based on the data reduction prescribed by the ASTM D6415 test standard. This task is accomplished via a simplified 2D FEM approach. The second objective is to develop a direct, practical and cost-effective modification to the standard to reduce the magnitude of these errors. To this end, mechanical stiffening-sleeves that function in a manner similar to that of bonded doublers are proposed. This design forgoes the need for additional specimen manufacturing steps, can easily be set at an adjustable, arbitrary offset distance from the start of the corner region, and is fully reusable. The third and final objective is to account for corner opening in the ILTS calculation. The use of stiffening-sleeves allows for the assumption that flanges remain straight under load to be made. A simple analytical correction of the corner radius at failure can thus be derived that works well for small sleeve-to-corner offsets, in which case deformation is constrained to the corner. The modelling analysis and experimental validation utilize a UD-tape specimen with all the fibres being nominally oriented in the hoop-direction. In addition, both the ASTM and custom specimen geometries (§ 2.3.1) are modeled for the sake of comparison.

The chapter outline is as follows. First, the stiffening-sleeve design is presented, and its implementation explained within the context of the standard test procedure (§ 3.3). The CBS and ILTS error estimation for the standard case and reduction for the sleeve modification case are then determined via a simplified 2D FEM approach implemented in Abaqus/Standard 6.16 (§§ 3.4-3.6). Finally, the use of stiffening-sleeves is validated (§ 3.7) via mechanical testing and a fractographic assessment of failed specimen sections via scanning electron microscopy (SEM) to ensure that the sleeves do not affect the onset of failure (first delamination) in the corner region.

3.3 Mechanical stiffening-sleeve design and testing methodology

3.3.1 Mechanical stiffening-sleeve design

The fundamental concept behind the mechanical stiffening-sleeve design is akin to the use of bonded doublers, whereby pairs of significantly stiffer and often thicker plates are secured to either side of a given flange in order to directly restrict flexure under load. A guiding principle of mechanical test standards is to provide simple, practical, rapid and cost-effective methods whenever possible. To this end, the reusability and adjustability of a mechanically-fastened stiffener design represent vital improvements over the bonded doublers alternative.

The sleeve assembly is illustrated in Fig. 3-1 along with the corner specimen positioning features. Fig. B-3 and B-4 in Appendix B provide the machined features and dimensions. The assembly comprises an upper and lower stiffener fastened together by four machine screws. The upper stiffener performs dual duties as it also serves to align and center the sleeve assembly to the flange via two lateral pins and a corner offset bolt. The latter sets the distance between the loading nose and the shoulder (inflection point) of the corner region. Complex contact pressure gradients arise between the specimen and inner stiffener surfaces as the sleeves restrict flange deformation. Fig. 3-2 illustrates the complex contact state predicted via a high-fidelity 3D FE model implemented in Abaqus/Standard 6.16 (§ 3.6.2). Friction alone suffices to maintain the sleeves in place during testing and prevents slippage. Fasteners therefore only need to be finger-tightened resulting in negligible preloading of the fastener and specimen (T-T compression).

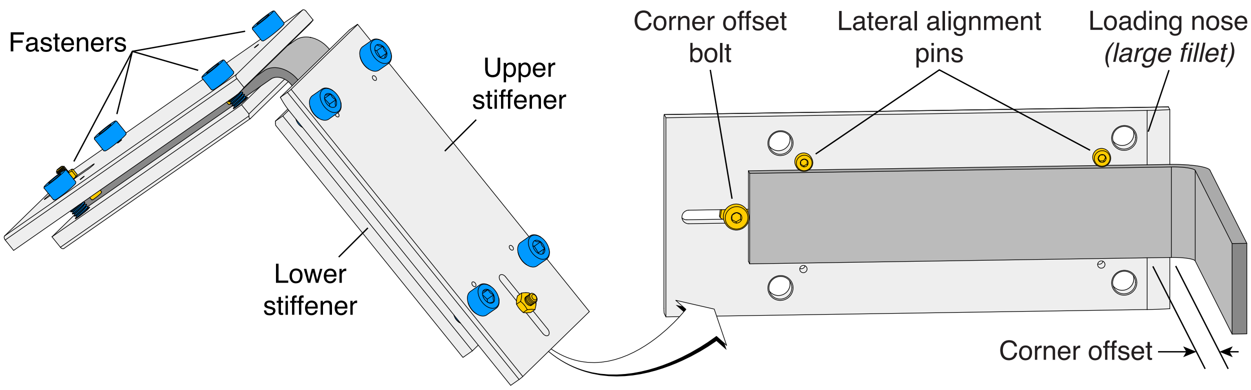

Fig. 3-1. Mechanical stiffening-sleeve assembly and corner specimen positioning.

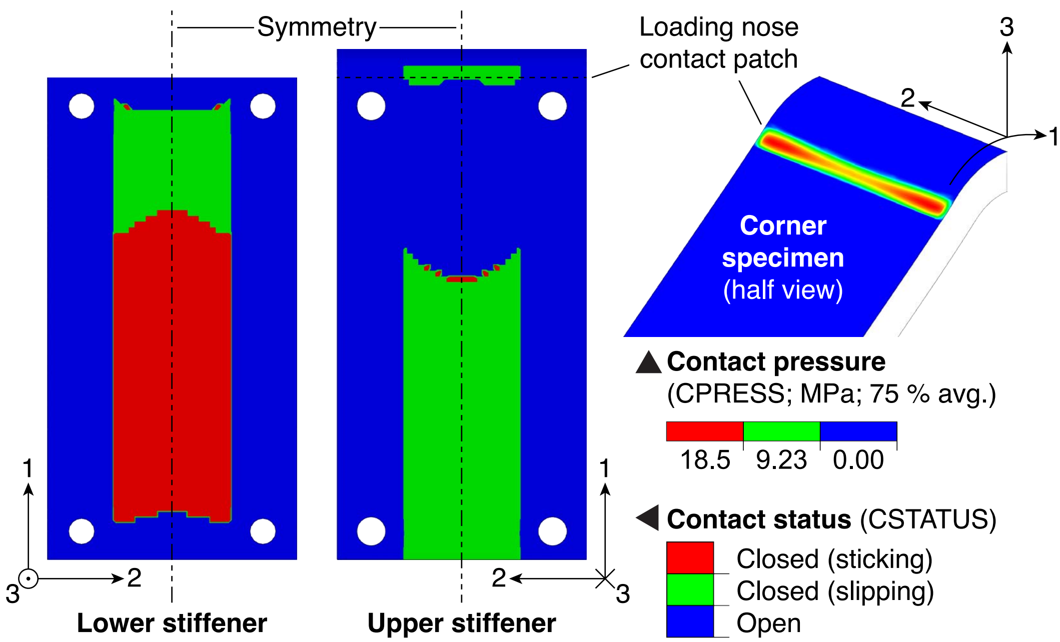

Fig. 3-2. 3D FEM predictions of the complex stiffener-specimen contact state via Abaqus/Standard 6.16.

The stiffeners are machined from extruded stainless steel 17-4 PH, which is a high-performance, martensitic-precipitation-hardening stainless steel that is typically used in mechanical test fixtures on account of an impressive combination of high stiffness and strength, and good corrosion, hardness and wear properties [186, 187]. Stiffeners are precision ground to a thickness of 5 ± 0.03 mm and a parallelism tolerance of 0.03 mm over all surfaces. A nominal stiffener thickness of 5 mm is used for the data reduction. The loading nose of the upper stiffener consists of a large 20 ± 0.1 mm fillet radius that is cotangent with the inner stiffener contact surface. The radius is selected based on FEM results to reduce the peak contact pressure while minimizing the travel distance of this point towards the corner region bisector as the corner opens under load. It should be noted that the corresponding, corner-proximal edge of the lower stiffener loses contact with the specimen immediately upon loading and is therefore left unrounded. Finally, flanges are machined to a width of 44 ± 0.03 mm given the nominal custom specimen width of 20 mm. It should be noted that dimensions such as the sleeve width evidently need to be updated for wider specimens, while other dimensions such as the loading nose radius may also need to be updated.

The selected hardware (i.e. machine screws, alignment pins and offset bolt and nut) are also made of corrosion resistant, high-stiffness and -strength stainless steel to handle the rigors of testing. The layout of the fasteners is such that they can never come into contact with the loading rollers of the particular 4PB fixture used in this work irrespective of the fixture closure distance. They are also positioned to be sufficiently close to the specimen edges such as to minimize stiffener deformation and sufficiently distant from the stiffener edges such as to minimize open-hole effects.

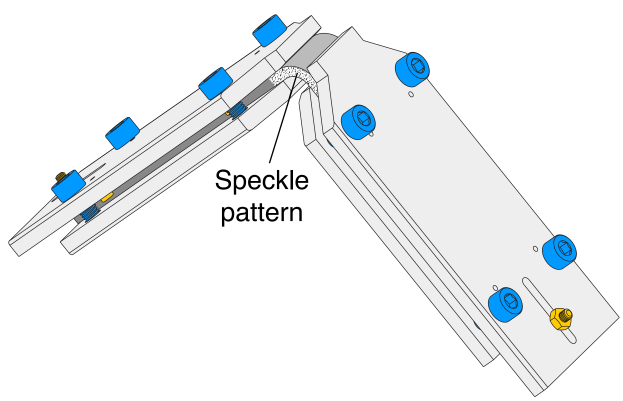

Fig. 3-3. Mechanical stiffening-sleeve concept adapted for digital image correlation.

It can be shown from the results of a high-fidelity, 3D FE model (§ 3.6.2) and the successful testing of over 200 corner specimens with a single pair of stiffening-sleeves that the current design is mechanically sound. However, there is room for further refinement of the design such as the creation of a compatible version for digital image correlation (DIC), as illustrated in Fig. 3-3, which is a popular technique to experimentally determine edge-surface stresses in the corner region and detect the location of the initial delamination failure [93, 94, 96, 178]. Furthermore, a global sensitivity analysis similar to that performed by Kobyé *et al.* in the case of a hybrid bolted-bonded lap joint would be beneficial to address the full complexity of the stiffening-sleeve design and highlight the factors that most affect the sleeve performance [106, 188]. In this work, all the design properties, both material and geometric, are fixed and only the effect of the stiffener offset distance is considered. It can be shown that the stiffeners otherwise behave as practically rigid bodies.

3.3.2 Modified mechanical testing methodology

The focus of this section is to present the experimental test equipment and setup. The specimen preparation and measurements are covered in §§ 2.3 and 2.4, resp. It should be noted that the test procedure recommended in the ASTM D6415 test standard is largely unchanged by the adoption of stiffening-sleeves. In addition, the methodology described herein is observed for all mechanical tests performed for this thesis.

The fixture used in experiments was manufactured by Wyoming Test Fixtures Inc., USA, out of stainless steel 17-4 PH with custom length rollers (104 and 125 mm). The loading rollers have a diameter of 9.525 mm and are spaced 76.2 and 101.6 mm apart. It should be noted that the loading rollers should ideally be only slightly longer than the stiffener width to minimize roller flexure and provide adequate clearance (0.5 to 1 mm longer). In addition, thicker rollers could be used such as in the case of the alternative Airbus AITM1-0069 test method [91]. The fixture is installed on an MTS Insight™ testing frame set in displacement control with an effective load cell capacity of 4.5 kN (AINSI class 0.5 accuracy from 1 and 100%). The fixture halves are inverted to have the specimen pointing down rather than up as per the standard. This minor deviation allows for the simpler placement of the specimen without having to lower the machine crosshead in order to keep the specimen from sliding off of the loading rollers during installation. It has no effect on the actual test results. Fig. 3-4 illustrates the 4PB-CBS fixture and experimental setup, and Fig. B-5 in Appendix B provides the principal fixture dimensions.

Next, the sleeves are fitted to the specimen, and the assembly is installed roughly at the center-span of the rollers. A clever feature of the 4PB test configuration is that the corner specimen automatically centers itself between the rollers once a load is applied. The specimen installation concludes with the taring of the load cell and lowering of the crosshead until the specimen makes full contact with all four rollers and a very small load is observed *in situ* (> 10 N). The crosshead is subsequently lifted until the specimen is fully unloaded, and the crosshead is finally tared.

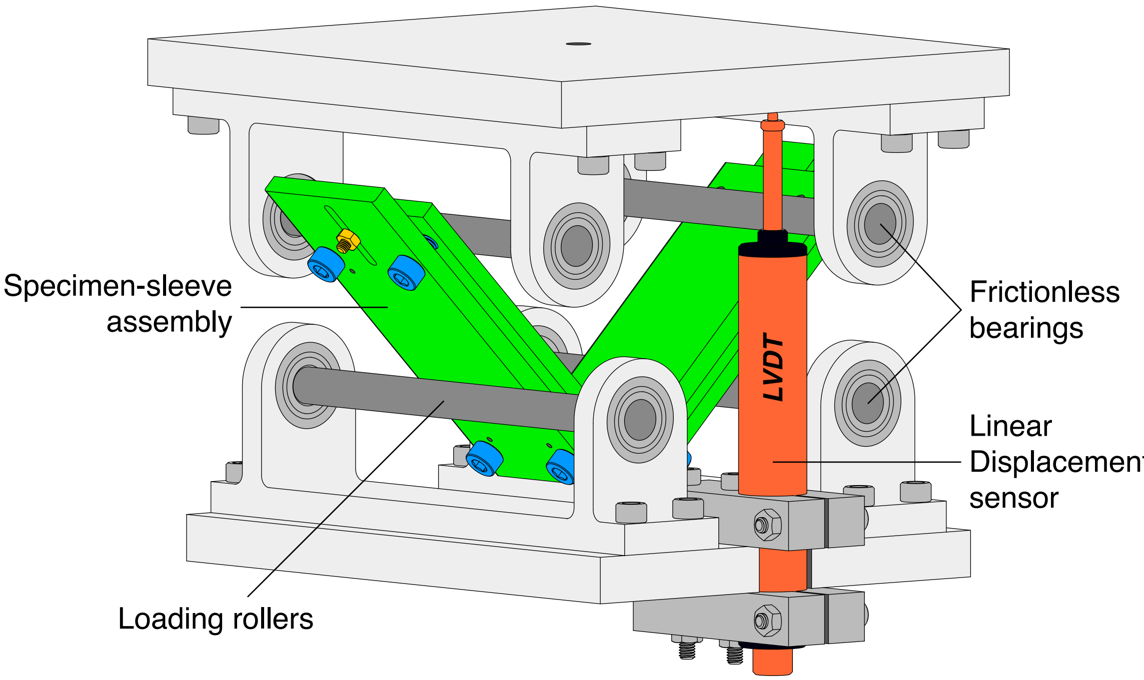

Fig. 3-4. Customized 4PB-CBS test fixture and experimental setup.

The relative displacement between the two fixture halves, i.e. the closure distance, is recorded by a high-precision linear displacement sensor (Micro-Measurements HS25) with a range of 25 ± 0.001 mm, which is well within the prescribed accuracy requirement. It is adjusted and tared prior to testing. In turn, the speed of testing (loading rate) is set to 0.50 mm/min, which is a typical rate for quasi-static testing of advanced polymer composites. Finally, the sampling rate for data recording is set to 5 Hz to acquire sufficient data points, and the machine clock, load cell force reading, and LVDT-measured displacement are outputted as text files.

Failure is defined for the purpose of this work as the appearance of the first ILT delamination in the corner region, which is typically associated with the first load-drop [81, 83, 90]. The test may thus be terminated after the first load-drop rather a 50% load-drop as prescribed by the standard—unless damage propagation is of interest. To this end, the adjustability of the stiffening-sleeve design is invaluable as it allows for rapid adjustments based on the performance of an exploratory specimen. The final step of the test method, data reduction, is automated via a custom m-script written with Mathworks Matlab (R2015b) that processes the corresponding specimen result text-files outputted by the MTS test frame and the corner thickness profiling script (§ 2.4.3) generating the necessary specimen-geometry measurements.

Two important changes are made to the standard data reduction. First, the assembled sleeve thickness (t_A) is used instead of the nominal flange thickness (t) in the CBS calculation (Eq. (1-1)) to account for the additional distance between the loading rollers due to the presence of stiffeners. The modified CBS equation can be rewritten as follows,

$$CBS = \frac{P}{2wcos(\phi)}\left(\frac{d_x}{cos(\phi)} + (D+t)\cdot tan(\phi)\right)$$

$$\text{where: } \phi = sin^{-1}\left(\frac{-d_x(D+t_A)+d_y\left(d_x^2+d_y^2-D^2-2\cdot Dt_A-t_A^2\right)^{0.5}}{d_x^2+d_y^2}\right) \tag{3-1}$$

$$\text{and: } d_y = d_x\cdot tan(\phi) + (D+t_A)\cdot cos(\phi) - \Delta$$

Second, the corrected corner radius at failure (r') is introduced and replaces the uncorrected radius (r) in the ILTS calculation and Kedward approximation (Eq. (1-4) and (1-5), resp.). The radius correction is given by Eq. (3-2) and is contingent on the following three assumptions: the flanges do not deform, they are cotangent with the plane of curvature of the corner region, and the arc length of the corner remains constant.

$$r_{i,o}{}' = r_{i,o}\cdot\phi_i \div \phi \tag{3-2}$$

The Kedward approximation can thus be rewritten as follows,

$$ILTS = (3\cdot CBS) \div \left(2t\sqrt{r_i{}'\cdot r_o{}'}\right) \tag{3-3}$$

3.4 Basis of the 2D FEM validation

The true values of the CBS and ILTS must be known to determine the errors of the values calculated using the standard and modified data reductions (§§ 1.4.3 and 3.3). The true values however cannot be known and must therefore be estimated via either experimental or modelling means. No practical experimental approaches exist that can estimate with high-accuracy the true applied moment and ILT stress independently of the test configuration and specimen used. For one, DIC is affected by free-edge stresses [80, 92]. In contrast, finite element modelling (FEM) has been adopted as a tool to validate advances in methodology since the inception of interlaminar strength testing [41, 80, 82, 104]. In particular, Wimmer *et al.* [178] and Matsuo *et al.* [100] demonstrated that a simplified 2D, symmetric, plane-strain, FE model adequately predicts the load-displacement curve for the clamped L-bracket and the tensile-HLM test configurations, resp. In turn, Blanchfield *et al.* used the load and roller displacement data from the same FEM approach to validate a proposed, semi-empirical methodology to account for the deformed specimen geometry of the 4PB test configuration [95]. A similar FEM approach is therefore used in the present work to validate the use of stiffening-sleeves.

It should be noted that the FE modelling performed in the following two sections captures the elastic response of the corner specimen but does not predict its failure nor does it capture plastic deformation or other known factors such as fibre waviness. In addition, the CBS and ILTS are single strength values. The modelling curves that are generated in the analysis are therefore technically those of the applied moment per unit width, M/w and the ILT stress. That being the case, these curves represent the set of strength values were the specimen to fail at a given stress level. Eq. (3-1) and (3-3) are thus used to populate the M/w and ILT stress curves as functions of the fixture closure distance.

Finally, the predicted values are taken as estimates of the true values. The predicted value of the M/w is determined from the overall computed moment acting at the line of symmetry that bisects the corner region in the y-direction and normalized by the specimen width—the yz-plane of symmetry for 3D models. In turn, the predicted ILT stress is the maximum radial stress value probed on that same line (or plane) of symmetry. And finally, the load and displacement data used in the standard and modified data reductions are taken as the respective vertical components of force and displacement acting on either the loading or support roller. It should be noted that the force value must be multiplied by factor of 2 in the case of a 2D-symmetric model, and the force and moment values by factors of 4 and 2, resp., in the case of a 3D quarter (bisymmetric) model.

3.5 Estimation of the standard CBS and ILTS errors

3.5.1 2D FEM implementation

Per the rationale presented in the previous section, the CBS and ILTS errors caused by the complex specimen deformation are estimated via a simplified 2D FE model that is symmetric about the corner bisector of the corner region. This model is illustrated in Fig. 3-5 and implemented in Abaqus/Standard 6.16. It is henceforth referred to as the *standard 2D model*. The loading rollers are modelled as analytically rigid wires that are coupled to reference points superimposed over the roller axes. A clamped (*encastre*) boundary condition is defined for the "support" roller (stationary) at its reference point, i.e. $U_1 = U_2 = U_3 = \Psi_1 = \Psi_2 = \Psi_3 = 0$, where U and Ψ are translations and rotations about the principal axes. The "loading" roller (mobile) is also clamped except in the y-direction ($U_2 \neq 0$), for which a displacement ($\Delta = \Delta_{max}$) of -14 mm is set. This value is given by Eq. (3-4) and represents the maximum fixture closure distance for the given specimen thickness and fixture geometry, which is the difference of the initial and final vertical roller separation (fixture-fixture contact). The geometric variables and constants are visually defined in Fig. 1-12.

$$\Delta_{max} = d_{yi} - d_{yf} = \left[d_x \tan(\phi_i) + \frac{D+t}{\cos(\phi_i)}\right] - \left[\left(R_S + \frac{D}{2}\right)^2 - d_x^2\right]^{0.5} \tag{3-4}$$

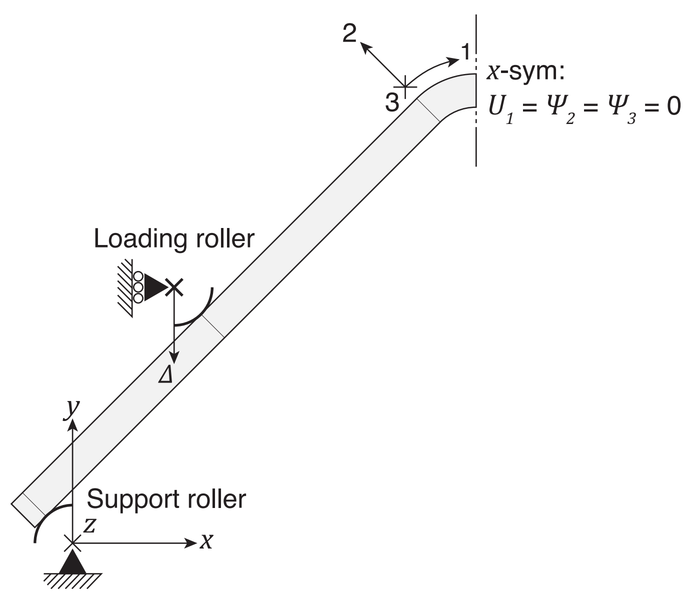

Fig. 3-5. 2D-symmetric plane-strain FE model for the standard test configuration.

The corner specimen is modelled as a planar deformable part with solid, homogeneous sections and a linear elastic material model populated with the engineering constants provided in Table 2-4. The material orientation is set to follow the plane of curvature of the specimen. The same material model and orientation is used to model the specimen in all subsequent 2D and 3D models. In turn, the specimen is modelled with CPE8R structural elements: biquadratic, plane-strain, solid quadrilateral elements (8 nodes; 2 DOF) with reduced-integration (second-order interpolation: 4 integration points) [189]. Second-order, reduced-integration elements perform well in bending ($\varepsilon_{xx} \neq 0$, $\varepsilon_{yy} = \varepsilon_{xy} = 0$; no shear-locking), and minimize the risk of hourglassing and computational costs. The models contain 25.6-32.6k elements with 78.5-99.4k nodes and require 157-199k equations to be solved. Lastly, the only boundary condition applied to the specimen is symmetry about the *x*-axis (*x*-sym: $U_1 = \Psi_2 = \Psi_3 = 0$).

Contact between the rollers and the specimen is defined via the general surface-to-surface contact formulation—the primary formulation in Abaqus/Standard. The "finite-sliding" option is selected to account for large deformations, and state-tracking is selected by default given the presence of analytically rigid master surfaces (rollers). In turn, friction and hard-contact are selected for the tangential and normal contact behaviours, resp. Hard-contact is enforced with a penalty constraint, and the surfaces are allowed to separate after the first simulation increment.

Finally, the model is solved for the given displacement imposed on the loading roller in a single step and using the Standard Solver (traditional implicit integration scheme; direct Newton method). The "nonlinear geometry" option is selected to account for the large specimen deformation, and the "automatic stabilization" option via a specified dissipated energy fraction of 2×10^{-4} is selected to help reach equilibrium in the case of local instability due to contact separation. The online Abaqus 2016 documentation may be consulted for further details on the settings mentioned in this section [190].

3.5.2 Mesh sensitivity and model validation

The specimen is discretized with a global structured mesh with an element aspect ratio of ≤ 1.34 and internal angles of 90° to minimize element distortion and improve accuracy [189]. A mesh sensitivity analysis is performed to determine the global seed size with which the ILT stress (S22) and the internal model energy (total strain energy, ALLIE) converge. With the aspect ratio set to roughly 1 and the CPE8R element being relatively cheap, the only meshing parameter that is considered is the number of T-T elements per mm (N_{TT}). Fig. 3-6 presents the results of the analysis whereby convergence is measured as the relative difference in results between a given degree of mesh refinement and the finest mesh used ($N_{TT} = 25$). The solution is deemed to have converged when the relative difference dips below a relatively strict threshold of 0.5% [106]. A value for N_{TT} of 5 is therefore selected, which translates to 21 and 17 T-T elements for the ASTM and custom specimen cases, resp.

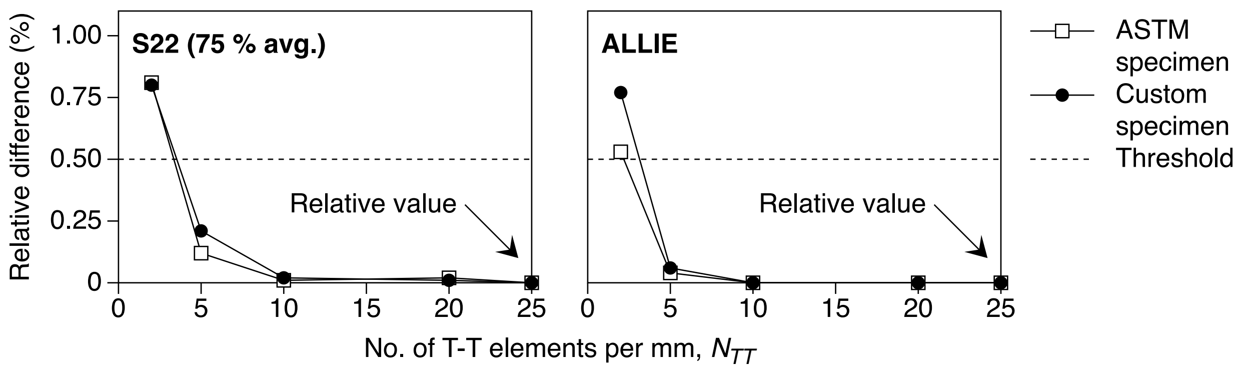

Fig. 3-6. Global mesh sensitivity analysis results for the standard 2D model.

Finally, an important step when using automatic stabilization is to check that the model reaches static equilibrium by taking the ratio of the viscous dissipated and the total strain energies (ALLSD/ALLIE). For $N_{TT} \leq 5$, this ratio is ≤ 0.265 and $\leq 0.215\%$ for the ASTM and custom specimen cases, resp.—static equilibrium is therefore satisfied as the ratios are well below 1%. It should be noted that the thicker ASTM specimen requires more T-T elements than the custom specimen as demonstrated by the overlapping convergence curve in Fig. 3-6, which is why the N_{TT} ratio is used rather than the total number of T-T elements.

The Lekhnitskii solution and Keward approximation (Eq. (1-4) and (1-5), resp.) are calculated from the load-displacement data to check the validity of the approximation for the given specimen geometries and materials (Fig. 1-14). An error of 1.23 and 1.46% is determined for the ASTM and custom specimen cases, resp. The Kedward approximation is therefore deemed to be acceptable for the purposes of this work as the error falls below the stated 2% threshold [41, 90].

Finally, the standard 2D model is validated with two, high-fidelity, quarter (bisymmetric) 3D models illustrated in Fig. 3-7 and henceforth referred to as the *3D-standard* models. The loading rollers are modelled as both analytically rigid surfaces and 3D deformable parts with solid homogeneous sections. The deformable roller material is defined as a linear elastic, isotropic material with the typical properties of stainless steel 17-4 PH: $E = 197$ GPa and $\nu = 0.272$ [187]. The specimen and deformable rollers are discretized with structured meshes and C3D20R continuum elements: solid hexahedral elements (brick; 20 nodes; 3 DOF) with reduced-integration (8 integration points). These are excellent general-purpose elements that perform well in bending (no shear-locking) and rarely exhibit hour-glassing, similar to the CPE8R element.

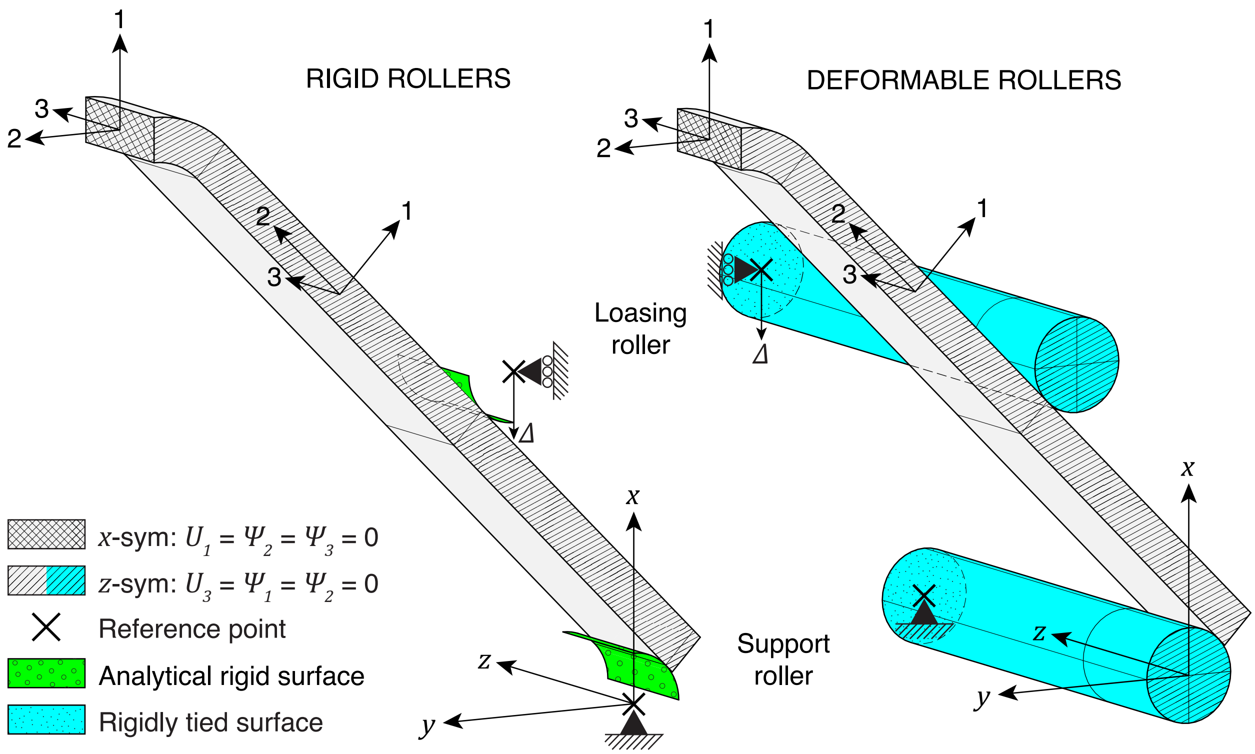

Fig. 3-7. 3D FE models of the standard test configuration.

The *encastre* and vertical displacement boundary conditions are applied at reference points that are rigidly tied to the respective roller end-faces. Symmetric boundary conditions are defined for the specimen and deformable roller faces that lie in the *xy*- and *xz*-planes (x-sym: $U_1 = \Psi_2 = \Psi_3 = 0$; z-sym: $U_3 = \Psi_1 = \Psi_2 = 0$). Finally, the same specimen-roller contact behaviours as for the standard 2D model are defined except that "path-tracking" is enabled for the deformable roller case, which is more accurate than "state-tracking" given that it uses the deformed rather than the initial surfaces of contact pairs. All other settings presented in the previous section for the standard 2D model remain unchanged.

The 3D-standard models are too expensive to follow the mesh sensitivity applied to the standard 2D model given that they contain 107-140k elements with 463-600k nodes and require 1.38-1.79M equations to be solved. Global seeding for the specimen and biased seeding for the deformable rollers are instead based on an appropriate Abaqus benchmark problem [191] and published work [97]. The custom and ASTM specimen are discretized with 17 and 21 T-T elements ($N_{TT} = 5$), resp. A global seeding of 0.5 mm is otherwise defined resulting in 20-25 width-elements and 9-12 radial elements, resp. An acceptable maximum element aspect ratio of 3.47 is present in the corner region of the ASTM specimen. It should be noted that bias-seeding is not used for the flanges since free-edge stresses are not of interest, the loading rollers slide a large distance over the flange surfaces ($\Delta = -14$ mm) and large bending deformations are expected—a relatively finer mesh is required throughout the specimen. On the other hand, the rollers are discretized with a bias-seeding ratio of 3, i.e. global seed size of 0.5 mm for the section directly over the specimen and 1.5 mm at the rigidly-tied edges.

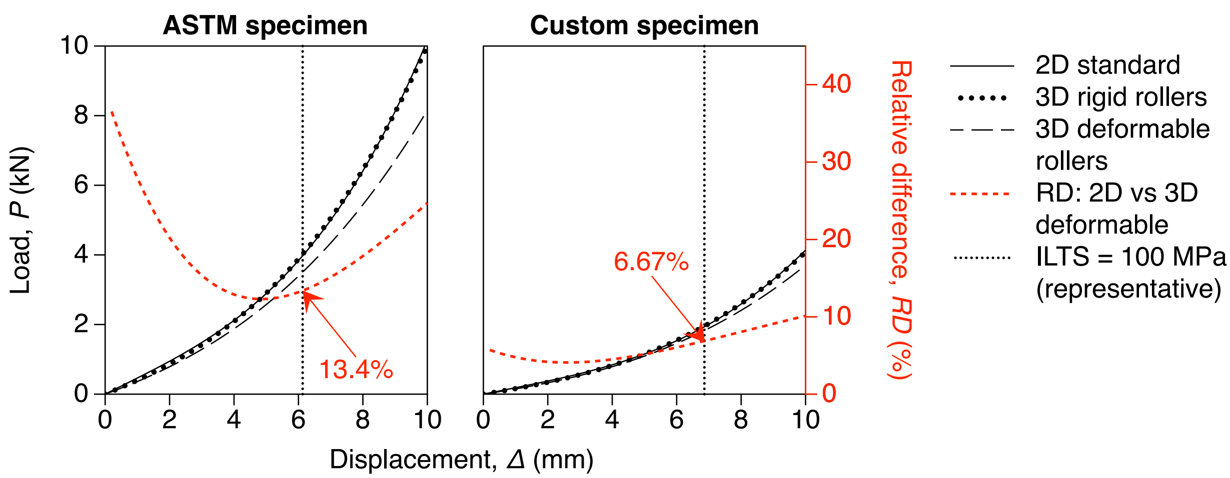

Fig. 3-8. Load-displacement validation of the simplified standard 2D model.

The resultant load-displacement curves for the simplified 2D and high-fidelity 3D standard models are presented in Fig. 3-8. The load and displacement for an ILTS value of 100 MPa is included in the plots, which is a rough approximation of the ILTS for the selected UD-tape. The 2D and 3D FEM results agree very well when the loading rollers are modelled as analytically rigid. In turn, the 3D model with deformable rollers captures the roller deflection of the custom 4PB-CBS fixture. As presented earlier in Fig. 2-5, the use of the smaller custom specimen significantly minimizes the amount of deflection and lowers the failure load. As a result, the relative difference between the 2D and 3D deformable roller models falls below 7%. The simplified 2D FEM approach is therefore deemed to be valid to estimate the magnitude of the CBS and ILTS errors.

Though the accuracy of the standard 2D model in the case of the custom specimen geometry yields passable results compared to the 3D-standard model with deformable rollers, a much better agreement can be obtained by using a 4PB-CBS fixture with appropriately sized rollers that negligibly flex.

3.5.3 Results and discussion

The 2D-sleeve model predicts that the ASTM and custom specimens should fail at displacements of 6.13 and 6.86 mm and loads of 4.04 and 1.97 kN, resp. (Fig. 3-8) for a representative ILTS value of 100 MPa. A significant error in CBS and ILTS is therefore expected in both cases as the displacements surpass the 5-mm threshold introduced in the ASTM D6415 test standard [90]. The specimen deformation and T-T tensile stress (S22) contours are illustrated in Fig. 3-9 at different displacements for the custom specimen. Flange flexure is clearly visible at a displacement of 5 mm. In turn, the change in corner inner radius and thickness as a function of displacement are presented in Fig. 3-10. The thicknesses increase slightly by 0.50% due to the Poisson's effect, whereas the inner radii increase more significantly by 3.96 and 4.30% for the custom and ASTM specimen, resp. The thinner flanges of the custom specimen flex more than those of the ASTM specimen, which translates to a smaller corner opening.

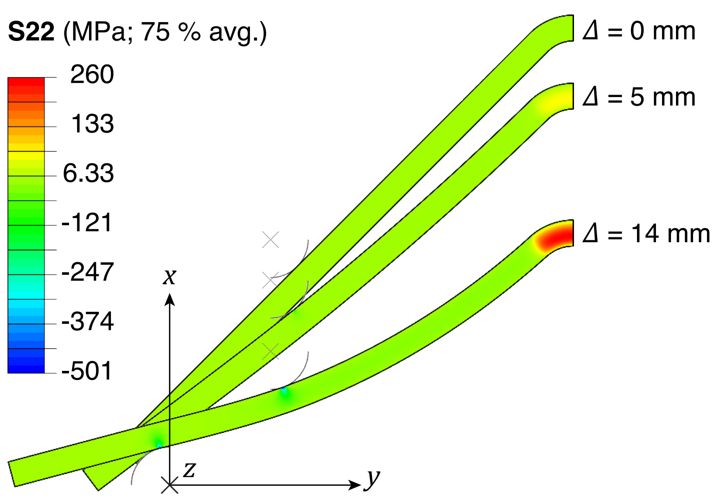

Fig. 3-9. Corner specimen deformation for the standard test configuration (custom specimen only).

The load-displacement data at the rollers is used in the standard data reduction presented in § 1.4.3. to calculate M/w and $\sigma_{r,max}$. The results are plotted in Fig. 3-11 as functions of displacement. The error (inaccuracy) of the calculated values is estimated by calculating the percent error (difference) between the calculated values and the predicted value at the plane symmetry. For a representative ILTS value of 100 MPa, the CBS and ILTS errors are estimated to be, resp., 5.50 and 9.71% for the ASTM specimen and 6.80 and 10.7% for the custom specimen. The larger errors associated with the custom specimen are due to the increased degree of flange flexure compared to the ASTM specimen case. The bulk of the error is due to flange flexure and not the opening of the corner radius as can be deduced by comparing the proportions of the errors between the four results. It should be noted that the error increases with displacement as higher loads result in greater flange flexure and corner opening. However, the beginning portions of the estimated error curves (0 to ~1 mm) is unreliable as the percent difference of values approaching zero goes to infinity.

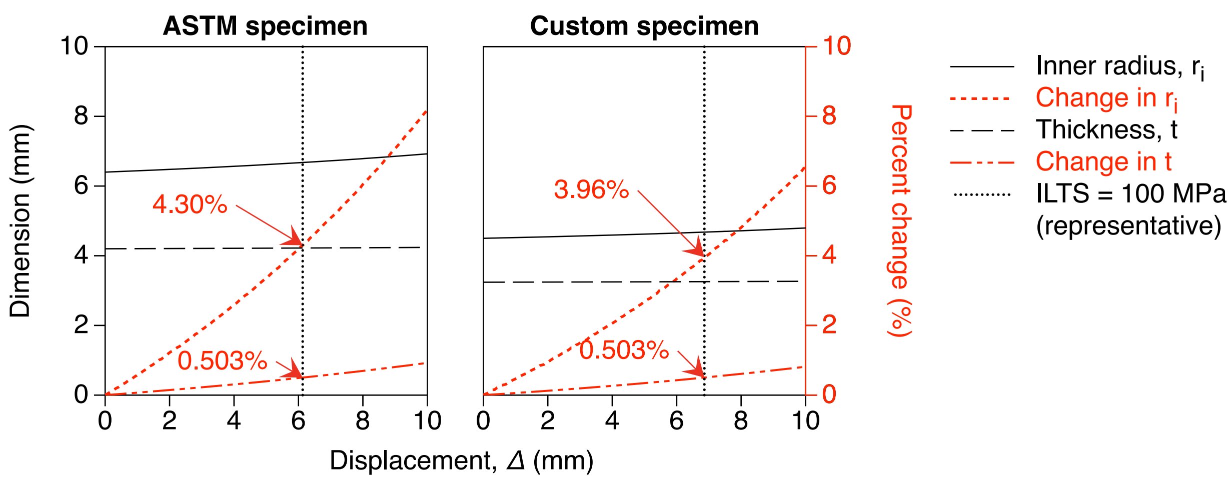

Fig. 3-10. Changes in corner inner radius and thickness for the standard test configuration.

The 2D FEM approach is validated and generates reasonable error estimates that can be expected in actual experimentally-determined values. It can be confidently stated that errors in accuracy of more than 5.0% are indeed significant. The error sources in the test method must therefore be addressed, i.e. flange flexure, and secondarily corner opening must be accounted for. The materials tested in this thesis are representative of advanced composites tapes, for which the ASTM standard was designed, but by no means do they represent a worst-case scenario whereby the errors would be larger still. The next section follows the same structure as this section to estimate the reduced errors that can be expected from using stiffening-sleeves and a corner radius correction in the data reduction.

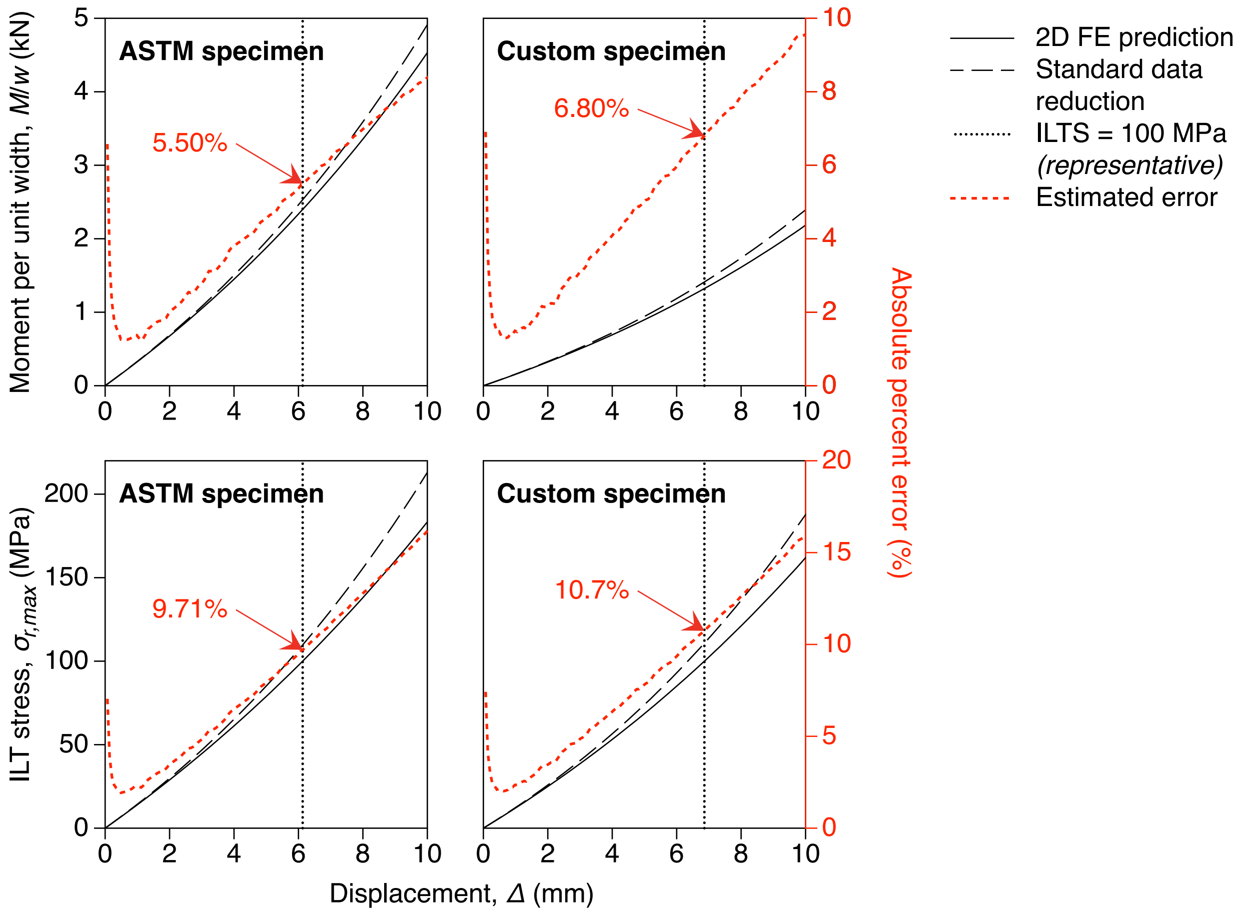

Fig. 3-11. Estimation of the CBS and ILTS errors for the standard test configuration.

3.6 Reduction of the CBS and ILTS errors via the use of stiffening-sleeves

3.6.1 2D FEM implementation

A second 2D symmetric plane-strain model is developed to idealize the use of stiffening-sleeves. The model is illustrated in Fig. 3-12 and is henceforth referred to as the *2D-sleeve* model It shares many of the details of the equivalent no-sleeve (standard 2D) model described in § 3.5.1, including: the element type (CPE8R), boundary conditions (*encastre*, *x*-symmetry and *y*-

displacement), specimen geometries, the use of analytically rigid wires to model the rollers, frictionless-hard roller contact defined in this case between the rollers and stiffener outer surfaces, and solver settings.

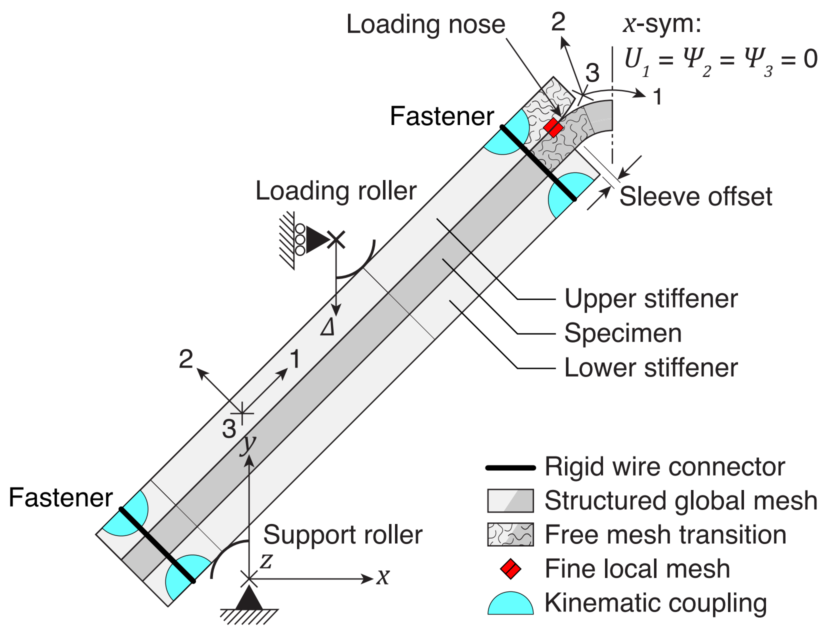

Fig. 3-12. 2D-symmetric plane-strain FE model for the sleeve-modified test configuration.

The upper and lower stiffeners are modelled as 2D deformable parts with solid homogenous sections and the same linear elastic isotropic material model used for the 3D deformable stainless-steel rollers in § 3.5.2 (E= 197 GPa and ν= 0.272). In turn, the inner stiffener edges initially contact the specimen edges. Contact is defined via the general surface-to-surface contact formulation with “finite-sliding”, “path-tracking” and the stiffener edges selected as the master surfaces. Hard-contact via penalty constraint enforcement is used in the normal direction, and the surfaces are allowed to separate after the first simulation increment. A simple friction behavior is used in the tangential direction and enforced by penalty constraint and a friction coefficient of 0.3, which is a reasonable estimate of the static friction coefficient between epoxy and smooth steel. Finally, the fasteners are modelled as analytically rigid wires, whose end-nodes are tied to the local stiffener section via kinematic coupling for all DOFs over a radius of 4 mm. Wires are selected instead of deformable beams as it is unclear how superimposed 3D bolts may be accurately modelled in a 2D plane-strain model. It should be noted that no dashpot or spring elements are needed on account that there is no rigid body motion.

The CPE8R element uses a bilinear interpolation to extrapolate nodal values on account that it has four integration points that lie roughly one quarter of the element size from its edges. A fine mesh is therefore necessary to accurately capture the high stress concentrations that is expected at the specimen surface edge under the loading nose. To this end, a new section is defined for local, structured mesh refinement that encapsulates the linear contact area under the loading nose and accounts for the shift of the peak contact pressure towards the specimen corner and over the outer curved surface during testing. Mesh-transition sections are also defined to connect the refined mesh section to the remaining stiffener and specimen sections, which use structured meshes and a global seed size of 0.1 mm. The transition sections are defined as structured when the global and local mesh size are equal and are otherwise defined as unstructured. This approach allows to investigate the convergence of the peak contact pressure under the loading nose for an increasing degree of local mesh refinement or bias. It should be noted that linear elements are generally preferred to quadratic elements for contact calculations; however, the primary objective of the model is to capture the bending deformation of the specimen, for which quadratic elements are more accurate. The model in its different versions contains a total of 116-129k elements with 354-393k nodes and requires 647-727k equations to be solved.

3.6.2 Mesh sensitivity and model validation

The sensitivity analysis and model validation of the 2D-sleeve model broadly follows the approach used for the standard 2D model (§ 3.5.2). The 2D-sleeve model is discretized with an element aspect ratio of roughly 1 and internal element angles of 90°. A mesh sensitivity analysis is performed to determine the global seed size in terms of the ILT stress (S22) and the total strain energy (ALLIE). In addition, the mesh sensitivity to the peak contact pressure (CPRESS) under the loading roller is investigated via local mesh refinement. A preferred offset distance of 1 mm is selected for the analysis. In turn, the meshing parameter under consideration is the number of T-T elements per mm (N_{TT}), which in the case of bias meshing is simply the number of finest elements per mm (N) in the locally refined sections.

Fig. 3-13 presents the results of the analysis, whereby convergence is again measured as the difference in results relative to the results of the finest mesh tested ($N_{TT} = 25$ and $N = 1$k). A relative difference under a 0.5% threshold indicates that the solution has converged, however a value for N_{TT} of 10 is ultimately selected to reduce the computational costs. The S22 solution converges and the ALLIE solution very nearly converges. It is still deemed satisfactorily converged when considering a more relaxed and typical convergence criterion of 1%. This ratio translates to 42 and 33 T-T elements for the ASTM and custom specimen cases, resp. The local mesh refinement analysis indicates that a much finer mesh of roughly 1k elements per mm, would be necessary to meet the 0.5% threshold. The solution converges locally but at great computational cost. Lastly, static equilibrium is checked given that automatic stabilization is also used for this model. The ratio of the viscous dissipated and total strain energies (ALLSD/ALLIE) is less than 0.31% in the case of global seeding-only ($N_{TT} \leq 25$), and smaller than 0.76% for all degrees of local mesh refinement.

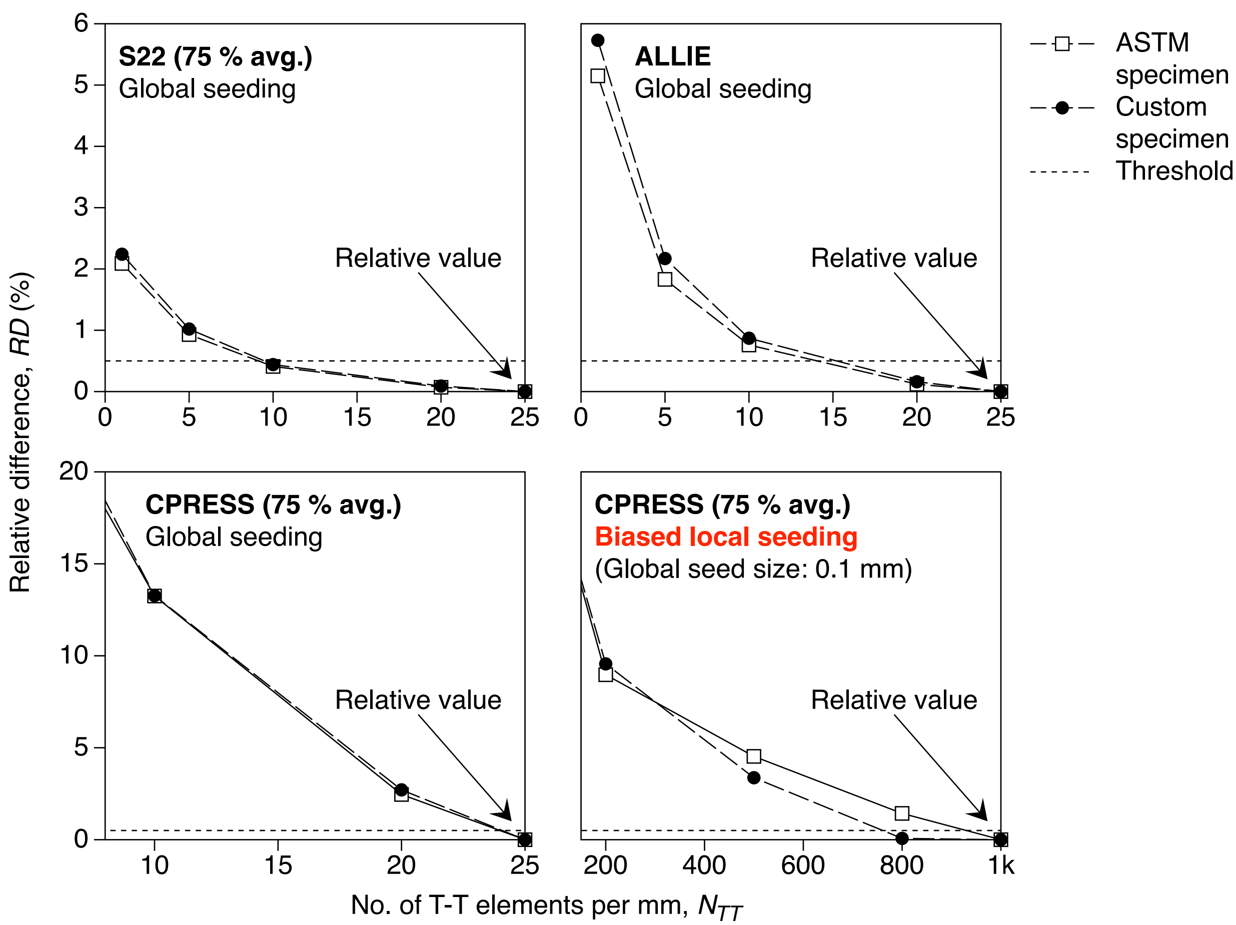

Fig. 3-13. Global and local mesh sensitivity analysis results for the 2D-sleeve model (1 mm sleeve-offset).

As anticipated, the CPE8R element is not ideal to capture the sharp contact pressure gradient generated under the loading nose. In addition, the simplified geometry of the specimen edge (no roughness, perfect contact) and the perfectly elastic material properties (no plastic deformation) result in local idealization errors. In reality, the specimen will locally plastically deform, and the roughness of the specimen and presence of resin-rich surface peaks due to the peel-ply imprint will help to diffuse the contact pressure. The local contact forces are therefore deemed to be unreliable and are not further investigated, even though no singularities are observed. Though the local stress field may not be accurate, the local and overall specimen deformation is unaffected and the stress-field in the corner is accurate given St. Venant's principle.

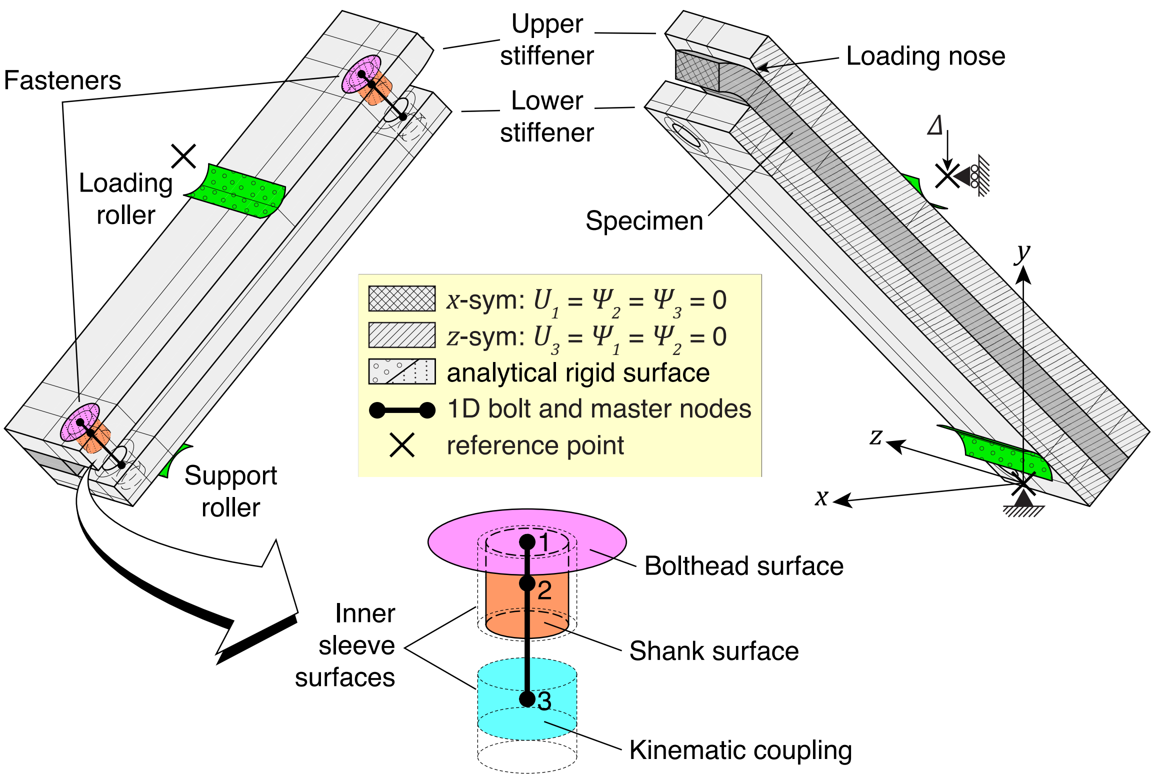

Fig. 3-14. High-fidelity 3D FE model of the sleeve-modified test configuration.

The 2D-sleeve model is validated with a single, high-fidelity, quarter-view, 3D model illustrated in Fig. 3-14, which shares many of the details of the two 3D standard models and the 2D-sleeve model (§§ 3.5.2-3.6.1, resp.). This model is henceforth referred to as the *3D-sleeve* model. The loading rollers are modelled as analytically rigid surfaces tied to reference points and specimen and stiffeners as 3D deformable parts with solid homogenous sections. The aim of the study is not to model the particular experimental fixture and its overly-long rollers, which are expected to deflect for the sleeve-modified test configuration as they do for the standard configuration (Fig. 3-8). Analytically rigid rollers will adequately model rollers of a more appropriate length. In turn, the same material models (tape and stainless steel 17-4 PH) and surface-surface contact definitions (roller-stiffener and stiffener-specimen) are defined as for the 2D-sleeve model. Next, the same boundary conditions (*encastre*, y-displacement, x-symmetry and z-symmetry) are defined as for the 3D-standard models, except that a displacement (Δ) of 5 mm is instead selected and the z-symmetry is also defined for xy-midplane sections of the stiffeners.

The specimen and stiffeners are discretized with structured meshes consisting of C3D20R quadratic and C3D8I linear incompatible-mode elements, resp. The C3D8I element offers improved performance in bending (no shear locking and reduced volumetric locking) compared to the standard and reduced-integration versions (C3D8 and C3D8R). There still is a trade-off between computational cost and accuracy compared to quadratic elements (C3D20R), which is negligible given the much higher-stiffness and small-deformation of the stiffeners. Meshes are all structured with a bias seeding and maximum element aspect ratio of 3 (0.6 to 0.2 mm seed size) in the specimen corner and upper stiffener loading nose region. The number of T-T elements is 16 and 21 for the custom and ASTM specimens ($N_{TT} = 5$), and 6 for the stiffeners. It should be noted that no local mesh refinement is used under the loading nose given that only the load-displacement data is sought for the validation. The bias seeding is simply aimed at reducing the computational costs. Furthermore, as is previously mentioned, the specimen deformation is unaffected by the local contact pressure concentration given St. Venant's principle.

Finally, the fasteners are modelled as deformable assemblies following 3D-approaches by Kobyé *et al.* [106] and Kim *et al.* [192]. The fasteners are modeled as 1D deformable parts with 9 quadratic beam elements (B32) each. Three nodes are defined, two of which are rigidly tied (fixed in all DOF) to analytically rigid surfaces (bolt-head and bolt shaft), and the third of which is tied in all DOF via kinematic coupling to the stiffener hole surface and represents the engaged, threaded portion of the fastener. Small-sliding contact is defined between the two analytical rigid bolt surfaces and the corresponding stiffener surfaces with the same friction-hard contact behaviour as for the specimen-stiffener contact. This approach is an idealization of the complex geometry and contact of the actual assembly that has nevertheless been shown to be accurate [106]. The models contain a total of 121-316k elements with 312k-1.23M nodes. Finally, the same solver parameters are used as with the other models (§ 3.5.1).

The resultant load-displacement curves for the simplified 2D-sleeve and high-fidelity 3D-sleeve models are presented in Fig. 3-15 for a sleeve-offset (s_{off}) of 2 mm. A load difference of 5.59 and 5.35% is observed for a representative ILTS value of 100 MPa. The 2D response is slightly stiffer than the 3D response owing to the use of rigid wires to model the fasteners as opposed to the deformable nature of the 3D fastener assembly. In addition, the specimen and stiffeners are free to deform in the *z*-direction in the 3D model, whereas their deformation is constrained to the *xy*-plane in the 2D plane-strain model. Nevertheless, the agreement between the two model solutions is deemed to be satisfactory given the complexity of the 3D model—unlike the standard, no-sleeve case. Further detail can be added in future iterations of the 2D-sleeve model to improve its accuracy such as developing an approach to adequately model the deformation of two superimposed fasteners. The current work requires many simulations to investigate the effect of sleeve-offset for the two specimen cases, to which end a high-fidelity 3D model is impractical given computer limitations and correspondingly long run times.

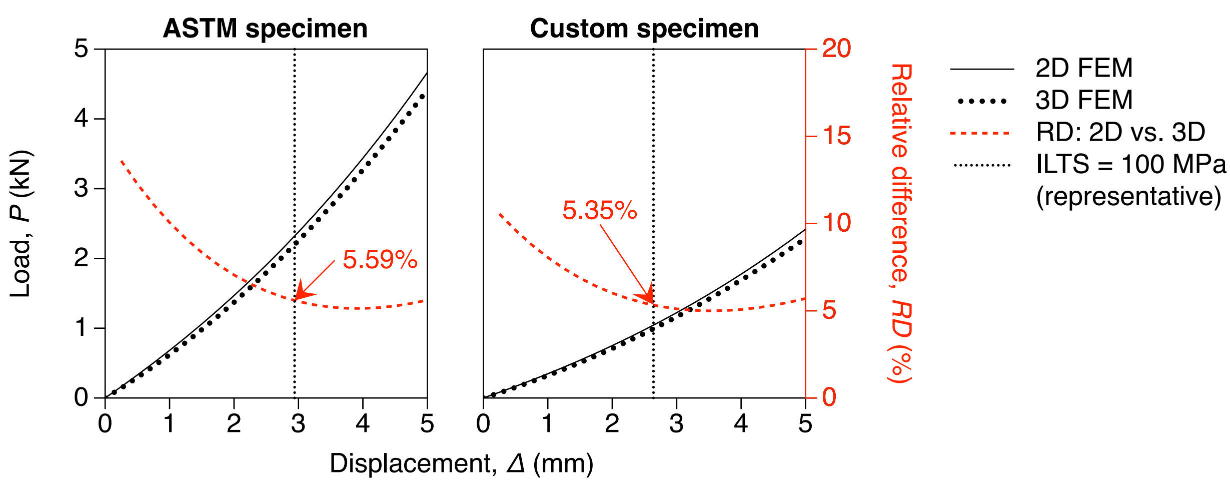

Fig. 3-15. Load-displacement validation of the simplified 2D-sleeve model (2 mm sleeve-offset).

3.6.3 Results and discussion

The use of stiffening-sleeves allows for significantly smaller failure loads and displacements (Fig. 3-15) than the standard test configuration allows without sleeves (Fig. 3-8). In addition, by constraining the specimen deformation to the corner and eliminating flange flexure, the smaller custom specimen fails at a lower displacement than the larger ASTM specimen (2.64 and 2.95 mm, resp.). The lower load-displacement failure point translates into much lower energy-to-failure (the area under the load-displacement curve) as the flanges cease to store spring energy in flexure. Significantly less failure-induced damage (mostly delamination) is therefore expected in the corner region, which has the benefit of possibly isolating the initial delamination and simplifying any subsequent fractography work.

The predicted specimen deformation and stress contour plots for the custom specimen case are presented in Fig. 3-16 for sleeve-offsets of 0, 2 and 10 mm. The sharp contact pressure gradient under the loading nose results in very localized compressive stress concentrations in- and out-of-plane (S11 and S22) as well as an interlaminar shear stress concentration (S12), the worst-case scenario being a sleeve-offset of 0 mm. The exact magnitudes of the stresses under the loading nose must again be taken with a grain of salt. The stress contours are otherwise accurate away from this very localized region and demonstrate that the stress-state in the corner is free of shear-stresses and unaffected by the stress concentration, notably as the sleeve-offset distance is increased to 2 mm. Beyond the visual evidence of the data, it is difficult to ascertain with absolute certainty whether the presence of the stress concentration will affect the onset of delamination in the corner. This aspect of the validation is explored experimentally in the next section.

The estimated errors (between FE-predictions and the modified data reduction) for the corrected inner radius, and the CBS and ILTS are presented in Fig. 3-17 for the ASTM and custom specimens and sleeve-offsets of 0:2:10 mm. First, the radius correction is off by less than 2.7% for a sleeve-offset of 2 mm or less. The error increases as more of the flanges are exposed and free to flex, which reduces the degree of corner opening. Second, the CBS error is reduced by more than tenfold from 5.50 to 0.158% and 6.80 to 0.608% for the ASTM and custom specimens, resp. In turn, the ILTS error is reduced by more than fivefold from 9.71 to 1.85% and 10.7 to 1.37%, resp. It should be noted that the errors will increase or decrease slightly for higher or lower ILTS values. That being the case, the errors increase much more slowly as a function of displacement than for the standard 2D-case (Fig. 3-11).

The magnitudes of the estimated errors for the 2D-sleeve model are not exact as the load-displacement curves are not perfectly smooth, which is due to the high degree of non-linearity of the problem and the complex contact between the stiffeners and sleeves. Nevertheless, it can be stated with confidence that the CBS and ILTS errors should be below 1% for sleeve-offsets up to 10 mm and 2% for the sleeve-offsets up to 4 mm, resp., for the UD-tape material used in this study (ILTS ≈ 100 MPa). The estimated CBS and ILTS errors are presented in Fig. 3-18 as functions of the sleeve-offset distance for both specimens. The zone of interest is highlighted, within which the errors are minimized while allowing for a reasonable offset distance between the loading nose stress concentration and the stress-state in the corner region.

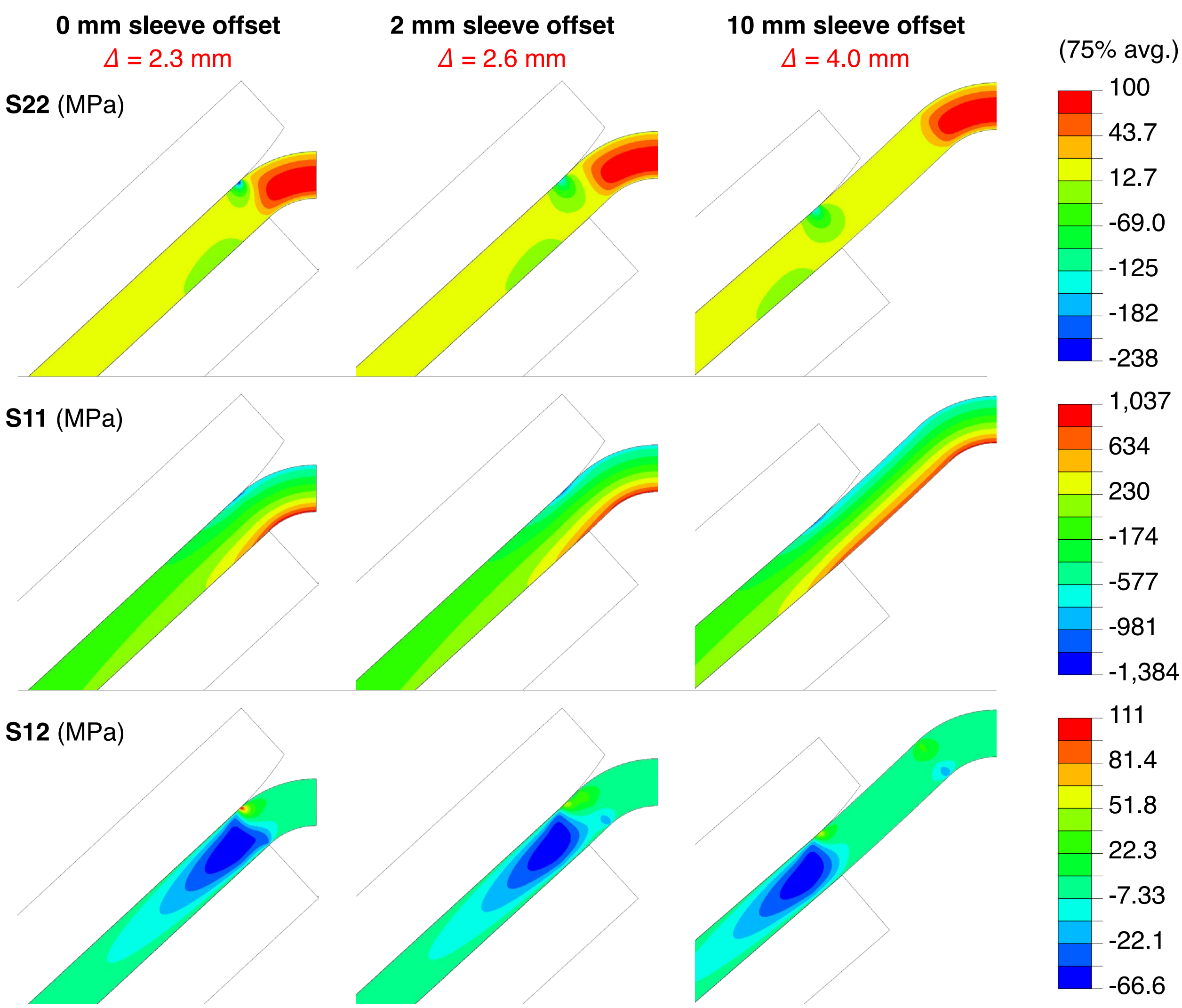

Fig. 3-16. Predicted specimen deformation and stress contour plots for the sleeve modification.

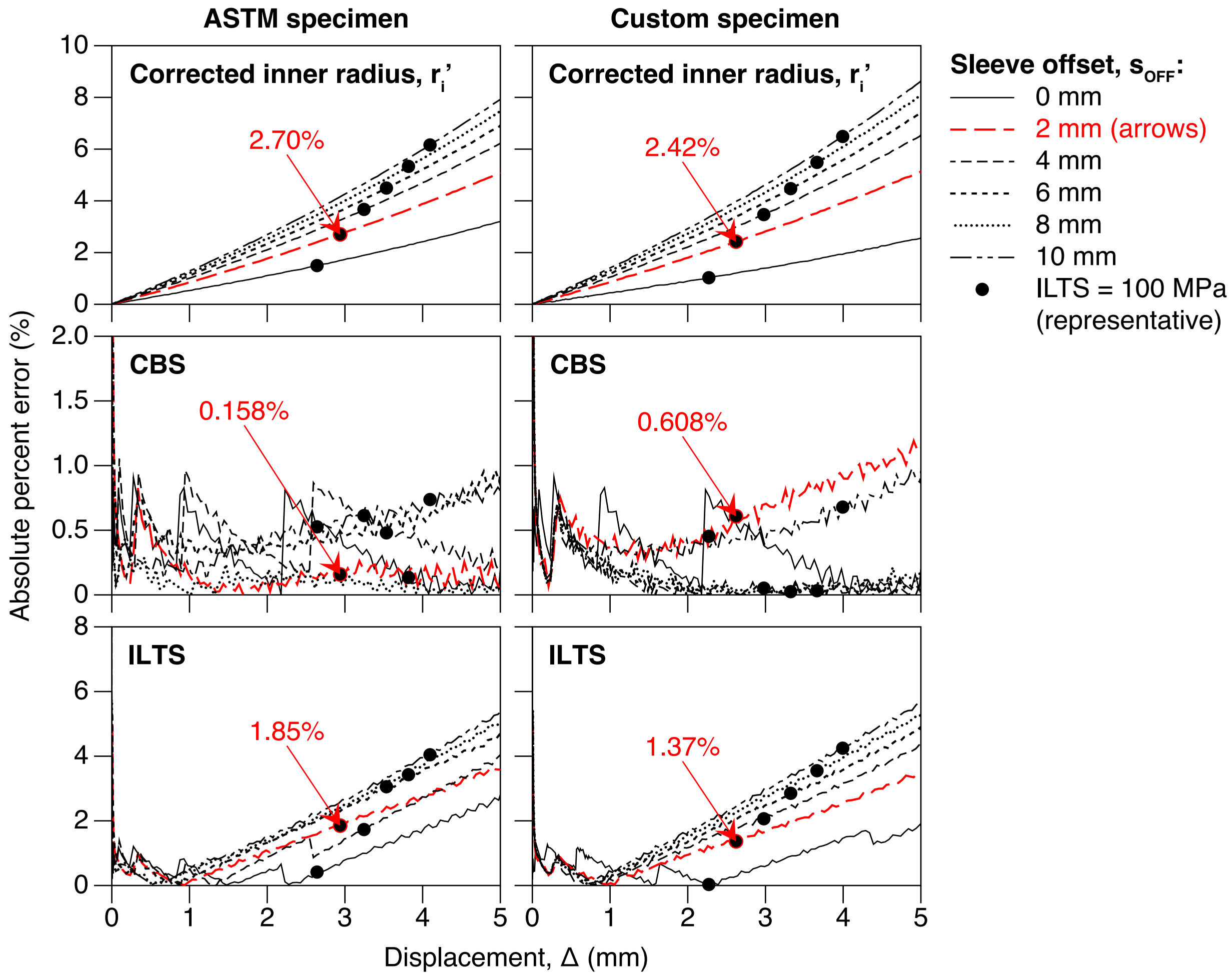

Fig. 3-17. Estimation of the inner radius correction, CBS and ILTS errors for the sleeve modification.

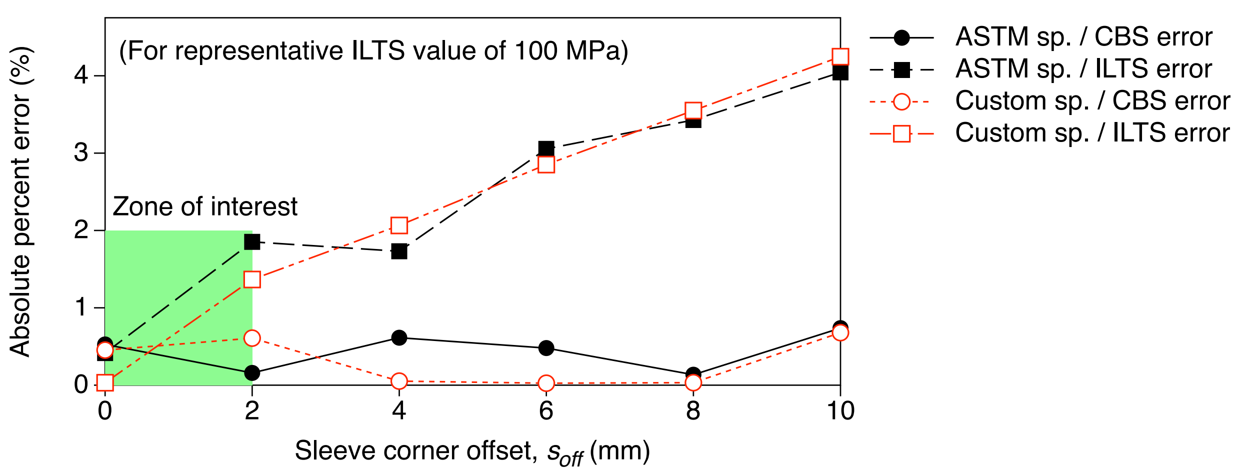

Fig. 3-18. Sleeve-offset effect on the estimated CBS and ILTS errors.

3.7 Experimental validation

3.7.1 Mechanical testing preparation

A series of mechanical tests are performed to: 1) compare experimental results obtained with and without the proposed stiffening-sleeve and data reduction modifications to the ASTM D6415 test standard; and 2) ensure that the presence of a stress concentration under the loading nose of the upper stiffener does not adversely influence the onset of failure in the corner region. Ten UD-tape specimens are prepared from a single corner beam using the custom specimen geometry and following the methodology and baseline process cycle presented in §§ 2.2-2.3. The specimens have the following mean dimensions as determined via the corner thickness profiling method: a width of 20.7 ± 0.233 mm, a flange thickness of 3.32 ± 0.0346 mm, an inner corner radius of 4.44 ± 0.0878 mm, percent corner thickening of 2.76 ± 0.889% (below the 5% limit prescribed by the test standard) and a corner angle of 89.1 ± 0.0210°. Half of the specimens are tested without sleeves via the standard test configuration and data reduction (§ 1.4.3), and the other half is tested with stiffening-sleeves and analyzed via the modified data reduction (§ 3.3.2). A sleeve-offset of 1.0 ± 0.5 mm is used in all cases, which is representative of the preferred range from 0-2 mm discussed in § 3.6.3.

3.7.2 SEM sample preparation

The stress concentration underneath the loading nose contact-patch should not influence the far-field stress state in the corner region, as evidenced in Fig. 3-16. Were this stress concentration to adversely influence the onset of delamination failure in the corner region, evidence of damage initiation in and progression from this critical region is to be expected, namely matrix yielding and T-T matrix micro-cracking at and near the specimen surface, as illustrated in Fig. 3-19. A straightforward failure analysis is therefore conducted on each failed specimen tested with the aid of stiffening-sleeves to find evidence of damage. To this end, one frontal and one sagittal cross-section are prepared per specimen to be viewed and imaged via field-emission scanning electron microscopy (FE-SEM), which offers higher-resolution and improved image quality for applications requiring lower accelerating voltages (< 5 kV) compared to regular SEM.

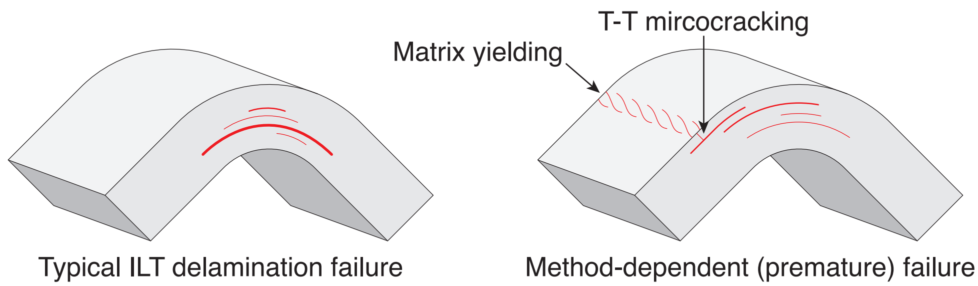

Fig. 3-19. Expected corner specimen failure types for the sleeve-modified test configuration.

Sections are dissected via a lab-scale, low-speed circular saw equipped with a composite-specific, diamond wafer-blade that is water-cooled (Electron Microscopy Sciences Model 650). The bulk cross-sectional surfaces are then manually polished in four steps, similar to the preparation of optical microscopy specimens (§ 2.5.2): fine plane-grinding with a silicon-carbide abrasive (~5 µm), fine polishing with 3 and 1 µm diamond suspensions, and lastly final polishing with a 0.05 µm de-agglomerated alumina water-based suspension. Next, a Hitachi IM-3000 Flat Ion Milling system is used to perform ion beam milling with the following parameters: angle of incidence with the surface of 58°; accelerating voltage of 3 kV; a beam current of 100 mA; and a milling time of 15 min. This process smooths the surfaces, removes polishing debris, and slightly etches the epoxy matrix to render the carbon fibres more visible after coating. The aforementioned steps represent the first part of a method developed by Brodusch *et al.* to efficiently prepare hard polymer composite cross-sections for high-resolution FE-SEM imaging [193]. Finally, the surfaces are coated with a 2-2.5 nm-thick chromium sputter coating (Electron Microscopy Sciences 150R ES sputter coater/carbon evaporator), which yields a uniform surface deposition, improves electrical conductivity over the surface being imaged and removes electron charging issues.

Once prepared, specimen sections are mounted on dedicated sample holders, as illustrated in Fig. 3-20. Silver paint and paste are applied at key locations to improve electrical conductivity between the prepared surface and the metal holder. The sections are viewed and imaged with an ultra-high-resolution FE-SEM (Hitachi SU 8230) using the following parameters: accelerating voltage of 1.0 kV; working distances of 15 and 10 mm for frontal and sagittal cross-sections, resp.; an emission current of 21.5 µA; and a chamber vacuum of 1×10^{-4} Pa. The microscope is setup in secondary electron detection mode using an in-chamber Everhart-Thornley-type detector to collect topographical information from inelastically-scattered electrons (independent of material). Reference works by Sawyer *et al.* [194] and Greenhalgh [179] may be consulted to gain a fuller understanding of SEM methods and their application to the failure analysis of advanced composite materials, resp.

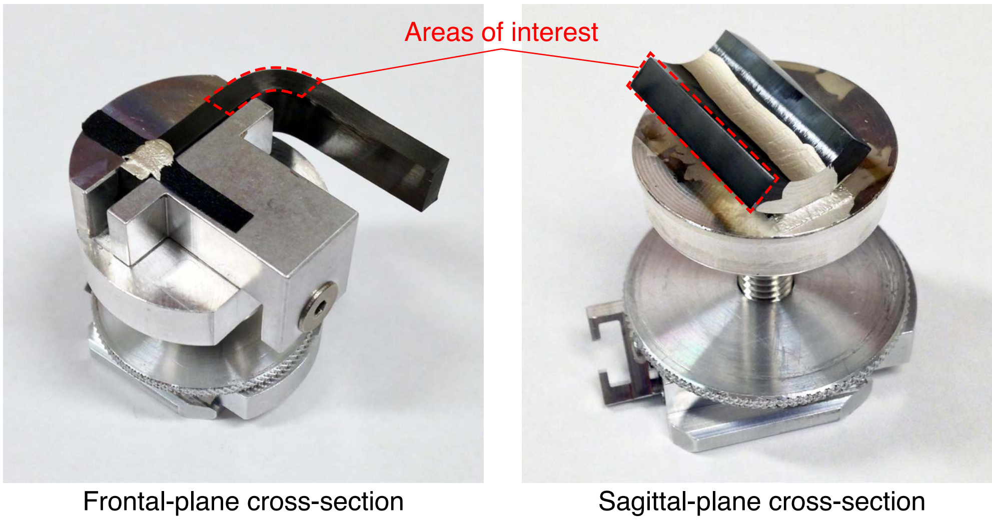

Fig. 3-20. SEM sample holder setups for failed corner specimen sections.

3.7.3 Results and discussion

The results of the curved beam strength tests with and without the aid of stiffening-sleeves are presented in Fig. 3-21. Specimens tested with sleeves fail at half of the load and less than half of the displacement of the specimens tested without sleeves. These results are expected and are owed to the specimen deformation being constrained to the corner region. The no-sleeve tests yield a displacement-to-failure of 9.61 ± 0.586 mm. A significant error in the experimentally-determined CBS and ILTS values is therefore expected that approaches 10 and 15%, resp. In contrast, the sleeve specimens fail at a mean displacement of 4.53 ± 0.448 mm, which should result in a CBS and ILTS errors equal to or less than 1 and 3%, resp. The CBS values are relatively similar in both cases, though the data scatter is comparatively large. The ILTS values however are significantly different, with the no-sleeve tests yielding a mean strength value that is more that 14% greater than the sleeve tests—a likely overestimation. A side-benefit of the lower failure load-displacement point is a halving of the time needed to test a single specimen.

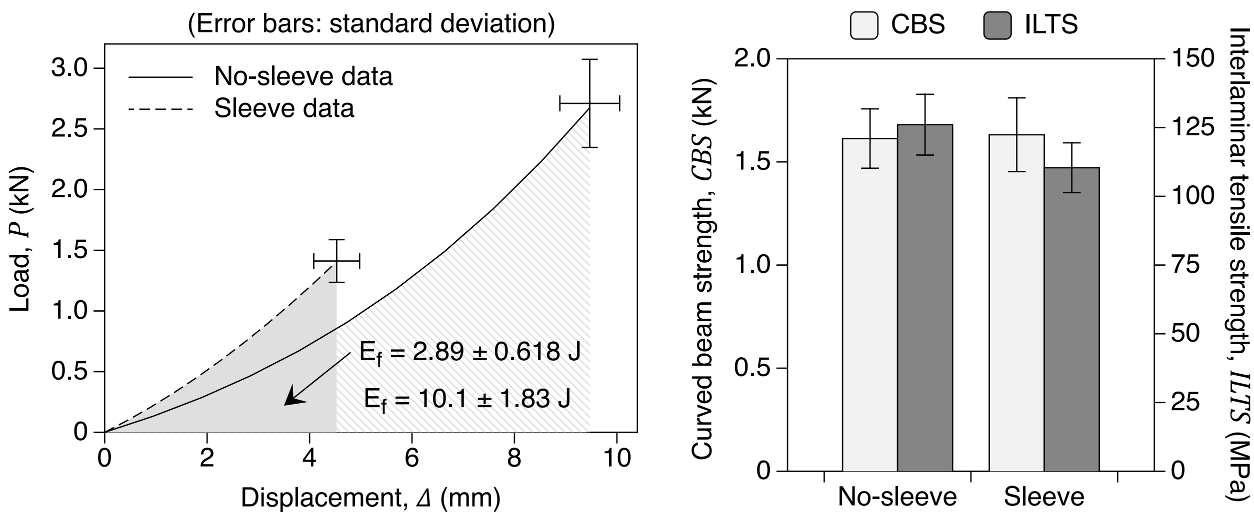

Fig. 3-21. Sleeve and no-sleeve curved beam strength test results for UD-tape corner specimens.

Care must be taken in associating the FEM-estimated errors to the actual experimental results as the 2D FE models overestimate the experimental load-displacement curves. The discrepancy owes to the use of the simplified 2D plane-strain approach, the modelling of loading rollers as analytically rigid wires that do not capture the actual roller deflection, and the presence of significant fibre waviness in the corner region (Fig. 4-9), which degrades the elastic properties used in the models (procured from flat laminates). Still, the amount of error reduction should be relatively proportional (10x and 5x for CBS and ILTS measurements, resp.). More work remains to be done to directly predict the error of experimentally-determined values via higher-fidelity 3D models that more fully address the aforementioned shortcomings of the current 2D models.

In turn, the resulting energy-to-failure (area under the load-displacement curve) of the sleeve tests is less than a third of that of the no-sleeve tests. The typical extent of failure-induced damage in representative corners tested with and without sleeves is illustrated in Fig. 3-22 in the form of two corner cross-sectional micrographs taken in the sagittal plane (refer to § 2.5.2). The extent of visible matrix macro-cracking and branching is much more severe in the no-sleeve case owing to the much larger release of elastic energy stored in the flanges during the loading phase compared to the much smaller amount of elastic energy stored in the corner region. The limited extent of damage is beneficial for failure analysis such as that performed by Seon *et al.* via micro-CT scanning to observe whether delamination cracks in failed specimens intersect pre-visualized critical voids in the region of highest radial stress that are selected as candidates for delamination crack initiation [94]. Lastly, two representative failed specimens presented in Fig. 3-22 illustrate the significantly larger plastic deformation observed in specimens tested without sleeves compared to with sleeves. The sleeve modification allows for the specimen to fail while the in-plane behaviour remains mostly elastic.

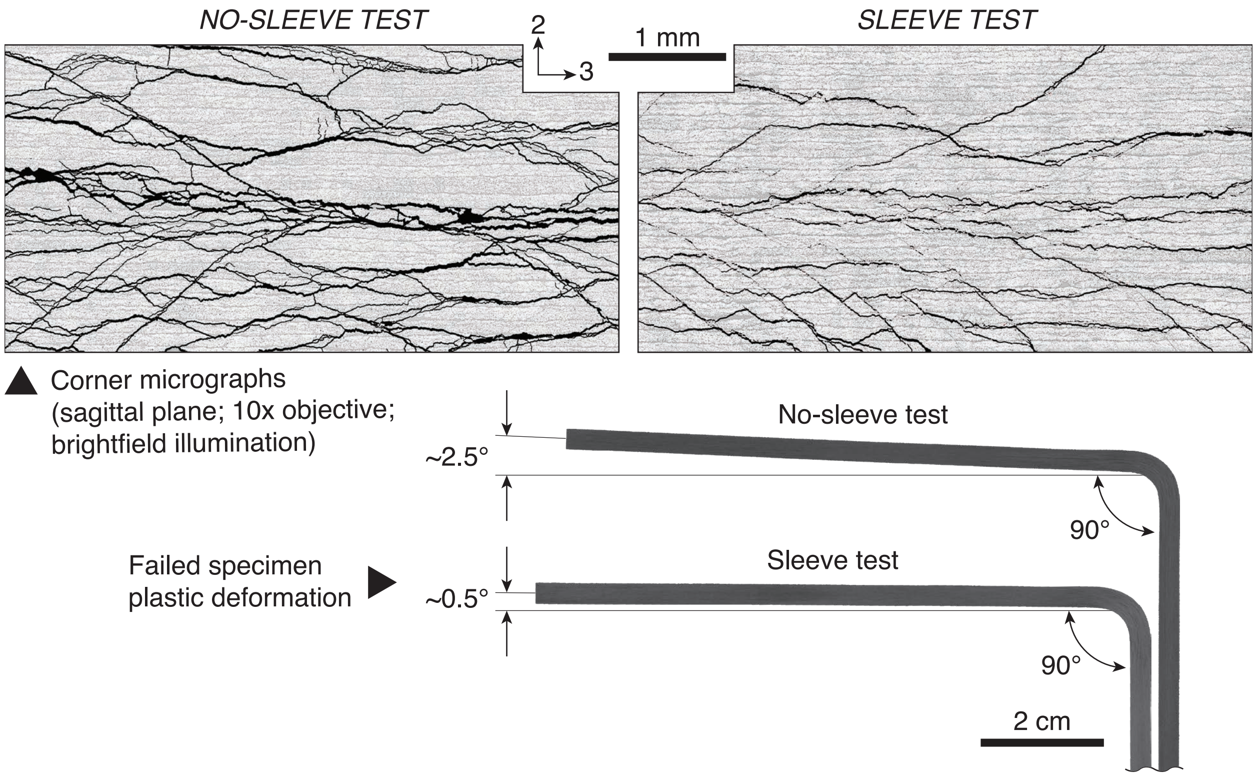

Fig. 3-22. Extent of corner specimen deformation and failure-induced damage.

Finally, no evidence of damage is found on the top specimen surfaces where the loading nose made contact. The failure analysis thus proceeds directly to the FE-SEM imaging of the frontal and sagittal cross-sections intersecting the critical zone of stress concentration, which are presented in Fig. 3-23 for one of the five specimens tested with sleeves. It should be noted that all five specimens were dissected and analyzed. Delamination cracks are observed in the frontal cross-section with a somewhat higher concentration in the area of highest radial stress (roughly a third of the radial thickness from the inner surface). Evidence of ribbon formation is found inside of the cracks, which suggests a mode I or mixed-mode I/II crack growth [33]. However, the mode(s) of crack-growth cannot be readily determined without resorting to opening the crack surfaces and peering directly onto them, which is difficult given the out-of-plane nature of the crack network as seen in the sagittal view and the presence of fibre-bridging. In addition, interpretation of fractographic features is further complicated in the case of toughened resins, as is the case herein, which exhibit more highly deformed matrix regions [33]. The limited evidence suggests that cracks initiate in the corner region and propagate outward as expected. No evidence of damage is found in the critical stress concentration zone of the frontal cross-section.

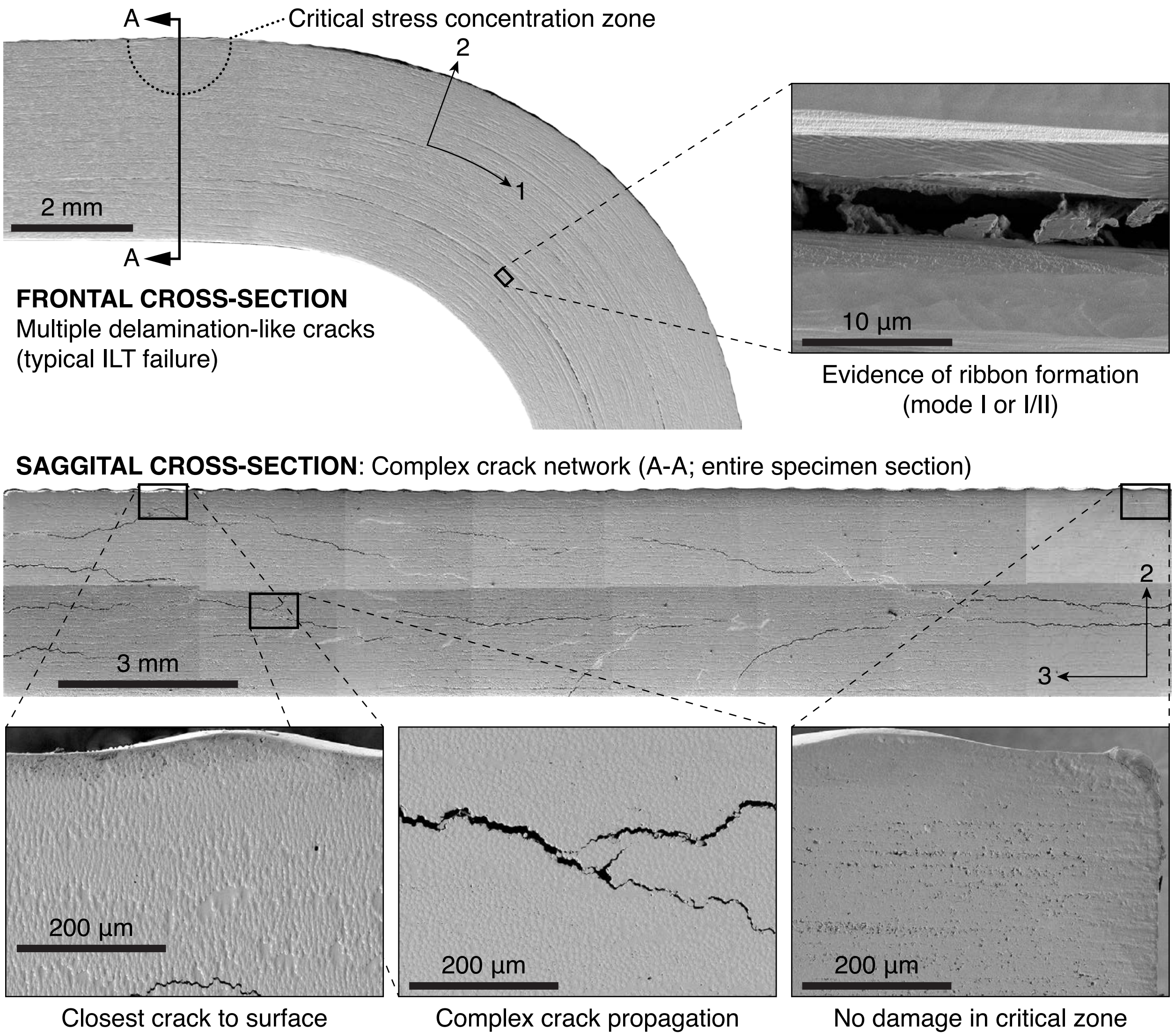

Fig. 3-23. FE-SEM imaging of a typical failed corner specimen tested with the aid of stiffening-sleeves.

Sagittal sections are better candidates to observe matrix micro-cracking due to the high in-plane and T-T compressive stresses under the loading roller. The upper specimen edge is the most susceptible location for damage, as is illustrated Fig. 3-2, where the contact-patch is seen to be widest at the specimen edges and not the centre of the contact area ("bowtie" shape). Again, no evidence of damage can be found in this critical zone or over the entirety of the contact surface edge for any of the five specimens tested with sleeves. The presence of the loading roller instead appears to constrain the direction of the crack growth. Some cracks can be seen extending towards the bottom specimen surface and visible surface damage is observed for some specimens; however, no crack is found to come closer than roughly 0.4 mm to the upper surface, and in all cases, the crack tip diverts back towards the center of the specimen. The stress state in the actual specimen is evidently more complex than the 3D FE simulation lets on. It can nonetheless be stated with a reasonable degree of confidence that the stress concentration under the loading nose does not introduce damage into the current specimen configuration (selected geometry, material and layup), and thus does not affect the onset and mode of failure in the corner region.

3.8 Summary

This chapter presents a direct, practical and cost-effective modification to the ASTM D6415 test standard for determining the CBS and ILTS of polymer matrix composites. The standard corner specimen and 4PB-CBS test configuration constitute a test method that is representative of curved details in structural parts and that is economical and practical to implement. That being the case, a significant error surfaces in the experimentally-determined CBS and ILTS values in the case of laminates of intermediary stiffness, high toughness and thinner cross-section due to excessive flange flexure and opening of the corner region. To this end, a novel stiffening-sleeve design is proposed that is mechanically-fastened. This solution effectively eliminates flange flexure and enables a simple correction of the corner region radius, which, in turn, drastically lowers the error in the CBS and ILTS determination. Finally, a key feature of the stiffening-sleeve design is the ability to precisely offset the sleeve from the corner region.

The initial magnitude of the CBS and ILTS errors for the standard test method is estimated via a simplified 2D plane-strain FE modelling approach that is validated with a high-fidelity FE model and follows the approach presented by multiple studies published on the mechanical testing and modelling of corner specimens. A detailed mesh-sensitivity analysis is also conducted to ensure proper convergence of the 2D-model. Based on the modelling results, the distance-to-failure of the UD-tape corner specimens used in this thesis is expected to exceed the standard's 5-

mm threshold, beyond which the error is stated to become significant. The magnitude of the errors is estimated to be roughly 7 and 11% for the CBS and ILTS, resp.

In turn, a similar approach is undertaken to estimate the CBS and ILTS error reductions associated with the use of stiffening-sleeves and the modified data reduction, which includes the corner radius correction. The simplified 2D plane-strain model is adapted to include stiffeners and validated with a detailed mesh-sensitivity analysis and high-fidelity 3D model. In addition, the effect of the sleeve-offset distance on the magnitude of the error is investigated to determine the sleeve-offset range that maintains an acceptably-low degree of error. Based on the modelling results, significant error reductions of tenfold and fivefold can be expected for the CBS and ILTS determination for a sleeve offset of 2 mm or less (CBS and ILTS errors of < 1 and < 2%, resp.).

Finally, the results of the modelling work are corroborated by mechanical testing and a failure analysis of failed specimens. As expected, specimens tested with sleeves fail in half of the test time of specimens tested without sleeves and with much lower load-displacement failure points and energy-to-failure. In turn, an FE-SEM investigation of frontal and sagittal corner cross-sections of failed specimens finds that the stiffener-sleeve contact under the loading nose does not introduce damage in the vicinity of the corner region despite there being a highly-local stress concentration in this region. No evidence can be found that suggests that the use of stiffening-sleeves adversely affects the onset and mode of failure in the corner region. The development and investigation of stiffening-sleeves was presented for review to the ASTM committee on interlaminar properties [195], which considers modifications to existing standards.

4

Laminate quality in corners: variability and defects

4.1 Introduction

The material and shape are created simultaneously when manufacturing a PMC part notably in the case of thermosetting resins. The laminate quality is thus dually affected by processing parameters and part design. This chapter focuses on the effect that processing and design factors of interest have on laminate quality in corners. The effects of variability and defects on mechanical performance in corners are investigated in the next chapter.

The processing cycle established in § 2.2.2 is a combination of temperature ramps and isotherms, and the application of constant vacuum pressure. The purpose of this cycle is to consolidate and cure laminates to a near-optimal laminate quality, i.e. practically defect-free. It is henceforth referred to as the *baseline* processing cycle. The vacuum-bag pressure is drastically reduced during the RT-hold by pulling vacuum through the corner beam tool. The ensuing pressure differential between the ambient and bag pressures generates a consolidation pressure that acts to consolidate the laminate by first allowing fibres to nest and plies to locally slip—if possible. The vacuum pressure is maintained during the cure as the warming resin begins to flow and fully impregnate dry-fibre regions prior to gelation. A high consolidation pressure typically results in a likewise high hydrostatic resin pressure, which in turn collapses voids that contain a mixture of remaining air, water vapors and resin volatiles. The initial temperature ramp of the cure cycle is therefore critical in achieving full impregnation prior to gelation, and the consolidation pressure is critical in collapsing voids during the resin-flow phase of the cure. A review of the VBO semipreg processing by Centea *et al.* can be consulted for a more detailed explanation of the key consolidation mechanisms involved in VBO processing [49].

Ensuring near-optimal processing of parts is challenging in an industrial setting, notably in the case of complex-shape and large-scale parts (integrated structures). A number of factors may degrade laminate quality, which can generally be categorized as follows: 1) design factors, 2) generally deficient processing conditions—most notably consolidation pressure, and 3) noteworthy industrial processing cases pertinent to VBO semipreg processing. Centea and Hubert [114, 128] performed several similar experimental studies on VBO flat laminates that partly inspired this work and with some crossover in the selection of test conditions and materials. In addition, the following work builds on a preliminary study by Krumenacker and Hubert performed on VBO convex corners [99] and a study by Ma *et al.* performed on convex and concave corner laminates of varying angle, radius and thickness [121], which was limited to two harness-satin woven reinforcement architectures. As an aside, the later study furthermore investigated strategies to reduce corner thickening and void content in concave corners via intermediary debulking during the layup and the use of pressure intensifier strips.

A near-optimal, baseline processing cycle and near-flawless experimental or industrial processing setup—though indispensable—do not alone guarantee a defect-free part. Part design plays an influential role: an improper design can yield low-quality parts even in the case of ideal processing conditions. The three factors of interest here are material selection (i.e. tape, PW and 8HS), tool-shape (i.e. convex or concave), and stacking sequence (i.e. UD, QI and XP). As described in § 1.5.3, sharply-curved features create significant pressure gradients within the laminate and complex interply forces during the RT-hold and cure cycle [121, 130, 137], whether convex or concave, which in most practical cases yield local laminate thickening and can further result in increased void content, decreased fibre content and significant fibre waviness—investigated in the next chapter. Meanwhile, stacking sequence may play a related role that affects interply friction, ply bridging and shearing, and fibre and ply nesting, all of which are mechanisms that affect quality within and in the vicinity of sharply-curved features [130, 131].

In turn, generally deficient processing conditions are deviations from the baseline (near-optimal) processing cycle. These are classified as "general", because they affect any part regardless of scale or complexity—albeit to different degrees: larger parts and more complex geometries will further exacerbate the adverse effects of general process deviations. With regards first to the temperature and time parameters, undesirable thermal gradients and temperature peaks may arise within the laminate during the cure due to poor tool design, an inadequate selection of vacuum-bagging consumables, and well as variable or excessive laminate thickness [43]. However, investigating these effects in corner regions is beyond the research scope given limited experimental resources (single processing tool and finite semipreg supplies).

With respect to the following experimental work, the aim is simply to control the temperature and time parameters in order to investigate the remaining processing parameter, consolidation pressure. The selected nominal laminate thickness of approximately 3 mm (§ 2.3.1) is deemed to be thin enough such that thermal gradients are generally controlled during the cure. In addition, a high degree of repeatability in part temperature curves is achieved irrespective of material and tool-side (i.e. convex or concave) on account of the combination of the particular mechanical convection oven and PID controller utilized, the corner beam tool design and the established cure and post-cure cycles (Fig. 2-2).

In contrast, consolidation pressure is affected by multiple factors that cannot be so readily controlled—if at all. The key factors are as follows: the operator's ability to create a leak-free bag, the quality of the bagging consumables and their performance at elevated cure temperatures, the airtightness of vacuum-fittings and hoses, the power of the vacuum pump, and fluctuations in the ambient air pressure in the oven. All but the last factor can be addressed to a degree: the bagging and air evacuation processes increase in complexity as part-scale and shape-complexity increase, which increases the prevalence of process deficiencies. Meanwhile, ambient air pressure fluctuations can only be controlled in the case of internal building factors (e.g. HVAC systems), whereas the lower pressures associated with higher elevation and weather cannot generally be managed. The high-cost of operating in an air tight and highly controlled environment would negate the economic benefits of utilizing the VBO semipreg processing route in the first place. As described in § 1.5.3, a lower consolidation pressure will adversely affect laminate quality by impeding laminate consolidation, air evacuation and void collapse during cure [114, 118, 119].

Lastly, the aerospace industry works on larger and more complex parts than those that are normally produced for academic research. As such, certain processing cases are common only to industry and have arisen from the nature of the industrial parts being manufactured and the need to compromise between quality and productivity. Three noteworthy industrial cases are herein selected that are particularly pertinent to VBO semipreg processing.

First, air evacuation may be restricted due to any number of the following occurrences: the use of a dull blade for ply cutting, which can close-off vital air evacuation channels—most notably dry tow-cores; improper intermediary debulking during layup, which may collapse vital dry-fibre channels and impede air evacuation during the RT-hold; improper edge-breathing, i.e. dry GFRP tape fails to connect the laminate edge to the breather; insufficient RT-hold duration, which is especially important for effective distances in the decimeter range and larger; and problematic design features, e.g. large effective air evacuation distances (part center-to-edges), inserts, and sharply-curved features. The presence of air within the laminate during layup becomes permanently entrapped and leads to high void content [114].

Second, large parts with variable thickness can generate problematic thermal gradients and peaks due to an uneven exothermic reaction across the part. Slower temperature ramps may resolve these issues by slowing the rate of reaction. The trade-off is an elevated viscosity profile during the cure, which may impede the impregnation of dry-fibre regions and, in turn, void collapse [128].

Third, large-scale, complex-shape parts require long and complicated layups. One solution to reduce the layup duration is to limit the number and duration of intermediary debulking steps during layup or to dispense with them entirely. Intermediary debulking is useful in the case of complex-shape parts to control corner thickening and wrinkling [121]. No-debulking may therefore have the inverse effect of promoting corner thickening and ply wrinkling. In addition, no-debulking will result in inferior ply collation over concave features and likely promote ply bridging, which in turn may result in higher void content. It should be re-iterated that intermediary debulking may collapse vital air evacuations channels over sharp, convex features, and may thus potentially decrease the local in-plane permeability thereby resulting in increased void content [114].

4.2 Chapter objectives and outline

The objectives of this chapter are twofold: 1) investigate the repeatability of the experiments to assess the dependability of the findings with respect specifically to laminate quality measurements; 2) investigate the effect that design factors (i.e. material selection, tool-shape and stacking sequence), deficient consolidation pressure and noteworthy industrial processing cases have on laminate quality. The desired outcome of this work is to corroborate and add to the laminate quality findings of Centea and Hubert [114] *vis-à-vis* VBO flat laminates and Ma *et al.* [121] *vis-à-vis* select VBO woven corner laminates, and to better understand the robustness of VBO semipreg processing regarding large-scale, complex-shape parts.

The chapter outline is as follows, starting with an overview of the experimental test matrix presented in § 4.3. The study on the repeatability of experiments is then presented in § 4.4, which focuses on laminate quality measurements; the repeatability of interlaminar strength measurements is presented in Chapter 5, which focuses on mechanical performance in corners. Finally, laminate quality results for the experimental test matrix are presented in § 4.5 and divided into the three aforementioned categories of factors.

4.3 Experimental test matrix

The experimental test matrix is summarized in Table 4-1 and consists of a total of 26 test conditions that are combinations of materials, processing parameters and design factors. The methods detailed in Chapter 2 regarding the processing and preparation of corner beam samples and specimens are observed for every sample unless otherwise specified herein. A single sample is manufactured for most test conditions except in the case of the tape and PW baseline processing conditions, in which case five samples are manufactured for the repeatability study presented in the following section (refer to § 2.1 for the definition of *sample*). The baseline processing condition (B) is the standard process cycle outlined for the three selected semipregs in § 2.2.2. The standard process cycle comprises a respective RT-hold for each of the three selected semipregs and common cure and post-cure cycles. Baseline samples (*baselines* for short) are created for each material and mould-type permutation and represent the corresponding near-optimal processing condition, relative to which all other test-conditions are compared. In other words, the baselines are akin to *control* test conditions.

The test matrix includes the following three categories of factors that affect laminate quality: 1) design factors, i.e. material, tool-shape and stacking sequence; 2) deficient consolidation pressures; and 3) noteworthy industrial cases, i.e. restricted air evacuation (R), slow temperature cure ramp during the cure (SR) and no-intermediary debulking during the layup (ND). It should be noted that the test matrix is limited as follows due to the short supply of semipregs: effect of stacking sequence is limited to the convex tool-shape; effect of deficient consolidation pressure is limited to the tape and PW and a UD layup; and investigation of industrial cases is limited to the PW, convex tool-shape and UD layup with the one exception being one 8HS restricted air evacuation sample.

Table 4-1. Experimental test matrix summary.

Layup (ply count)	Tool-shape (M or F)	Processing condition (B, L1, L2, L3, SR, ND and R)	No. of samples	Sample code (§ 2.3.3)
Tape semipreg (T)				
UD (24)	Convex	Baseline	5	Tape-UD-M-B
UD (24)	Convex	10% consolidation pressure loss	1	Tape-UD-M-L1
UD (24)	Convex	20% consolidation pressure loss	1	Tape-UD-M-L2
UD (24)	Convex	30% consolidation pressure loss	1	Tape-UD-M-L3
XP (24)	Convex	Baseline	1	Tape-XP-M-B
QI (24)	Convex	Baseline	1	Tape-QI-M-B
UD (24)	Concave	Baseline	1	Tape-UD-F-B
UD (24)	Concave	10% consolidation pressure loss	1	Tape-UD-F-L1
UD (24)	Concave	20% consolidation pressure loss	1	Tape-UD-F-L2
UD (24)	Concave	30% consolidation pressure loss	1	Tape-UD-F-L3
PW semipreg				
UD (16)	Convex	Baseline	5	PW-UD-M-B
UD (16)	Convex	10% consolidation pressure loss	1	PW-UD-M-L1
UD (16)	Convex	20% consolidation pressure loss	1	PW-UD-M-L2
UD (16)	Convex	30% consolidation pressure loss	1	PW-UD-M-L3
QI (16)	Convex	Baseline	1	PW-QI-M-B
UD (16)	Convex	Slow ramp (0.5 °C/min)	1	PW-UD-M-SR
UD (16)	Convex	Baseline without intermediary debulking	1	PW-UD-M-ND
UD (16)	Convex	Baseline with restricted air evacuation	1	PW-UD-M-R
UD (16)	Concave	Baseline	1	PW-UD-F-B
UD (16)	Concave	10% consolidation pressure loss	1	PW-UD-F-L1
UD (16)	Concave	20% consolidation pressure loss	1	PW-UD-F-L2
UD (16)	Concave	30% consolidation pressure loss	1	PW-UD-F-L3
8HS semipreg				
UD (8)	Convex	Baseline	1	8HS-UD-M-B
QI (8)	Convex	Baseline	1	8HS-QI-M-B
UD (8)	Convex	Baseline with restricted air evacuation	1	8HS-UD-M-R
UD (8)	Concave	Baseline	1	8HS-UD-F-B

The first category of factors is that of design factors, namely the tool-shape and stacking sequence. Two baselines, one convex and one concave, are manufactured for each of the three selected semipregs. All six baselines utilize a UD layup ($[0°]_{ns}$). In turn, a standard QI layup ($[45°/0°/-45°/90°]_{ns}$) is manufactured for all three materials, and an additional XP layup ($[0°/90°]_{ns}$) is manufactured for the tape only—it is assumed that the two selected fabric semipregs behave sufficiently similarly in the warp and fill directions. The QI layup is widely-used in the aerospace industry for complex-shape, primary structural parts such as hat-stiffeners. Lastly, the baseline processing cycle is applied in all cases.

The second category of factors is that of deficient consolidation pressure, which consists of three consolidation pressure levels (CPLs) in addition to the baseline: 90, 80 and 70%, symbolized by L1, L2 and L3, resp. Deficient consolidation pressure combines the effect of vacuum-bag air pressure loss (i.e. leaks and pump effects) and ambient air pressure fluctuations (i.e. weather and altitude effects). The corresponding vacuum-bag depressurization level given a known ambient pressure is attained via an analog vacuum regulator that is in-line with the vacuum-bag air evacuation hose. Centea and Hubert selected a CPL of 77.5% as a reasonable estimate of the lowest pressure that can in practice be expected for VBO processing of flat semipreg laminates, and a CPL of 55% as an extreme case to accentuate the effects of deficient consolidation pressure on laminate quality [114]. The adverse processing conditions in corner regions should further exacerbate pressure-loss effects, which is why higher CPLs are selected in this study. It should be noted that a CPL greater than 100% is possible for baselines in the event that the ambient air pressure surpasses atmospheric pressure at sea-level.

The third and final category of factors is that of noteworthy industrial cases with regards to the industrial processing of large-scale, complex-shape parts. First, the effect of restricted air evacuation (R) is investigated by effectively sealing the air within the laminate. The conventional edge-breather is simply replaced with sealant-tape insuring continuous ply collation with the top and bottom release-films, i.e. no wrinkling. The RT-hold is additionally skipped such that the layup and vacuum-bagging process progresses directly to the cure cycle. Two convex samples are manufactured, one for the PW and one for the 8HS. Second, the effect of slow temperature ramp during the cure (SR) is investigated by manufacturing a single PW sample with a 0.5 °C/min initial temperature ramp, which is estimated to be representative of the lowest acceptable ramp-rate used in industry for VBO processing. Third, the effect of intermediary debulking is investigated by manufacturing a single PW sample without intermediary debulking (ND). All four industrial processing case samples otherwise utilize the baseline processing cycle and consist of the UD layup and the convex tool-shape such as to be comparable to the respective PW and 8HS convex baselines.

4.4 Experimental repeatability study

4.4.1 Motivation and objectives

The *repeatability* and *reproducibility* of experiments, and the *reproducibility of research* are three concepts that are often confused in a similar vein as the interchangeable lay usage of the terms *precision* and *accuracy*. The third concept of reproducible research will not be elaborated on beyond a simple explanation here as it strays from the research scope. The increasing irreproducibility of results presented in published studies and academic reports is a predicament that has for decades plagued the computational sciences among many other research fields [196, 197]. At the core of the concept is the understanding that results only represent one aspect of academic research and are incomplete and difficult to reproduce—if not impossible—without access to the full research environment, e.g. the raw data, experimental notes, computational codes, etc. A general aim across research fields is, therefore, to facilitate access to the tangible aspects of a research environment by notably promulgating the use of *open-source* databases to freely share and access raw experimental data and disseminate computational codes [198]. This approach improves research transparency and provides a return on investment of sorts for what is often publicly-funded research. Reproducible research ultimately speaks to the growing concern over the current and future integrity and efficacy of academic research.

A more practical concern is the *precision* of experimental methods, which combines the *repeatability* and *reproducibility* of results. These measures respectively assess the statistical significance of the variability in results within and between research environments [199, 200]. *Repeatability* is a measure of the probability of repeated (or replicated) experiments yielding statistically significantly different results when conducted under *repeatability conditions*, i.e. identical research environment (same test materials, equipment, operator and laboratory) within a short period of time. In turn, *reproducibility* is a measure of the probability of the same experiment yielding statistically significantly different results when conducted under *reproducibility conditions*, i.e. identical materials in independent research environments (different equipment, operator and laboratory). A probability or confidence level of 95% is typically selected to assess the precision of experimental methods for advanced fibre composites [161]. In turn, the standard deviations within and between sets of experimental results obtained under repeatability and reproducibility conditions are given as respective statistical measures of precision. These statistics are determined from the results of a round robin test program performed between laboratories, i.e. *inter-laboratory study* (ILS), which is standardized in the ASTM E691 test method [199].

With regards specifically to repeatability, it is the experience of the author that a significant portion of peer-reviewed studies in the field of composites engineering reach important conclusions on the sole basis of single or bi-replicate data samples, i.e. observations made on only one or two repeated composite panels. The high cost and extensive resources required to prepare composite panels and specimens often discourage the testing of a greater number of panels and specimens for a particular test condition. This fact is however seldom acknowledged in published studies, though it importantly qualifies the dependability of the findings—or lack thereof.

The following section presents a study that investigates the repeatability of experiments presented later in this chapter and the next. Establishing the reproducibility of the experiments—though important—is beyond the research scope. This study aims to answer the following two questions: 1) Do samples for a given test condition and measurement type belong to a single population? In other words, do sample means under repeatability conditions tend to statistically significantly differ? And 2), what is the associated inter- and intra-sample variability? In other words, how do samples differ in practicality.

With regards to the experimental work presented in this thesis, only one sample per test condition can generally be tested given the small quantities of available semipregs. That being the case, five-sample sets are manufactured and tested under repeatability conditions for the tape and PW convex baselines (Cytec CYCOM® 5320, § 2.2.1) in order to investigate the repeatability of the experiments for at least one test condition. The same statistical analysis is then performed on publicly-available tape and PW datasets that utilize a similar OOA resin system (Cytec CYCOM® 5320-1 [162]) and a representative autoclave system (Hexcel Hexply® 8552 [68]). A *dataset* is defined for the purposes of this study as the set of samples of a given material for single measurement type (e.g. laminate thickness measurements for the 5320/tape). The variability observed for the experimental work can thus be placed in the context of similar and more conventional VBO and autoclave laminates, resp. The convex baselines variability may be further associated to the likely variability of single-sample test conditions given the shared research environment in which samples are prepared and tested in this work.

Lastly, it should be noted that many peer-reviewed studies that conduct inferential tests contain significant statistical errors. For instance, 15% of neuroscience studies [201] and 20% of psychology studies [202] recently published in high-impact factor scientific journals were found to make errors in reporting and interpreting statistical results that would likely change the corresponding findings. Fields of clinical study are generally developers, early adopters and extensive users of the kinds of statistical tools under consideration in this study. A study that analyzes the prevalence of statistical errors in material science and engineering could not be found, though a similarly significant portion of composites engineering studies that perform similar statistical analyses ought to likewise be affected. Great care is thus taken herein to avoid known statistical errors by utilizing appropriate statistical tests to analyze datasets and by correctly reporting and interpreting the results.

4.4.2 Data selection

As previously stated, three resin systems and two reinforcement architectures (tape and PW) are selected for this study, for a total of six composite materials. The key aspects of the selected materials are presented in Table 4-2. Experimental data for the Cytec CYCOM® 5320 resin system (5320 for short) is obtained directly from work performed by the author. Meanwhile, experimental data for the two other selected systems, Cytec CYCOM® 5320-1 and Hexcel HexPly® 8552 (5320-1 and 8552 for short, resp.) is obtained from the National Center for Advanced Materials Performance (NCAMP). NCAMP is a joint initiative between the National Institute for Aviation Research (NIAR), Wichita University and the US Federal Aviation Agency (FAA) that is aimed at speeding-up material qualification for civil aerospace and populate a publicly-accessible material database [76]. The NCAMP database is comprised of Process Specification Reports that present the processing route for each resin system, Material Data Property Reports (MDPR) that summarize the results of mechanical testing programs for a given composite material, and Statistical Analysis Reports (SAR) that present the corresponding statistically-determined material properties, namely the B-basis design allowables (95% probability of a value being within the 10th percentile of the population).

Table 4-2. Materials and dataset sizes for the repeatability analysis of laminate quality measurements.

	5320/tape	5320/PW	5320-1/tape	5320-1/PW	8552/tape	8552/PW
Resin system	Cytec CYCOM® 5320 [170]		Cytec CYCOM® 5320-1 [162]		Hexcel HexPly® 8552 [68]	
Carbon fibre	Thornel® T650/35 [171]		Thornel® T650/35 [171]		HexTow® AS4 [203]	
Tow count	6k	3k	6k	3k	n/a	3k
Process	VBO (§ 2.2)		VBO [204]		Autoclave [205]	
Condition	Baseline / optimal		Baseline / optimal		Baseline / optimal	
Geometry	Convex corner beam (§ 2.3.1)		SBS flat panel		SBS flat panel	
(Dataset)	*(No. of panels × No. of observations = total No. of observations)*					
Thickness	5 x 10 = 50 (ea.)		6 x 30 = 180 (ea.)		6 x 30 = 180 (ea.)	
Fibre content	5 x 5 = 25 (ea.)		6 x 3 = 18 (ea.)		6 x 3 = 18 (ea.)	
Void content	5 x 5 = 25 (ea.)		6 x 3 = 18 (ea.)		6 x 3 = 18 (ea.)	
Data source:	Current work		[163]	[164]	[165]	[166]

In turn, three laminate quality measurements are selected for each of the six materials: laminate thickness, and percent fibre and void contents. Variability in mechanical properties is also considered but will be investigated as part of the next chapter on interlaminar mechanical performance. It should be noted that the NCAMP MDPRs contain limited laminate quality data as it is not directly pertinent to the aim of these reports, which is to present datasets for the calculation of design allowables. NIAR was contacted directly for supplemental data. In addition, the void content utilized in this study is global; no distinctions are made between void species. The dataset sizes for each measurement are given in Table 4-2, and the associated test methods employed in this work and by NIAR, in the case of the NCAMP datasets, are summarized in Table 4-3.

The 5320-1 resin system is selected on account that it is very similar to the 5320 system—both systems are toughened epoxy resins formulated specifically for VBO structural applications. In turn, the 8552 resin-system is selected as a representative autoclave system given its widespread use in the aerospace industry. By comparing the inter- and intra-sample variability statistics for a given measurement, the repeatability of the experimental work insofar as the 5320/tape and 5320/PW baselines are concerned can be generally compared to the repeatability of similar VBO semipreg and conventional autoclave prepreg laminates tested under similar, repeated conditions. In addition, the test data obtained from the NCAMP database was generated by NIAR, which observes strict testing and reporting norms required for commercial material qualification. The adequacy of the research environment for this work can thus be indirectly compared to that of an expertly controlled environment.

Table 4-3. Laminate quality measurements and associated test methods.

Source	Measurement	Method	Reference
Current work: 5320-system [170]	Thickness*	Corner thickness profiling method	§ 2.4
	Fibre content* Void content*	Optical microscopy image analysis	§ 2.5
NCAMP datasets: 5320-1 and 8552 systems [68, 162]	Thickness**	Direct measurements	ASTM D2344 [206]
	Fibre content**	Matrix digestion (Method I)	ASTM D3171 [207]
	Void content**	Density comparison via ignition loss	ASTM D2734 [208]

*Measurements made on same 5 corner beams and **6 SBS flat panels for each respective material.

A number of additional clarifications are necessary to fully explain the nature of the selected datasets. First, the NCAMP datasets are comprised of sample pairs from three different material batches, which adds an additional level of variability. Nevertheless, inter-batch variability is assumed to be very small compared to inter-sample variability and is therefore disregarded for the purpose of this investigation. The inter-sample variability of the combined datasets may therefore be marginally larger than for single-batch datasets owing to the confounding of these two levels of variability.

Second, all measurements are taken on the same set of five convex corner beams for the 5320/tape and 5320/PW, and on the same set of six short beam strength (SBS) flat panels for each of the selected materials from the NCAMP database. The test-matrix guidelines established in Chapter 2 of the *Mil-Handbook-17* [140] cannot be strictly observed for the 5320 datasets: five repeated baseline samples are manufactured instead of the prescribed six; however, the prescribed number of specimen per panel ($n = 5$) is respected. That being the case, the datasets collected from the experimental work (5320 resin system) contain a suitable number of samples and total number of observations ($N \geq 25$) when compared to the size of corresponding datasets obtained from the NCAMP database.

Third, each corner beam and SBS flat panel consists of a UD layup ($[0°]_{ns}$; 0° orientation lies in the hoop-direction) and is manufactured according to the optimal baseline process (§ 2.2.2, [204] and [205] for the 5320, 5320-1 and 8552 resin systems, resp.). In addition, all six materials use comparable high-strength pan-based carbon fibres with similar tow fibre-counts.

Finally, laminate thickness, and fibre and void content data is available from the corner region of the 5320/tape and 5320/PW corner beams and is therefore analyzed for comparison with the variability in laminate quality observed in the corner beam flanges and SBS flat panels.

4.4.3 Inferential statistical methodology

The following inferential statistical analysis comprises two parts: parametric and non-parametric methods are first utilized to test the difference in sample means for a given dataset (question 1), and inferential statistics are subsequently calculated to determine the degree of inter- and intra-sample variability for this dataset (question 2). The statistical tests are borrowed from the calculation of statistically-based material properties (design allowables) detailed in Chapter 8 of the *Mil-Handbook-17* [140]. In turn, the variability statistics are borrowed from the ILS method for testing the precision of experimental methods detailed in the ASTM E691 test method [199]. These two references should be perused to gain a more detailed understanding of the fundamental concepts and terminology that underlie this analysis. A flowchart of the statistical analysis is illustrated in Fig. 4-1 and implemented in a Mathworks Matlab (R2015b) m-script presented in Appendix C.1.

It is important for the reader to have a foundational grasp of inferential statistics. To this end, Wolstenholme presents a more approachable overview of the common statistical methods utilized to model and test the data variability observed in the mechanical testing of advanced composites [200]. It should also be noted that a 95% probability or confidence interval is utilized throughout this study, i.e. a 5% significance level ($\alpha = 0.05$) or likelihood of committing a Type I error (false-positive) given a two-sided test. Finally, the following dataset parameters must first be defined as they are used throughout this section: i and j are the observation and sample indices such that x_{ij} is the i^{th} observation of the j^{th} sample; k is the number of samples; n_j is the sample size ($n_j = n$ in the case of equal sample sizes); n' is the effective sample size in the case of unequal sample sizes; and N is the total observation count.

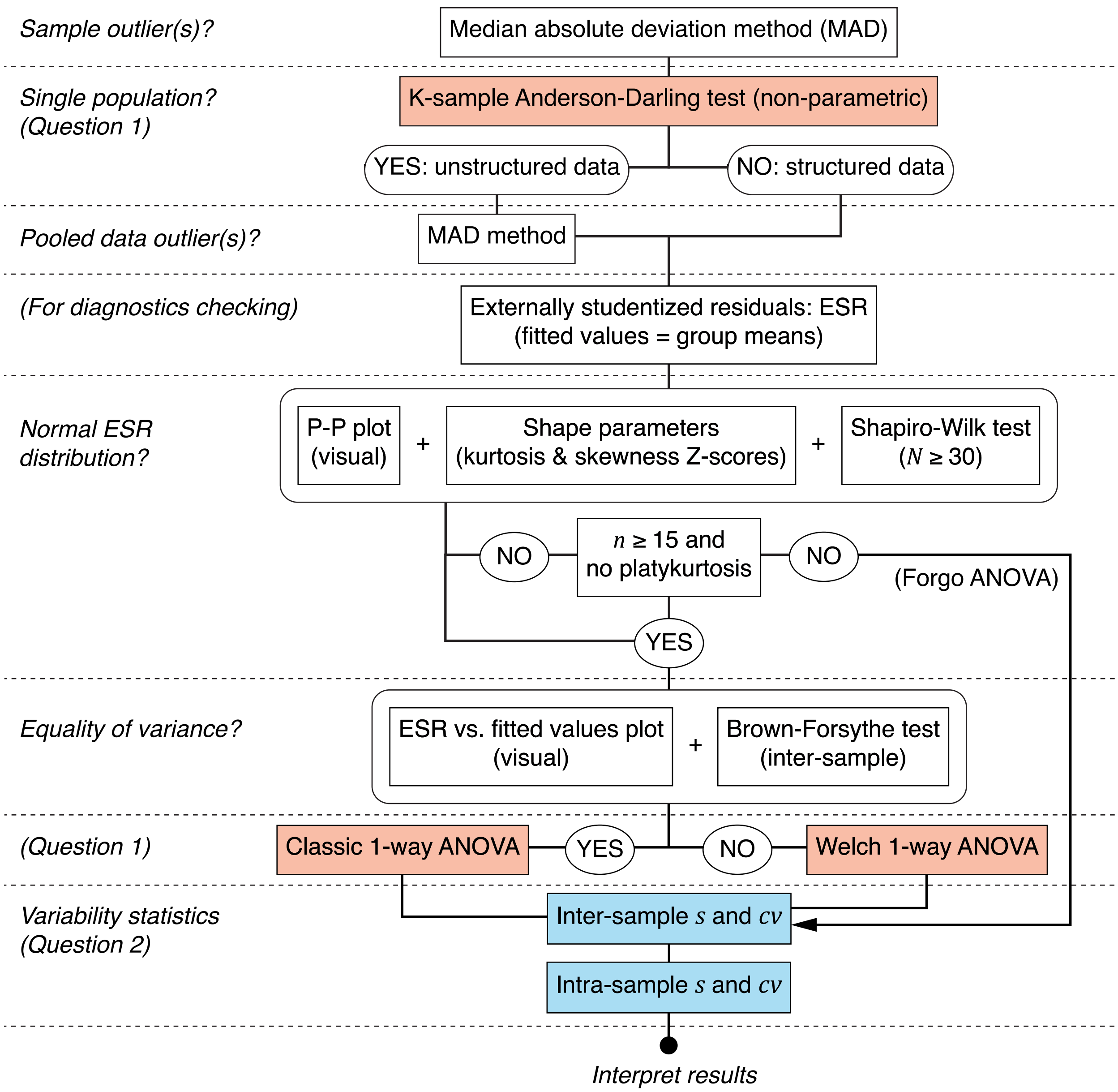

Fig. 4-1. Flowchart of the experimental repeatability statistical analysis.

The first step of the analysis is to check the data for outliers. Leys *et al.* highlight the fact that the widely-used interquartile method of detecting outliers is problematic for the following reasons: 1) it assumes a normal distribution; 2) outliers strongly influence the sample mean ($\bar{x}$)

and standard deviation (s); and 3) this technique is very unlikely to detect outliers [209]. The *Mil-Handbook-17* recommends the use of the maximum normed residual method, which is also based on sample means and can only detect one outlier at a time [140]. Leys *et al.* instead propose to use the median absolute deviation (MAD) method, which does not presuppose a normal population. It is given by Eq. (4-1), where x_i is the i^{th} observation of the data series under scrutiny (individual sample or unstructured data); $\tilde{x}$ is the median of this series; m is a multiplication constant that is arbitrarily selected based on the researcher criteria (m = 2.5 is a moderately conservative value used in this study); and b is a multiplication constant based on the assumed distribution that discounts the influence of outliers (b = 1.4925 for a normal distribution). Outliers are first investigated at the sample-level. The observations are corrected if applicable and retained if no causes are found.

$$\begin{gathered} \tilde{x} - m \cdot MAD < x_i < \tilde{x} + m \cdot MAD \\ \text{where: } MAD = b \cdot median(x_i - \tilde{x}) \end{gathered} \qquad (4\text{-}1)$$

The second step is to determine whether the sample means belong to a single population (question 1). To this end, the *Mil-Handbook-17* proposes the k-sample Anderson-Darling test (ADK), which is a non-parametric method, whose sole requirements are that each sample population be random and independent with ideally no inter-sample ties (identical values) [140]. There is a 95% probability that at least one sample belongs to a different population if the calculated test statistic is smaller than a critical calculated value. The calculations are covered in Chapter 8 of the *Mil-Handbook-17*. This test works well for small sample sizes ($n \approx 5$) and is not restricted by parametric assumptions [210]; however, it is not as powerful as comparable parametric methods [200]: non-parametric tests generally rely on rank-statistics to test the null hypothesis that samples are identical rather than the data itself, which increases the probability of committing a Type II error (false-negative). In other words, stronger evidence is required to reject the null hypothesis.

The k-sample Anderson-Darling test reveals the structure of the dataset. Identical samples may be pooled, in which case the dataset is said to be *unstructured*. Conversely, samples with statistically significantly different means may not be pooled, in which case the dataset is said to be *structured*. The MAD method is subsequently reapplied to check for outliers in pooled dataset and outliers are again corrected if applicable or are otherwise retained.

The third step is to check the results of the k-sample Anderson-Darling test with a more powerful parametric test for datasets that satisfy certain parametric assumptions. A one-way (one-factor) analysis of variance (one-way ANOVA) is selected with the single independent factor simply being the sample number, whose rank is random and therefore immaterial. This method employs the same model as that of a linear regression and is covered in the aforementioned reference works [140, 200] in addition to most elementary statistical textbooks. The first of four assumptions is that samples contain observations that are random and independent from the population, which is assumed to be the case based on the nature of the measurements under scrutiny [140, 200]. The second assumption is that the sample means are normally distributed, which is disregarded as there currently exist no reliable statistical test or visual exploratory technique that can reliably check for normality given a small sample number ($30 >> k = 5, 6$) [140]. The remaining two assumptions are that sample populations are likewise normally distributed and that sample variances are equal (homogeneity of variance).

No one statistical method is best to check the normality of a data series, therefore the recommended practice is to select a mix of statistical tests and visual techniques to check the normality of the pooled residuals [200]. This crucial process is referred to as a *regression diagnostic* or *residuals analysis*. To this end, the *externally* (*deleted*) *studentized residuals* (ESR) are calculated based on the fitted values, which in the case of a one-way ANOVA are simply the sample means. *Studentized* residuals are normalized with an estimate of the standard deviation, which lends itself well to the detection of outliers. The benefit of utilizing ESRs rather than conventional, *internally* studentized residuals is that the influence of the i^{th} observation is removed from the estimate of the sample standard deviation, which in the case of an outlier may otherwise significantly influence the standard deviation. The ESR calculation and interpretation of exploratory data plots for diagnostic checking are covered in most elementary statistical reference works such as Cooks and Wiseberg's *Residuals and influence in regression* [211].

The normality check is first comprised of a visual exploratory inspection of a probability-probability (P-P) plot of the pooled ESRs, i.e. a plot of the ESR empirical cumulative probabilities as a function of the theoretical ones, as illustrated in Fig. 4-2. In turn, the shape parameters of the plotted data are calculated, namely the kurtosis and skewness Z-scores, which are measures of the pointiness and symmetry of the data, resp. Specifically, kurtosis is a measure of the of the degree of difference between the tails of the empirical and normal distributions ("pointiness" or "peakedness" of the distribution; i.e. short, long or normal tails) [212]. Furthermore, z-scores are simply the number of standard deviations from the mean of a data point. Values that fall outside the -2.96 to 2.96 range are indicative of statistically significant deviations from normality for relatively small datasets ($N \leq 200$). Finally, the Shapiro-Wilk test for normality is performed for sufficiently-large datasets ($N \geq 30$). The Shapiro-Wilk test has been shown to be more powerful than the Anderson-Darling normality test prescribed in Chapter 8 of the *Mil-Handbook-17* for a wide range of population distributions [213].

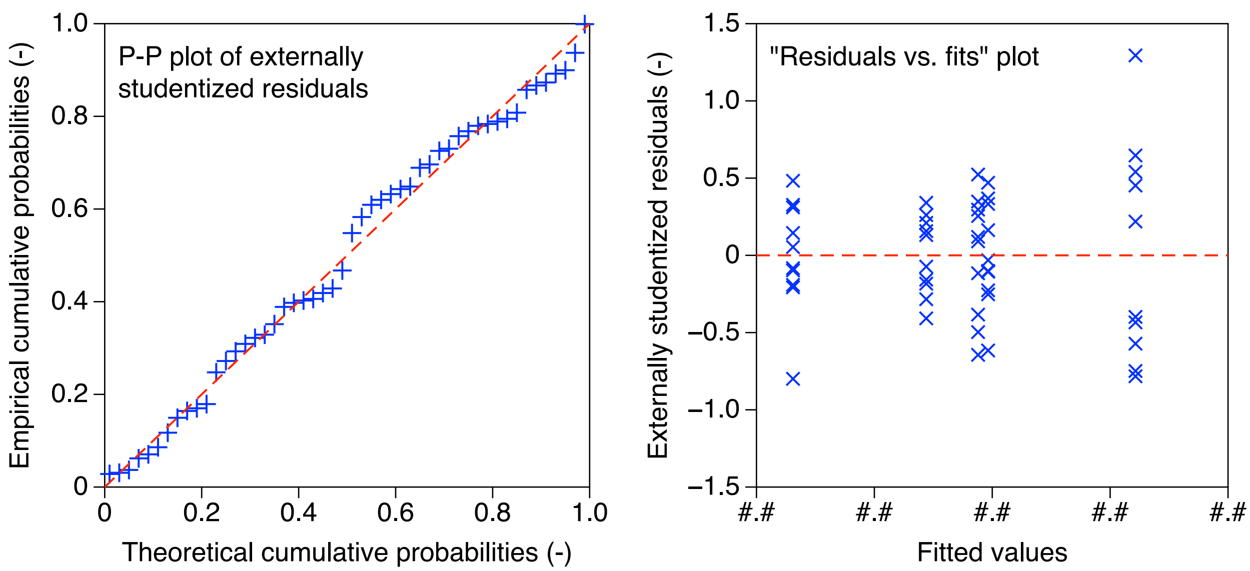

Fig. 4-2. Diagnostic plots of externally studentized residuals.

The one-way ANOVA is relatively robust in the case of moderate deviations from normality so long as the sample size is sufficiently large; a good rule of thumb is $n \geq 15$ [214]. A statistical test is considered to be "robust" when it is only marginally affected by violations of the underlying assumptions. The one type of abnormal distribution that is most problematic for the one-way ANOVA is *platykurtosis*, which is a long-tailed or flat-peak distribution. In case of sample sizes that are too small or display clear, visual evidence of platykurtosis, the analysis forgoes the one-way ANOVA and relies solely on the results of the less powerful, k-sample Anderson-Darling test to test the difference between sample means.

The fourth assumption of the one-way ANOVA can finally be checked, which is the equality of variance between samples. To this end, both a visual exploratory technique and a statistical test are performed, and a decision on the equality of variance is subsequently made on the basis of both results. The visual check is performed on a plot of ESRs vs. fitted values [211], as illustrated in Fig. 4-2. The aim is to determine whether the plotted data is symmetric about the horizontal axis and whether the data envelope is constant across the range of fitted values, which indicates equal variance across samples (homogeneity). Similar to the P-P plot, interpreting the results is subjective and can be difficult. Equality of variance is thus additionally tested with the Brown-Forsythe test, which can handle deviations from normality [215]. This test is a modified version of the Levene's test (recommended in Chapter 8 of the *Mil-Hanbook-17*), which uses the sample median instead of the mean in its formulation—similarly to the MAD method for outlier detection.

The difference in sample means can then be tested once all four assumptions have been checked. Fisher's classic one-way ANOVA is selected in the event that all four assumptions are met, whereas Welch's modified one-way ANOVA is instead utilized in the event of unequal variances [214]. The classic ANOVA is vulnerable to an increase in Type I error notably in the case of unequal and small group sizes, whereas the error rate of the Welch ANOVA remains significantly closer to the original 5% significance-level. The statistical power of both methods is otherwise comparable in the case of equal variances. Moder corroborated the fact that the Welch ANOVA is suitable for cases of unequal variances so long as the number of factors is kept to less than 3 [216], which qualifies the present single-factor analysis. The classic formulation is still preferred over the Welch formulation in cases of unequal sample size with equal variances. One-way ANOVA is covered in the two aforementioned reference works [140, 200] in addition to most elementary statistical textbooks. In turn, the Welch ANOVA is presented in Welch's original paper [217] and a Minitab Inc. technical paper [214] as well as some textbooks. Lastly, reviews by Glass *et al.* [218] and Lix *et al.* [219] may be consulted for a greater understanding of the effects that violating assumptions have on the results of a one-way ANOVA. It is expected that these results will confirm those of the k-sample Anderson-Darling test and validate whether the null-hypothesis stands that samples belong to a single population and may thus be pooled.

The non-parametric and parametric methods thus far described only indicate whether sample means of a given dataset significantly statistically differ, but they do not indicate the degree of inter- and intra-sample variation (question 2). The final step is therefore to calculate the inter- and intra-sample variability statistics, namely the respective standard deviations and corresponding coefficients of variations. The datasets analyzed herein have the same structure as that of an ILS test conducted with a single sample per material and per laboratory, which is often the case. The dataset structure is as follows: multiple independent and random samples that contain independent and random observations. The one noteworthy difference in data is that samples manufactured in an inter-laboratory study follow reproducibility and not repeatability conditions between laboratories. Nevertheless, the formulas for repeatability (inter-laboratory) and reproducibility (intra-laboratory) standard deviation (s) and coefficient of variation (cv) can be adapted for the purposes of the current analysis to quantify the inter- and intra-sample variability.

Table 4-4. Definitions of inter-and intra-sample statistics.

Statistic	Equation	
Effective sample size: (in case of unequal sample sizes)	$n' = \frac{1}{k-1}\left(N - \sum_{i=1}^{k} \frac{n_i^2}{N}\right)$	(4-2)
Sample mean:	$\bar{x}_j = \frac{1}{n_j}\sum_{i=1}^{n_j} x_{ij}$	(4-3)
Grand mean:	$\bar{\bar{x}} = \sum_{j=1}^{k} \frac{\bar{x}_j \cdot n_j}{N}$	(4-4)
Sample standard deviation:	$s_j = \left(\frac{1}{n_j - 1}\sum_{i=1}^{n_j}\left(x_{ij} - \bar{x}_j\right)^2\right)^{0.5}$	(4-5)
Within (pooled) standard deviation:	$s_W = \left(\frac{1}{N-k}\sum_{j=1}^{k} s_j^2\left(n_j - 1\right)\right)^{0.5}$	(4-6)
Within coefficient of variation:	$cv_W = s_W / \bar{\bar{x}}$	(4-7)
Standard deviation of sample means:	$s_m = \left(\frac{1}{k-1}\sum_{j=1}^{k}\left(\bar{x}_j - \bar{\bar{x}}\right)^2\right)^{0.5}$	(4-8)
Between standard deviation:	$s_B = \left(s_m^2 + s_W^2 \cdot \frac{(n'-1)}{n'}\right)^{0.5}$	(4-9)
Between coefficient of variation:	$cv_B = s_B / \bar{\bar{x}}$	(4-10)

The adapted statistics borrowed from the ASTM E691 test method [199] are presented in Table 4-4. The subscripts b and w stand for "between" and "within" and indicate inter- and intra-sample statistics, resp.

The ILS test is simply a one-way ANOVA with the single-factor being laboratories—or test panels in the context of the present analysis. In turn, the inter-sample standard deviation (s_W) is simply the *pooled* standard deviation, which assumes equal sample variances, and is accepted as a reliable estimate of the population standard deviation. This equal variance assumption ought to be valid under repeatability conditions, but it is often violated in practice. Nevertheless, it is generally taken to be valid if the samples are manufactured within a short period of time. The same rationale may be applied to the assumptions of normality for sample and sample-mean distributions. Samples that strictly follow repeatability conditions—as is the case in this study and the datasets obtained from the NCAMP database—may therefore generally be pooled [199].

4.4.4 Statistical results and implications

The statistical results of the repeatability study associated with laminate quality measurements are summarized in Table 4-5. In answer to the first question (do samples belong to a single population?), 18 of the 24 datasets analyzed (75%) contain at least one statistically significantly different sample. A one-way ANOVA (either classic Fisher of modified Welch formulation) is performed for 15 of the 24 datasets that satisfy the assumptions (62.5%). In all cases, the ANOVA confirms the results of the less powerful k-sample Anderson-Darling test (ADK). No discernable pattern is found to explain the six seemingly random datasets with identical sample means. The nature of composite testing and laminate quality measurements is such that a considerable degree of inter-sample variability can be expected for a given population, irrespective of the processing route (VBO or autoclave) as inferred from the resin systems tested in this study.

Next, the grand means of the fibre and void content datasets can be compared to assess the relative laminate quality of each material. The similar VBO semipregs have very comparable fibre contents: 60.4 and 60.5% for the tapes, and 58.5 and 57.6% for the PW. In contrast, the autoclave materials have surprisingly lower fibre contents, despite the fact that panels are prepared under a consolidation pressure that is nearly seven times larger than the vacuum-bag pressure of VBO processing and with autoclave prepregs designed for resin-bleeding [68]. The image analysis method utilized in this work (§ 2.5) is seemingly as accurate as the matrix digestion method (ASTM D3171, Method I [207]) utilized by NIAR in determining fibre content.

Table 4-5. Summary of the statistical results for the laminate quality datasets.

Material (location)	Single population?	Method	$\bar{\bar{x}}$	s_W	cv_W (%)	s_B	cv_B (%)
Laminate thickness (mm)							
5320 / tape (flange)	no	Welch	3.34	0.0310	0.930	0.0181	0.541
5320 / tape (corner)	no	Welch	3.41	0.0304	0.891	0.0291	0.853
5320 / PW (flange)	no	regular	3.11	0.0196	0.629	0.0107	0.343
5320 / PW (corner)	no	Welch	3.36	0.0226	0.673	0.0125	0.371
5320-1 / tape	no	Welch	6.07	0.147	2.42	0.0747	1.23
5320-1 / PW	no	Welch	6.08	0.0333	0.548	0.0354	0.583
8552 / tape	no	Welch	6.24	0.170	2.72	0.0822	1.32
8552 / PW	no	regular	6.22	0.130	2.09	0.0945	1.52
Fibre content (%)							
5320 / tape (flange)	no	Welch	60.4	1.13	1.87	0.789	1.31
5320 / tape (corner)	no	ADK	58.1	2.01	3.46	1.28	2.19
5320 / PW (flange)	yes	Fisher	58.5	2.63	4.50	1.37	2.34
5320 / PW (corner)	yes	Fisher	50.1	2.42	4.83	1.36	2.72
5320-1 / tape	yes	ADK	60.5	1.29	2.12	0.565	0.932
5320-1 / PW	no	Fisher	57.6	0.228	0.397	0.355	0.617
8552 / tape	no	ADK	56.6	1.53	2.70	1.31	2.32
8552 / PW	no	ADK	55.7	1.28	2.29	0.958	1.72
Void content (%)							
5320 / tape (flange)	no	Welch	0.0224	0.0129	57.5	0.00939	42.0
5320 / tape (corner)	no	Welch	0.0271	0.0110	40.6	0.00774	28.5
5320 / PW (flange)	yes	ADK	0.0281	0.0148	52.7	0.00777	27.6
5320 / PW (corner)	no	ADK	1.24	0.689	55.8	0.399	32.3
5320-1 / tape	yes	ADK	0.661	0.429	64.8	0.200	30.3
5320-1 / PW	yes	ADK	2.73	0.595	21.8	0.322	11.8
8552 / tape	no	ADK	-0.509	0.568	112	0.547	107
8552 / PW	no	Fisher	0.369	0.083	22.5	0.138	37.5

With regards then to void content, the grand means are significantly lower for the 5320 datasets compared to the NCAMP datasets. NIAR utilizes the ASTM D2734 test method [208], which is a density-based method that relies on ignition loss. This method has a typical accuracy of ±0.5% and is known to be sensitive to variations in density and percent weight measurements used to determine the constituent volume fractions [140]. Small negative values within this error range are therefore possible and can be taken to be zero. The image analysis utilized in this work is significantly more accurate in the case of void content determination.

In addition, the 5320/tape corner regions have a slightly smaller fibre content (-2.3%) than the corresponding flanges but a similar void content, and the 5320/PW corner regions have a significantly smaller fibre content (-8.4%) and larger void content (1.24%). Smaller fibre contents and larger void contents are expected in corner regions due to the consolidation pressure differential that exist in convex corners [130] and the lack of interply slippage [137], which both result in corner thickening in the case of a UD layup and convex tool-shape. The larger areal weight and bulk-factor of the PW (reported in Table 2-1) further contribute to the degradation of laminate quality in the corner [69].

Finally, the calculated variability statistics for each dataset are plotted in Fig. 4-3 in answer to the second question (how samples differ in practicality?). Overall, datasets display relatively small variability notably between samples. Only 3 of the 24 datasets (12.5%) display greater inter-sample than intra-sample variability. The coefficients of variation are less than 3 and 5% for the thickness and fibre content datasets, including datasets for corner regions that are expected to display the most variability. Likewise, standard deviations of the void content datasets are less than 1%. It should be noted that standard deviations are plotted in the case of void content rather than coefficients of variation. As means approach zero—which is often the case for the void content of optimal baseline processing conditions—the corresponding coefficients of variation approach infinity and become increasingly affected by small changes in means. It is therefore preferable in such cases to compare standard deviations.

In turn, the datasets obtained from this work (5320/tape and 5320/PW) display less inter- and intra-sample variability than the corresponding NCAMP datasets, except in the case of fibre content. The matrix digestion method (ASTM D3171, Method I [207]) is shown to be somewhat more precise than the image analysis method used in this work (§ 2.5.3), which is based on thresholding. This conclusion can be reached on account that the fibre content grand means are relatively similar across all datasets, and the tape and PW reinforcement types are nearly identical across resin systems.

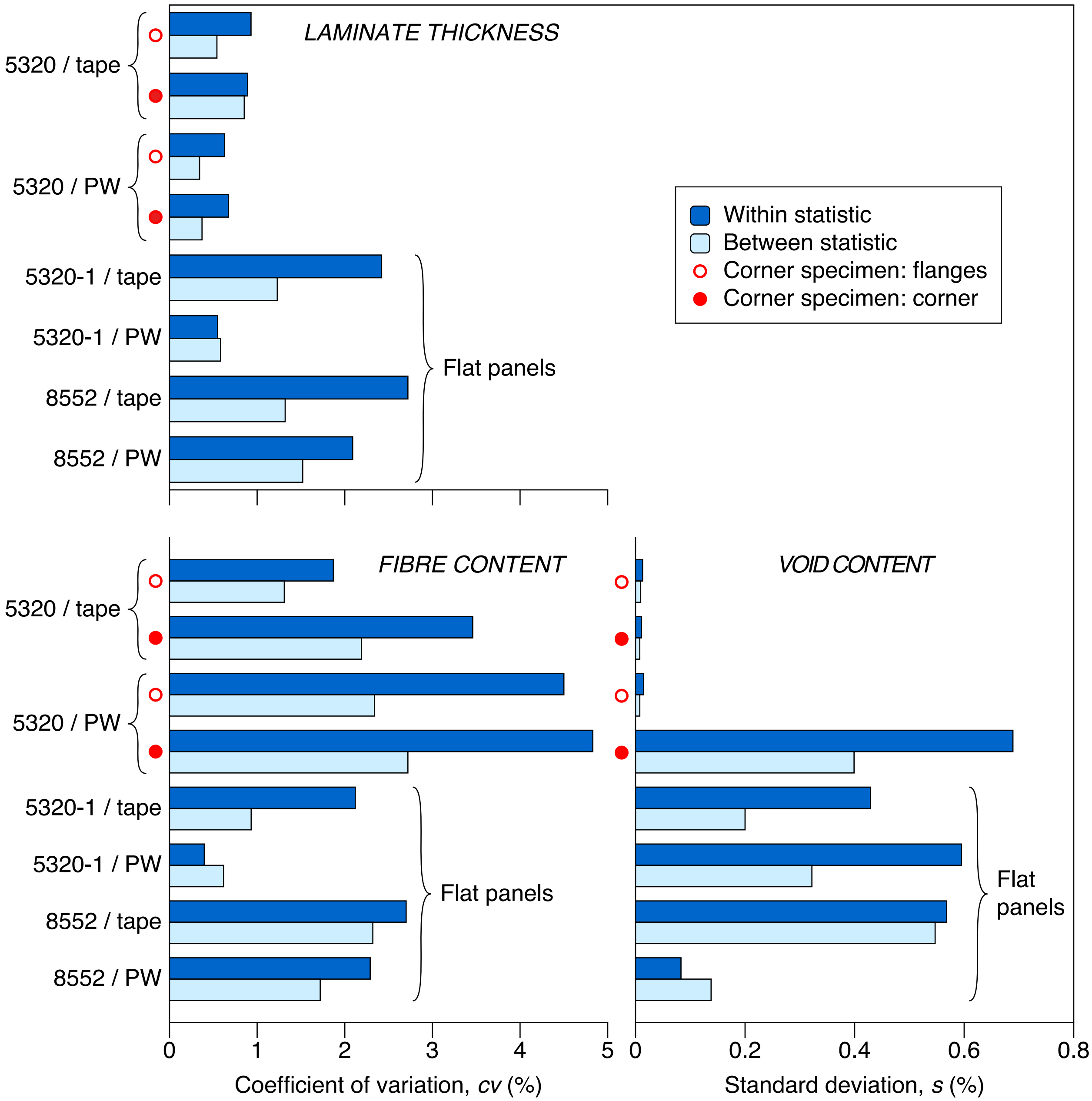

Fig. 4-3. Inter- and intra-sample variability statistics for the laminate quality datasets.

In conclusion, samples cannot generally be assumed to come from a single population, even though the inter-sample variability is often lower than the intra-sample variability—there is an inherent variability in composite testing. The experimental findings presented in the remainder of this chapter, which are based on single-sample datasets, speak to general, observable trends, but they are statistically inconclusive and should therefore only be considered in the same vein as the results of a pilot study. That being the case, the research environment created for this work compares favorably to the expert testing environment that exists at NIAR and similar institutes. The variability statistics reveal that the processing and testing methods employed in this thesis generate results with similar or lower variability than results generated by NIAR. Lastly and with proper care, VBO semipreg processing is shown to generate near-optimal, baseline corner beams that have a variability on par with or lower than flat panels processed in an autoclave.

4.5 Laminate quality results and discussion

4.5.1 Overview

Laminate quality is assessed herein in terms of three quantitative measurements: corner thickening, fibre content and void content, which is divided into inter- and intra-tow void species as defined in § 2.5.3. The findings are corroborated with qualitative observations made via visual inspection of specimen corner surfaces and optical micrographs of representative corner laminate cross-sections taken in the frontal plane (§ 2.5.3). Of the roughly 15 specimens prepared for each sample corner beam (§ 2.3.2), five specimens are randomly selected for the sample thickness analysis according to the corner thickness profiling method described in § 2.4.3; these specimens are subsequently reserved for the mechanical testing presented in Chapter 5. In turn, a second set of five specimens is randomly selected and dissected for the determination of constituent contents according to the optical microscopy and image analysis methods described in § 2.5. It should be noted that, even though fibre and void content T-T distributions are obtained for every sample, the results are herein omitted as they are deemed to be seemingly random and insufficient to be conclusive. The reliable observation of T-T effects may require a nominal laminate thickness greater than 3 mm and a number of optical micrographic cross-sections greater than five.

The target and actual mean consolidation pressures during the RT-hold and cure cycle are given in Fig. 4-4. The measurements are made via the experimental setup and data reduction described in § 2.3.2. The tape and PW convex baseline values (Tape/PW-M-UD-B) are grand means accompanied by pooled standard deviations of the five-sample sets (Eq. (4-4) and (4-6), resp.). Overall, the actual CPLs are satisfactorily close to the nominal target values. A maximum deviation of 4.45% occurs for the worst-case test condition, which is a combination of the highest bulk-factor material (8HS) and the restricted air evacuation industrial processing case. Centea and Hubert achieved similarly pressure deviations below 4.6% using the same method and a similar experimental setup to process VBO semipreg laminates under similar conditions [114].

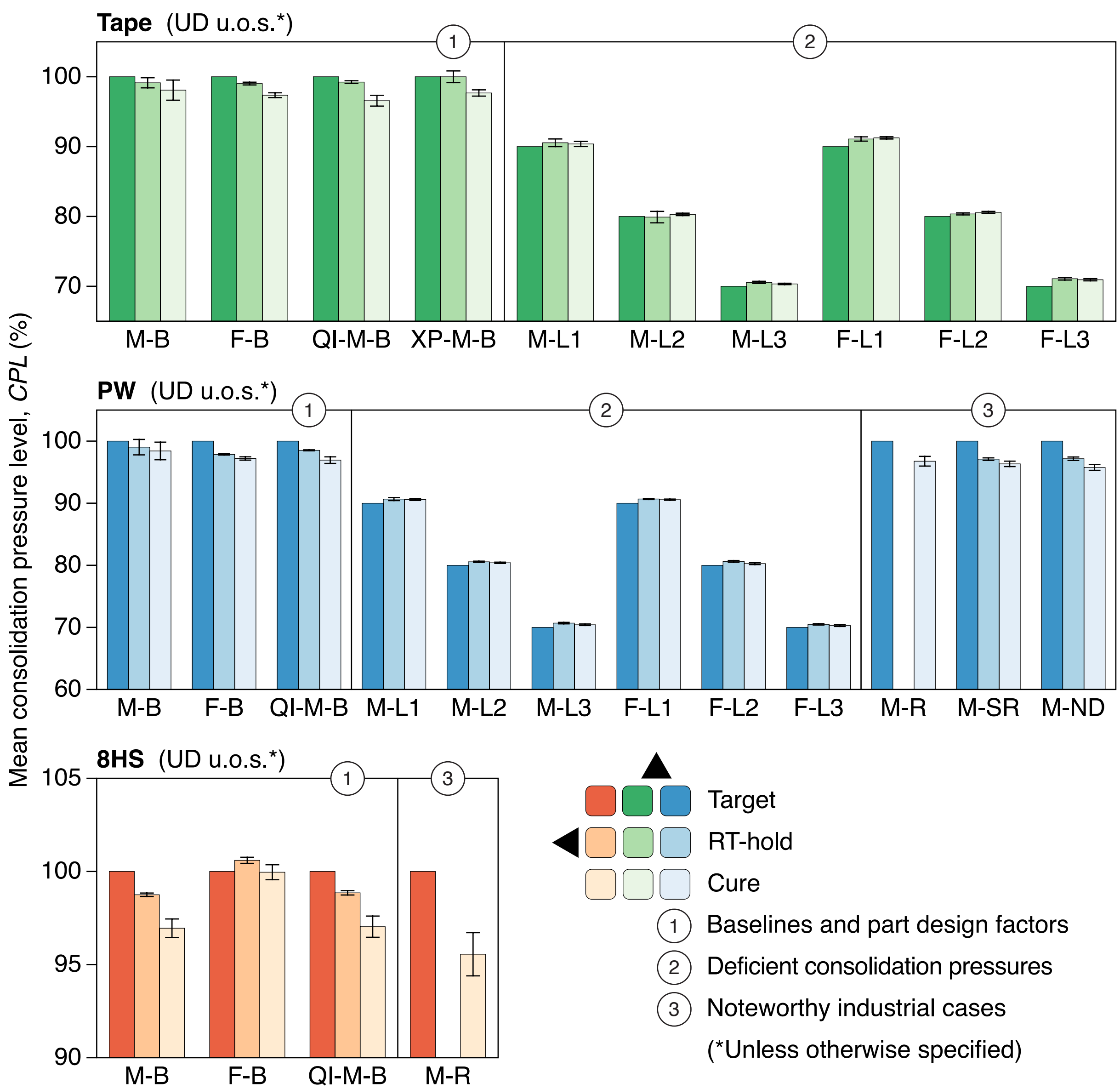

Fig. 4-4. Mean sample consolidation pressure levels.

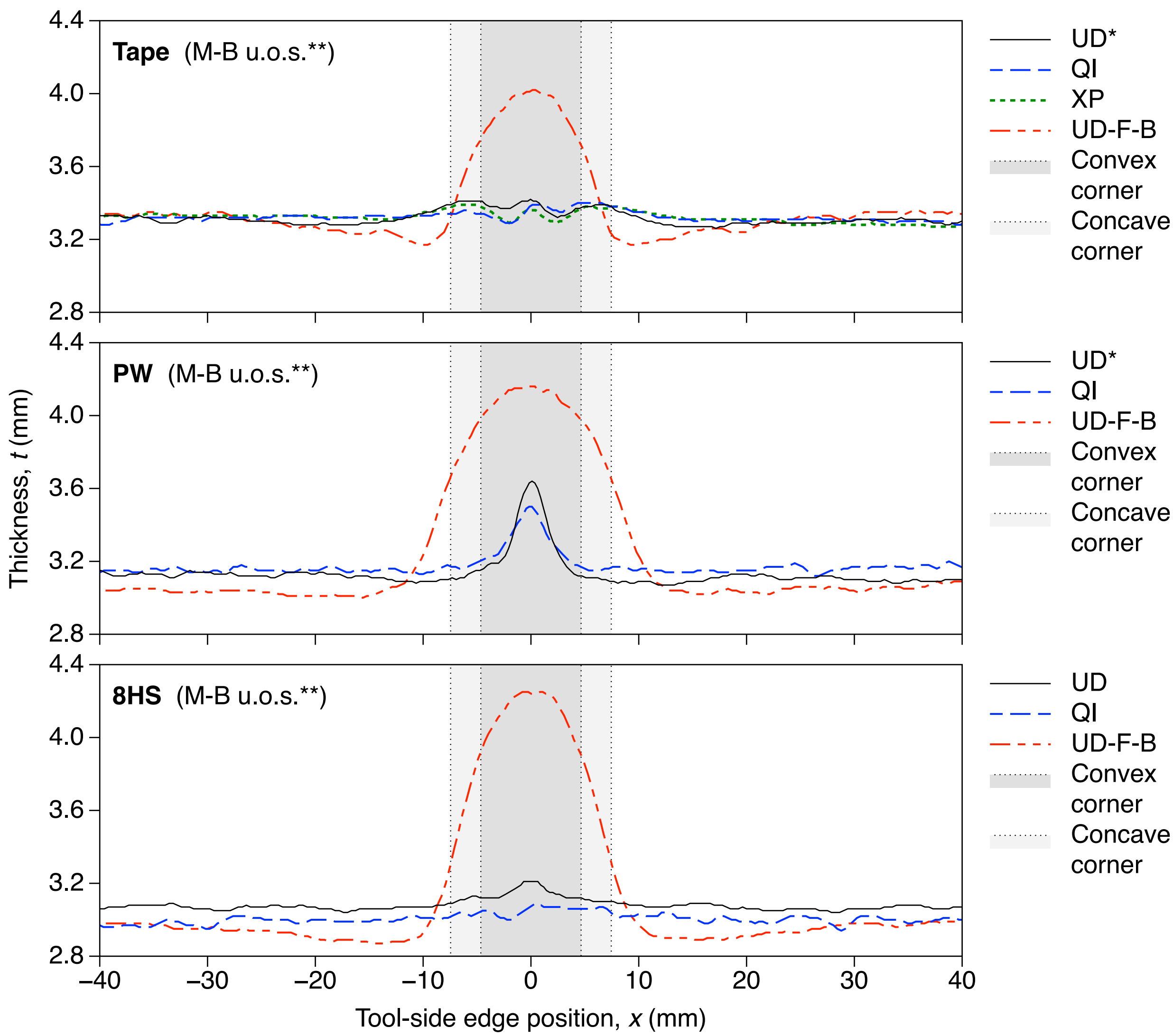

Fig. 4-5. Effect of selected design factors on sample thickness profile.

Mean consolidation pressure deviations are typically largest during the cure cycle compared with the RT-hold: the consolidation pressure effectively reaches a steady-state during the RT-hold, whereas it drops during the resin-flow phase at the beginning of the cure (Fig. 2-2 and 2-3). In turn, the nominal target values are most readily achieved for the deficient consolidation pressure samples (L1, L2 and L3), which experience mean pressure deviations of 0.618 ± 0.271% and 0.525 ± 0.295% during the RT-hold and cure cycle, resp. The maximum attainable consolidation pressure is otherwise limited for samples utilizing near-optimal consolidation pressure (B, R, ND and SR) due to operator skill, specific consumables and equipment used, and atmospheric conditions. These samples experience larger mean pressure deviations of 1.26 ± 0.967% and 2.61 ± 1.29% during the RT-hold and cure cycle, resp.

For the purpose of this work, a CPL greater than 95% is considered to be sufficiently high for test conditions that utilize near-optimal consolidation pressure. This pressure range is readily attained for all the samples concerned and is deemed to be representative of what is achievable in standard academic research and industrial environments. Overall, the relatively small pressure deviations along with the effective lack of T-T temperature gradients during the cure (< 3 °C) indicate that the desired processing conditions are achieved for each manufactured sample.

4.5.2 Baselines and design factors

The discussion of laminate quality results begins with the three selected design factors: material selection, tool-shape and stacking sequence. The sample thickness profiles for the six baselines (Tape/PW/8HS-UD-M/F-B) and the four samples consisting of alternate stacking sequences other than the UD (i.e. QI and XP) are presented in Fig. 4-5. It should be noted that corners are of a similar size irrespective of tool-shape despite the graphical representation of corner regions: the corner thickness profiling method measures thickness as a function of the smoother and more predictable tool-side edge, which is simply the longer edge in the case of a concave sample (§ 2.3.1). In turn, the corresponding laminate quality results are presented in Fig. 4-6 in terms of mean corner thickening, and fibre and void contents. It should be noted that the tape and PW convex baseline values (Tape/PW-UD-M-B) are each comprised of grand means and pooled standard deviations determined from five-sample sets (Eq. (4-4) and (4-6), resp.). Lastly, optical micrographs of corner cross-sections for representative baseline specimens and specimens containing alternate stacking sequences are presented in Fig. 4-7 and 4-8, resp. The results in these figures are jointly discussed throughout this section.

Thickness deviation

The six baselines all exhibit significant corner thickening, as evidenced in Fig. 4-5 and 4-6. Tool-shape and material selection—to a lesser extent—are shown to have a large influence over corner thickening. First, the three convex baselines exhibit markedly less corner thickening than the three concave baselines. The tape convex baseline (Tape-UD-M-B) exhibit the lowest amount of corner thickening of all the baselines with a mean value of only 1.64 ± 1.48%. In turn, the next best performers are the two woven convex baselines (PW/8HS-UD-M-B) with the 8HS exhibiting less corner thickening than the PW given a mean value of 3.09 ± 4.51% compared to 7.83 ± 0.588%. The tape and 8HS convex baselines are the only tested conditions to meet the 5% maximum corner thickening requirement set by the ASTM D6415 test standard [90]. With respect then to concave baselines, the tape is again the best performer (Tape-UD-F-B) with a mean corner thickening value of 13.5 ± 0.979%. Finally, the worst performers by a wide margin are the two woven concave baselines (PW/8HS-UD-F-B) with the PW—this time—exhibiting less corner thickening than the 8HS given a mean value of 26.4 ± 0.850% compared to 33.2 ± 2.42%.

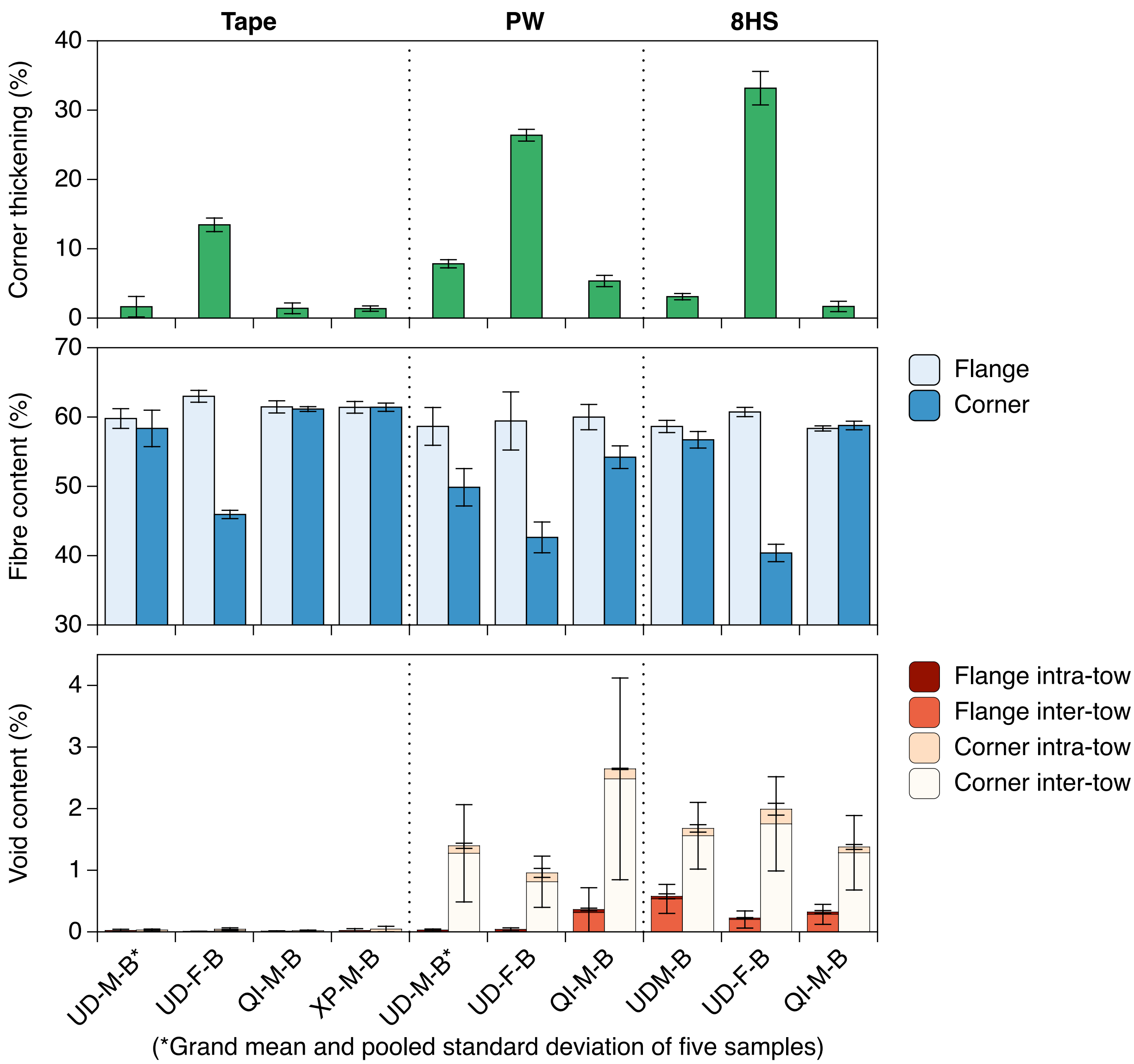

Fig. 4-6. Effect of selected design factors on laminate quality.

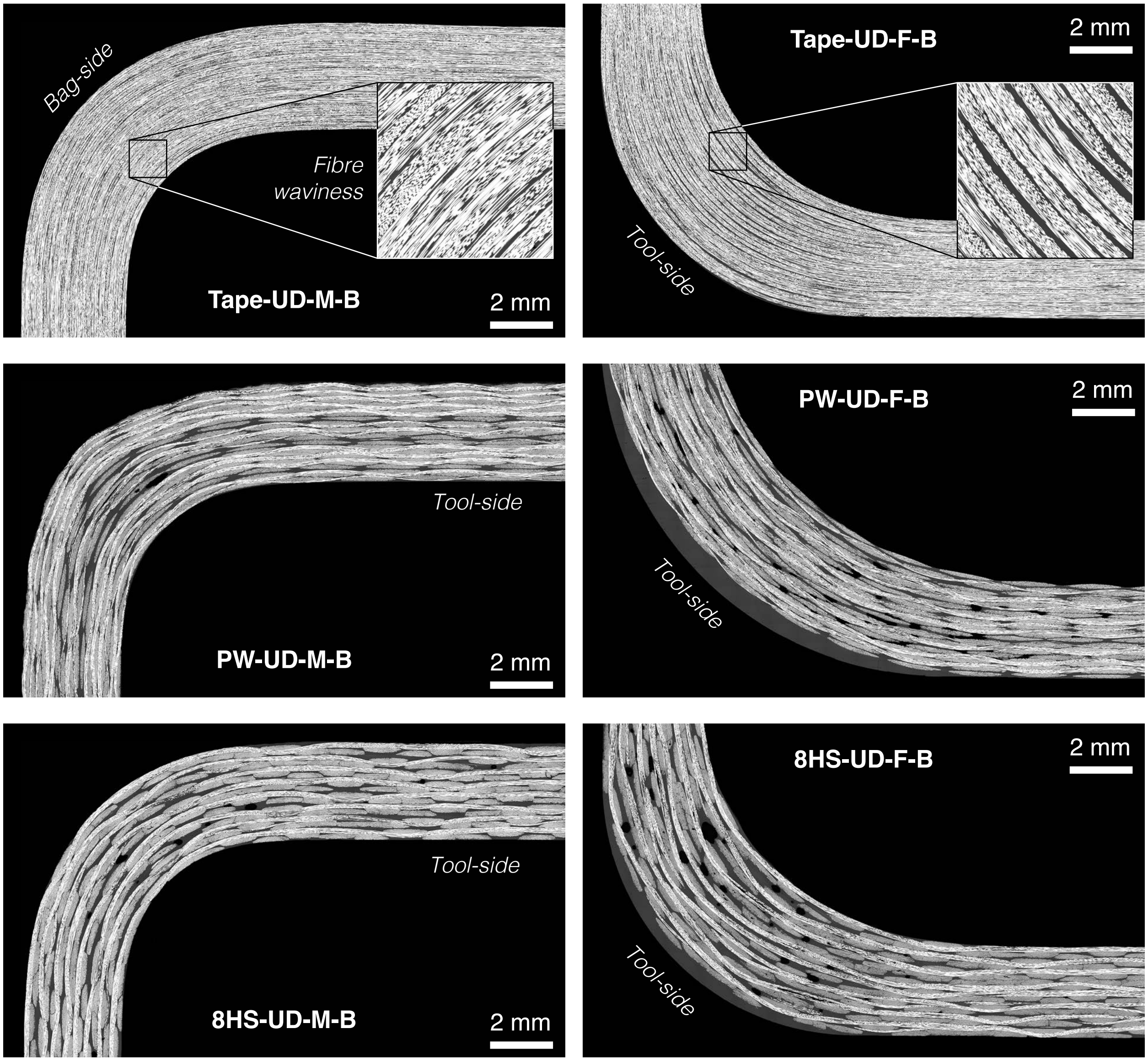

Fig. 4-7. Optical micrographs of representative baseline specimens (frontal plane; brightfield illumination; 10x objective).

The micrographic evidence presented Fig. 4-7 corroborates the corner thickening findings. The laminate quality of the tape and 8HS convex baselines (Tape/8HS-UD-M-B) is visually superior to that of the other baselines given the uniformity of the laminate mesostructure throughout the samples. Conversely, the PW convex baseline (PW-UD-M-B) is the only convex baseline to exhibit noticeable corner thickening along with several interply resin-rich regions in the corner. In turn, all three concave baselines exhibit significant corner thickening with prevalent ply bridging and resin-rich regions delineating plies across the corner. In particular, the tape concave baseline (Tape-UD-F-B) conforms relatively well to the concave tool compared to the PW and 8HS concave baselines (PW/8HS-UD-F-B), which do not conform well at all and instead exhibit thick resin-only regions on the tool-side edges that span the entirety of the corner.

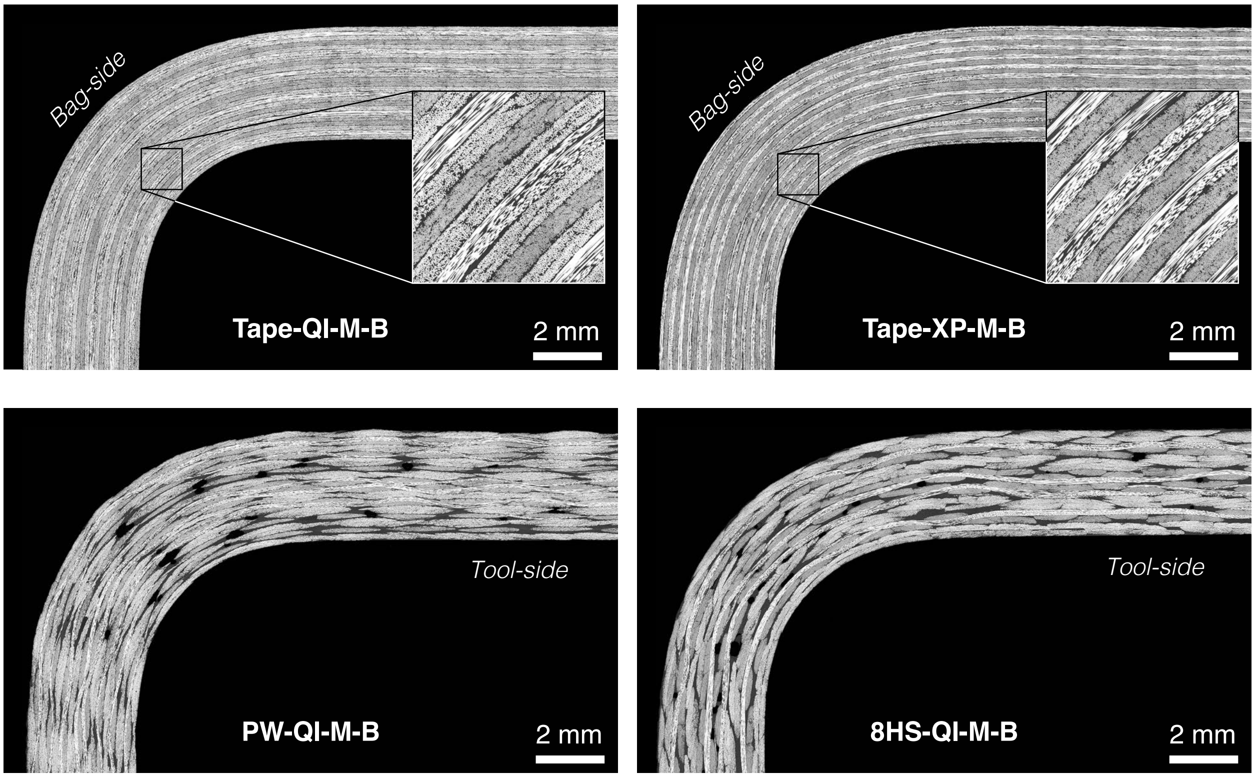

Fig. 4-8. Optical micrographs of representative specimens for the selected alternate stacking sequences (frontal plane; brightfield illumination; 10x objective).

The presence of corner thickening in all six baselines may generally be attributed to the following mechanisms. First, interply slippage is vital for laminates with substantial bulk-factors ($\gtrsim 1.1$) to conform well to the tool-shape. Plies will otherwise tend to amass over convex corners and bridge across concave ones. Even in the case of interply slippage, the consolidation pressure differential that arises between corners and flanges will result in thickness deviation [130, 137]. In this work, the flange length of all the manufactured samples exceeds 10 cm prior to specimen machining, which is sufficiently long to effectively constrain interply slippage due to interply friction [135, 137]. In addition, edge-breather strips oppose interply slippage in convex corner laminates [69]—though the effect may be restricted to laminate edges given sufficiently long flanges; and the presence of tow crossovers in woven laminates adds to the surface topology that collated plies must overcome to conform to the tool-shape.

In turn, all six baselines consist of the UD layup ($[0°]_{ns}$) with fibres oriented in the hoop-direction (warp tows in the case of PW samples). The fibre-bed is stiffest in this direction and for this stacking sequence, and directly resists laminate consolidation through compressive and tensile loading of convex and concave corners, resp. [130, 131]. In comparison, the only case to consistently promote corner thinning is a convex tape laminate with a transverse layup ($[90°]_{ns}$) [130, 131, 134]. The fibre-bed is the least stiff in this direction and for this stacking sequence, and effectively shears under the consolidation pressure thus better conforming to the tool-shape. Lastly, ply nesting may occur in woven laminates; however, the woven reinforcement architecture may impede intra-ply deformation.

More specifically, fibre nesting lessens the extent of corner thickening in the tape convex baseline and effectively transforms the laminate into a single, thick lamina [114]. In turn, the interply resin-rich regions present in the corner of the PW convex baseline may be attributed to the stiffness of the UD fibre-bed resisting the bulk of the consolidation pressure [130]. The hydrostatic resin pressure consequentially dips in the corner, allowing for some degree of resin accumulation despite the higher consolidation pressure experienced over convex features. Next, the comparatively smaller extent of corner thickening exhibited by the 8HS convex baseline compared to the PW convex baseline is surprising given the greater areal weight and bulk-factor of the 8HS reported § 2.2.1. This finding may be explained by the tighter criss-cross pattern of the PW compared to that of the 8HS (i.e. crossovers every tow rather than every eight tows), which may more severely impede ply deformation in the corner. Next, the corner thickening trend observed across the concave baselines may be attributed to the respective areal weights and bulk-factors of the three semipregs (§ 2.2.1), which increase as the extent of corner thickening increases [69, 137]. The tape has the lowest values and thus exhibits relatively better laminate conformation. Meanwhile, the higher values of the PW and the higher values still of the 8HS explain the lack of corner conformation exhibited in both cases. Lastly, the corner resin accumulation present in all three concave baselines is simply due to the lower consolidation pressure and, in turn, resin hydrostatic pressure in the corner [130].

Compared to tool-shape and material selection, stacking sequence appears to have a much more muted effect. The QI samples of all three materials and the tape-XP sample exhibit slightly less corner thickening than the corresponding UD samples—albeit negligibly so in the case of the tape samples given the overlap in error bars. This trend may be explained by an increased amount of transverse fibres, which promotes tangential ply and tow shearing in tape and woven corners, resp. [130]. In addition, a QI stacking sequence may improve interply nesting in woven corner laminates by rendering it less likely for tow crossovers to overlap. The muted response in the case of the tape samples may be further attributed to the presence of interply angles, which impede interply fibre nesting, and the relative thinness of plies, which may limit the extent of ply shearing. In turn, the greater degree of corner thickening exhibited in the PW-QI sample compared to the 8HS-QI sample mirrors the finding of the PW-UD and 8HS-UD baselines. The 8HS conforms best to the convex tool-shape despite having a greater areal weight and bulk-factor. there is no clear evidence of corner thickening or resin accumulation in the corners of any of the four, alternate stacking sequence samples, as evidenced in Fig. 4-8.

The significant corner thickening present in the PW convex and both concave baselines, indicates that more generous corner radii—notably that of the concave tool-side—are generally required to control corner thickening given the selected combinations of material, stacking sequence and above all flange length. This finding corroborates the conclusion reached by Ma *et al.* stemming from experiments investigating in part the effect tool corner radius on corner thickness deviation of 2D-woven semipregs [121]. The friction-dominated consolidation mechanism effectively locks-in corner thickening during the layup process, which is the prevalent case as far as large industrial parts are concerned. Larger tool radii would in practicality help the operator conform plies to the tool-shape during layup. It should be noted that specimen geometry is herein selected on the basis of curved beam strength testing (§ 2.3.1) and not to control thickness.

In a broader context, thickness deviations extend nearly 15 mm into the flanges of the tape samples as observed in Fig. 4-5 irrespective of stacking sequence and tool-shape. There is a noticeable dip in thickness before the start of the corner region in both the convex and concave sample profiles. In addition, distinct local thickness peaks overlap the corner inflection points of the convex sample profiles, which is a manifestation of the convex shoulder thickening effect mentioned in § 2.4.1 (so-called "Mickey Mouse [ears]" effect). In contrast, no thickness deviations are observed in PW sample profiles outside of the corner region irrespective of tool-shape. The complex deviations observed in the tape sample profiles are likely the result of in-plane fibre waviness within corner regions (Fig. 4-7: Tape-UD-M-B). Fibre waviness is visually detectable on the inner, tool-side surfaces of tape convex samples and as presented in Fig. 4-9.

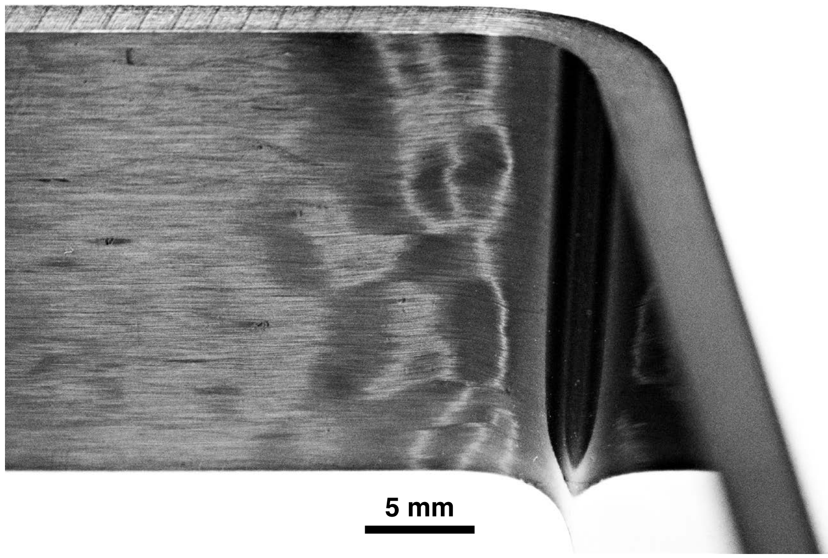

Fig. 4-9. Example of in-plane fibre waviness on the tool-side surface of a convex tape corner specimen.

Fibres in tape convex samples are unconstrained in the transverse ply direction and are therefore prone to undulate within plies with angles approaching 0° as a result of compressive forces experienced in the hoop-direction during laminate consolidation. They are in turn much more constrained in the radial direction due to consolidation pressure and the presence of adjacent plies and vacuum-bagging consumables. Ply wrinkling, which entails significant out-of-plane waviness, is most likely to occur as a result of a poor layup, wrinkles in the vacuum-bagging consumables and large ratios of laminate thickness-to-tool radius [130]. It should be noted that fibre misalignment is also present in the optical micrographs of the tape concave specimens—though it is not visually detectable on the specimen surfaces. This misalignment is however due to the slight misplacement of plies by the operator and is not attributed to fibre waviness induced by laminate consolidation. Plies over concave features experience tensile loading in the hoop-direction that effectively aligns fibres. Fibre waviness in the case of the tape convex baselines is investigated in greater detail in the next chapter.

Fibre content

The fibre content results generally support the corner thickening findings. The three convex baselines exhibit similar flange fibre content irrespective of material, although it should be noted that only half of the fibres in the PW- and 8HS-UD samples are oriented in the hoop-direction. In addition, the local fibre content of woven laminates is much more variable than that of tape laminates owing to the very different mesostructures. The flange fibre contents of the tape, PW and 8HS convex baselines are 59.8 ± 1.42%, 58.6 ± 2.72% and 58.6 ± 0.880%, resp. The similar fibre content is owed to semipreg design with all three materials containing similar, net resin contents as reported in § 2.2.1— “net” meaning that all three semipregs are designed for bleed-free processing. Meanwhile, all three concave baselines exhibit slightly higher fibre content than the respective convex baselines. The flange fibre contents of the tape, PW and 8HS concave baselines are 63.0 ± 0.853%, 59.4 ± 4.19% and 60.7 ± 0.670%, resp. This slight increase in fibre content may be attributed to higher flange compaction owing to significant resin migration from the flanges to the corners.

In turn, the three convex baselines exhibit lower fibre content in corners compared to flanges. The corner fibre contents of the tape, PW and 8HS convex baselines are 58.4 ± 2.63%, 49.9 ± 2.69% and 56.7 ± 1.19%, resp. Meanwhile, the three concave baselines exhibit lower fibre content still in corners compared to flanges. The corner fibre contents of the tape, PW and 8HS concave baselines are 45.9 ± 0.600%, 42.6 ± 2.22% and 40.4 ± 1.26%, resp. The significant decrease in corner fibre content corresponds to the corner thickening findings: the convex baselines all experience some degree of corner thickening and resin accumulation in the corner with the PW being the worst performer; meanwhile, concave baselines exhibit significantly more corner thickening and resin accumulation than the convex baselines.

With respect then to QI and XP samples, the flange and corner fibre contents are roughly equal in the tape and 8HS samples (overlapping error bars). Meanwhile, the corner fibre content is markedly lower than the flange fibre content in the PW-QI sample. These observations generally support the corner thickening findings, notably that the PW conforms the least well to the selected convex tool radius. It should be stressed that fibre content values must be taken with a grain of salt when comparing UD values to QI and XP values for the tape, and tape values to PW and 8HS values. As explained in § 2.5.3 and exemplified in Fig. 4-10, longitudinal fibres (< 30° with the micrograph plane) are much more reflective owing to the heterogeneous structure of carbon fibres.

A thresholding error thus arises in addition to the inherent variability in fibre content measurements, whereby longitudinal fibres are oversampled compared to transverse fibres.

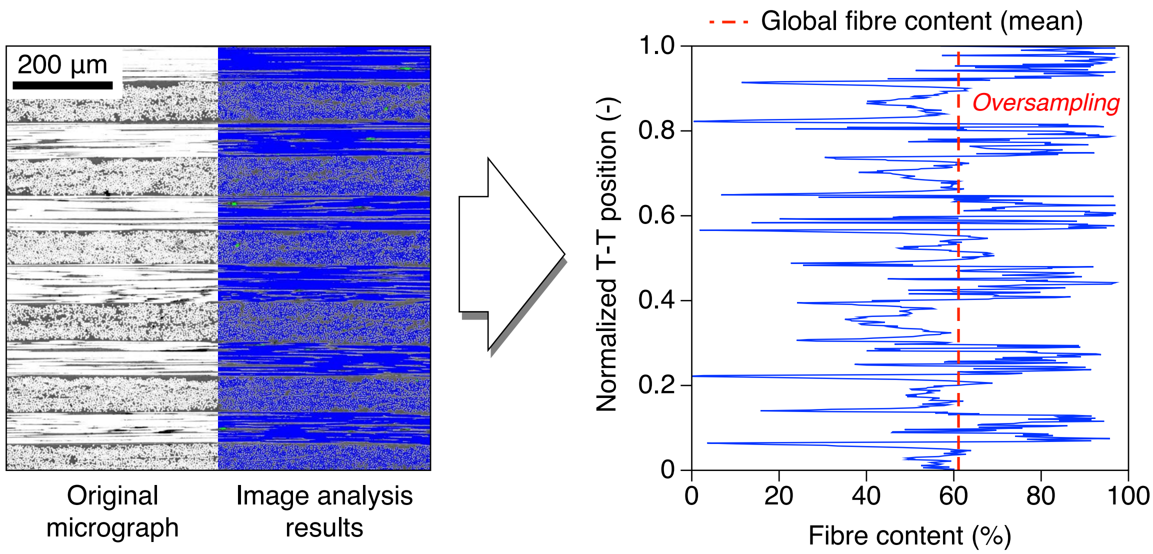

Fig. 4-10. Example of thresholding error in the case of a tape cross-ply laminate section.

Void content

Material selection is found to have a significant influence over void content, whereas tool-shape and stacking sequence are not found to have a discernable influence. With respect first to the tape, all four samples contain very low void contents well below 0.1% irrespective of location, as evidenced in Fig. 4-6. First, the RT-hold durations employed for tape samples are noticeably longer than those employed for woven samples owing to the relatively low in-plane air permeability of the tape as reported in Table 2-2. That being the case, Centea and Hubert performed micro-CT scans on similar semipregs and noted that tape laminates entrap little air during layup owing to the relatively smooth semipreg surface and prevalence of fibre nesting. In contrast, woven laminates entrap more air owing to the rougher semipreg surface and the presence of large unimpregnated spaces between tows. Lastly, the hydrostatic resin pressure in the corner of the tape concave baseline must be sufficiently high such as to effectively collapse remaining voids despite there being substantial corner thickening.

In turn, the six woven samples contain significantly more porosity, which consists mostly of inter-tow voids and only marginally of intra-tow voids. These findings are corroborated by the micrographic evidence presented in Fig. 4-7 and 4-8 and the aforementioned observations of Centea and Hubert [114]. That being the case, the PW-UD samples contain very low porosity in the flanges owing to the improved air evacuation strategy employed in this next-generation woven semipregs described in § 2.2.1 and [72]. In contrast, the 8HS semipreg does not possess surface openings that improve T-T air permeability, which explain the greater porosity found in the flanges of 8HS-UD samples. These improvements however do not seemingly extend to corners, where the PW behaves as poorly as the 8HS with global void contents above 1% despite the near-optimal processing cycle being utilized. The relatively high bulk-factor of the woven samples and the greater amount of air entrapped in woven laminates during layup seemingly outweigh the effect of improved T-T air evacuation irrespective of tool-shape.

Finally, the PW-QI sample behaves especially poorly given a mean global void content of 2.45 ± 1.64% in the corner. The 45° interply angle of the QI stacking sequence may improve interply nesting and result in less corner thickening, but it may concurrently seal the semipreg surface openings, which would explain the higher void content. The large sample standard deviation further indicates that this phenomenon may be highly localized. It would be interesting to investigate the interply compaction of next-generation woven semipregs via a hot-stage micro-CT experiment such as the one designed by Centea and Hubert for VBO flat laminates [173].

4.5.3 Deficient consolidation pressure

The discussion now shifts to the effect of deficient consolidation pressure on corner laminate quality. The mean sample thickness profiles of the twelve deficient consolidation pressure samples (Tape/PW-UD-M/F-L1/L2/L3) are presented in Fig. 4-11 alongside the four corresponding baseline profiles discussed in the previous section (Tape/PW-UD-M/F-B). In turn, the corresponding laminate quality results are presented in Fig. 4-12 in terms of mean corner thickening, and fibre and void contents. Lastly, optical micrographs of representative corner cross-sections are presented in Fig. 4-13. It should be noted that micrographs of representative, PW convex and concave baseline cross-sections (frontal plane) have already been presented in Fig. 4-7 and are therefore omitted. The results in these figures are jointly discussed throughout this section.

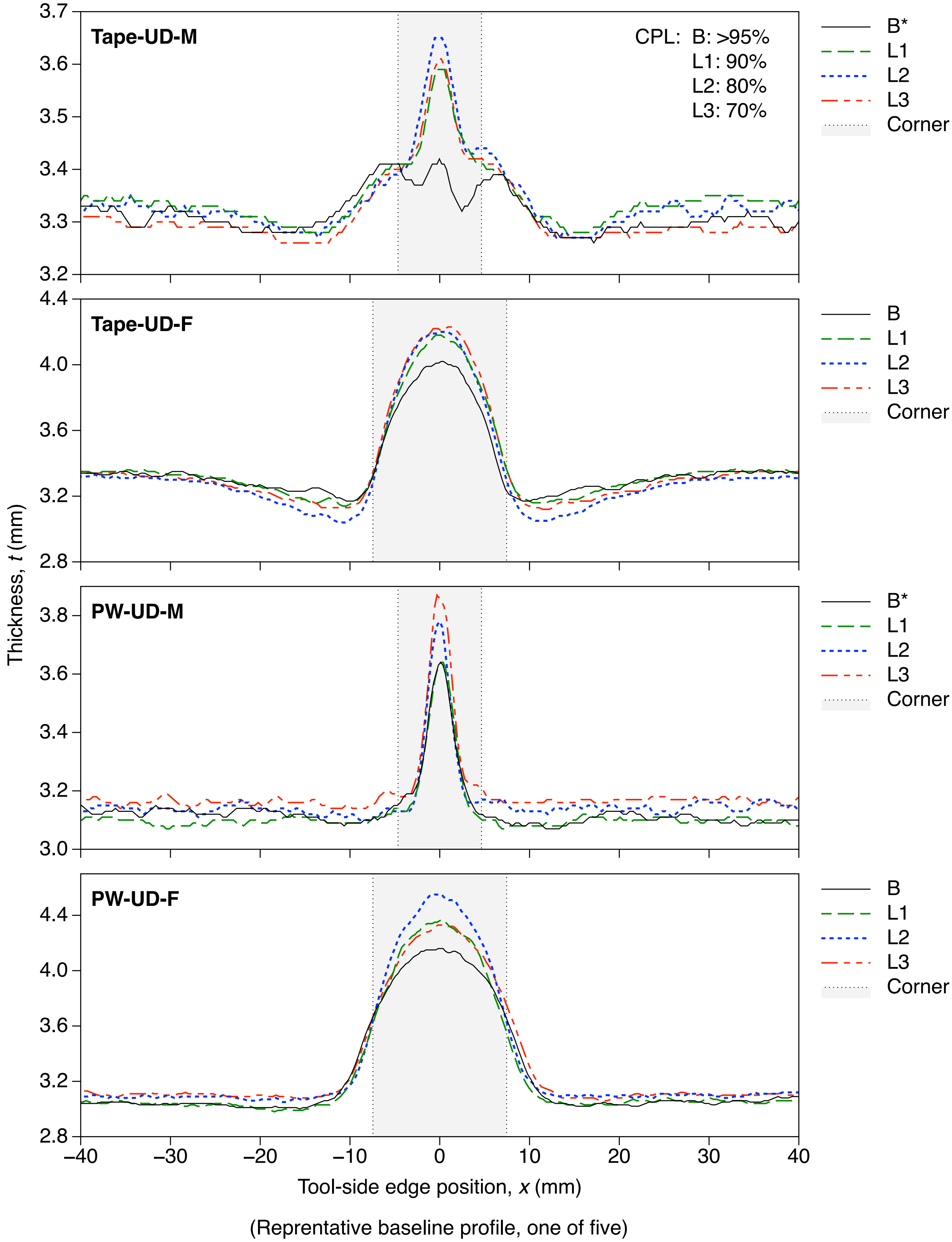

Fig. 4-11. Effect of deficient consolidation pressure on sample thickness profile.

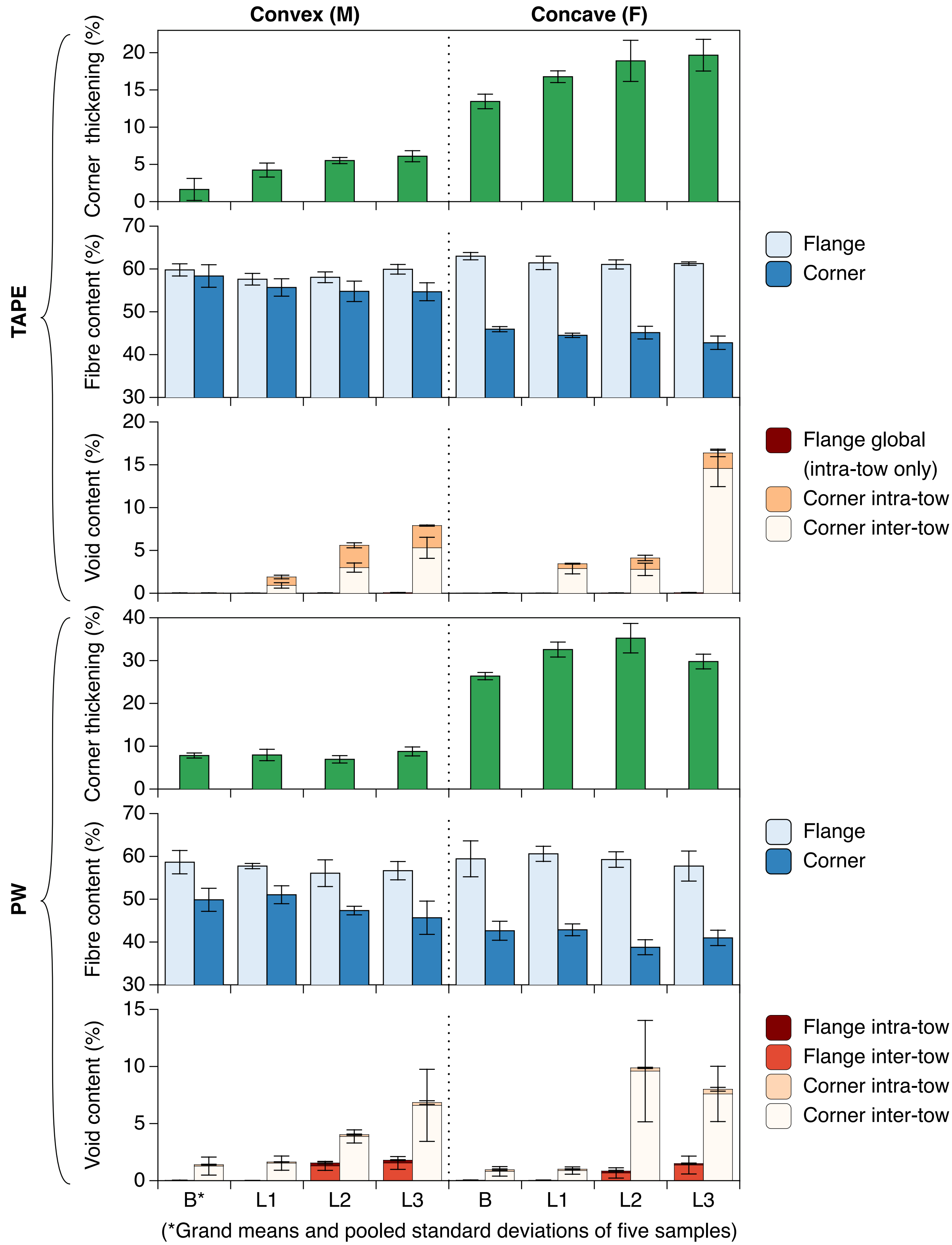

Fig. 4-12. Effect of deficient consolidation pressure on laminate quality.

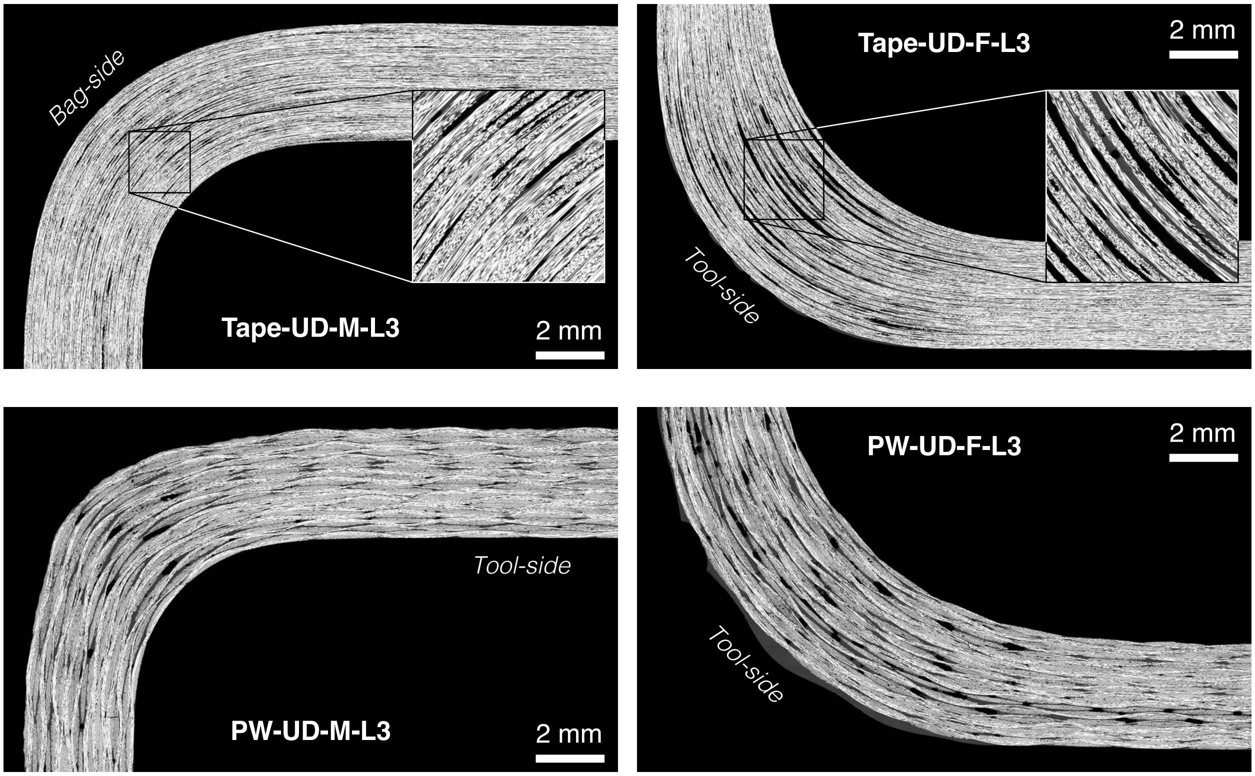

Fig. 4-13. Optical micrographs of representative deficient consolidation pressure specimens (frontal plane; brightfield illumination; 10x objective).

Thickness deviation

Deficient consolidation pressure samples follow the same, general corner thickening trend observed in baselines. As evidenced in Fig. 4-11 and 4-12, tool-shape has a noticeably greater influence on thickness deviation than does material selection, though both design factors play key roles. More specifically, the tape convex samples exhibit the least degree of corner thickening compared to the PW concave samples, which are the most affected by a wide margin.

With respect first to the tape, consolidation pressure clearly affects corner thickening in both convex and concave samples. Corner thickening increases as consolidation pressure decreases, as evidenced in Fig. 4-12. The worst consolidation pressure tested (L3: CPL of 70%) results in increases of 4.60 and 6.21% in corner thickening for convex and concave samples, resp., over the corresponding baseline mean values. Centea and Hubert observed a smaller yet distinct increase in laminate thickness due to deficient consolidation pressure in VBO flat laminates consisting of very similar materials [114]. Deficient consolidation pressure thus has a more pronounced influence over laminate thickness in corners. Furthermore, the relative difference in corner thickening between samples decreases along with consolidation pressure, which suggests a flattening of the trend. That being the case, determining the critical CPL, below which corner thickening reaches a maximum value irrespective of consolidation pressure, is futile as it occurs well below the lowest CPL to yield acceptable levels of defects. Lastly and as an aside, the thickness deviations present in the deficient tape samples effectively overlap the thickness deviations observed in baselines and discussed in the previous section. The presence of these defects is seemingly unaffected by consolidation pressure and is instead likely caused by the structure of the tape semipreg, i.e. unsupported fibres in the unimpregnated midplane.

Meanwhile, the PW samples generally exhibit a more variable trend between corner thickening and consolidation pressure, as evidenced in Fig. 4-12. First, the convex samples exhibit seemingly constant corner thickening irrespective of consolidation pressure. The lowest consolidation pressure tested (L3: CPL of 70%) results in an increase of only 0.952% in corner thickening over the corresponding baseline mean value, which is smaller than the average sample error range. In turn, the concave samples exhibit an increase in corner thickening with a decrease in consolidation pressure similar to the tape concave samples. The second lowest consolidation pressure tested (L2: CPL of 80%) results in an increase of 8.85% in corner thickening over the corresponding baseline mean value. It should be noted that the corner thickening values of the L2 convex and L3 concave samples are suspiciously small compared to the other values and may therefore be outliers.

Finally, the micrographic evidence in Fig. 4-13 corroborates the corner thickening findings. All four deficient micrographs exhibit increased ply separation and defect levels in the corners compared to the flanges. In turn, the only sample not to exhibit flagrant corner thickening is the deficient tape convex micrograph, which exhibits the least amount of corner thickening. Lastly, the two deficient concave micrographs exhibit thick resin-only regions on the tool-side edges with prevalent surface porosity.

Fibre content

Unlike corner thickening, deficient consolidation pressure has a more muted influence over fibre content, as evidenced in Fig. 4-12: the fibre content decreases slightly as consolidation pressure decreases. As noted in § 2.5.3, however, image analysis based on thresholding is not very precise with regards to fibre content measurements, which partly explains the relatively high variability of the measurements. The deficient samples have a mean and a maximum coefficient of variation of 3.51 and 8.51%, resp., which are on the order of the observed mean differences.

With regards first to flanges, maximum decreases of 2.18 and 1.99% in fibre content are observed for the tape and PW samples irrespective of tool-shape or consolidation pressure, which do not seem to bare much influence—if any. With respect then to corners, the lowest consolidation pressure tested (L3: CPL of 70%) results in decreases of 3.68 and 3.17% in fibre content for the tape convex and concave samples, resp., relative to the corresponding baseline fibre contents. Meanwhile, the lowest and second-lowest consolidation pressures tested (L3: CPL of 70%, and L2: CPL of 80%) respectively result in decreases of 4.19 and 3.86% in fibre content for the tape convex and concave samples relative to the corresponding baseline fibre contents.

Void content

Deficient consolidation pressure has a large influence on porosity, as evidenced in Fig. 4-12. Concave samples are generally more affected than convex ones similarly to corner thickening, most notably at the lowest two consolidation pressures tested (L2 and L3). That being the case, tape and PW samples are affected to a relatively similar extent.

With respect first to flanges, the tape samples exhibit negligible porosity irrespective of consolidation pressure, as evidenced in Fig. 4-12. Meanwhile, the PW samples exhibit negligible porosity only down to the first level of consolidation pressure loss (L1: CPL of 90%). The global void content rises thereafter up to a value of $1.50 \pm 0.820\%$ for the lowest consolidation pressure tested (L3: CPL of 70%). These results corroborate the observation by Centea and Hubert that tape semipreg laminates generally entrap less air during layup [114]. Nonetheless, the improved T-T air permeability of the PW renders it more resistant to porosity in the face of deficient consolidation pressure than similar woven semipregs.

With respect then to corner regions, the tape baselines exhibit negligible porosity compared to the PW baselines, which contain $1.40 \pm 0.776\%$ and $0.957 \pm 0.470\%$ for the convex and concave baselines, resp. As noted previously, the PW does not consolidate as well as the tape in corners under baseline processing conditions due to its relatively larger bulk-factor (§ 2.2.1). In turn, the corner void content significantly increases as a function of consolidation pressure unlike the flange void content. The lowest consolidation pressure tested (L3: CPL of 70%) results in global void contents of 7.90 ± 1.19% and 16.4 ± 1.18% in tape convex and concave corners, resp. Meanwhile, the lowest and second-lowest consolidation pressures tested (L3: CPL of 70%, and L2: CPL of 80%) respectively result in global void contents of 6.84 ± 3.25% and 9.88 ± 4.44 % in PW convex and concave corners. The similar global void contents between the PW and tape samples across the tested consolidation pressure range may be attributed to the improved T-T air permeability of the PW. As an aside, the intra-sample variability increases markedly as consolidation pressure decreases, notably for the lowest two consolidation pressures tested.

With respect specifically to void species, the tape baselines act akin to thick laminae given the UD stacking sequence and therefore only include intra-tow voids under near-optimal consolidation pressure. At a certain point below a CPL of 90%, the larger inter-tow voids overtake intra-tow voids as the dominant void species. In contrast, intra-tow voids are marginal in the PW samples across the spectrum of deficient consolidation pressures. Inter-tow voids are the dominant void species in all cases except the utmost attainable consolidation pressure (CPL greater than 95%). These findings are corroborated by the micrographic evidence presented in Fig. 4-13. In particular, micrographs of the tape and PW deficient, concave samples (Tape/PW-UD-F-L3) include very large intra-tow voids that partly bridge across the corner region. These voids are indicative of poor ply conformation and insufficient hydrostatic resin pressure during the cure.

Finally, empirical correlations between consolidation pressure and void species contents are presented in Fig. 4-14. Centea and Hubert found similar linear trends in VBO flat laminates for global void content [114]. Such trends are here shown to also apply to VBO corner laminates, albeit with more variability. They offer reasonable estimates of porosity in terms of void species, i.e. size and location relative to the mesostructure, with minimal experimental work (two panels or corner beams with at least five corner-sagittal micrographic cross-sections each). An acceptable consolidation pressure range based on a maximum acceptable void content may ultimately be defined for a complex-shape laminate application. In addition, such trends may be utilized to intentionally impart certain levels of porosity into experimental, complex-shape panels.

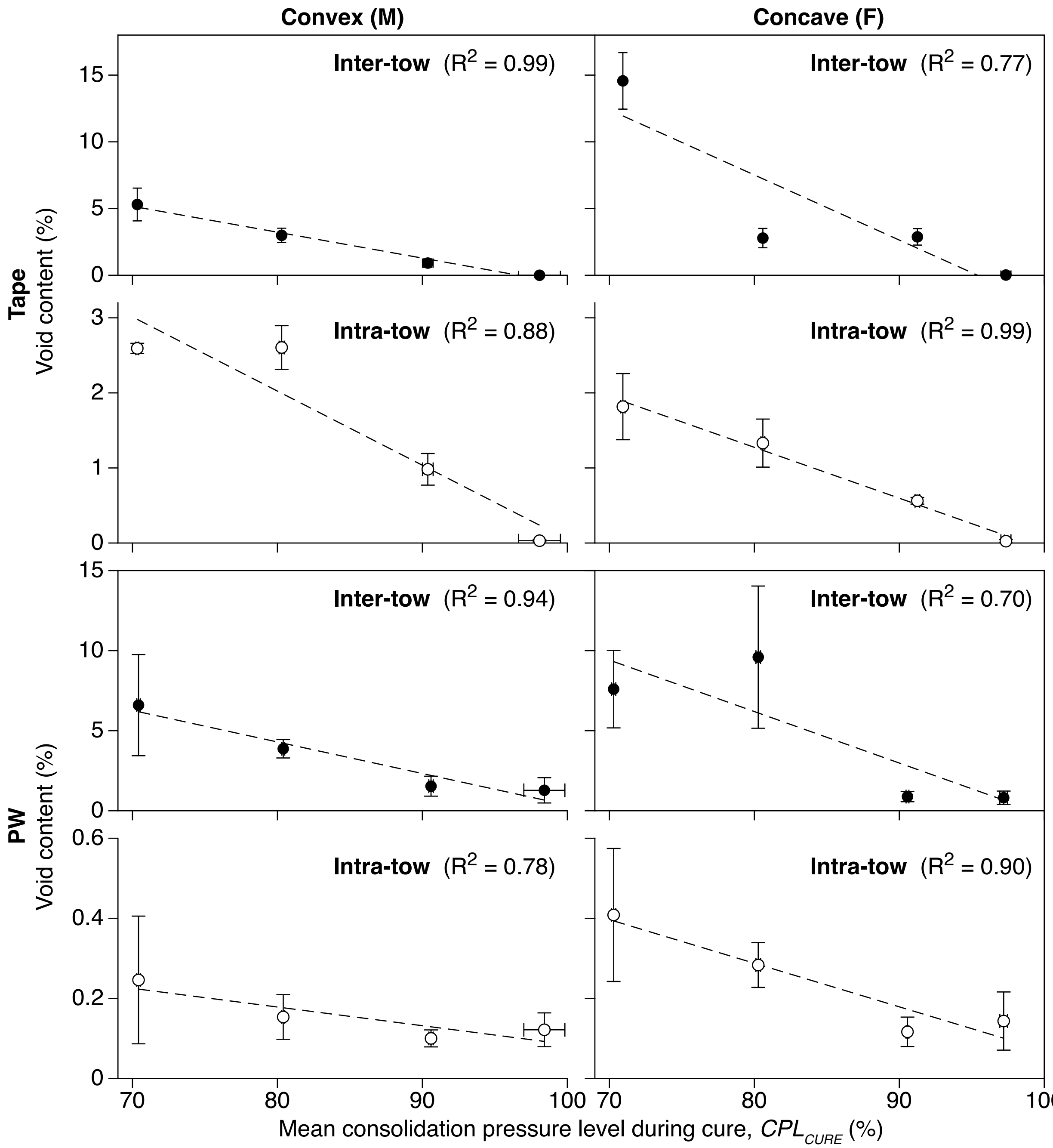

Fig. 4-14. Linear correlations between consolidation pressure and void content by species.

4.5.4 Industrial processing cases

The discussion finally shifts to the three selected industrial processing cases that deviate from the baseline process: slow temperature ramp during the cure cycle (SR), no-intermediary debulking during layup (ND) and restricted air evacuation (R). The mean sample thickness profiles are presented in Fig. 4-15, including the corresponding baseline profiles. In turn, the corresponding laminate quality results are presented in Fig. 4-16 in terms of laminate thickness, mean corner thickening, and fibre and void contents. Lastly, optical micrographs of representative corner cross-sections are presented in Fig. 4-17. It should be noted that optical micrographs of the PW and 8HS, convex and concave baselines have already been presented in Fig. 4-7 and are therefore omitted. The results in these figures are jointly discussed throughout this section.

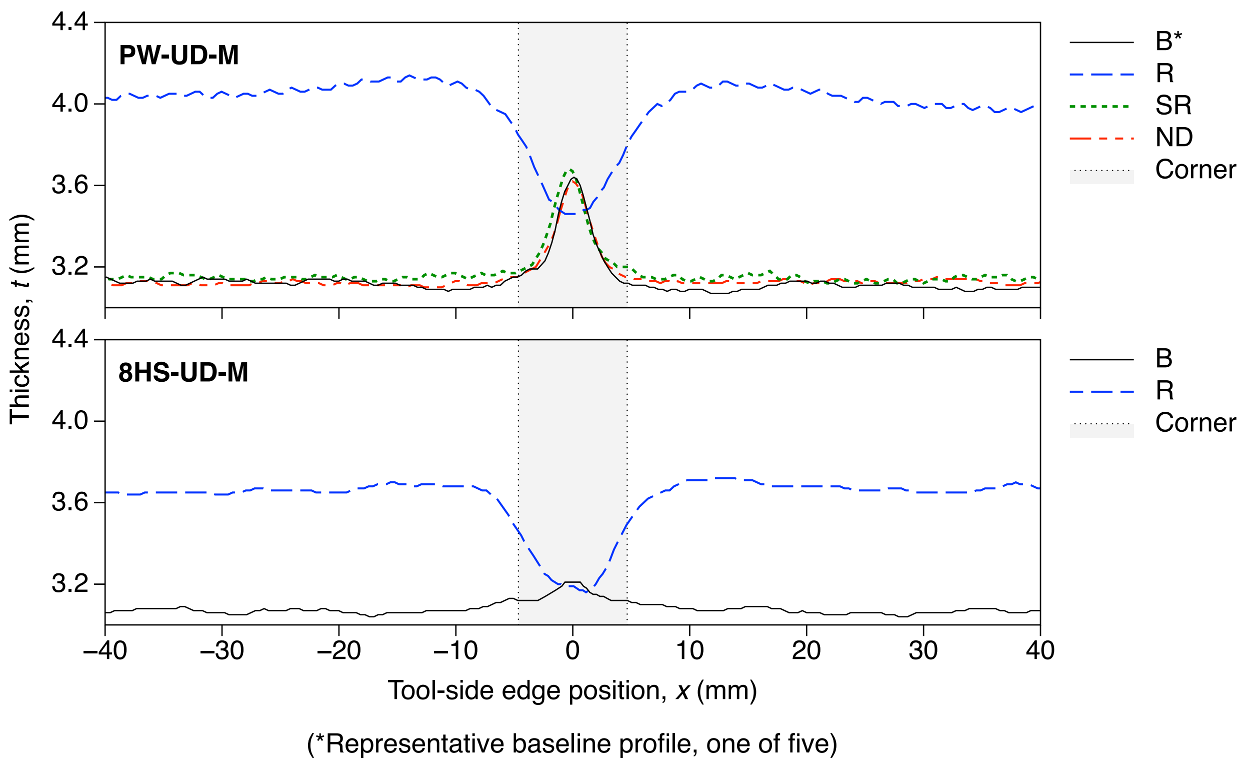

Fig. 4-15. Effect of selected industrial processing cases on sample thickness profile.

Restricted air evacuation

Centea and Hubert found restricted air evacuation to be the worst-case deficient consolidation processing condition in VBO flat laminates irrespective of reinforcement architecture [114]. The results herein indicate that complex tool-shapes further accentuate the degradation in laminate quality: restricted air evacuation results in the poorest laminate quality of any investigated convex test condition in both corners and flanges. Concave, deficient consolidation pressure samples are the only test conditions to exhibit poorer laminate quality in corners.

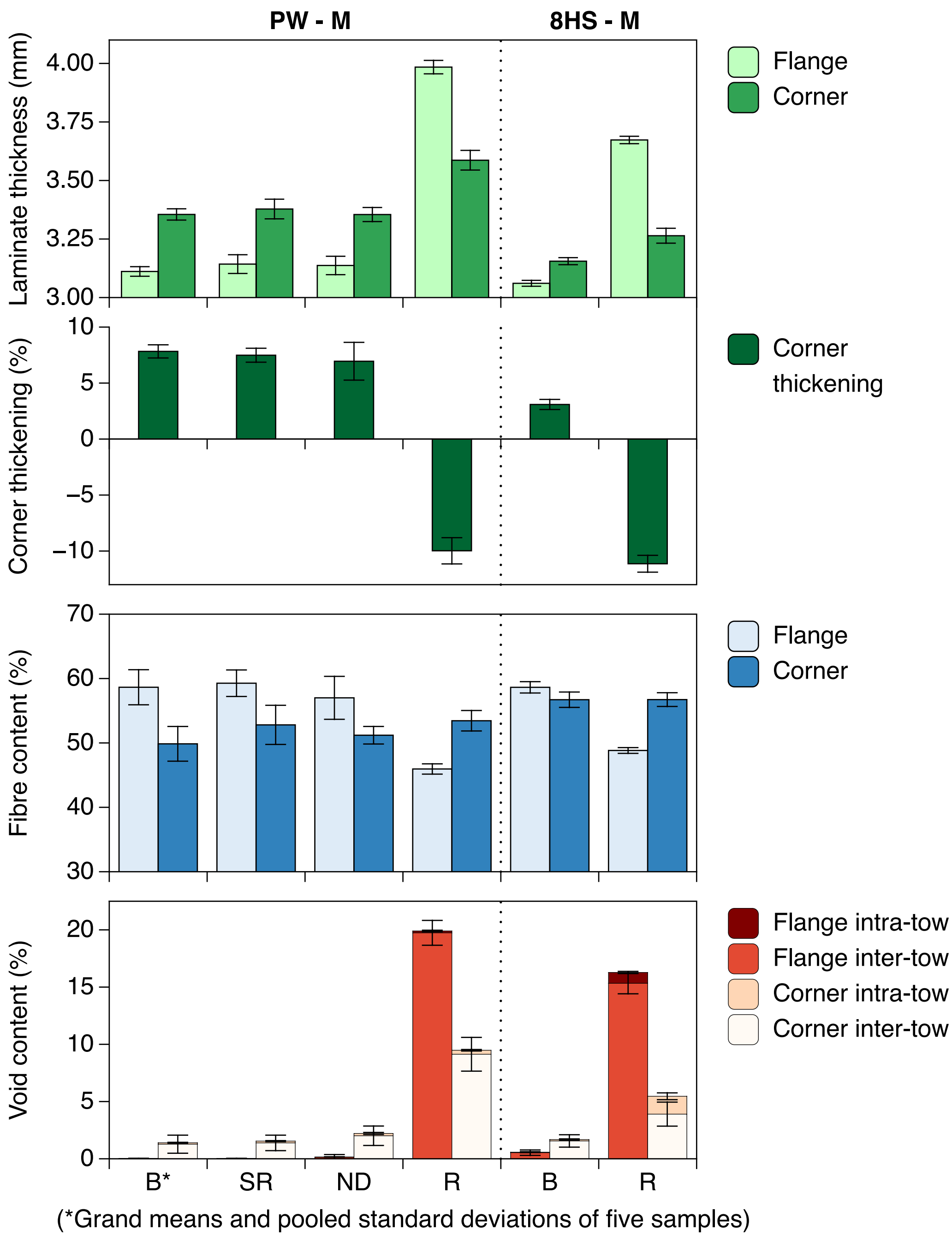

Fig. 4-16. Effect of selected industrial processing cases on laminate quality.

With respect first to thickness deviation, R-samples are thicker in the corner and thicker still in the flanges than any other convex PW and 8HS samples manufactured, as evidenced in Fig. 4-15 and 4-16. That being the case, restricted air evacuation is the only test condition to result in corner thinning compared to the flanges. The PW and 8HS R-samples exhibit 9.98 ± 1.17% and 11.1 ± 0.750% corner thinning, resp. In contrast, the flanges of the PW and 8HS R-samples are a staggering 28.1 ± 1.15% and 20.0 ± 0.666% thicker than the flanges of the respective baselines. The micrographic evidence in Fig. 4-17 corroborates these findings: flanges are very noticeably thicker than corners (PW/8HS-UD-M-R).

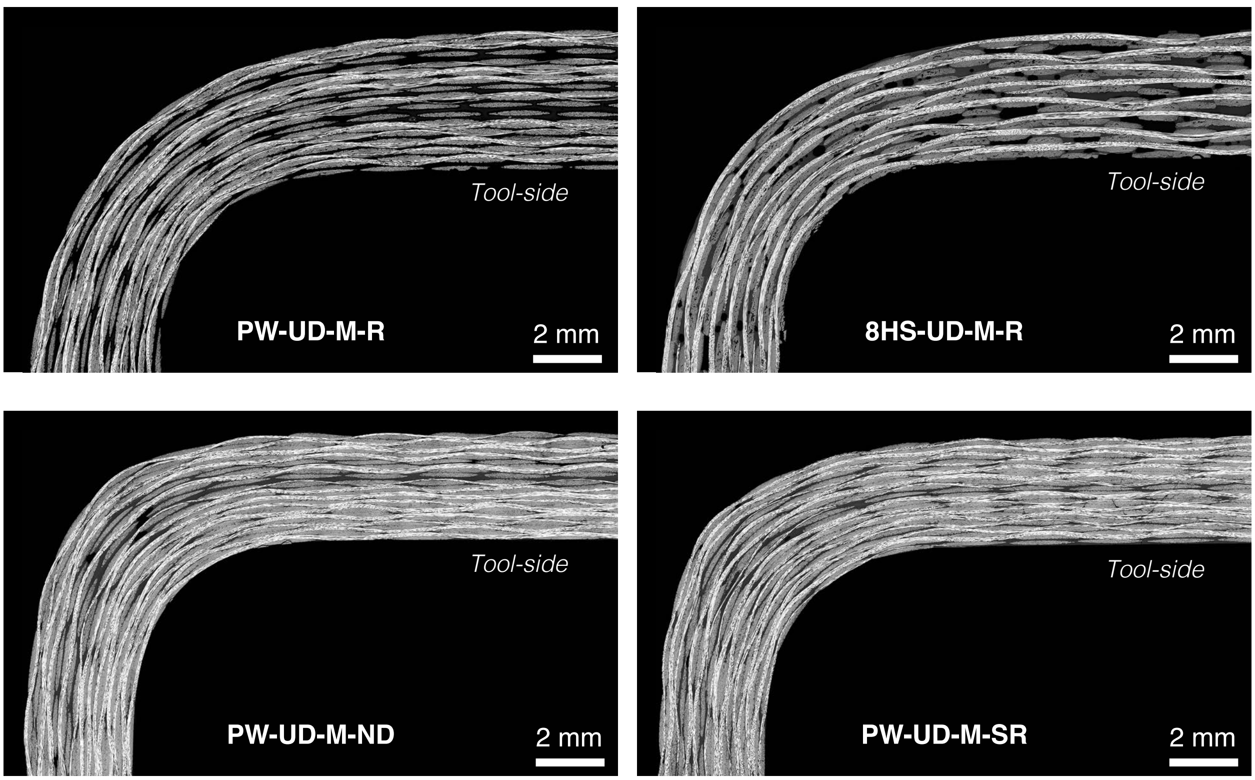

Fig. 4-17. Optical micrographs of representative specimens for the selected industrial processing cases

With regards then to constituents, the R-samples exhibit larger fibre content in corners than in flanges owing to the presence of corner thinning, as evidenced in Fig. 4-16. The PW R-sample exhibits fibre contents of 53.4 ± 1.59% and 46.0 ± 0.798% in the corner and flanges, resp., and the 8HS R-sample exhibits similar fibre contents of 56.7 ± 1.07% and 48.8 ± 0.450% in the corner and flanges, resp. In turn, the flanges of R-samples exhibit markedly smaller fibre content than the flanges of respective baselines, whereas the corner fibre contents are more similar between R-samples and respective baselines owing to similar corner thickness.

With regards finally to void content, the results match the flange thickening and corner thinning results: the flanges of both woven materials contain much larger void contents than the corners by a factor greater than two. The PW R-sample exhibits fibre contents of 19.9 ± 1.06% and 9.48 ± 1.42% in the corner and flanges, resp., and the 8HS R-sample exhibits similar fibre contents of 16.3 ± 0.831% and 5.46 ± 0.982% in the corner and flanges, resp. Furthermore, the porosity is comprised nearly entirely of intra-tow voids. The PW sample in particular exhibits an interconnected void network and very little resin between tows as evidenced Fig. 4-17. Meanwhile, large intra-tow voids in the 8HS sample are unconnected.

These findings may be generally explained by the fact that woven semipregs entrap a substantial volume of air during layup, and that the generally poorer ply conformation in corners results in a greater volume of entrapped air compared to adjacent flanges. This air remains permanently trapped inside of the laminate during consolidation and curing under restricted air evacuation. The positive differential in consolidation pressure that arises over convex corners relative to the adjacent flanges effectively squeezes the air out of corners and into adjacent flanges. The air pressure inside of the laminate keeps the inter- and intra-ply interstices resin-free and pushes the resin into the tows with the help of surface tension and capillary forces, which explains the much lower intra-tow void content of both R-samples.

More specifically, the greater level and interconnectivity of the porosity present in the PW R-sample compared to the 8HS may be attributed to the different semipreg impregnation strategies employed for each material. The PW semipreg is partially impregnated leaving surface openings that extend from surface-to-surface as observed by Préau via micro-CT scanning of a PW-UD uncured laminate [172] and as described in the patent for this new impregnation strategy [72]. Meanwhile, the 8HS semipreg is impregnated via the traditional hot-melt process that leaves no surface openings and a visibly smaller intra-ply air volume, as evidenced by micro-CT scans of an 8HS-UD uncured laminate taken by Centea and Hubert [114].

Slow cure ramp and no-intermediary debulking

Unlike the restricted air evacuation case, a slow temperature ramp during the cure cycle and the no-intermediary debulking during layup yield the same laminate quality as the baseline for

PW across all four measures of quality, as evidenced in Fig. 4-15 and 4-16. A slower temperature ramp of 0.5 °C/min is employed during the cure cycle for the SR-sample instead of 2 °C/min for the baseline, which results in a slightly higher, predicted resin viscosity minimum of 19.3 compared to 6.66 Pa·s, resp. The effect of temperature ramp on viscosity during the cure cycle is presented in Fig. 4-18. The higher viscosity does not seem to affect resin-flow nor the collapsing of voids. In turn, the use of intermediary debulking steps to improve ply collation and conformation to the tool-shape may have negligible benefits for higher areal weight and bulk-factor semipregs. It should be noted that these two industrial processing cases may significantly affect laminate quality in tape corners owing to lesser areal weights and bulk-factors, as well as the densely-packed structure of the fibre-bed, which, in turn, may impede resin flow.

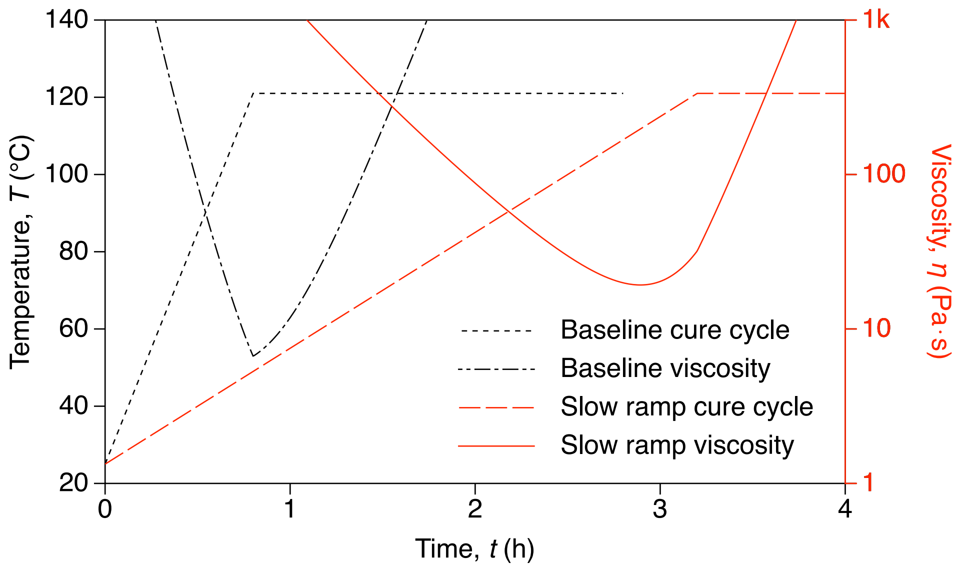

Fig. 4-18. Effect of temperature ramp rate on viscosity during the cure cycle.

4.6 Summary

This experimental chapter investigates the effect of three categories of factors identified as likely to affect laminate quality in corners, namely design factors, generally deficient processing conditions and noteworthy industrial processing cases. The novelty of this work lies in the systematic investigation of factors that have previously either been investigated only in the case of

VBO flat laminates (i.e. deficient consolidation pressure, restricted air evacuation and slow temperature cure ramp [114, 118, 124]) or for a limited selection of current VBO woven semipregs (i.e. PW, 5HS and 8HS Cytec CYCOM 5320-1 [69, 121]). In addition, an in-depth statistical analysis of the repeatability of experiments is conducted to qualify the soundness of the findings, which is very seldom attempted in this type of research. A number of key findings may thus be extracted from the results to aid in future, complex-shape part design with next-generation semipregs.

Experimental repeatability. A comprehensive statistical analysis is assembled to answer two fundamental questions about the proposed experiments: are the findings statistically repeatable? And what is the intrinsic variability of experimental measurements? The analysis adapts statistical tests and methods used in the determination of statistically-based material properties and interferential statistics used in interlaboratory studies. The present experiments are not strictly repeatable given the statistically significant difference in repeated sample means for three selected laminate quality measurements (i.e. laminate thickness, and fibre and void contents). This finding is shown to be true for sets of repeated VBO tape and PW samples manufactured for this work and for very similar sets of repeated VBO and autoclave, tape and PW samples obtained from an expert research environment (i.e. NIAR). Single-sample test conditions must therefore be interpreted with caution. That being the case, the precision of the present research environment compares favorably to that of an expert research environment given the generally lower inter- and intra-sample variability of the laminate quality datasets from samples manufactured for this work.

Design factors. With respect first to material selection, tape samples exhibit less corner thickening, better conformation to both convex and concave tool-shapes, and negligible void content in both corners and flanges compared to PW and 8HS samples. Tape generally result in higher laminate quality in corners given a smaller areal weight and bulk-factor and given that significantly less air is entrapped during layup despite a lower in-plane permeability. In addition, the next-generation PW with improved T-T air permeability performs as advertised in flanges and results in negligible void content. The benefits however do not translate to corners, where bulk-factor and ply conformation and deformation play dominant roles. The use of a perforated peel-ply and breather layer that lets air escape but effectively blocks resin-bleeding should be considered to improve the PW's performance in corners.

With respect then to tool-shape, concave corners result in markedly lower laminate quality in terms of corner thickening, and more muted effects in terms of baseline void contents. Nonetheless, corner thickening occurs for all baselines given a combination of phenomena, namely interply friction in flanges, pressure differentials between corners and flanges, and the effect of bulk-factor.

With respect finally to stacking sequence, QI and XP layups do not significantly affect the laminate quality of tape corners. That being the case, a QI layup results in a small decrease in corner thickening for both the PW and 8HS and a small decrease in corner void content for the 8HS. In general, corners with fewer fibres in the hoop direction conform better to the tool-shape and exhibit fewer voids thanks to a sufficiently high hydrostatic resin-pressure. The presence of interply angles impedes ply nesting in tape corners and thus explains the muted improvement in quality. In contrast, interply angle may improve ply nesting in woven corners. Lastly, the next-generation PW behaves surprisingly poorly: a side-effect of the improved ply nesting may be the effective sealing of T-T air evacuation channels.

Process deviations and deficiencies. With respect first to deficient consolidation pressure, the effects of material and tool-shape are accentuated: corner thickening and void content generally increase as the consolidation pressure drops. VBO semipreg processing relies crucially on the limited consolidation pressure available to consolidate the laminate and supress void formation. Any deficiency therefore translates directly into higher defect levels. In turn, corners are much more affected than flanges, owing to the complexity and interaction of the aforementioned phenomena. That being the case, tape laminates are demonstrably more robust than the 2D-woven semipregs on account of the smaller volume of entrapped air.

Furthermore, void species vary predictably with consolidation pressure irrespective of material or tool-shape. Empirical linear correlations may be generated for a given design case with minimal experimental work. Porosity may therefore be estimated in terms of void species for a given consolidation pressure. Conversely, linear correlations may be utilized to impart desired levels of porosity into experimental, complex-shape panels to investigate the effect on interlaminar mechanical properties.

With respect then to noteworthy industrial cases, restricted air evacuation results in the worst overall laminate quality. The entrapped air pressure impedes laminate consolidation and results in very significant intra-tow void contents, which form an interconnected network in the case of the next-generation PW given the lesser extent of initial resin impregnation and the presence of T-T air evacuation channels. In addition, the higher consolidation pressure in corners result in corner thinning, though corners are thicker than the corresponding convex baseline corners. The air is effectively squeezed into the neighbouring flanges given the positive pressure differential in convex corners, and in turn, the flanges are markedly thicker than for the corresponding convex baseline flanges. Though untested, the tape is likely to also be significantly affected by restricted air evacuation based on the results of experiments conducted on VBO flat laminates by Centea and Hubert [114]. Finally, the other two industrial cases, namely the slow temperature cure ramp and no-intermediary debulking, did not significantly affect laminate quality—although they could only be tested for the PW.

Design guidelines. the experimental results herein make clear that producing high-quality semipreg laminates via VBO processing is more challenging for complex-shape parts than flat ones, though it may be achieved by following certain guidelines and best practices:

- A tape laminate generally yields superior laminate quality compared to 2D-woven semipregs over singly-curved features (e.g. corners). Meanwhile, doubly-curved features may necessitate semipregs with superior drapability (e.g. PW).
- Air evacuation is a critical factor. Limiting the volume of entrapped air during layup is vital and may be partly achieved via material selection (e.g. tape). In turn, fully evacuating entrapped air prior to the cure cycle may be achieved by designing a sufficiently long RT-hold, which requires: 1) accurate air permeability values for the given laminate, and 2) appropriate part design and vacuum-bagging arrangement so as to limit air evacuation distance and the number of obstacles that may locally collapse air evacuation channels (e.g. sharp tool features, inserts, ply-drops).
- In this same vein, consolidation pressure must be maximized by ensuring an adequate ambient pressure (i.e. minimizing the effects of elevation and weather) and an adequate vacuum-bag pressure (i.e. reliable equipment and proper vacuum-bagging technique). A CPL of 98 kPa (29 inHg) is recommended for sharply-curved details, whereas 95 kPa (28 inHg) is typically sufficient for flat laminates.
- Finally, laminate consolidation in corners is most often impeded by interply friction and at the very least local pressure differentials. Uniform part thickness is therefore best achieved by selecting convex tool features over concave ones and relaxing the radius of curvature

whenever possible. In turn, proper ply collation and conformation during layup via proper operator skill and intermediary debulking are vital. The use of a pressure intensifier strip may also be considered in problematic but necessary concave features.

5

Mechanical performance of corners

5.1 Introduction

Large-scale, complex-shape composite parts such as primary aircraft structures are functionally-critical, load-bearing structures that may experience complex load cases with critical out-of-plane components. Laminate regions containing sharply-curved features are especially prone to interlaminar tensile (ILT) failure via delamination given the intrinsic weakness of the T-T mechanical performance of composite laminates, which is largely influenced by matrix properties [33, 41]. Furthermore, curved laminates produced via VBO semipreg processing have an increased propensity for variability and the presence of failure-initiating defects in corners, as evidenced in Chapter 4 and the available literature [69, 121, 130, 138].

A handful of numerical and experimental studies have hitherto investigated the robustness of VBO semipreg processing with respect specifically to curved laminates [69, 121, 129, 137, 138]. These studies are however limited in scope to laminate quality. In order to develop a full understanding of the robustness of semipregs for large-scale, complex-shape applications, it is important to additionally investigate the ILT performance of representative specimens and establish a causal link wherever possible with the key factors influencing laminate quality. To this end, Olsson ascertains that the 4PB-CBS test method and the corner specimen are well suited to investigate defect-dependent, material properties associated with actual complex-shape parts [32], rather than ideal material properties that are independent of specimen geometry and laminate quality.

Key factors are selected and investigated in Chapter 4 for their likely effect on laminate quality, which may generally be sorted into the following three categories: 1) design factors, 2) generally deficient processing conditions and 3) noteworthy industrial processing cases pertinent to VBO semipreg processing. These same factors are retained for this chapter to assess their respective effect on ILT performance via the 4PB-CBS test method. In particular, the selected design factors include material selection (i.e. tape, PW and 8HS), tool-shape (i.e. convex or concave) and stacking sequence (i.e. UD, QI and XP). In turn, the selected, generally deficient processing conditions are limited to a single process parameter: consolidation pressure, which is manipulated by simply reducing vacuum pressure inside of the vacuum-bag during the RT-hold and cure cycle. Lastly, the selected, noteworthy industrial cases consist of a slower temperature ramp during the cure cycle (SR), layup without intermediary debulking steps (ND), which improve ply collation, and restricted air evacuation (R). It should be noted that these factors and the rationale for their selection are presented in full in the introductory section of Chapter 4.

Lastly, complex-shape parts exhibit a type of variability that has not yet been investigated in this work: fibre misalignment and more specifically waviness [130, 141, 153]. This irregularity is not necessarily a defect in the sense that it is an unavoidable outcome of design decisions that cannot simply be remedied via a stricter adherence to an established processing cycle. Potter *et al.* further discuss the dichotomy between design allowables obtained from flat coupon testing programs and the properties of actual composite parts, which are often larger in scale and contain complex features and geometries [220]; their literature survey focuses on fibre waviness and misalignment. Visual inspection of the smooth, tool-side surfaces of tape convex baseline specimens (Fig. 4-9) indicates significant in-plane fibre waviness as noted in § 4.5.2. This finding warrants a more in-depth investigation of the extent of fibre waviness into the corner specimen flanges, its magnitude and morphology in the corner, and its effect on corner mechanical performance.

5.2 Chapter objectives and outline

The objectives of the following chapter are threefold: 1) as in Chapter 4, investigate the repeatability of the experiments to assess the dependability of the findings, this time with respect specifically to interlaminar strength measurements; 2) investigate the effect that design factors, deficient consolidation pressure and noteworthy industrial processing cases have on interlaminar mechanical performance in corners; and 3) investigate the extent, magnitude and morphology of fibre waviness in baseline convex tape specimens and its effect on stiffness (i.e. elastic properties). The desired outcome of this work is to link the corner laminate quality findings presented in Chapter 4 to interlaminar mechanical performance. Previous studies that have investigated the key factors influencing the laminate quality of VBO corner laminates forgo interlaminar mechanical characterization [69, 121, 129, 137, 138], which is an integral aspect of complex-shape, composite part design. Lastly, this work aims to further investigate the observation by Farnand *et al.* that the presence of air evacuation midplanes of semipreg tapes play an important role in the formation of in-plane waviness in corners [153].

The chapter outline is as follows. The repeatability study presented in § 4.4 is continued in § 5.3 with a focus on interlaminar strength measurements. Mechanical testing results for the experimental test matrix are then presented and discussed in § 5.4 and divided into the three aforementioned categories of factors. It should be noted that these results are based on the experimental test matrix presented in § 4.3, which is shared between Chapter 4 and this chapter. Finally, the work on fibre waviness is presented in its entirety in § 5.5.

5.3 Experimental repeatability study

5.3.1 Overview

The following section is a continuation of the repeatability study presented in § 4.4. The attention now shifts from the repeatability of laminate quality measurements to that of interlaminar strength measurements. The original motivation, material selection and inferential statistical methodology remain otherwise unchanged. To reiterate the stated objectives, the investigation centers on answering the following two questions: 1) Do samples for a given test condition and measurement type (i.e. a single dataset) belong to a single population? And 2) what is the associated inter- and intra-sample variability for this dataset? How the variability of interlaminar strength measurements differs from that of laminate quality measurements is of particular interest given that the two categories of measurements are evidently different in nature and that interlaminar properties are highly dependent on laminate quality [32, 88, 90].

5.3.2 Data selection

The same six materials selected and detailed in § 4.4.2 are herein utilized. The 5320 datasets are procured from the experimental work performed by the author, and datasets for the remaining four materials are procured from NCAMP: the 5320-1 datasets [163, 164] are representative of an advanced VBO semipreg system that is very similar to the 5320 system, and the 8552 datasets [165, 166] are representative of a typical autoclave system. In turn, two interlaminar mechanical properties are selected: interlaminar tensile strength (ILTS), which is a focal point of this chapter, and apparent interlaminar shear strength as measured via short-beam strength (SBS) testing. The dataset sizes for each measurement type and the associated test methods are given in Tables 5-1 and 5-2.

Table 5-1. Dataset sizes for the repeatability analysis of interlaminar strength measurements.

	5320/tape	5320/PW	5320-1/tape	5320-1/PW	8552/tape	8552/PW
(Datasets)	*(No. of panels × No. of observations = total No. of observations)*					
ILTS	5 x 5 = 25 (ea.)		1 x 7 = 7 (ea.)		1 x 8 = 8 (ea.)	
SBS	n/a (ea.)		6 x 3.49* = 21 (ea.)		6 x 4 = 24	6 x 3.49* = 21
Data source:	Current work		[163]	[164]	[165]	[166]

*Effective sample size (i.e. unequal sample sizes)

Table 5-2. Interlaminar strength measurements and associated test methods.

Source	Measurement	Method	Reference
Current work: 5320-system [170]	ILTS*	4PB-CBS test with stiffening-sleeves	Sect. 3.3
NCAMP datasets: 5320-1 8552 systems [68, 162]	ILTS** SBS^	Regular 4PB-CBS test 3-point bending test	ASTM D6415 [90] ASTM D7028 [206]

Dataset comprising of *5 and **1 corner beams, and ^6 SBS flat panels for each respective material.

It should be noted that the 5320 ILTS datasets and the NCAMP SBS datasets originate from the same sets of five convex corner beams and six SBS flat panels, resp., from which the laminate quality measurements detailed in § 4.4.2 originate. This section should thus be revisited for a more comprehensive presentation of the materials, layup and baseline processing conditions, as well as to recall important clarifications concerning the structure of the datasets. In particular, the NCAMP datasets are comprised of samples from different material batches, which may slightly inflate inter-sample variability by inextricably including a small degree of inter-batch variability.

The NCAMP Material Data Property Reports (MDPRs) follow the guidelines for property testing of composites set in Chapter 2 of the *Mil-Handbook-17*, which include SBS as a lamina property to be tested for material qualification but do not include ILTS [140]. The MDPRs nonetheless include single-sample ILTS datasets that may thus only be compared to the corresponding 5320 five-sample datasets in terms of intra-sample variability. Multi-sample SBS datasets are instead analyzed for each of the four NCAMP materials to approximate the statistical significance in mean sample differences and inter-sample variability associated with interlaminar strength measurements procured from an external and expert research environment.

It should finally be noted that ILTS values determined via the 4PB-CBS method are widely reported to be especially affected by specimen geometry, and laminate and edge quality [32, 88, 90, 92]. Most notably, Makeev at al. linked the very low void content expected for CFRP tape samples processed via baseline processing conditions to high data scatters with coefficients of variation that may surpass the 20% mark [93]. In contrast, Wisnom *et al.* demonstrated that SBS values are likewise affected by the presence of large critical voids and heterogeneous void distributions, although coefficients of variation are typically within the 5% mark irrespective of laminate quality [221]. These coefficients of variation are representative of the expected intra-sample variability from the available literature and may be compared to respective variability statistics obtained from the selected datasets.

5.3.3 Statistical results and implications

The statistical results of the repeatability study associated with interlaminar strength measurements are summarized in Table 5-3. In answer to the first question (do samples belong to a single population?), 3 of the 6 datasets analyzed contain at least one statistically significantly different sample. A one-way ANOVA (either classic Fisher of modified Welch formulation) is performed for 3 of the 6 datasets that satisfy the assumptions. As is the case for the laminate quality datasets, the ANOVA confirms the results of the less powerful k-sample Anderson-Darling test (ADK). In addition, no discernable pattern is found to explain the trend beyond noting once again the relatively high inter-sample variability that is generally associated with composite laminates.

Next, the ILTS grand means may be compared to assess the relative interlaminar performance of each material. With respect first to the similar VBO materials, the 5320/tape performs more than twice as well as the 5320-1/tape given mean ILTS values of 113 and 51.0

MPa, resp., corresponding to a 55% difference. Meanwhile, the 5320/PW and 5320-1/PW perform very similarly given mean ILTS values of 35.1 and 35.0 MPa, resp. As presented in Table 4-5, the 5320/tape contains very little corner porosity compared to the 5320/PW (0.0271 and 1.24%, resp.). Even though no void content data is available for the NCAMP ILTS datasets, it can be deduced that the 5320-1/PW samples share a similarly-large void content with the 5320/PW samples, which ensures a high-likelihood that a critical void is present in the region of highest radial stress to initiate failure. In turn, the 5320-1/tape must additionally have a relatively large void content to explain the much lower ILTS value despite being essentially identical on paper to the 5320/tape laminate.

Table 5-3. Summary of the statistical results for the interlaminar strength datasets.

Material	Single population?	Method	$\bar{\bar{x}}$	s_W	cv_W (%)	s_B	cv_B (%)
ILTS (MPa)							
5320 / tape	yes	ADK	113	5.23	4.62	3.04	2.69
5320 / PW	no	Fisher	35.1	1.66	4.74	2.22	6.32
5320-1 / tape	n/a	n/a	51.0	5.59	11.0	n/a	n/a
5320-1 / PW	n/a	n/a	35.0	2.30	6.57	n/a	n/a
8552 / tape	n/a	n/a	58.2	14.6	25.1	n/a	n/a
8552 / PW	n/a	n/a	83.5	8.80	10.5	n/a	n/a
SBS (MPa)							
5320-1 / tape	no	ADK	108	2.96	2.75	1.80	1.67
5320-1 / PW	yes	Welch	76.1	2.47	3.25	1.29	1.70
8552 / tape	yes	ADK	144	4.00	2.78	1.82	1.26
8552 / PW	no	Welch	89.6	2.11	2.36	1.57	1.75

It would be remiss not to acknowledge the effect of specimen size on ILTS. The corner specimen utilized in this thesis is dimensionally 20% smaller than the regular corner specimen prescribed by the ASTM D6415 test standard, which NIAR utilizes to generate the NCAMP ILTS datasets (§ 2.3.1). Wisnom and Jones demonstrated that the determination of ILTS via the 4PB-CBS method is especially sensitive to size-effect with a four-fold increase in specimen dimensions yielding a 44% decrease in ILTS compared to a smaller 12% decrease in SBS [88]. The specimen size difference herein is likely responsible for at most 15 of the 55% difference in ILTS values observed between the 5320/tape and 5320-1/tape datasets. It should further be noted, as evidenced in Chapter 3, that the use of stiffening-sleeves effectively eliminates the otherwise significant error in the applied bending moment determination, which results in a more conservative and accurate determination of the ILTS. The difference in actual ILTS is therefore likely greater than the observed 55%.

With respect then to the autoclave materials, the 8552/tape performs similarly to the 5210-1/tape and significantly worse than the 5320/tape given a mean ILTS of 58.2 MPa. The samples likely contain substantial porosity in the corners. Meanwhile, the 8552/PW performs seemingly significantly better than the two VBO PW given a mean ILTS of 83.5 MPa. This unusually high reported value for a 2D-woven laminate may partly be explained by the overestimation of the applied bending moment given that no stiffening-sleeves were used by NIAR.

Finally, the calculated variability statistics for each dataset are plotted in Fig. 5-1 in answer to the second question (how samples differ in practicality?). First, only 1 of the 6 datasets (16.7%) displays a greater inter-sample than intra-sample variability, which follows the trend observed for the laminate quality measurements. Second, the inter- and intra-sample variabilities of short beam strength measurements fall below the 5% mark as expected and irrespective of the resin system and reinforcement architecture. Meanwhile, the variability in ILTS measurements for the 5320 datasets is markedly lower than anticipated most notably for the 5320/tape, which also falls below the 5% mark. This result may be attributed to a very high-quality corner region for the 5320/tape samples (Fig. 4-7) and a generally excellent specimen preparation. The intra-sample variability of the NCAMP single-sample ILTS datasets are comparatively much larger given that 3 of the 4 datasets exhibit coefficients of variation in excess of 10% with one reaching a staggering 25.1%. The latter dataset is likely not solely explained by the presence of corner porosity; it may rather be indicative of potential issues regarding specimen preparation.

In conclusion, the statistical results obtained for interlaminar strength datasets generally corroborate the findings from the first part of this experimental repeatability study regarding laminate quality measurements. Samples in a given dataset cannot generally be assumed to belong to a single population given seemingly random yet statistically significant differences in sample means. The experimental findings presented in the remainder of this chapter, which are based on single-sample datasets, speak to general, observable trends, but they are statistically inconclusive and should therefore only be considered in the same vein as the results of a pilot study. That being the case, the research environment created for this work compares favorably to the expert testing environment that exists at NIAR and similar, expert research and industrial institutes. The variability statistics reveal that the corner specimen preparation and mechanical testing methods employed in this thesis generate interlaminar strength data with lower variability than similar results generated by NIAR or typically reported in the literature.

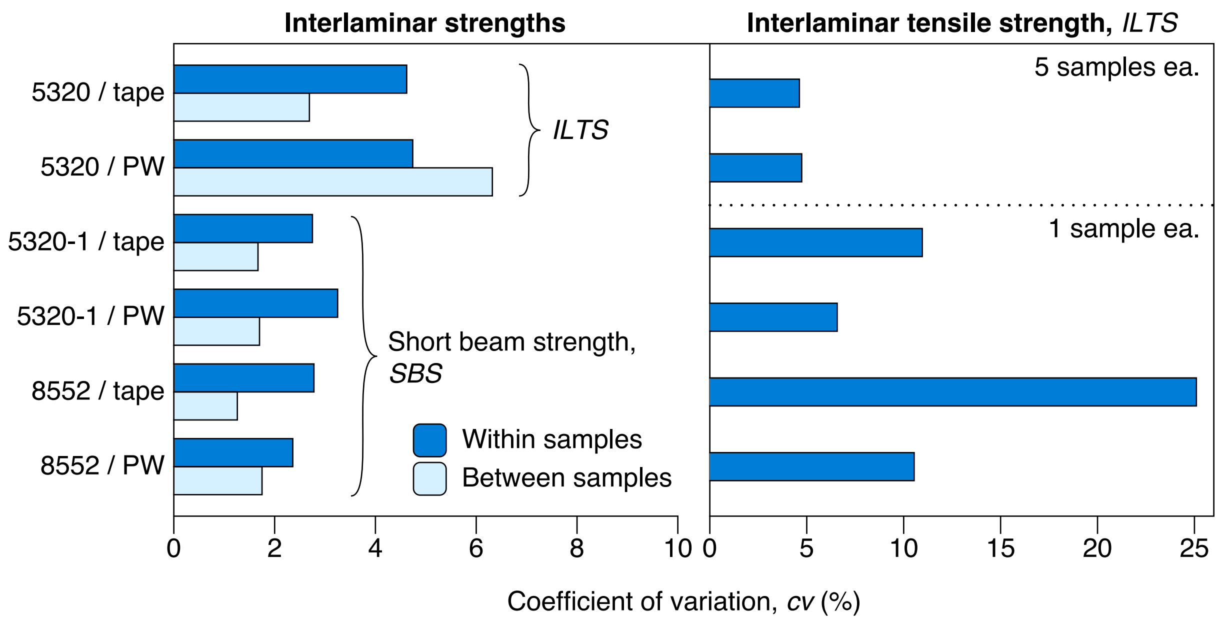

Fig. 5-1. Inter- and intra-sample variability for the interlaminar strength datasets.

5.4 Corner mechanical performance results and discussion

5.4.1 Overview

The mechanical performance in corners is assessed herein in terms of three quantitative measurements with a focus on ILTS: curved beam strength (CBS), interlaminar tensile strength (ILTS) and energy-to-failure (E_f). The findings are corroborated with qualitative observations made via visual inspection of load-displacement curves, specimen free-edge surfaces and optical micrographs of representative, failed corner specimen cross-sections taken in the corner sagittal plane (§ 2.5.3). The same five-specimen sets randomly selected in Chapter 4 for the sample thickness analysis are herein tested to failure in 4PB-CBS with the aid of stiffening-sleeves (§ 3.3.2). It should be reiterated that the failure point is defined for the purposes of this work as the first substantial load-drop, which is typically associated with the onset of ILT delamination [81, 83, 90]. The pertinent methods for specimen preparation, and mechanical testing and analysis are listed in Table 5-4 for reference.

Table 5-4. List of pertinent methods for the mechanical testing of corner specimens.

Method	Section
Material selection	§ 2.2.1
General processing cycle	§ 2.2.2
General specimen preparation	§ 2.3
Specimen thickness measurement	§ 2.4
4PB-CBS mechanical testing method with the aid of stiffening-sleeves	§ 3.3.2
General optical microscopy sample preparation and imaging	§ 2.5.3
Energy-to-failure measurement description	§ 3.7.3
Experimental test matrix and special sample conditioning	§ 4.3

5.4.2 Baselines and design factors

The discussion of mechanical testing results begins with the three selected design factors: material selection, tool-shape and stacking sequence. Typical load-displacement curves are presented in Fig. 5-2 for the six baselines (Tape/PW/8HS-UD-M/F-B) and the four samples consisting of alternate stacking sequences other than the UD layup (i.e. QI and XP). It should be noted that specimens selected for plotting were loaded beyond failure to a maximum displacement of 10 mm whenever applicable to capture the damage propagation following the initial load-drop. Curves that end abruptly, however, experienced sudden load-drops surpassing the selected test frame safety limit of 80% of the peak load, which results in immediate test termination. In turn, optical micrographs of representative, failed specimen cross-sections are presented in Fig. 5-3 and 5-4 for baseline and alternate stacking sequence samples, resp. It should be noted that the selected failed specimens were loaded up to and not beyond the first load-drop such as to only incur damage related to the onset of ILT delamination.

Lastly, the mean mechanical properties are presented in Fig. 5-5. It should be noted that the tape and PW convex baseline values (Tape/PW-UD-M-B) are each comprised of grand means and pooled standard deviations determined from five-sample sets (Eq. (4-4) and (4-6), resp.). The results in these figures are jointly discussed throughout this section alongside references to result figures presented in the previous chapter (§ 4.5).

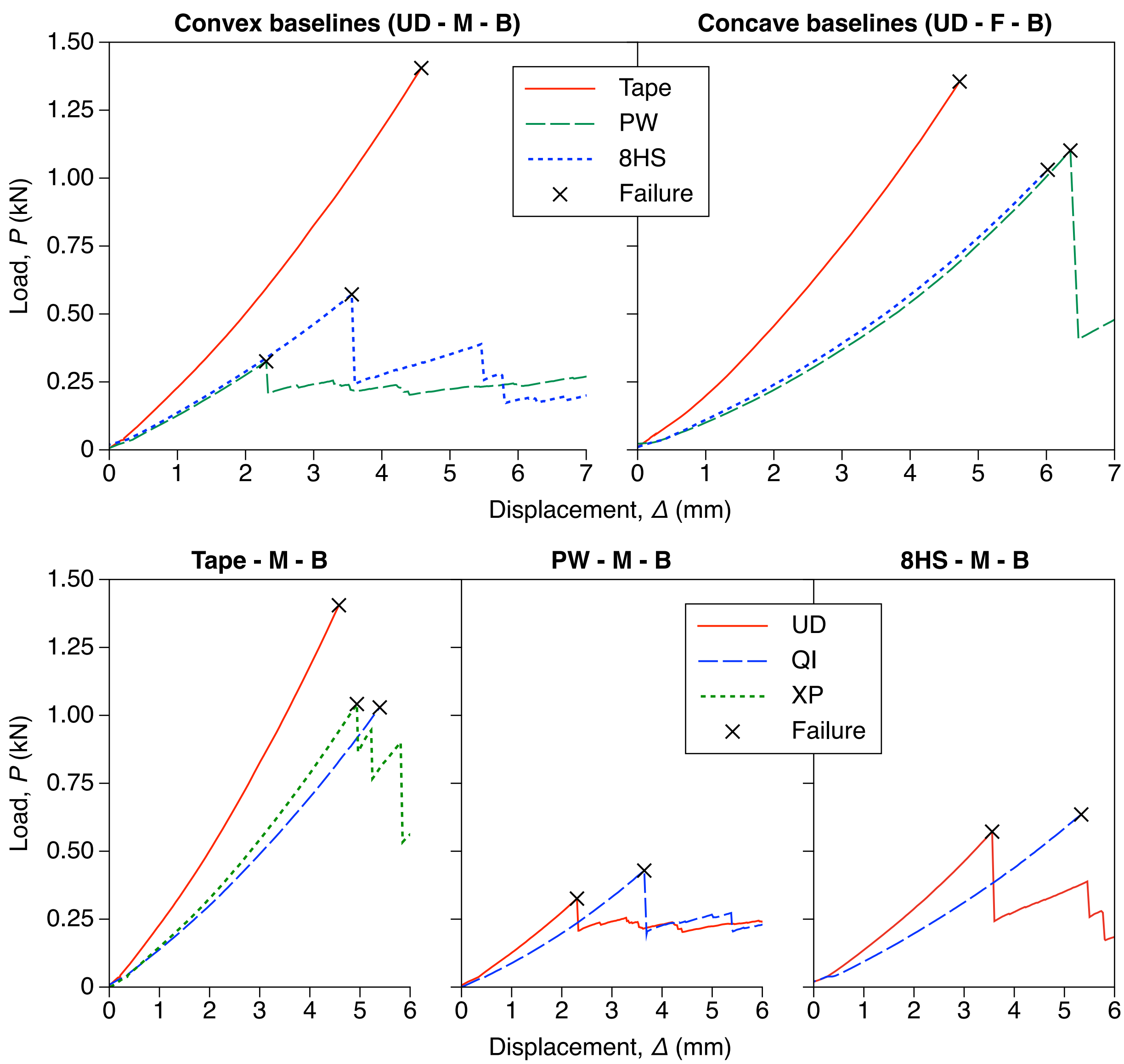

Fig. 5-2. Typical load-displacement curves for the selected design factors.

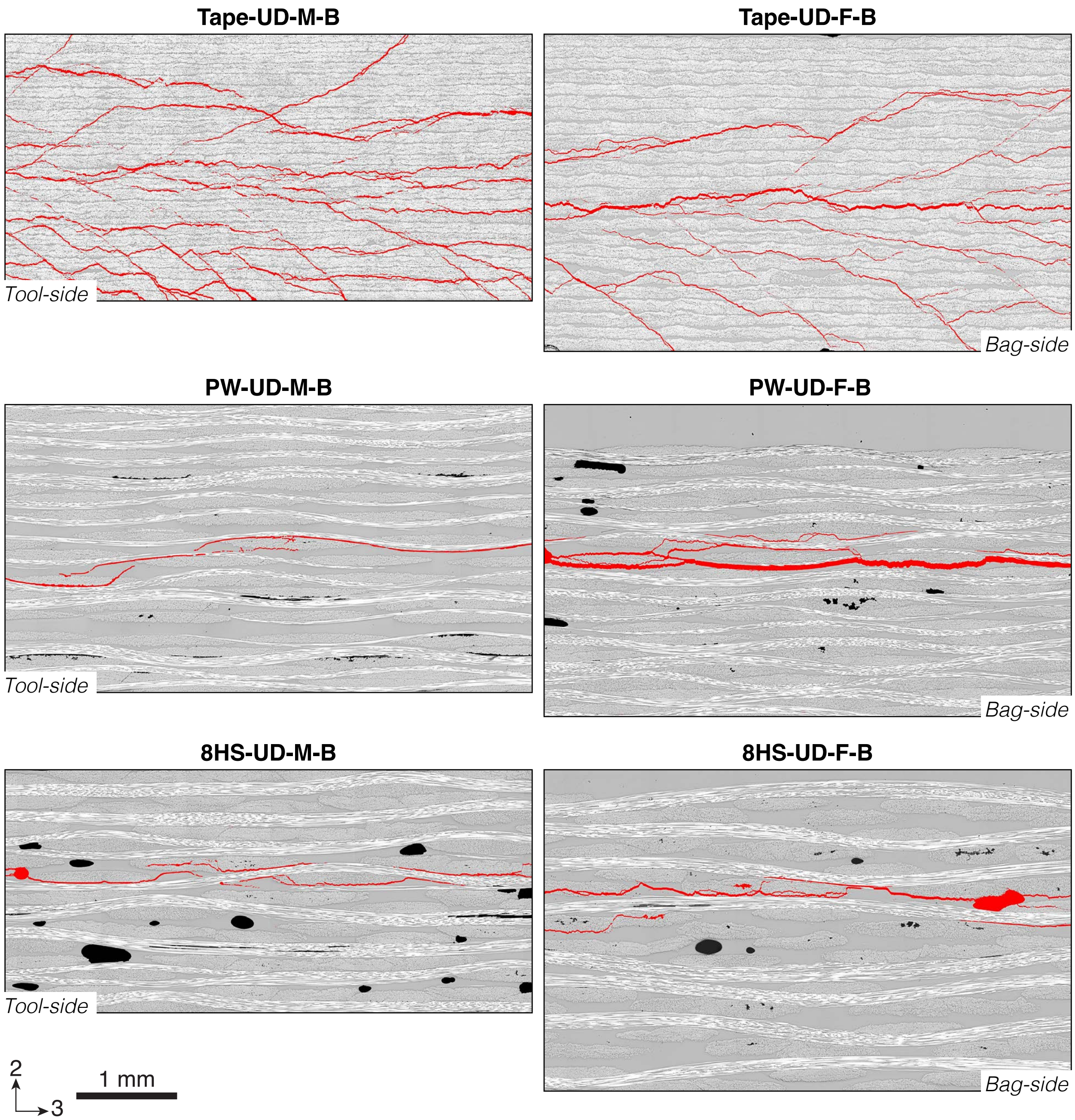

Fig. 5-3. Optical micrographs of representative failed baseline specimens (corner sagittal plane; brightfield illumination; 10x objective).

Load-displacement curves

The typical load-displacement curves shown in Fig. 5-2 reveal the relative differences in corner bending stiffness and failure state for the selected design factors. First, a common observation that applies to all the tested specimens regardless of the selected materials, tool-shapes and stacking sequences is the absence of subcritical, pre-failure damage, as evidenced by the smoothness of the curves prior to the initial load-drop.

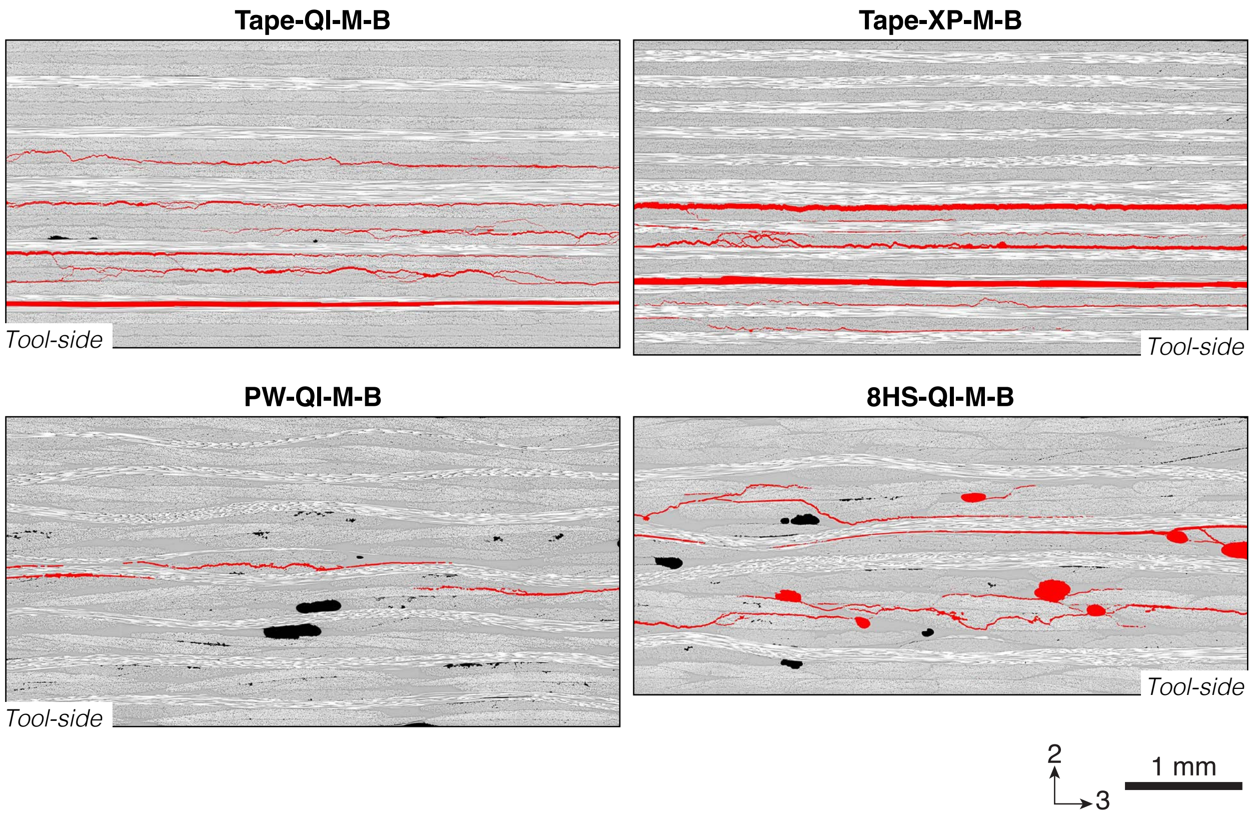

Fig. 5-4. Optical micrographs of representative specimens for the selected alternate stacking sequences (corner sagittal plane; brightfield illumination; 10x objective).

Second, specimen failure is always accompanied by a sharp load-drop of at least 17.0% of the peak load (T-XP-M-B). As noted by Jackson and Martin, the load-drop percentage typically increases with increasing failure load [81]. In particular, tape specimens with a UD layup, which experience the highest failure loads, tend to experience abrupt and catastrophic failures (load-drops in excess of 80%) compared to 2D-woven and alternate layup specimens. The latter show smaller initial load-drops that are followed by a staggered series of secondary load-drops beyond the initial failure point as new interlaminar and translaminar delaminations appear and grow. It should be noted that machine and fixture compliance effects are herein minimized by the use of an LVDT sensor to measure the displacement between the 4PB-CBS fixture halves (Fig. 3-4).

Lastly, the corner bending stiffness drops considerably as a function of the percentage of aligned fibres in the hoop-direction (0°). The tape convex and concave baselines (Tape-UD-M/F-B) are thus stiffer than the corresponding PW and 8HS baselines, which nearly overlap. Similarly, UD layups are stiffer than corresponding QI layups, with the tape XP layup only being marginally stiffer than the tape QI layup.

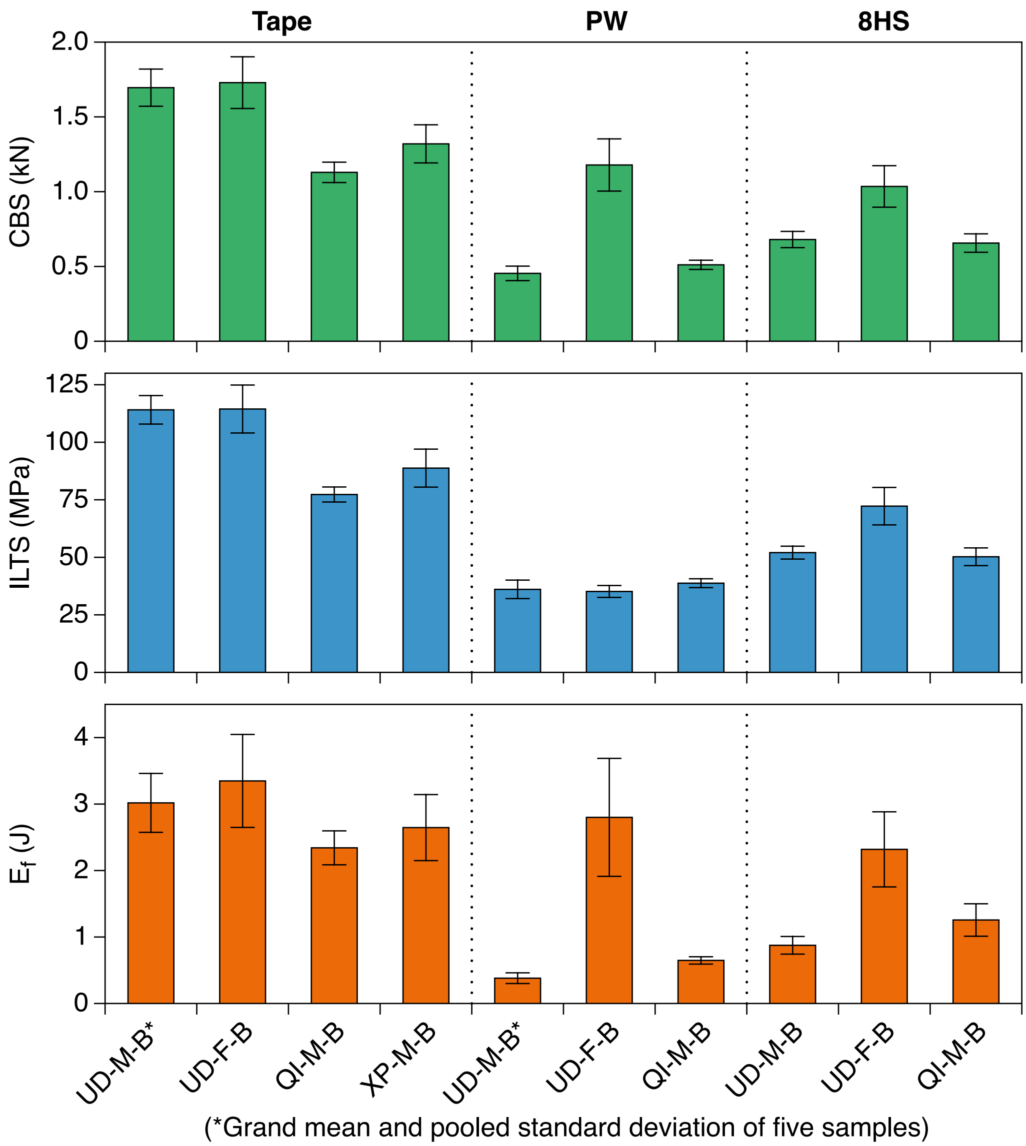

Fig. 5-5. Effect of selected design factors on corner mechanical performance.

Failure behaviour

Visual inspection of failed specimen free-edge surfaces and optical micrographs of representative failed sagittal corner cross-sections presented in Fig. 5-3 and 5-4 reveal three general failure regimes that may be correlated to the energy-to-failure (E_f) values presented in Fig. 5-5. Initial visual inspection of specimen free-edge surfaces reveals, in all cases, the presence of mostly-tangential cracks concentrated in the center of the corner region; however, key differences are already discernable at this stage. The tape baselines (Tape-UD-M/F-B) contain significantly more tangential cracks spread throughout the thickness with some cracks reaching the inner specimen surfaces that undergo the maximum tensile loading. In turn, tape specimens with alternate stacking sequences (Tape-XP/QI-M-B) contain fewer tangential cracks. In addition, QI specimens contain noticeable translaminar cracks as delaminations bridge from one ply interface to another, whereas XP specimens tend to contain mostly tangential cracks. Lastly, 2D-woven specimens tend to contain more "tortuous" cracks than the tape specimens on account of the unevenness of interply regions as well as interply nesting.

Secondary visual inspection of representative optical micrographs corroborates the initial observations. The tape baseline micrographs (Tape-UD-M/F-B in Fig. 5-3) exhibit significant out-of-plane branching of cracks throughout the cross-section, which may in part be explained by the presence of fibre waviness in these laminates. Jackson and Martin described this effectively-simultaneous fracture pattern as having a "shattered" appearance and observe increased branching at higher failure loads [81]. Hao *et al.* further observed that relatively thin specimens similar in thicknesses to the specimens tested herein (t < 3.8 mm) tend to fail suddenly and catastrophically, whereas thicker specimens tend to fail more progressively [96]. In turn, tape specimens with alternate stacking sequences (Tape-XP/QI-M-B in Fig. 5-4) do not exhibit out-of-plane branching of cracks. Delaminations are instead generally contained at the ply interfaces and connected with some noticeable intralaminar cracks—albeit less frequent. Lastly, the 2D-woven micrographs (Fig. 5-3 and 5-4) exhibit fewer inter-and intralaminar cracks, which tortuously undulate around and through tows while intersecting inter-tow voids. Jackson and Ifju [83] and Avalon *et al.* [97] observed very similar fracture patterns in the 2D-woven corner specimens that they tested.

Lastly, the energy-to-failure values (E_f) presented in Fig. 5-5 generally corroborate the visual observations and the finding by Jackson and Martin that the extent of the failure damage is linked to the failure load [81]. The tape baselines exhibit the highest failure loads and energies, followed by the tape samples with alternate stacking sequences and finally the 2D-woven samples (Fig. 5-2 and 5-5, resp.). The 2D concave baselines (PW/8HS-UD-F-B) are the two exceptions on account of significant corner thickening, which corresponds to a higher bending stiffness and failure load. A higher failure load will result in a higher energy-to-failure, which is simply the area under the load-displacement curve. This energy is mostly stored in the form of elastic energy, which is suddenly released and dissipated via unstable crack growth following the initial ILT delamination(s) [83, 222]. Branching and secondary delaminations subsequently appear due to the load being redistributed to the remaining groups of uncompromised plies [83]. In the case of stiffer UD laminates, the high redistributed load overwhelms the remaining sub-laminates, which effectively fail simultaneously resulting in the very large load-drops observed in Fig. 5-2.

Strength properties

Material selection and tool-shape—to a lesser extent—are shown to have a large influence over the strength values of the six baselines, as evidenced in Fig. 5-5. First, the tape baselines (T-UD-M/F-B) exhibit markedly higher CBS and ILTS values than the corresponding woven baselines: the PW convex and concave baselines (PW-UD-M/F-B) respectively exhibit mean CBS values that are 73.2 and 31.8% lower and mean ILTS values that are 68.4 and 69.3% lower; and the 8HS convex and concave baselines (8HS-UD-M/F-B) respectively exhibit mean CBS values that are 59.9 and 40.1% lower and mean ILTS values that are 54.4 and 36.9% lower. Second, concave baselines generally exhibit higher values than corresponding convex baselines for PW and 8HS. The one exception to the latter observation is the PW ILTS values, which have overlapping error bars as is the case for the tape CBS and ILTS values.

The stark difference in performance observed between the tape and 2D-woven semipregs may first be explained by the significant corner porosity present in the PW and 8HS baselines compared to tape baselines, as evidenced in Fig. 4-6. In addition, the results are in accordance with the experimental findings of Jackson and Ifju [83], who noted that the ILTS drops precipitously with fibre content—even though it is expected that 2D-woven laminates outperform tape laminates in interlaminar tension and shear. They concluded that the best predictor for ILTS is the local ply thickness in the region of highest radial stress. In this work, the fibre content of the tape baselines cannot be readily compared to that of the 2D-woven baselines on account of the thresholding error explained in § 2.5.3 and § 4.5.2; however, visual inspection of frontal plane micrographs in Fig.

4-7 clearly establishes a discernable difference in fibre content between the tape and 2D-woven baselines with higher fibre contents in the tape baselines.

In turn, the difference in CBS values observed between 2D-woven convex and concave baselines may be intuitively explained by corner thickening. The 2D-woven concave baselines (PW/8HS-UD-F-B) exhibit significant corner thickening compared to the corresponding convex baselines (PW/8HS-UD-M-B), as evidenced in Fig. 4-6, which results in a higher respective CBS value. Hao *et al.* experimentally investigated the effect of laminate thickness on CBS and found that, indeed, CBS increases as a function of laminate thickness [96]. In contrast, the observed difference in ILTS between the 8HS convex and concave baselines (8HS-UD-M/F-B) is not readily explainable. Charrier *et al.* demonstrated experimentally that ILTS values remain more or less constant for relatively thin to moderately thick laminates (t < 10 mm) and only begins to drop due to volumetric effects for very thick specimens [222]. Whereas this may explain the parity in ILTS values for convex and concave baselines in the case of tape and PW, it does not explain the observed difference in the case of 8HS. Beyond acknowledging that this particular observation may be the product of a sample outlier, the occurrence is further obfuscated by the complexity and non-uniform nature of the concave corner geometry and mesostructure (Fig. 4-7) as well as the previously noted and significant presence of corner porosity.

With regards then to stacking sequence, this factor is shown to have an influence over the strength properties of tape convex corners but no discernable effect on 2D-woven convex corners. Compared with the tape-UD sample, the XP and QI samples respectively exhibit mean CBS values that are 22.2 and 33.4% lower and mean ILTS values that are 22.2 and 32.3% lower. The QI sample has the worst performance of the three stacking sequences investigated for the tape convex corners.

Charrier *et al.* observed a similar drop in strength between tape UD and QI corners of moderate thickness (t = 4.19 mm) [222]. In turn, Hao *et al.* observed that delaminations in laminates comprised of 0, ±45 and 90° plies tend to initiate and propagate in 0° plies in the case of critical and non-singular stress distributions [96]. Indeed, the critical energy release rate of 0/0° interfaces is lower than for other interfaces. Simulation work by Borg *et al.* confirms this fact and estimates that 0/0° interfaces are approximately four times weaker than 0/90° interfaces and approximately twice as weak as ±45° interfaces [223]. These findings explain the higher strength values obtained for the XP layup compared to the QI layup as well as the presence of intralaminar cracks (Fig. 5-4); however, they do not explain the decline in strength observed for both of these layups compared to the UD layup strength. This difference may rather be attributed to the sensitivity of non-UD layups to singular stresses at or near the specimen free-edges [92], which are typically the product of machining-induced damage. Martin and Jackson further noted that the location of 90° plies relative to regions of high tensile stresses in the tangential direction and maximum interfacial angles of 90° relative to regions of high radial stresses will minimize the risk of matrix micro-cracking and free-edge delaminations, resp. [80].

Lastly, the absence of a discernable difference between the 2D-woven UD and QI corners may simply be explained by their relatively similar and heterogeneous mesostructures (Fig. 5-3 Fig. 5-4), which will engender similar interply stress distributions and singularities. In addition, all the 2D-woven samples are similarly affected by a significant presence of stress risers in the form of interlayer voids that are seemingly-stochastically-distributed throughout the corner regions (Fig. 4-6).

5.4.3 Deficient consolidation pressure

The discussion now shifts to the effect of deficient consolidation pressure on corner mechanical performance. Typical load-displacement curves are presented in Fig. 5-6 for the twelve deficient consolidation pressure samples (Tape/PW-UD-M/F-L1/L2/L3) and the four corresponding baselines discussed in the previous section (Tape/PW-UD-M/F-B). It should be reiterated that the selected specimens were loaded beyond the initial load-drop for the purpose of capturing damage propagation whenever applicable. In turn, optical micrographs of representative, failed specimen cross-sections are presented in Fig. 5-7. The corresponding representative baseline micrographs are omitted as they are already presented in Fig. 5-3. It should additionally be reiterated that these particular specimens were only loaded up to but not beyond the initial load-drop to limit the extent of damage to the onset of ILT delamination. Lastly, the mean mechanical properties are presented in Fig. 5-8. The results in these figures are jointly discussed throughout this section alongside references to result figures presented in the previous chapter (§ 4.5).

Load-displacement curves and failure behaviour

The typical load-displacement curves presented in Fig. 5-6 reveal a change in failure regime between the tape baselines (Tape-UD-M/F-B) and the corresponding deficient consolidation pressure samples (Tape-UD-M/F-L1/L2/L3) irrespective of tool-shape. The baselines fail suddenly and catastrophically at a much higher load than the deficient pressure samples, which fail more progressively, as evidenced by the staggered nature of the corresponding load curves. In contrast, the PW samples fail at similar load levels and in a similar manner irrespective of void content, which is shown in Fig. 4-12 to increase as a function of decreasing consolidation pressure. It should be noted that the disparity in failure loads between convex and concave samples, notably with regards to PW samples, is attributed to corner thickening as explained in the previous section.

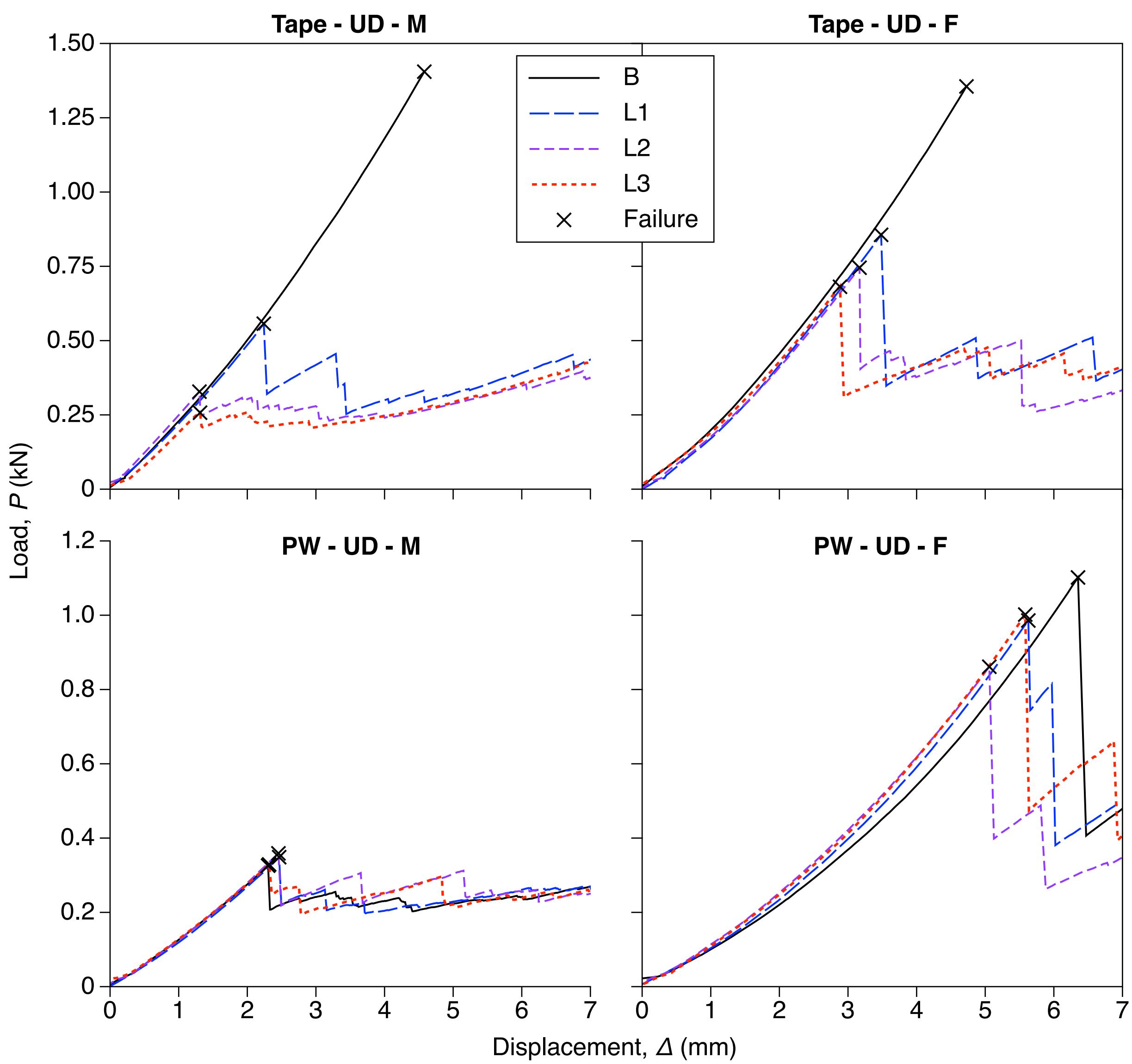

Fig. 5-6. Typical load-displacement curves for deficient consolidation pressure specimens.

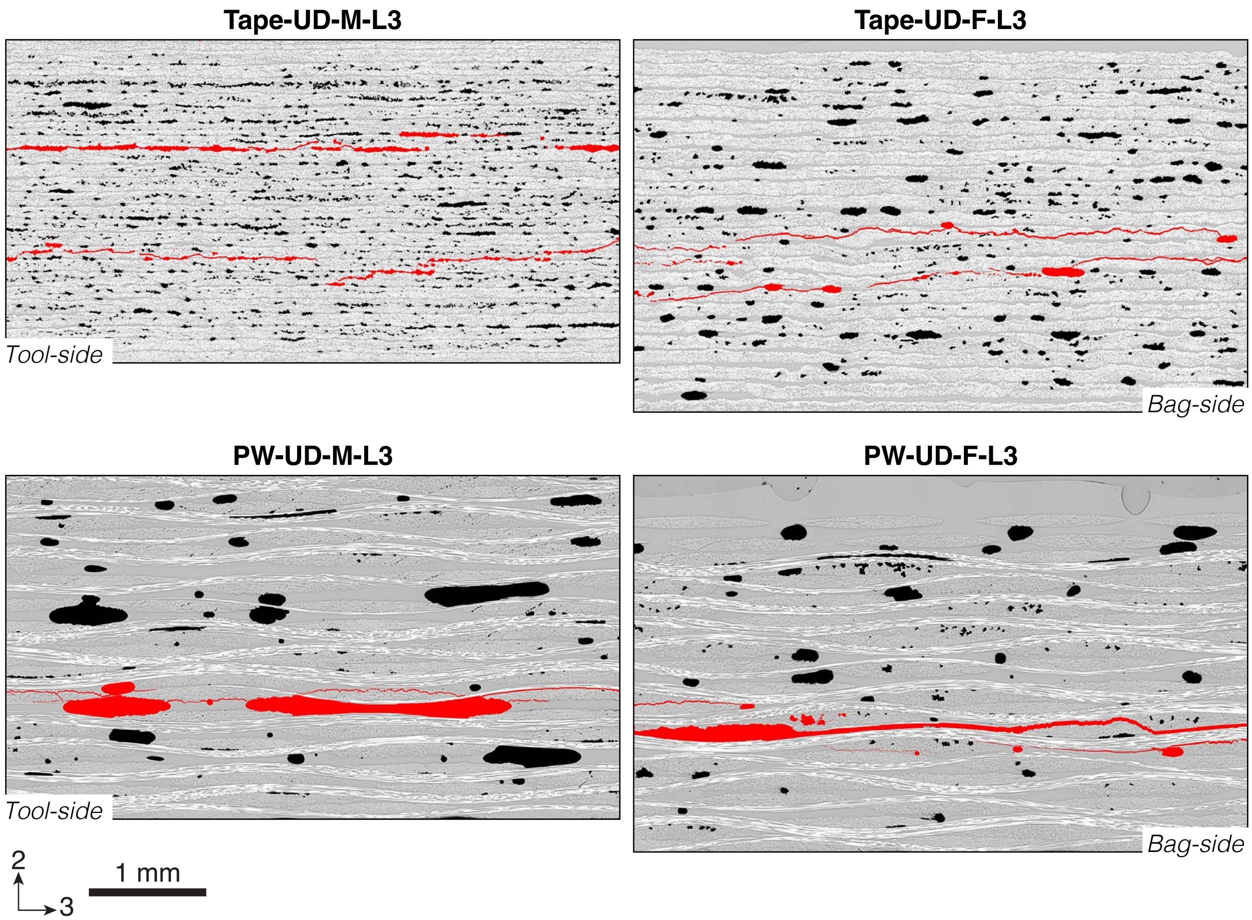

Fig. 5-7. Optical micrographs of representative deficient consolidation pressure specimens (corner sagittal plane; brightfield illumination; 10x objective).

In turn, visual inspection of the free-edge surfaces of failed specimens indicates fewer tangential cracks in the corner region of deficient tape samples compared to the corresponding baselines. Further inspection of the representative optical micrographs of failed cross-sections confirms this observation (Fig. 5-7). Cracks are mostly interlaminar and tend to propagate from one inter-tow void to the next with far fewer intralaminar cracks than are present in the corresponding baseline micrographs (Fig. 5-3). The difference in void content is additionally very clear. In contrast, visual inspection of PW specimen surfaces and optical micrographs reveals little difference in the extent and nature of the failure damage. The key difference is a higher visible inter-tow void content in the worst-case deficient consolidation pressure level tested (L3: CPL of 70%) compared to that of the baseline, albeit a much less significant difference than that visible between the corresponding tape samples.

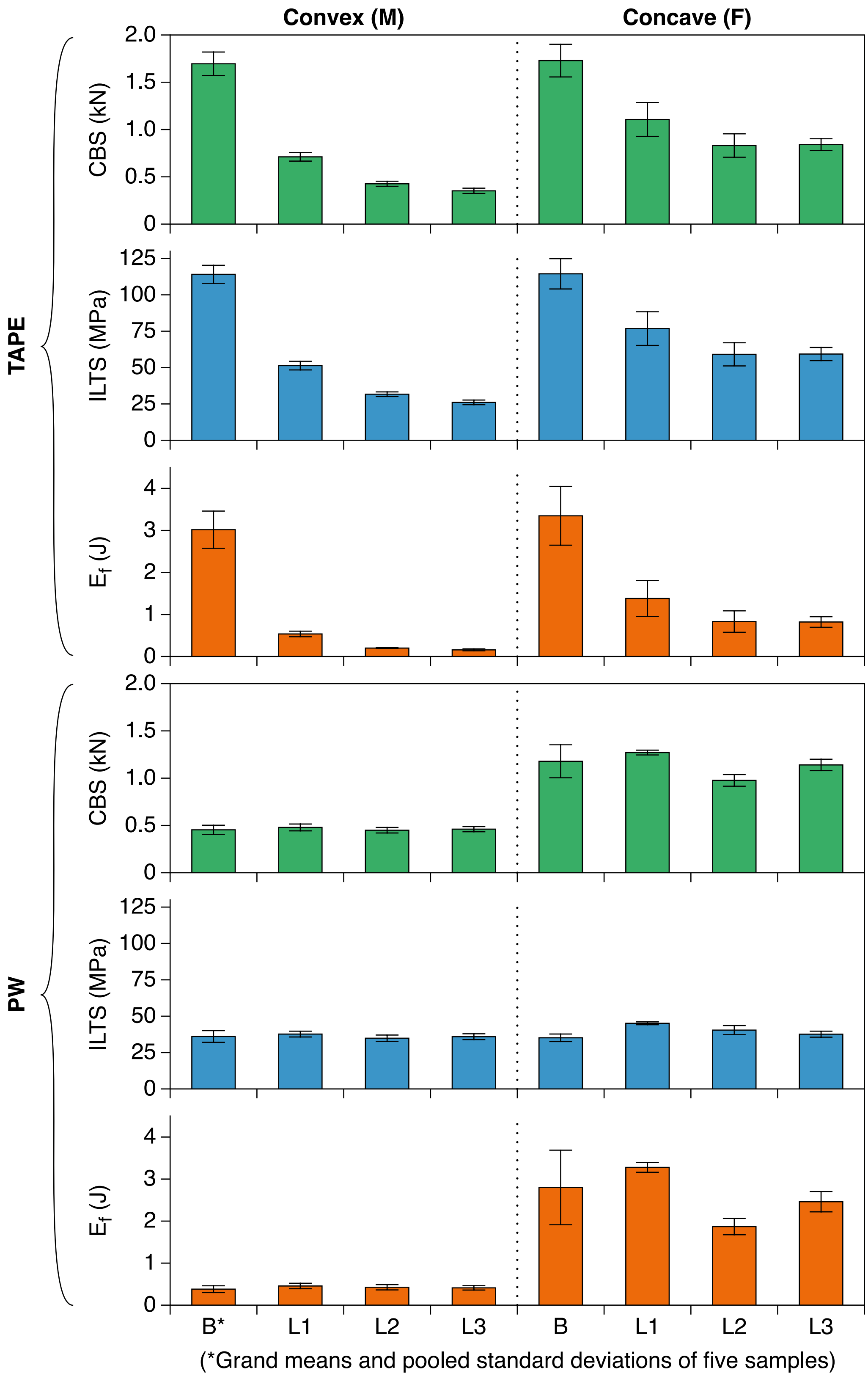

Fig. 5-8. Effect of deficient consolidation pressure on corner mechanical performance.

With regards then to the energy-to-failure (E_f) values presented in Fig. 5-8, the tape convex and concave cases respectively experience drops of 82.2 and 58.8% between the baseline (B: CPL > 95%) and first deficient consolidation pressure level (L1: CPL = 90%) and drops of 94.8 and 75.5% between the baseline and worst-case level tested (L3). In contrast, the energy-to-failure levels registered by the PW samples fall within each other's error ranges. The much more important energy release occurring during the tape baseline specimen failures accounts for the much more significant damage extent as well as the inability of the plies that are left uncompromised after the initial ILT delamination(s) to sustain the redistributed loads.

Strength properties

Deficient consolidation pressure is shown in Fig. 5-8 to clearly affect the strength values of tape samples, whereas PW samples appear to be unaffected. ILTS values of tape convex samples (T-UD-M-…) decrease by 55.0, 72.2 and 77.1% compared to the baseline value for nominal consolidation pressure losses of 10, 20 and 30%, resp., which correspond to the L1, L2 and L3 test conditions. Likewise, the ILTS values of tape concave samples (T-UD-F-…) decrease by 32.9, 48.4 and 48.2% for the corresponding test conditions. It is well understood in the literature that the 4PB-CBS test method and the corresponding, macroscopic data reduction based on Lekhnitskii's classical elasticity solution yield ILTS values that are highly dependent on laminate and specimen quality and—most notably—void content [32, 90, 93]. Voids act as stress singularities that initiate ILT delaminations in the region of highest radial stress.

ILTS values plotted as a function of corner global void content are presented in Fig. 5-9 for the tape convex and concave samples and follow a distinct logarithmic trend. The influence of corner porosity on ILTS values decreases considerably beyond 2% void content. In contrast, the PW baselines suffer from a significant corner porosity unlike the tape baselines, as evidenced in Fig. 4-6. The PW baselines contain a critical void content despite a near-optimal consolidation pressure level (CPL > 95%), which renders the ILTS performance effectively independent of porosity. These results highlight the importance of tailoring the processing cycle, part design and notably the material selection in order to achieve low corner porosity and high CBS and ILTS.

Lastly, Makeev *et al.* linked the very low void contents expected in near-optimally processed tape corners to high data scatters [93]. The influence of a single void on the onset of ILT delamination increases as the probability decreases of finding a critical void in the region of highest radial stress. First, the experimental variability of the present research environment is shown to be lower than what is typically expected, as evidenced in § 5.3.3. In turn, the standard deviations plotted in Fig. 5-8 decrease as the consolidation pressure loss increases, which corresponds to an increase in global void content, as evidenced in Fig. 4-6. The probability of finding a critical void increases along with void content. In turn, the influence of a single void decreases, which results in less data scatter.

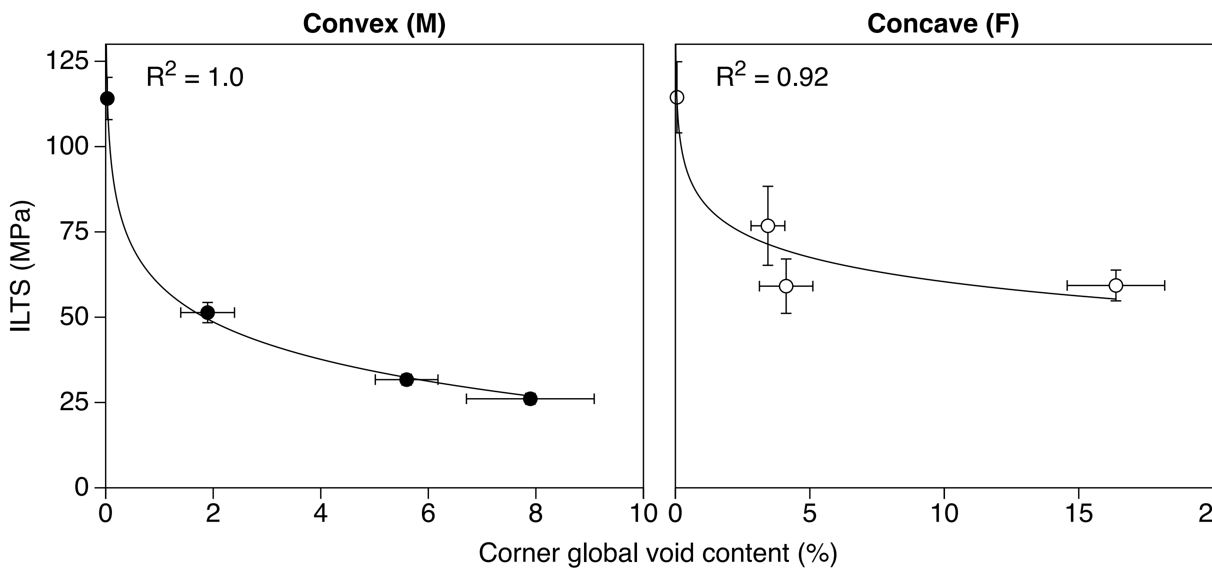

Fig. 5-9. Logarithmic correlations between ILTS and corner global void content.

5.4.4 Industrial processing cases

The discussion finally shifts to the three selected industrial processing cases that deviate from the baseline process: slow temperature ramp during the cure cycle (SR), no-intermediary debulking during layup (ND) and restricted air evacuation (R). Typical load-displacement curves are presented in Fig. 5-10 including the corresponding baseline curves. It should be reiterated a final time that the selected curves extend beyond the initial load-drop and failure point whenever applicable to capture the damage propagation. In turn, the corresponding mean mechanical properties are presented in Fig. 5-11. It should be noted that visual inspection of failed specimen, free-edge surfaces and optical micrographs of representative, failed cross-sections reveal the same failure patterns as observed in the corresponding, PW and 8HS baseline micrographs in Fig. 5-3—Micrographs are therefore omitted from this section.

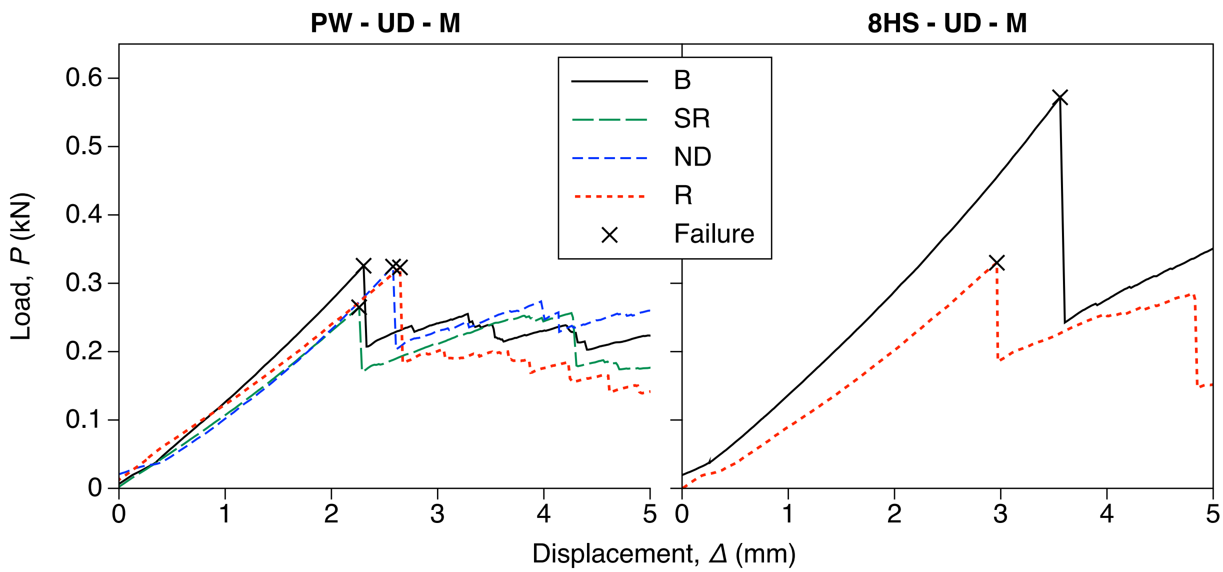

Fig. 5-10. Typical load-displacement curves for selected industrial cases.

Load-displacement curves

The typical load-displacement curves presented in Fig. 5-10 do not reveal any significant difference insofar as the PW samples are concerned. There seems to be a certain degree of variability in the stiffness of the PW curves prior to the initial load-drop that may simply be attributed to the inherent variability of the materials and manual layup process. The failure points are additionally closely grouped. In contrast, there is a much more pronounced difference between the 8HS baseline and restricted air evacuation sample. First, there is a small shift at the base of the R-sample curve, which may render the visible difference in stiffness between the two curves appear to be larger than it actually is. This shift may be attributed to the very rough flange surfaces of the restricted air evacuation specimens, which can affect the initial specimen-sleeve contact and alignment and result in small self-adjustments within the assembly as it becomes loaded. The thickness should otherwise theoretically be similar given similar corner thicknesses and fibre contents, as evidenced in Fig. 4-16. Second, there is a noticeable difference in failure load, which may be attributed to the higher corner porosity in the R-sample than the baseline (Fig. 4-16). The same influence of voids may not be observed in the corresponding PW specimens on account that the higher crimp angle of that fabric renders PW corners more susceptible to premature failure in the presence of more modest void content.

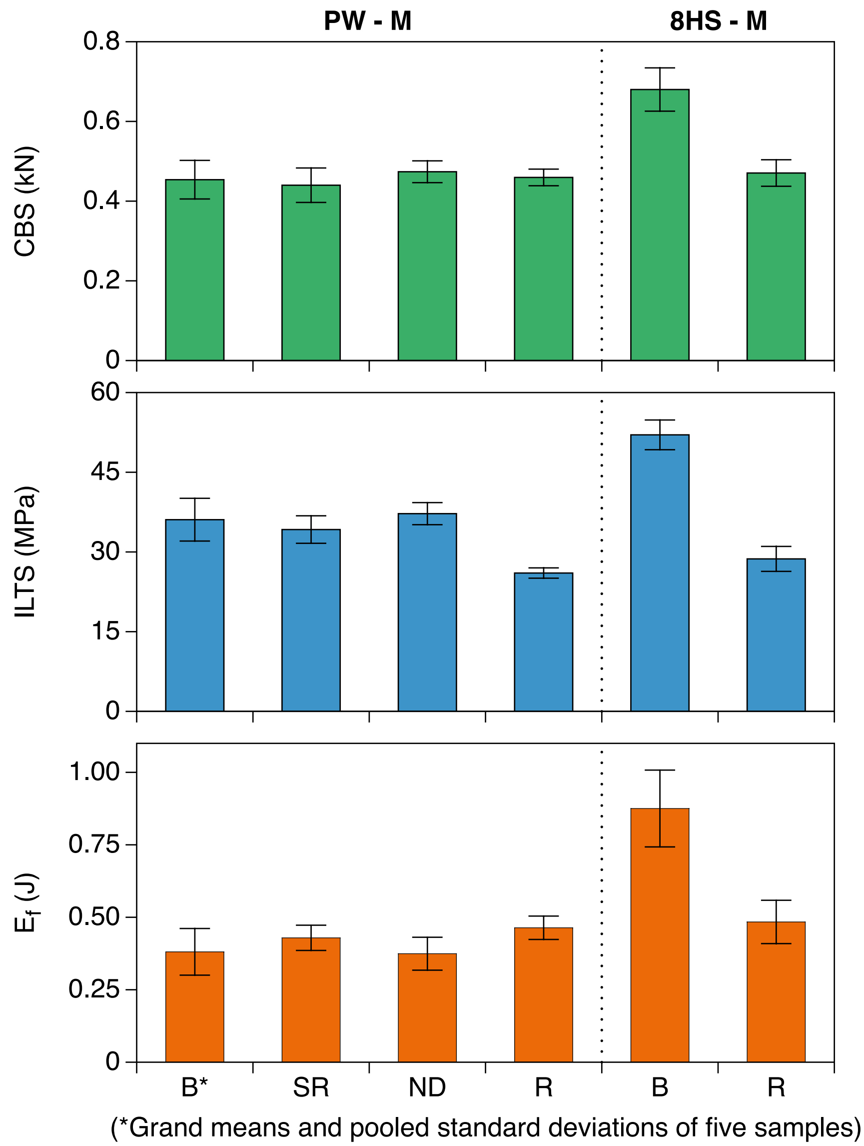

Fig. 5-11. Effect of selected industrial cases on corner mechanical performance.

Strength properties

Insofar as the PW samples are concerned, the SR and ND test conditions have no discernible influence on the mechanical performance of the PW-UD corner laminates, which corroborates the earlier finding that these conditions have no discernable influence either on the corner laminate quality. That is not to say that intermediary debulking with regard to ply collation is not an important consideration. In addition, these findings may not extend to 8HS comers and certainly do not apply to the tape corners. Similar experiments will be necessary in order to establish the effect of these industrial processing cases on the laminate quality and mechanical performance of semipregs comprised of different reinforcement types such as tape.

In turn, restricted air evacuation clearly influences the strength properties of the PW and 8HS. The PW and 8HS R-samples exhibit drops in ILTS values of 27.8 and 44.9%, resp., compared to the corresponding baseline values. The disparity in CBS value is less pronounced in the case of 8HS samples and imperceptible in the case of the PW samples, which may be attributed to the larger effect that specimen geometry plays on this metric. The baseline and corresponding R-sample thickness profiles are very different, and the R-samples are the only to register severe corner thinning, as evidenced in Fig. 4-15 and 4-16.

In contrast, the ILTS is less influenced by corner geometry and more so by laminate quality and in particular void content. In the case of the PW samples, it is demonstrated in the previous section that the PW baseline may contain a critical void content level, beyond which void content has less influence over ILTS values. This finding explains the smaller drop in ILTS value of the PW R-sample compared to the corresponding baseline despite its significantly higher corner global void content (Fig. 4-16). In turn, the 8HS experiences a higher load-drop despite a smaller difference between the corner global void content of the corresponding of baseline and R-sample, which may indicate that 8HS corners are less sensitive than PW ones to similar levels of corner porosity. For one, the 8HS has a smaller crimp angle than the PW in addition to a higher fibre content (Fig. 4-16).

Ultimately, the complexity of this particular industrial case requires a more in depth and extensive experimental program. At present, it can be stated that the restricted air evacuation case is the only one of the three selected industrial cases of interest to VBO semipreg processing to clearly and adversely affect the corner laminate quality and performance of 2D-woven semipregs.

5.5 Fibre waviness in tape convex laminates

5.5.1 Overview

The following section is devoted to the investigation of fibre waviness in the case of convex-tape baselines (T-UD-M-B) with a focus on in-plane *marcelling* (locally-periodic waviness), which will henceforth simply be referred to as “marcelling”. This particular material, stacking sequence and tool-shape combination appears to be the most egregious case out of all the sample combinations investigated in this work based on the qualitative assessment presented in § 4.5.2 (Fig. 4-9). It should however be noted that fibre waviness may also occur in tape corners processed on concave tools or comprising non-UD stacking sequences, as well as within tows of 2D-woven semipregs. These particular instances ought to be investigated, although doing so is beyond the present scope.

The work presented herein aims to answer the following three questions: 1) what is the extent of fibre waviness into the flanges of the selected convex-tape baseline sample? 2) What is the magnitude and morphology of the fibre waviness in the corner region? That is to say, what are the mean, absolute, in- and out-of-plane angular components of the waviness, and how does this irregularity present itself throughout the corner region? And 3), what is the effect of the fibre waviness magnitude on laminate stiffness in the corner (i.e. elastic constants)? These questions are consecutively answered in the following three sections, which contain the pertinent methodology and the corresponding results and discussion.

5.5.2 Extent of fibre waviness into flanges

The extent of fibre waviness into flanges is investigated via optical microscopy and image analysis of corner frontal cross-sections that include a sufficiently-long flange portion. The micrographs are then treated to isolate those fibres deemed to be critically-misaligned (i.e. approximately ±5°). Finally, the resulting T-T fraction of misaligned fibres is plotted as a function of the distance along the flange and away from the corner to determine the extent to which fibre waviness occurs in flanges, which is to say the point of transition from corner fibre waviness to the far-field fibre misalignment expected in manually-stacked semipregs.

It should be noted that the extent of fibre waviness is estimated herein on the basis of its marcelling component. Frontal cross-sections are most amenable to detect marcelling and are selected for being the most practical sectioning plane for the visualization of combined corner and flange regions via optical microscopy. A preliminary inspection of frontal plane micrographs indeed corroborates the visual inspection of tool-side specimen surfaces, which established that the predominant fibre waviness regime is marcelling (§ 4.5.2). The smaller out-of-plane component may in fact be due to fibres having to overcome local, marcelling fiber bundles rather than out-of-plane ply wrinkling. Determining the extent of fibre waviness based on marcelling is therefore deemed to be a valid approach in this case.

Cross-section preparation and imaging

The extent of fibre waviness is determined via the image analysis of five optical micrographs, which each comprise corner cross-sections taken in the frontal plane of spare corner specimens (remaining five T-UD-M-B-1 specimens out of original fifteen). Fig. 5-12 presents schematics of the cross-sections relative to a spare corner specimen and the cast resin mounting arrangement, as well as an optical micrograph example. It should be noted that the cross-sectional region of interest is too long (approximately 47 mm) to be placed into a single cast resin puck. It is therefore further sectioned into two halves, imaged separately and digitally reassembled in Adobe Photoshop. The general sample preparation and imaging methods presented in § 2.5.2 are otherwise observed.

Image treatment and analysis

The treatment and subsequent analysis of optical micrographs is performed in MathWorks Matlab (R2015b) via a custom m-script that is included in Appendix C.2. The key task of the script is to select critically-misaligned fibre regions, which is to say select pixel regions associated with fibres that are the most orthogonal to the plane of the micrograph and therefore form the shortest aspect ratio objects. A typical image treatment is presented in Fig. 5-13, Part 1.

The image treatment is loosely based on the method developed by Yurgartis to estimate the orientation of individual fibres in 2D-sections (micrographs) provided that the fibres have near-perfectly circular cross-sections [154]. The intersection of an off-axis, cylindrical fibre and a 2D-section plane forms an ellipse, whose minor axis is simply the fibre diameter. The fibre orientation can be estimated from the minor and major axial lengths and rudimentary trigonometry. That being the case, the particular carbon fibres (Cytec Thornel® T650/30 pan-based [171]) used in the selected tape semipreg have bean-shape cross-sections, as evidenced in Fig. 2-12. In this instance, it is impossible to accurately estimate fibre orientation given the unpredictable, non-circular fibre cross-sections. The selection of critically-misaligned fibres cannot, therefore, be based on fibre orientation. Nevertheless, knowing the exact fibre orientation is not required to estimate the extent of fibre waviness into the flanges—fibre objects may be readily selected and screened based on critical, equivalent geometric properties.

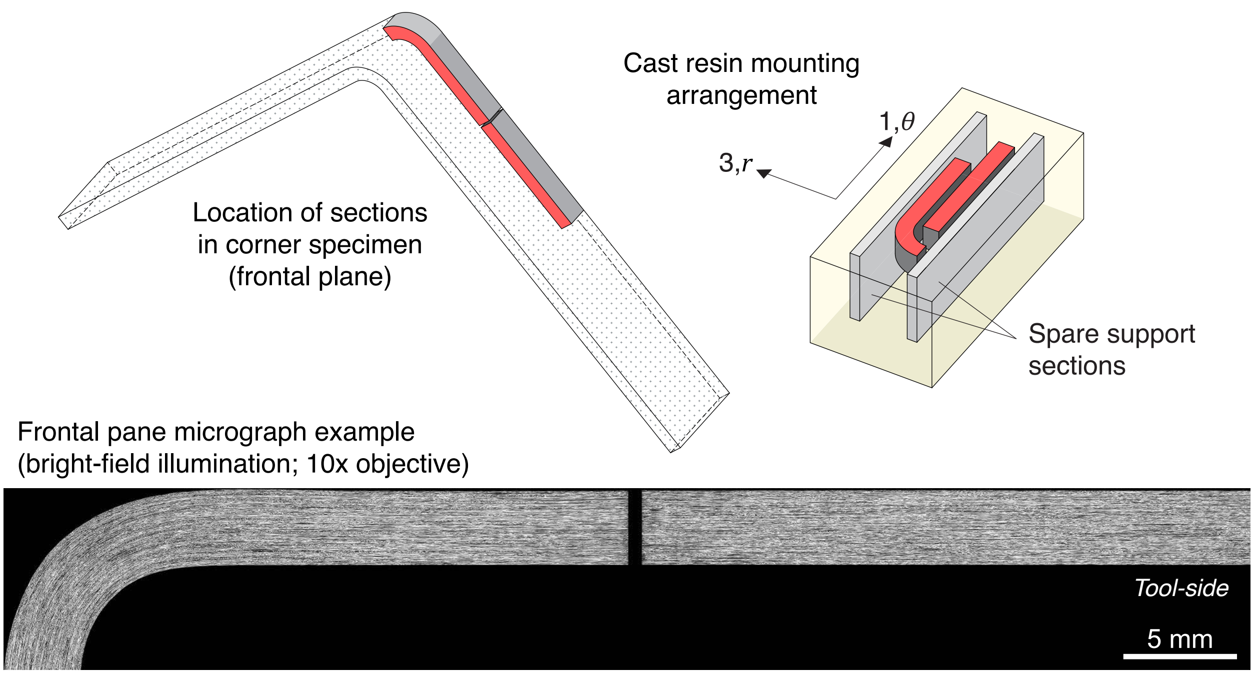

Fig. 5-12. Schematics of the cross-section location and microscopy resin-casting arrangement for the extent of fibre waviness determination.

The first part of the method is the image treatment. Micrographs are first segmented via thresholding into a binary mask that isolates the fibres. This mask is then segmented into individual objects each typically corresponding to a single fibre. Single objects with equivalent minor axial lengths that are more than twice as wide as the equivalent fibre diameter (6 μm) are likely comprised of multiple connected objects. Further segmenting such objects would require a more sophisticated and much more memory-intensive shape detection method such as one relying on Hough transforms, which is impractical given that the micrographs contain a minimum of 30k individual objects. As it stands, only a small proportion of objects is affected with those objects that are affected being stochastically-distributed. The results are therefore deemed to be sufficiently insensitive to the occurrence of such objects, which are simply discarded.

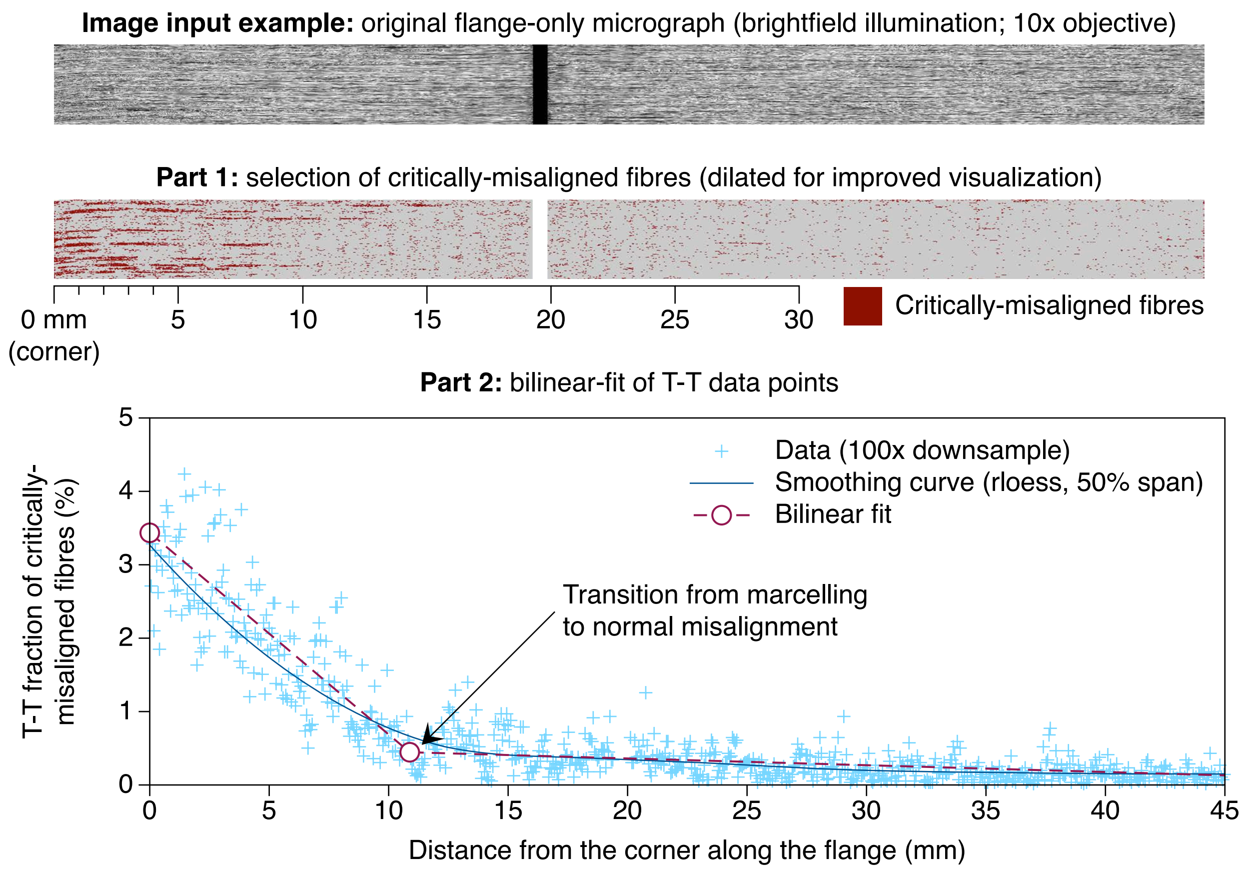

Fig. 5-13. Image analysis of optical micrographs to determine the extent of fibre waviness.

Finally, the remaining objects are screened to retain only those that are deemed to be critically-misaligned. To this end, a critical major axial length is calculated for a circular fibre with an equivalent diameter of 6 μm and a user-defined off-axis orientation of ±5°. It should be noted that a user-defined critical value of some sort is required irrespective of the object segmentation method in order to discriminate between critically and non-critically-misaligned fibres. In turn, all objects with equivalent major axial lengths smaller than this critical value are discarded, which only leaves those objects deemed to be the most critically-misaligned, as illustrated in Fig. 5-13, Part 1. This approach correctly selects those regions that are most affected by fibre waviness while being computationally inexpensive.

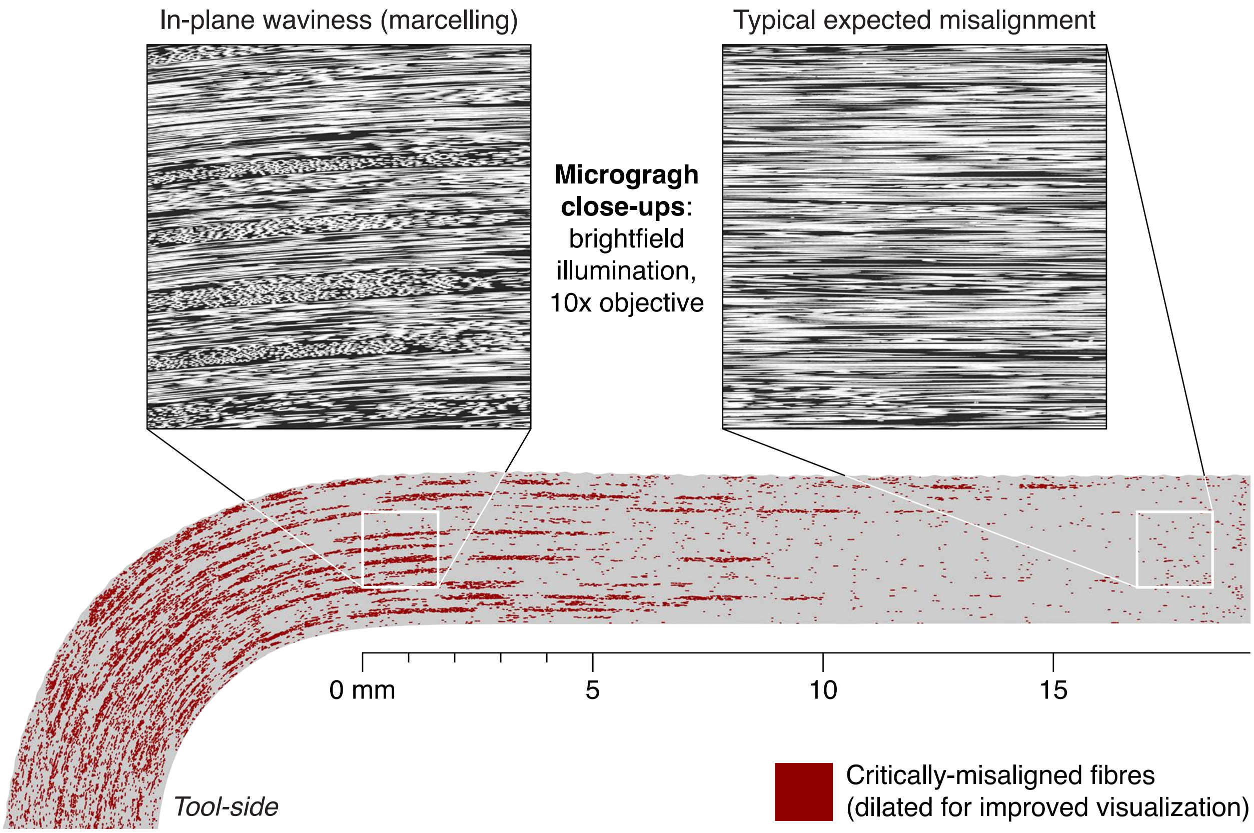

Fig. 5-14. Visualization of the fibre waviness extent into the flanges.

The image treatment results in a binary image comprised of critically misaligned fibres, the remainder of the laminate and the casting resin background. The results can now be analyzed in the second part of the method by counting the T-T fraction of critically-misaligned pixels as a function of the distance from the corner along the flange, as illustrated in Fig. 5-13, Part 2. The data is then fitted with a "broken-stick" piecewise function, which is found to best capture the bilinear nature of the data. Finally, the point of intersection between the two linear segments is taken to be the estimate of the extent of fibre waviness into the flange and represents the transition from corner fibre waviness to the typical fibre misalignment that may be expected in a manually-stacked VBO semipreg laminate.

Results and discussion

A representative image treatment result is presented for a single corner specimen in Fig. 5-14, which includes the full corner region and illustrates the corresponding types of fibre misalignment with corresponding micrographic close-ups. Fibre waviness appears to be relatively evenly distributed throughout the corner region and progressively subsides from 5 to 15 mm into the flange. The close-up located near the corner flange transition reveals distinct marcelling regions interleaved between regions of more ideal fibre alignment; the laminate resembles a UD layup containing evenly dispersed off-axis plies. In turn, the close-up located roughly 18 mm into the flange is representative of the far-field fibre orientation in the flange and contains no marcelling regions; fibres are visibly better aligned, and the alignment is much more homogeneous throughout the cross-section.

The treated flange sections of each of the five micrographs (e.g. Fig. 5-13, Part 1) are analyzed to generate corresponding datasets of the T-T fraction of critically-misaligned fibres as a function of distance from the corner along the flange. The combined datasets are plotted in Fig. 5-15. The plotting of smoothed data curves (via Matlab built-in *rloess* function using a 50% span) shows good repeatability between the specimens. The transition from fibre waviness to misalignment is estimated to occur at 10.1 ± 2.37 mm within the 5 to 15 mm range, in which corner fibre waviness subsides. It should be noted that a number of outliers appear in the vicinity of the sectioning gaps. These outliers are due to sectioning-induced artifacts, whereby well-aligned fibres are cut short and are thus mistaken for misaligned fibres. In any case, these outliers may be stricken from the data, although they are far too few to significantly influence the piecewise fit.

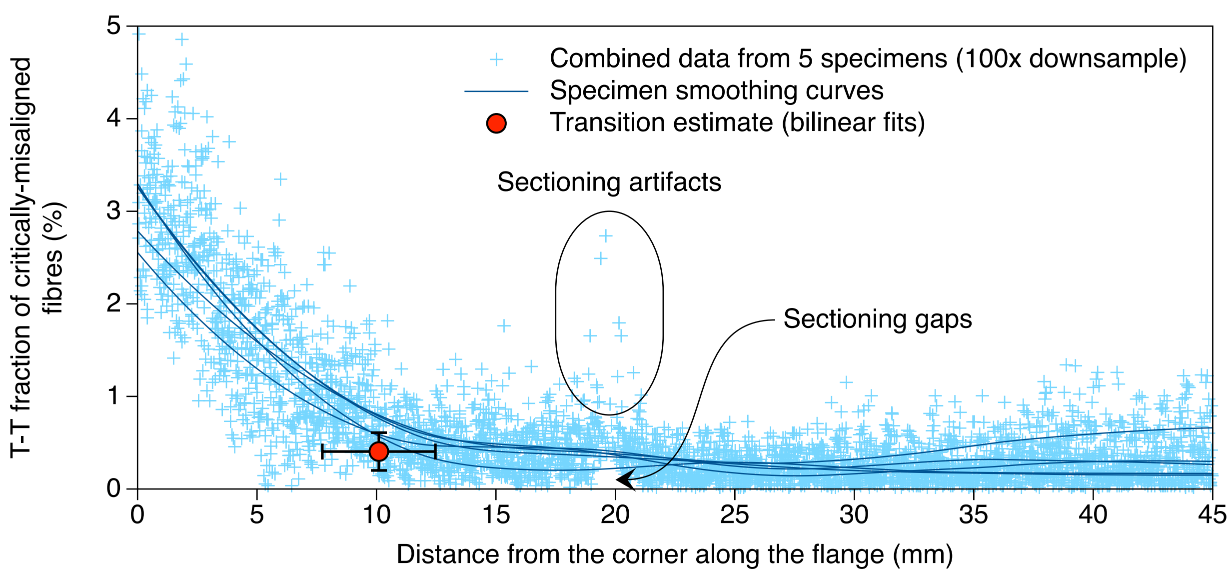

Fig. 5-15. Determination of the extent of fibre waviness for the tape convex baseline sample.

Finally, the T-T distribution of marcelling regions in the vicinity of the corner region is plotted in Fig. 5-16 for the five selected specimens. To this end, the original micrographs are cropped to the first 5 mm of flange. The plots consist of the lengthwise fraction of critically-misaligned pixels as a function of the normalized T-T position (dimensionless thickness ratio). The results provide an insight into the cause and formation of fibre waviness and more specifically the significant marcelling component.

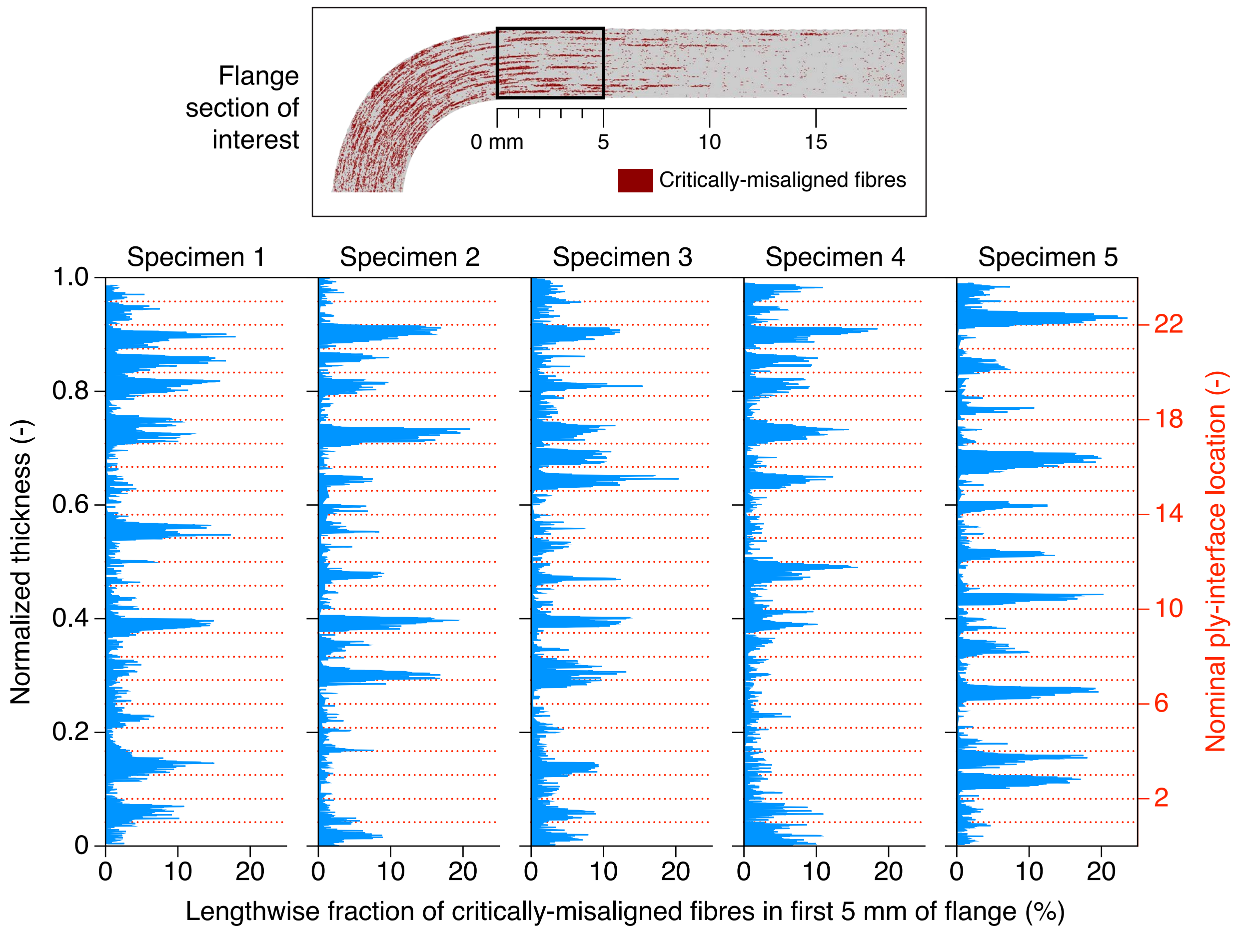

Fig. 5-16. Through-thickness distribution of fibre waviness at the start of the flange.

The regions of highest marcelling tend to fall within the nominal ply interface locations, which implies that the phenomenon occurs inside of plies rather than at interfaces. Indeed, the new generation of tape semipregs such as the one selected for this work are partially impregnated on both major surfaces leaving a resin-free midplane to improve air evacuation (§ 2.2.1). The fibres in this dry midplane are unsupported compared to the fibres in the top and bottom impregnated surface regions, which are relatively fixed in position by the b-stage resin. The midplane fibres are therefore much more prone to compaction-induced bucking during manual layup and intermediary debulking. The potential role that dry air evacuation channels may play in the formation of in-plane waviness was first noted by Farnand *et al.* [153]. Furthermore, it can be observed that the marcelling regions appear to be evenly dispersed throughout the laminate thickness, but they do not affect every ply: 12.4 ± 0.894 plies (~52%) in the 5 frontal cross-sections that are analyzed exhibit at least 5% of critically-misaligned fibres.

5.5.3 Magnitude and morphology of fibre waviness in corners

The discussion now shifts to determining the magnitude and morphology of the fibre waviness within corners. To this end, micro-CT scans performed on small, representative corner cross-sections are treated and analyzed. The results are both quantitative and qualitative. First, the mean, absolute, in- and out-of-plane angular components of the fibre waviness are calculated to estimate the magnitude of the irregularity at the macroscopic scale for the whole corner region. In turn, the treated micro-CT slices can be visually inspected to better understand the morphology of the fibre waviness and the root factors likely responsible for its occurrence.

Sample preparation and imaging

Three micro-CT scans are performed on small corner sections. These sections are taken from the non-dissected remainders of three of the five spare specimens used in the previous section to determine the extent of fibre waviness. It should be noted that Micro-CT scanning remains prohibitively expensive for most studies. A compromise must therefore be struck in terms of both the number of specimens and the scanned volume (or image resolution), both of which directly correlate with the scanning and reconstruction time and, in turn, cost. For the purpose of this study, a total of three corner sections is deemed to be adequate to characterize corner fibre waviness.

The three corner sections are machined per the section cutting procedure that is presented as part of the general optical microscopy methods in § 2.5.2. Their dimensions are roughly 5 × 10 mm in the global x- and y-dir., resp. Once prepared, the corner sections are mounted upright on a circular aluminum support with cyanoacrylate glue. Schematics of the corner section location relative to a corner specimen and the micro-CT support mounting arrangement are presented in

Fig. 5-17; the scanned volume is highlighted in green, and a reconstructed micro-CT slice is additionally included. The grayscale values in the image, which is referred to as a tomogram, correspond to the local X-ray attenuation coefficient (μ).

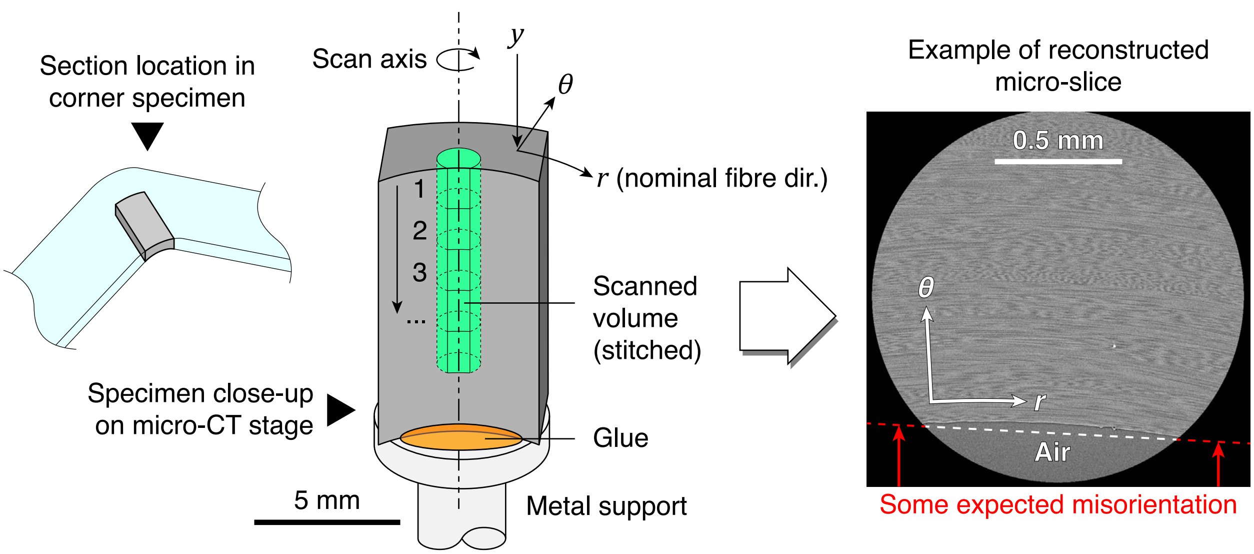

Fig. 5-17. Schematic of the micro-CT section scanning stage.

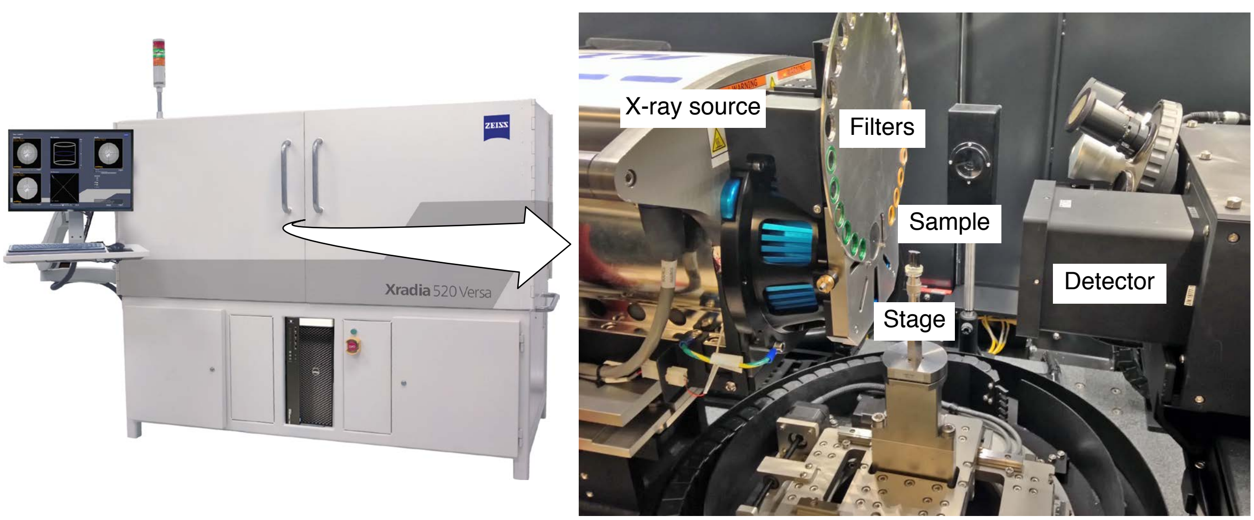

Fig. 5-18. External and internal views of the Zeiss Xradia 520 Versa micro-CT.

The corner sections are then scanned in a Zeiss Xradia 520 Versa micro-CT scanner pictured in Fig. 5-18. The pertinent scanning parameters are listed in Table 5-5. The scanning spatial resolution is 1.50 μm/px. Each of the three scans comprises four individual scans taken in succession along the transverse direction (2-dir.), as illustrated in Fig. 5-17, and semi-automatically stitched after scanning. The resulting cylindrical scanned volumes are approximately 5.28 mm long and 1.46 mm in diameter. It is impossible to scan the entire comer section at such a high resolution given the limitation of the Zeiss micro-CT. This limitation is nonetheless deemed to be inconsequential as the marcelling regions are shown to be relatively uniformly dispersed, as evidenced in Fig. 5-14. The curved, inner corner surface is purposefully included in each scan as a reference plane, from which the scanned volume can be reoriented along the correct corner specimen axes and subsequently flattened via warping.

Table 5-5. Scanning parameters used with Zeiss Xradia 520 Versa micro-CT.

Parameter	Value
Filter	None (air)
Image spatial resolution	1.50 μm/px
Optical magnification	3.99×
Image size	1011 x 988 px
No. images	3517
No. stitched scans	4
Approximate scanned volume	Cylinder: 5.28 mm tall x 1.46 mm dia.
Scanning angle of rotation	360°
No. projections	3201
X-ray source voltage / intensity (current)	60.3 kV / 82.1 μA

Image treatment and analysis

The following image treatment is inspired by the method developed by Nikishkov *et al.* to generate FE element meshes based on micro-CT scanning data of composite laminate that contain fibre waviness [220]. The novel procedure developed herein is applied to the stacks of 16-bit reconstructed micro-slices (i.e. tomograms) and comprises a sequence of four key steps: 1) tomogram segmentation (i.e. fibre masking), 2) 2D-registration (i.e. reorientation), 3) 2D-warping (i.e. effective flattening of the scanned corner laminate section), and 4) calculation of the fibre waviness mean, absolute, in- and out-of-plane angular components. It should be noted that the computational methods are too involved for a detailed presentation herein; a summary citing key references is instead presented.

Tomogram segmentation. In micro-CT imaging, the attenuation coefficient is often inconsistent in that it can vary between and even within scans, which is particularly prevalent when scanning in optical zooming mode as is the case herein. This inconsistency would likely influence the results of simpler gradient- or correlation-based algorithms. Moreover, it is not possible to volume-weight the results for such approaches. The first step is therefore image segmentation with a manually trained Fast-Random-Forest segmentation algorithm described in [224] to isolate the portions of the image corresponding to fibres. Two passes are performed in the *yz*-plane of each scan (i.e. the corner sagittal plane, § 2.5.2). Fibres in the *yz*-plane are mostly displayed as approximately circular shapes, which permits training of the algorithm with a higher confidence than for longitudinal fibre cross-sections (*xy*- and *xz*-planes) at the given resolution.

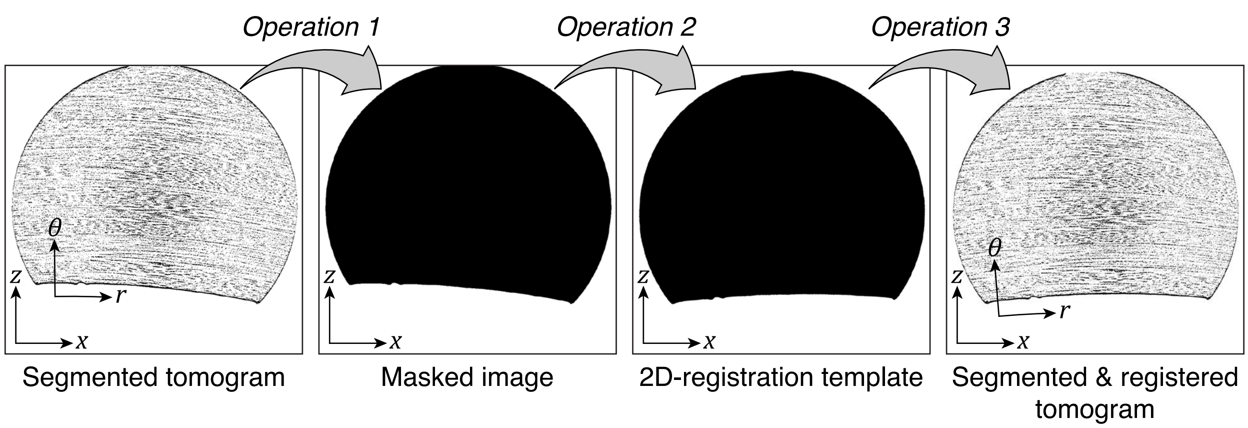

Fig. 5-19. 2D-registration of segmented tomograms in the *xz*-plane.

Registration. Micro-CT specimens are never perfectly aligned during setup (Fig. 5-17). The second step is therefore registration, whereby the scan is effectively reoriented such that the scan axes match the global specimen axes. Reorientation may be readily performed by applying a transformation matrix to the whole scanned volume at once in the case of low-resolution scans containing fewer than 100 micro-slices. This approach however typically engenders notable voxel (pixel volume) deformations and, in turn, rasterization-induced noise—even though the results are topologically correct. The significantly higher scanning resolution selected herein yields much larger numbers of micro-slices per scan (> 3.5k), which will result in unacceptable noise levels. A 2D-registration, micro-slice-based approach is therefore selected and applied to the *xz*-tomogram stacks from each scan (i.e. in the corner frontal plane, § 2.5.2). This approach consists of three consecutive operations illustrated in Fig. 5-19. First, a 2D-registration template is created by manually moving and rotating a masked image of the initially misoriented tomogram. A homographic transformation matrix is subsequently created between the initial masked image and the registration template. Lastly, this transformation matrix is applied to the initial tomogram to correctly reorient it.

It should be noted that the Enhanced Correlation Coefficient (ECC) Maximization algorithm is used to estimate the homographic transformation matrix as described in [225]. The use of a single template to transform every tomogram in a stack is only possible for masked images of the outer scanned boundary, i.e. the area in each tomogram defined by the included specimen surface edge and the circular scanning edge. The template is based on a manually selected tomogram that is representative of the entire stack. In the case of unmasked images, the ECC algorithm would require a separate, manually-created template for each tomogram to perform matching, which is unfeasible. It should be noted that the choice of manual template has been verified for multiple *xz*-tomograms and found to be an acceptable mean for uniform registration.

Warping. The micro-CT scans are taken in the center span of the corner region and thus comprise curved laminate sections that follow a nominally cylindrical frame (θ,y,r), whereas the global, reference frame of the registered scan is orthogonal (x,y,z). The third step is therefore to warp each segmented–registered tomogram in the *xz*-plane to effectively flatten the curved laminate section. Doing so greatly simplifies the subsequent calculation of the in- and out-of-plane fibre waviness angle components relative to the nominal fibre orientation (r-dir. becomes the x-dir.). The 2D-warping method is illustrated in Fig. 5-20. First, a template is manually fitted to the curved, specimen surface-edge included in a segmented–registered tomogram and selected from the center portion of the *xz*-tomogram stack. The curved edge is defined by the pixel height ($h(i)$) which varies as a function of the horizontal position in pixels (i). Subsequently, each pixel column in a given tomogram is shifted downward by the corresponding pixel height to effectively flatten the included laminate, frontal cross-section. This operation is applied to every tomogram in the stack based on a single template as is the case with the 2D-registration.

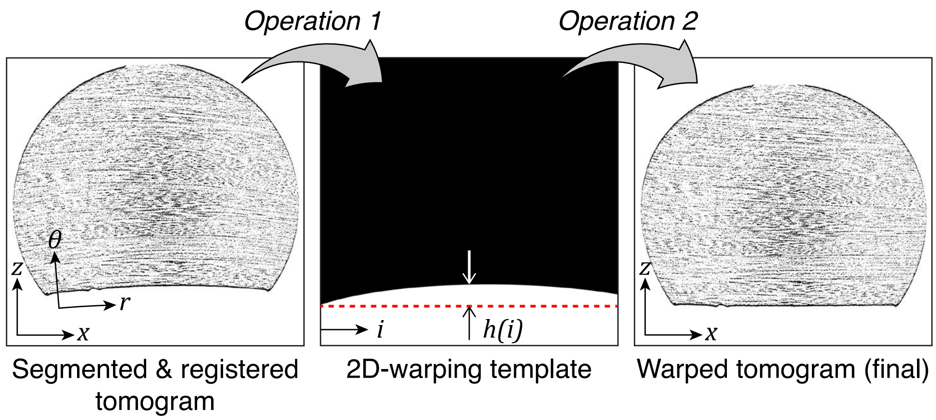

Fig. 5-20. 2D-warping of registered/segmented tomograms in the *xz*-plane.

It should first be noted that this approach introduces a small volumetric change as fibres are effectively compressed in the *z*-dir. but not correspondingly extended in the *x*-dir. The volumetric loss is nevertheless considered to be negligible and regarded as an essential compromise for the sake of computational efficiency. It should further be noted that the choice of manual template has been verified for multiple *xz*-tomograms and found to be an acceptable mean for uniform warping.

Angle calculations. The final step is the analysis of the segmented, registered and warped *xy*- and *xz*-tomogram stacks to respectively determine the mean, absolute, in- and out-of-plane angular components of the fibre waviness (α and ϕ, resp.). The approach consists of the following sequence of operations:

1) Tomograms are skeletonized, as illustrated in Fig. 5-21, i.e. reduced to the 1-px-thick representation of the central lines (or spines) of each fibre object. Skeletonization is useful for feature extraction and representing a binary (segmented) object's topology.

2) The skeletonized image is subjected to a unidirectional Sobel filter applied in the nominal fibre orientation (i.e. in the *x*-dir.), as illustrated in Fig. 5-21. The aim of this operation is to eliminate orthogonal lines created as by-products of the skeletonization, which would otherwise throw off the values of the mean, absolute angular components.

3) Pixel-size objects that are by-products of the Sobel filter are discarded to reduce noise.

4) The local orientation of each skeleton line-segments is calculated in the tomogram plane by passing a straight line through each.

5) Volume-based weighting is applied to each calculated angle by interpolating the angle to the corresponding fibre object area from the segmented image. The interpolation is further described in [226].

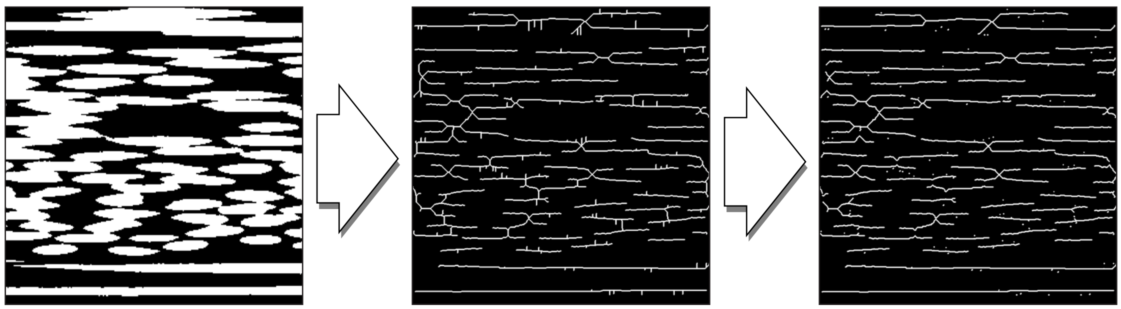

Fig. 5-21. Example of skeletonization and unidirectional Sobel filtering on a micrograph cross-section.

This approach for calculating the angular components finds a good balance between precision and computational efficiency. First, skeletonization drastically reduces the size of the data being processed while simultaneously focusing on the actual orientation of each fibre object rather than on fibre edges. In turn, the application of a unidirectional Sobel filter reduces the impact of critically misaligned fibre objects, which are especially prevalent in the *xz*-plane. Finally, the interpolation permits volume-based weighting, which addresses the notable influence that the fibre volume of a given ply has on the overall, mean, absolute angular components.

Results and discussion

Visual inspection of the processed *xy*- and *xz*-tomogram stacks of all three specimens corroborate the micrographic evidence presented in the previous section: marcelling is the predominant regime of fibre waviness in the corner regions. Representative, processed tomograms in the *xy*- and *xz*-plane are presented in Fig. 5-22. Fibres in the *xy*-tomogram are more or less parallel to one another through-the-thickness, whereas fibres in the *xy*-tomogram are more loosely oriented in the nominal fibre directions with stochastically dispersed bands of misaligned fibres.

With regards then to the magnitude of the angular components of fibre waviness, the angle calculations performed on the *xy*-tomogram stacks yield an overall, mean, absolute, in-plane angle (α) of ±7.65 ± 1.10°. The T-T distributions of α are plotted in Fig. 5-23 for all three specimens.

The distributions reveal that the degree of marcelling fluctuates through-the-thickness following suit with the micrographic findings of the previous section (Fig. 5-16). It is important, however, to note the fundamental differences in the nature of the width-wise data plotted in Fig. 5-23 compared to the length-wise data plotted in Fig. 5-16 in addition to the different nature of the measurements.

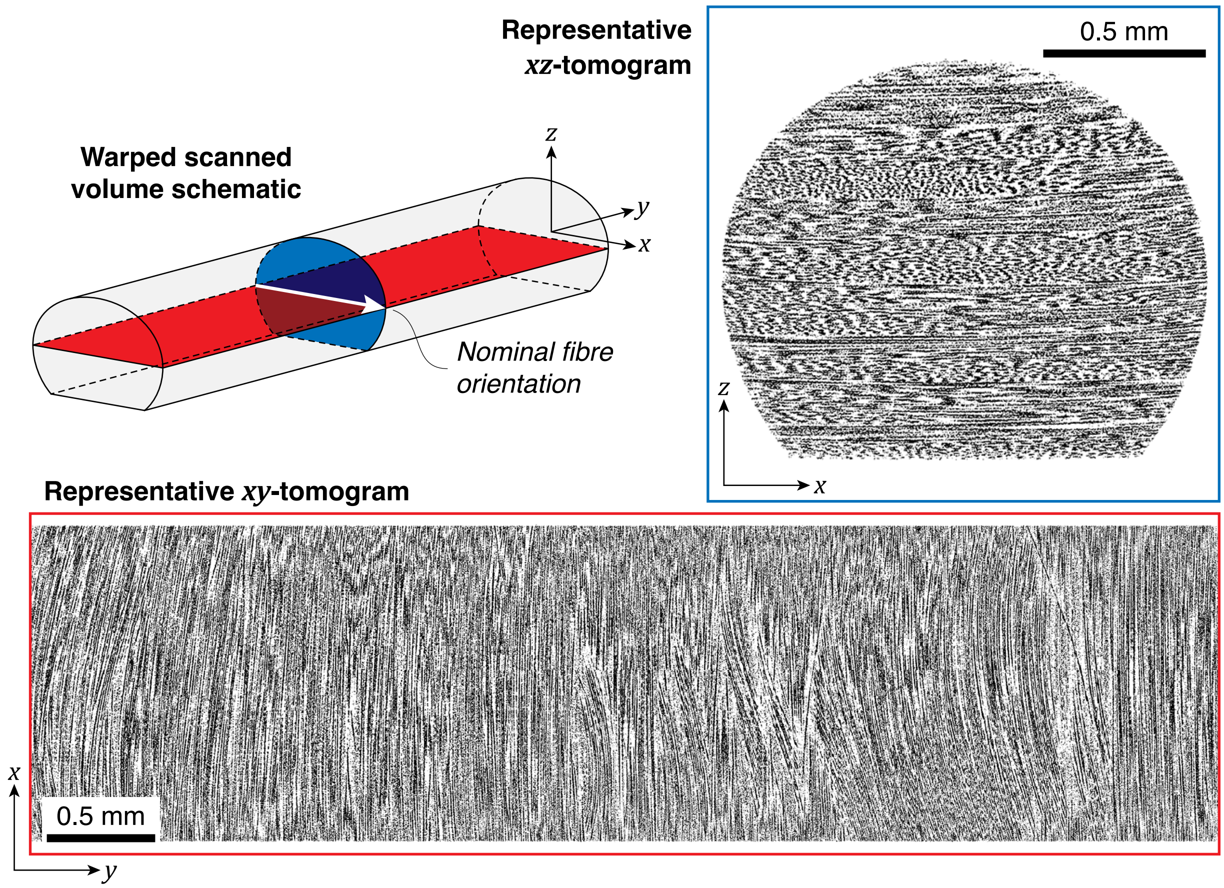

Fig. 5-22. Representative processed tomograms in the *xy*- and *xz*-planes of the specimen.

The in-plane angular component of fibre waviness can be readily calculated by the method developed herein at the selected resolution of 1.50 μm/px. In contrast, the processed *xz*-tomograms contain much greater numbers of short aspect ratio fibre objects that act akin to artifacts and are harder to separate, as evidenced by presence of zebra-patterning in the *xz*-tomogram included in Fig. 5-22. The adverse influence of these fibre objects is very difficult to address without rejecting significant portions of each tomograms or resorting to similarly destructive filtering approaches, which would significantly bias the angle calculations and run counter to the secondary goals of automation and computational efficiency. The preliminary results are on the order of ±8°, which is similar to the in-plane component and not physically possible. The selected micro-CT resolution is simply too low to reliably estimate the out-of-plane angular component of fibre waviness.

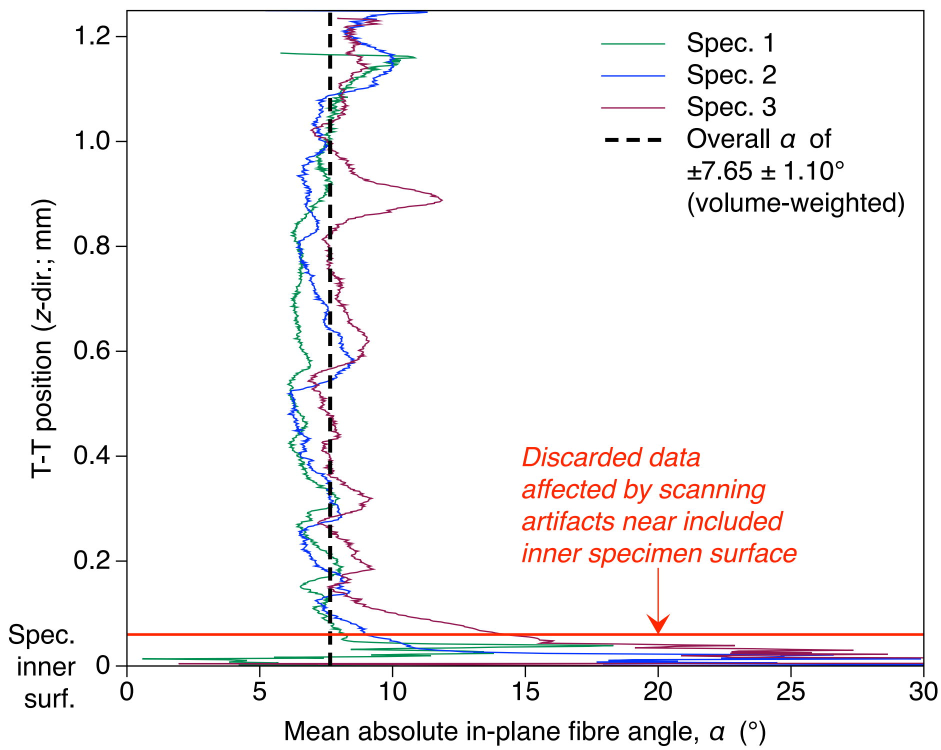

Fig. 5-23. T-T distribution of the mean absolute in-plane fibre angle (α).

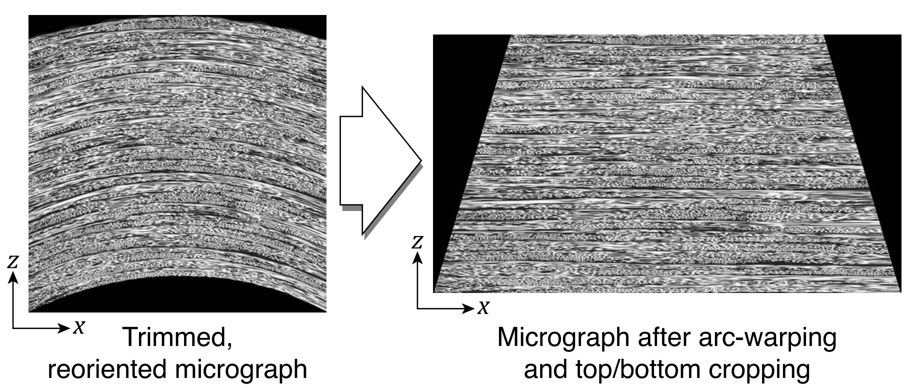

Fig. 5-24. Arc-warping of trimmed corner micrograph in Adobe Photoshop.

The angle calculations are instead performed on the five corner micrographs used in the previous section rather than micro-CT data. Their resolution is substantially higher at 0.581 µm/px. The micrographs are manually trimmed, reoriented, warped and cropped (top and bottom) in

Adobe Photoshop, as illustrated in Fig. 5-24. The use of arc-warping is deemed acceptable in the case of square images. The analysis yields a mean, absolute, out-of-plane angular component (ϕ) of $\pm 1.64 \pm 0.0415°$, which is roughly 4.7 times smaller than the in-plane component and physically consistent with visual inspection of micrographs and tomograms. Likewise, the variability of the out-of-plane component is much smaller than that of the in-plane component (coefficients of variation of 2.53 versus 14.4%, resp.).

Finally, three types of representative *xy*-tomogram regions are presented in Fig. 5-25 to illustrate the morphology of the marcelling in corners. The first representative region is one with minimal fibre misalignment, which is representative of the far-field fibre misalignment that may be expected in flanges given manually stacked semipregs. The second representative region is one with macro-scale marcelling (i.e. on the order of mm). The third representative region is one with stochastically-distributed and overlapping bands of marcelling fibres with varying mesoscale width (i.e. on the order of one to twenty fibres-wide). This third type of region is by far the most prevalent throughout the *xy*-tomogram stacks.

The visual evidence gleaned from *xy*-tomogram stacks supports the postulation put forth in the previous section that marcelling primarily occurs at intraply midplanes due to the air evacuation strategy of the tape semipreg. during layup and debulking. Fibres in the resin-free midplane of the tape semipreg are not as well supported transversely as are fibres in the partially impregnated, b-stage, top and bottom, planar regions. Dry fibres are therefore relatively free to undulate in the plane of the laminate insofar as they can overlap adjacent fibres. The stochastic distribution and varying width of marcelling fibre bands, which is the dominant regime of fibre waviness found, support this observation. The semipreg architecture, and in particular the design of air evacuation channels, should therefore be considered as playing an influential role in the extent, magnitude and morphology of fibre waviness in convex-tape corner laminates.

5.5.4 Effect of corner fibre waviness on elastic properties

The discussion finally shifts to determining the effect of the corner fibre waviness characterized in the previous two sections on the elastic properties of the corner laminate. To this end, the engineering constants of the selected tape semipreg provided in § 2.2.3 are degraded via a Euler-angle, 3D transformation of the compliance matrix using the mean, absolute in- and out-of-plane angular components of the fibre misalignment. Knockdowns in stiffness may subsequently be estimated.

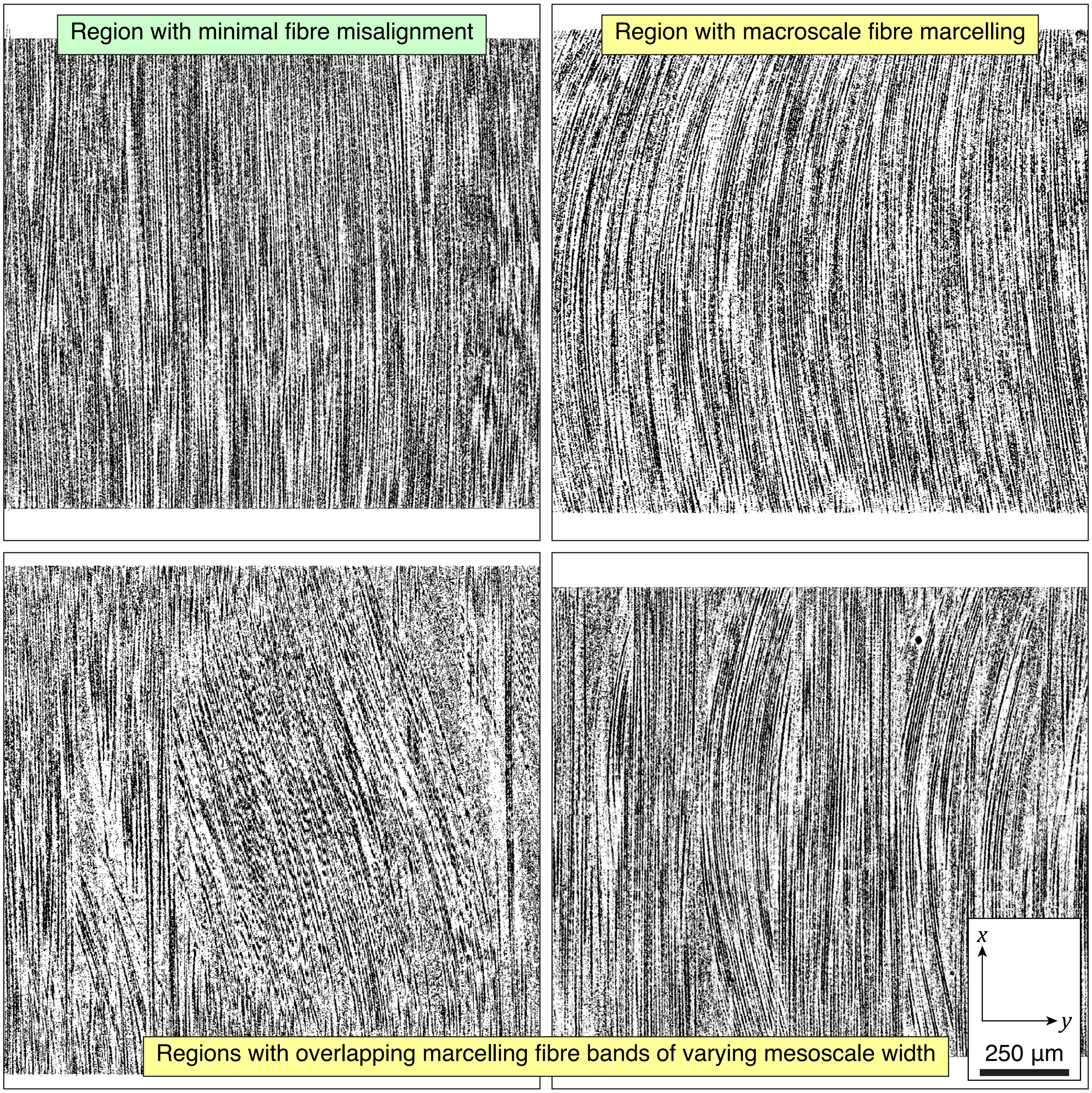

Fig. 5-25. Fibre waviness morphology in processed *xy*-tomograms.

Degradation of engineering constants

The mean, absolute, in- and out-of-plane angular components of the fibre waviness in the corner (α and ϕ, resp.) obtained in the previous section define the reference frame of the mean, absolute misaligned fibre (i.e. on-axis or local frame with 123-axes) relative to the reference frame of the corner specimen (i.e. off-axis or global frame with *xyz*-axes), which is that of a perfectly aligned fibre. These two reference frames are illustrated in Fig. 5-26, in addition to the unit vectors that define them, the angular components of the fibre waviness and the two Euler angle rotations and corresponding angles required to transform a vector from one frame to the other.

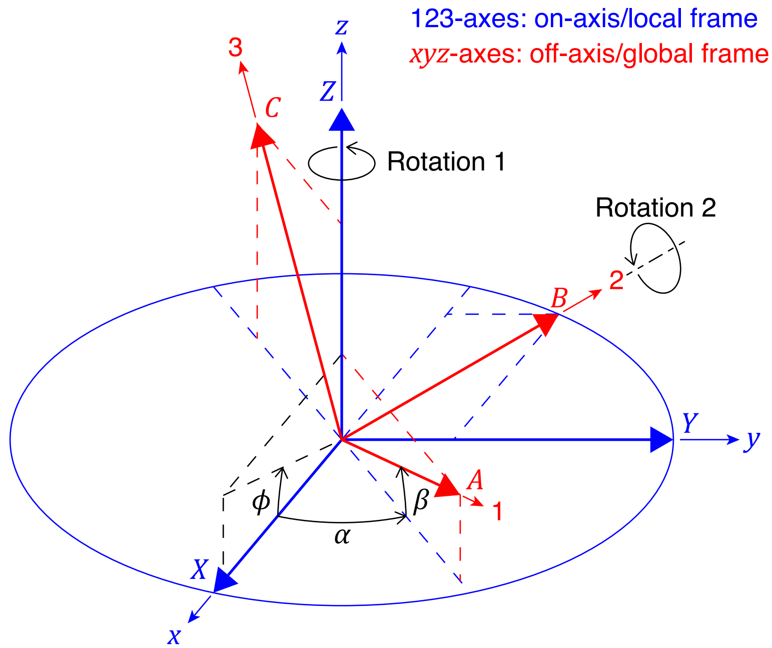

Fig. 5-26. Schematic of the on- and off-axis reference frames.

The engineering constants of the selected tape semipreg provided in § 2.2.3 are used to define the on-axis compliance matrix ($[S_{123}]$). The on-axis compliance matrix may then be transformed to the off-axis compliance matrix ($[S_{xyz}]$) via two, counter-clockwise Euler angle rotations following the alternate ZYZ convention, i.e.: first rotation of angle α about the z-axis followed by rotation two of angle β about the 2-axis (i.e. the y'-axis). It is assumed that the 2-axis lies in the xy-plane, which renders a third rotation of angle γ about the 3-axis (i.e. the z''-axis) unnecessary. The transformed engineering constants can finally be extracted from the terms of the off-axis compliance matrix. The compliance matrix transformation and subsequent degradation of engineering constants is implemented in a MathWorks Matlab (R2015b) m-script that is included in Appendix C.3 and uses as inputs the on-axis engineering constants and the two angular components of the fibre waviness. Textbooks such as *Classical mechanics* by Goldstein, Poole and Safko [227] and *Mechanics of fibrous composites* by Herakovich [228] can be perused to gain a more detailed understanding of Euler angle transformations, the alternate conventions for the rotational sequence and all the necessary derivations.

The transformation matrix ($[T]$) is simply the product of the two rotation matrices ($[T_1]$ and $[T_2]$) and is useful for defining the nine rotational components ($l_{1,2,3}$, $m_{1,2,3}$ and $n_{1,2,3}$) based on the first two Euler angles (α and β). These equations are simplified by the fact that the third Euler angle (γ) is null and therefore the corresponding *cosine* and *sine* terms equal 1 and 0, resp.

$$[T] = [T_2][T_1] = \begin{bmatrix} l_1 & m_1 & n_1 \\ l_2 & m_2 & n_2 \\ l_3 & m_3 & n_3 \end{bmatrix} = \begin{bmatrix} \cos(\alpha)\cos(\beta) & \sin(\alpha)\cos(\beta) & -\sin(\beta) \\ -\sin(\alpha) & \cos(\alpha) & 0 \\ \cos(\alpha)\sin(\beta) & \sin(\alpha)\sin(\beta) & \cos(\beta) \end{bmatrix} \tag{1-1}$$

The strain-transformation matrix ($[T_\varepsilon]$) can then be derived to transform the off-axis strain components ($\{\varepsilon_{xyz}\}$) into the corresponding on-axis components ($\{\varepsilon_{123}\}$),

$$\{\varepsilon_{123}\} = [T_\varepsilon]\{\varepsilon_{xyz}\} \tag{1-2}$$

where: $[T_\varepsilon] =$

$$\begin{bmatrix} l_1^2 & m_1^2 & n_1^2 & m_1 n_1 & n_1 l_1 & l_1 m_1 \\ l_2^2 & m_2^2 & n_2^2 & m_2 n_2 & n_2 l_2 & l_2 m_2 \\ l_3^2 & m_3^2 & n_3^2 & m_3 n_3 & n_3 l_3 & l_3 m_3 \\ 2l_2 l_3 & 2m_2 m_3 & 2n_2 n_3 & m_2 n_3 + m_3 n_2 & n_2 l_3 + n_3 l_2 & l_2 m_3 + l_3 m_2 \\ 2l_3 l_1 & 2m_3 m_1 & 2n_3 n_1 & m_3 n_1 + m_1 n_3 & n_3 l_1 + n_1 l_3 & l_3 m_1 + l_1 m_3 \\ 2l_1 l_2 & 2m_1 m_2 & 2n_1 n_2 & m_1 n_2 + m_2 n_1 & n_1 l_2 + n_2 l_1 & l_1 m_2 + l_2 m_1 \end{bmatrix}$$

Likewise, the stress-transformation matrix ($[T_\sigma]$) can be derived to transform the off-axis stress components ($\{\sigma_{xyz}\}$) into the corresponding on-axis components ($\{\sigma_{123}\}$),

$$\{\sigma_{123}\} = [T_\sigma]\{\sigma_{xyz}\}, \text{ where: } [T_\sigma] = [T_\varepsilon]^{-T} \tag{1-3}$$

These two transformation matrices further enable the transformation of the off-axis stiffness and compliance matrices ($[C_{xyz}]$ and $[S_{xyz}]$, resp.) into the corresponding on-axis matrices ($[C_{123}]$ and $[S_{123}]$, resp.),

$$[C_{123}] = [T_\sigma]^{-1}\,[C_{xyz}]\,[T_\varepsilon] \tag{1-4}$$

$$[S_{123}] = [T_\varepsilon]^{-1}\,[S_{xyz}]\,[T_\sigma] = [T_\sigma]^{T}\,[S_{xyz}]\,[T_\sigma] \tag{1-5}$$

It should be noted that a typical transformation is performed from the on-axis to the off-axis frame; however, in this particular case the two frames are reversed given the that α and ϕ are measured relative to the x-axis of the off-axis frame for practical considerations. The non-zero terms of the on-axis compliance matrix are known and may be calculated as follows based on the on-axis engineering constants provided in § 2.2.3,

$$\begin{aligned} &S_{11} = 1/E_{11} && S_{22} = S_{33} = 1/E_{22} \\ &S_{12} = S_{21} = S_{13} = S_{31} = -\nu_{12}/E_{11} && S_{23} = S_{32} = -\nu_{23}/E_{22} \\ &S_{44} = 1/G_{13} && S_{55} = S_{66} = 1/G_{12} \end{aligned} \tag{1-6}$$

The transformation can therefore be reversed in order to obtain the off-axis compliance matrix,

$$[S_{xyz}] = [T_\sigma]^{-T}\,[S_{123}]\,[T_\sigma]^{-1} \tag{1-7}$$

The off-axis engineering constants may finally be obtained from the off-axis compliance matrix as follows,

$$\begin{aligned} &E_{xx} = 1/S_{11}^{xyz} && E_{yy} = 1/S_{22}^{xyz} && E_{zz} = 1/S_{33}^{xyz} \\ &\nu_{xy} = -S_{12}^{xyz}/S_{11}^{xyz} && \nu_{xz} = -S_{13}^{xyz}/S_{11}^{xyz} && \nu_{yz} = -S_{23}^{xyz}/S_{22}^{xyz} \\ &G_{xy} = 1/S_{55}^{xyz} && G_{xz} = 1/S_{66}^{xyz} && G_{yz} = 1/S_{44}^{xyz} \end{aligned} \tag{1-8}$$

The transformed engineering constants are an estimation of the degraded elastic properties of the laminate due to the occurrence of fibre waviness in the corner. These constants vary as a function of the two angular components of fibre waviness (α and ϕ), as illustrated in Fig. 5-27 in the case of the off-axis modulus of elasticity (E_{xx}) in the nominal fibre orientation.

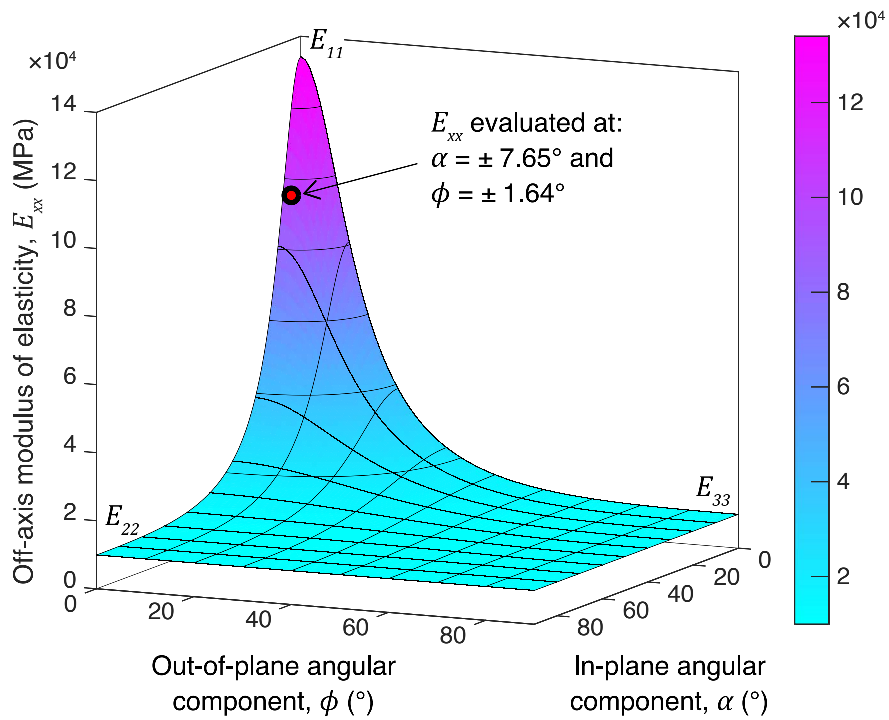

Fig. 5-27. Estimation of the off-axis elasticity modulus (E_{xx}) as a function of fibre waviness.

Results and discussion

The magnitude of the fibre waviness characterized in the previous section is found to significantly degrade the in-plane rigidity of the specimen in the corner region. The transformed elastic constants are presented in Table 5-6 along with the corresponding property knockdowns. As anticipated, the most affected property is the in-plane modulus of elasticity (E_{xx}) given a 28.9% property knockdown. This property drops precipitously with small angular components, as illustrated in Fig. 5-27. Meanwhile, the other elastic constants are only marginally affected. The loss of rigidity in the corner plays a key role in degrading the bending stiffness response. The original elastic constants utilized in the FE modelling of the specimen-sleeve assembly (§ 3.6) can be replaced by the degraded constants to obtain an improved agreement with experimental load curves. Given the relatively uniform distribution of marcelling throughout the corner region, a simple anisotropic material model may still be used to estimate the macroscopic specimen response.

Table 5-6. Transformed elastic constant values and corresponding percent knockdowns.

Elastic constant (unit)	Original value	Transformed value	Property knockdown
E_{xx} (MPa)	134,000	95,307	28.9%
E_{yy} (MPa)	9,930	9,970	-0.403%
E_{zz} (MPa)	9,930	9,932	-0.0201%
ν_{xy} (-)	0.330	0.357	n/a
ν_{xz} (-)	0.330	0.321	n/a
ν_{yz} (-)	0.500	0.493	n/a
G_{xy} (MPa)	5,410	5,557	-2.72%
G_{xz} (MPa)	5,410	5,356	1.00%
G_{yz} (MPa)	3,310	3,334	-0.725%

5.6 Summary

Three categories of factors are shown in Chapter 4 to affect laminate quality, namely design factors, generally deficient processing conditions and noteworthy industrial cases. The present chapter extends the investigation of these factors to encompass mechanical performance in corners with a focus on ILT behaviour. In doing so, the work ventures beyond the norm set in recent studies performed on VBO corner laminates, which evaluate the robustness of semipreg processing solely in terms of laminate quality [69, 121, 129, 137, 138]. Large and integrated, VBO parts are intended for functionally critical, load-bearing applications. To this end it is essential to additionally characterize the mechanical performance of representative, complex-shape coupons (i.e. corner specimens) and establish causal links whenever possible with laminate quality findings. A number of key findings that complement the design guidelines of Chapter 4 may thus be extracted from the results to aid in future, complex-shape part design with next-generation semipregs.

In addition, a novel, computational approach is developed to investigate the occurrence of fibre waviness in convex corner laminates comprised of tape-UD semipreg, which is found to be the most egregious occurrence out of all tested design factors. Fibre waviness is characterized in terms of extent, magnitude and morphology based on 2D micrographic and 3D micro-CT data. The magnitude consists of the mean, absolute in- and out-of-plane angular components of the misaligned fibres, which are subsequently used to degrade the nominal elastic properties of the semipreg and estimate the corresponding knockdown in in-plane stiffness.

Experimental repeatability (continued). The statistical results obtained from the interlaminar strength datasets generally corroborate the initial findings stemming from the statistical analysis of laminate quality datasets presented in § 4.4. The present experiments are not strictly repeatable given the statistically significant difference in repeated sample means. Single-sample test conditions must therefore be interpreted with caution. That being the case, the precision of the present research environment compares favorably to that of an expert research environment: the corner specimen preparation and mechanical testing methods employed in this thesis generate interlaminar strength data with lower variability than similar results generated by an expert research and industrial institute (i.e. NIAR) or typically reported in the literature.

Design factors. In general, all the samples tested fail suddenly via ILT delamination with substantial, initial load-drops; test curves are smooth and do not exhibit any subcritical, pre-failure damage. The initial delaminations form sub-laminates that take the remaining load if sufficiently low (i.e. presence of secondary load-drops). In turn, failure load and displacement, bending stiffness and energy-to-failure are generally all found to increase as a function of the percent of fibres oriented in the hoop direction (0°). The tape-UD configuration is therefore the highest performing sample given a pure bending moment.

With respect then to material selection, the tape exhibits significantly higher ILTS than the 2D-woven semipregs. The 2D-woven baselines contain significant corner porosity despite near-optimal processing conditions and, as indicated by Jackson and Ifju [83], ILTS drops precipitously as a function of fibre loading fraction, which is lower for the 2D-woven baselines. Secondly, the fibre-reinforcement architecture dictates the failure type. Failed tape cross-sections have "shattered" appearances with extensive, out-of-plane crack branching. This type of failure is indicative of the considerable elastic energy released at higher failure loads and displacements. Meanwhile, the 2D-woven baselines exhibit far fewer intralaminar delaminations with "tortuous" appearances that match the rougher ply topologies.

Next, tool-shape is not found to affect ILTS despite critically affecting corner laminate quality and notably engendering severe corner thickening as observed Chapter 4. Meanwhile, corner thickening, which is more prevalent in concave corners, yields higher failure loads and translates into higher CBS.

Finally, stacking sequence is shown to affect the ILTS of the tape but not of the 2D-woven semipregs, which share much more similar and heterogeneous mesostructures. Laminates with non-UD stacking sequences are much more sensitive to free edge effects and machining-induced damage. Furthermore, the critical, delamination energy release rate at ply interfaces varies based on the interply angle, rendering a typical QI-layup weaker than a XP-layup. Lastly, the presence of angled plies eliminates the branching crack behaviour observed in the case of tape-UD baselines; delamination cracks are mostly interlaminar and occasionally migrate through plies to adjacent ply interfaces.

Process deviations and deficiencies. First, deficient consolidation pressure is shown to greatly lower the ILTS of tape-UD samples. The loss in ILTS of the tape is best described by a logarithmic correlation with increasing corner void content, which indicates that void content ceases to influence ILTS beyond a critical value. In contrast, PW-UD samples are unaffected by deficient consolidation pressure loss given that the PW is hampered by a critically-high void content even at near-optimal consolidation pressure. As an aside, the failure behaviour of tape samples changes with increasing void content: secondary load-drops appear as the initial load-drop decreases.

With respect then to noteworthy industrial cases, the results mirror the laminate quality findings of Chapter 4. Restricted air evacuation results in the lowest ILTS on account of the high internal void content and rough major surfaces caused by surface pitting. Meanwhile, the other two industrial cases, namely the slow temperature cure ramp and no-intermediary debulking, did not significantly affect mechanical performance—although they could only be tested for the PW. Finally, though untested, the tape is likely to also be most affected by restricted air evacuation.

Fibre waviness in corners. A novel characterization approach is developed to investigate fibre waviness in tape corners based on the image analysis of optical micrographs and reconstructed micro-CT slices. In-plane marcelling (locally-periodic waviness) is found to be the dominant regime of fibre waviness in tape-UD corners. It extends roughly 10 mm into the flanges and is stochastically-distributed throughout the corner region affecting roughly 50% of plies for a given frontal cross-section. In turn, the resulting property knockdown on the in-plane modulus of elasticity reaches nearly 30%, which drastically degrades the corner specimen bending response. As an aside, fibre waviness also likely affects the ILTS, though this determination is beyond the scope of this work and remains to be investigated.

A secondary and noteworthy finding is the effect that the tape semipreg design appears to have on the fibre waviness morphology. Marcelling is found to prevail in the resin-free, mid-plane of semipreg plies designed to improve air evacuation. Dry fibres are free to undulate due to compaction-induced buckling during layup and intermediary debulking insofar as they can overcome adjacent fibres. Meanwhile, the cured laminate consists of stochastically-distributed, and overlapping bands of marcelling fibres with varying widths ranging from a single fibre diameter to the macroscale. These insights point to the notion that fibre waviness in the case of tape semipregs is an irregularity rather than a defect in that it cannot be readily remedied by a stricter adherence to a near-optimal process.

Design guidelines. Laminate quality in terms of constituent content and dimensional stability alone does not predict the performance of corner laminates. The percentage of 0° fibres, the presence and quality of machined edges, and the interfacial angle(s) in given stacking sequences all critically influence the interlaminar performance of corner laminates and must therefore be considered. To this end, the following design guidelines complement the guidelines given in § 4.6:

- A tape laminate generally yields superior ILTS compared to 2D-woven semipregs over singly-curved features (e.g. corners). Furthermore, tape laminates are more readily tailored to handle load cases that are more complex than pure bending.
- A corner tape laminate with a UD stacking sequence yields a substantially higher ILTS than alternate stacking sequences that contain off-axis plies (e.g. QI and XP). The presence of machined free edges and other discontinuities in the corner region as well as interfacial angles drastically reduces the ILTS of non-UD layups. In the event that a non-UD layup is required, a non-conventional stacking sequence may therefore be preferable that places longitudinal rather than transverse plies in regions of high-tensile, tangential stresses such as to minimize the risk of matrix micro-cracking, and places low interfacial angles (< 45°) in regions of high radial stresses such as to minimize the risk free-edge delaminations [80].
- Air evacuation remains a critical factor: as in the case of laminate quality, restricted air evacuation constitutes a worst-case scenario in terms of ILTS and must be avoided.
- Corner laminates consisting of novel tape semipregs are prone to fibre waviness and specifically marcelling, which severely degrades the local in-plane stiffness. In general, the effect on fibre waviness of dry, air evacuation regions in next-generation semipregs must

be taken into consideration following a similar approach as the one developed herein to estimate the effect on stiffness properties. Future work should also be conducted to estimate its effect on strength properties.

6
Conclusion

6.1 Research contributions

Semipregs and complex-shape laminates cured via VBO processing still exhibit to date a high degree of variability and defects that hinders in-service performance and reliability. In particular, the inferior robustness of VBO semipreg processing compared to autoclave prepreg processing poses a key challenge in the processing of sharply-curved details. Successful insertion of semipregs in large, integrated structures that include such details requires more research in terms of experimental methods and understanding. Improvements in corner laminate characterization approaches and more representative T-T mechanical testing methods can generate a deeper understanding of the key factors that affect laminate quality in corners and, in turn, their effect on interlaminar mechanical performance. To this end, the research presented in this thesis has led to notable contributions aimed at improving VBO processing of sharply-curved laminates. These contributions are presented below in the order that they appear in this thesis.

Development of a corner thickness profiling method (Obj. I.iii)

A novel, semi-automated thickness measurement method is presented in Chapter 2. It consists of analyzing corner specimen scans, from which individual thickness profiles are determined as a function of position along the reference, tool-side edges—no other currently known published studies use a similar approach to investigate complex-shape laminates. The analysis is implemented in Matlab and can be readily adapted to treat complex geometries other than L-shape corners and data other than 2D scans. In turn, the approach is validated against the more direct measurement methods that are currently used in the literature and prescribed by mechanical test standards. Importantly, sets of measurements made on tape and 2D-woven corners demonstrate that it yields more accurate, precise and insightful results. This method has thus far directly contributed to two conference papers that study the effect of processing parameters on VBO corners [99, 127], as well as generated data used for modelling thickness deviation [52].

Development of mechanical stiffening sleeves for CBS testing (Obj. I.i-ii)

A direct, practical and cost-effective modification of the current 4PB-CBS test method as standardized in ASTM D6415 is presented in Chapter 3 to improve the accuracy of determined properties. In particular, a novel stiffening sleeve design is developed to reduce the error in the applied bending moment calculation caused by excessive flexure of a corner specimen's flanges. The sleeves are mechanically fastened and easily adjustable. In addition, their use allows for a simple, geometric correction factor to account for the effect of corner opening, which current standards do not take into consideration. The use of stiffeners subsequently reduces the error in the CBS and ILTS calculations from 7 and 11% to below 1 and 2%, resp., for a sleeve-offset of 2 mm as estimated via FEM. The modification is validated via mechanical testing and a subsequent fractographic inspection of failed sections via FE-SEM. Together, the experiments demonstrate that the use of stiffening sleeves does not adversely affect the onset and desired mode of failure in corners. This work was presented for review to the ASTM committee on interlaminar properties [195], which considers modifications to existing standards.

Statistical investigation of the repeatability of experiments on VBO corners (Obj. II.i)

A significant portion of peer-reviewed studies in the field of composites engineering reach important conclusions on the sole basis of single or bi-replicate experimental samples. The determination of statistically significant measurements can be very costly and require extensive resources that are beyond the reach of most academic research laboratories. This reality is however seldom acknowledged in published studies, though it importantly qualifies the dependability of the findings—or lack thereof. To this end, a comprehensive statistical analysis is proposed to establish the statistical significance of the findings presented in Chapters 4 and 5, and to additionally determine the statistical variability of the measurements. The approach borrows statistical tests and methods used in the determination of statistically-based material properties and inferential statistics used in interlaboratory studies. In turn, it can be applied to any experimental work in the field of composites engineering and, more generally, materials research.

Insofar as the research presented in this thesis is concerned, the experimentally-determined laminate quality measurements and mechanical properties of corners are not strictly repeatable given statistically significant differences in repeated sample means in most cases. This finding also affects similar measurements and properties obtained from an expert research environment, namely NIAR's NCAMP database. That being the case, the precision of the present research environment compares favorably to that of an expert research environment such as NIAR given generally lower inter- and intra-sample variability. In other words, the experimental work conducted in this thesis is demonstrated to meet the same standards of expertise—thereby lending further credence to the findings.

Selection and investigation of key factors affecting the laminate quality and mechanical performance of VBO corners (Obj. II.ii-iii)

The general and improved experimental methods (Chapters 2 and 3) are ultimately used to systematically assess the effect of an extensive set of key design, processing and industrial factors on the laminate quality (Chapter 4) and mechanical performance (Chapter 5) of VBO corners. A special focus is placed on ILT performance given the susceptibility of sharply-curved details failing via delamination due to flexural loads. These factors are carefully selected from the available literature on VBO semipreg processing surveyed in Chapter 5 as well as from feedback from the aerospace industry. In addition, they have not yet been investigated together in a single study in the context of sharply-curved details, specifically. The selected design factors include material selection (i.e. tape, PW and 8HS), tool-shape (i.e. convex or concave), and stacking sequence (i.e. UD, QI and XP); next, the single, selected processing factor is deficient consolidation pressure inside of the vacuum-bag; and lastly, the selected, noteworthy industrial cases consist of slower thermal ramping, ply collation without intermediary-debulking and restricted air evacuation.

In turn, the mechanical characterization work performed in this thesis addresses the scarcity of studies investigating the mechanical performance of VBO corners, which are representative of critical details in large, integrated structures. The available literature on VBO semipreg processing mostly focuses on laminate quality measurements as the sole criteria for process robustness. Meanwhile, the handful of studies that consider mechanical performance are limited to flat coupons and in-plane properties. The experimental findings are summarized at the end of Chapters 4 and 5.

An unexpected and interesting finding is worth mentioning stemming from the testing of a PW semipreg from Cytec that contains dry, T-T air evacuation channels. This next-generation semipreg is found to yield relatively high macro-porosity in corners compared to a current, second-generation 8HS semipreg despite improved T-T air permeability. A likely explanation for the suboptimal quality is the effect of ply nesting during layup, which may seal the T-T air evacuation channels thereby entrapping a greater volume of air. This finding is most noticeable in the case of a QI layup, which promotes ply nesting.

Design and processing guidelines for industry (Obj. II.iv)

The experimental findings of Chapters 4 and 5 make it clear that producing high-quality semipreg laminates via VBO processing is more challenging for sharply-curved laminates than flat ones. In addition, laminate quality in terms of constituent content and dimensional stability alone does not predict the performance of corners. The percentage of 0° fibres, the presence and quality of machined edges and the interfacial angle(s) in a given stacking sequence all critically influence the interlaminar performance of corner laminates and must therefore be considered. To this end, the experimental findings are condensed into a set of important guidelines and best practices for the design and processing of sharply-curved details so as to achieve high-laminate quality and good resistance to delamination. The guidelines listed at the ends of Chapters 4 and 5 are compiled herein and add to the findings of Centea and Hubert [114] on VBO flat laminates and Ma *et al.* on VBO corners [121].

- **Material selection.** Semipreg tape is generally recommended instead of 2D-woven semipregs for singly-curved geometries. Tapes yield demonstrably superior corner laminate quality and ILTS values and are more readily tailored to handle complex load cases beyond pure bending. Meanwhile, doubly-curved features may necessitate the superior drapability of 2D-woven semipregs (e.g. PW) at the cost of relatively lower quality and resistance to delamination.
- **Stacking sequence.** Tape corners with a UD stacking sequence yield substantially higher ILTS values than alternate stacking sequences that contain off-axis plies (e.g. QI and XP). The presence of machined free edges and other discontinuities in the corner region as well

as interfacial angles drastically reduces the ILTS of non-UD layups. In the event that a non-UD layup is required, a non-conventional stacking sequence is preferable. Such a layup consists of placing longitudinal rather than transverse plies in regions of high-tensile, tangential stresses such as to minimize the risk of matrix micro-cracking, and placing off-axis plies with low interfacial angles (< 45°) in regions of high radial stresses such as to minimize the risk free-edge delaminations [80].

- **Tool-shape**. Laminate consolidation in corners is most often impeded by interply friction and at the very least local pressure differentials. Uniform part thickness is therefore best achieved by selecting convex tool features over concave ones and relaxing the radius of curvature whenever possible. In turn, proper ply collation and conformation during layup via proper operator skill and intermediary debulking are vital. The use of a pressure intensifier strip may also be considered for problematic but indispensable concave features as discussed by Ma *et al.* [121].
- **Consolidation pressure** must be maximized by ensuring an adequate ambient pressure (i.e. minimizing the effects of elevation and weather) and an adequate vacuum-bag pressure (i.e. reliable equipment and proper vacuum-bagging technique). A high-CPL above 98 kPa (29 inHg) is recommended for sharply-curved details, whereas a floor value of 91.5 kPa (27 inHg) is typically sufficient for flat laminates.
- **Restricted air evacuation** represents the worst-case scenario in terms of both laminate quality and ILTS. Limiting the volume of entrapped air during layup is vital and may be partly achieved via material selection (e.g. tape). In turn, fully evacuating entrapped air prior to the cure cycle may be achieved by designing a sufficiently long RT-hold, which requires: 1) accurate air permeability values for the given laminate, and 2) appropriate part design and vacuum-bagging arrangement so as to limit air evacuation distance and the number of obstacles that may locally collapse air evacuation channels (e.g. sharp tool features, inserts, ply-drops).
- **Next-generation semipregs (improved T-T air evacuation)**. First, the limited testing performed on Cytec's next-generation PW semipreg indicates higher macro-porosity in corners. In turn, tape corner laminates are prone to fibre waviness and specifically marcelling, which severely degrades the local in-plane stiffness. In general, the effect on fibre waviness of dry, air evacuation regions in next-generation semipregs must be taken

into consideration following a similar approach as the one developed herein to estimate the effect on stiffness properties. The reliability of next-generation semipregs with improved T-T air evacuation strategies for complex-shape applications ought to be better established in the literature before these advanced materials can be unreservedly recommended.

Characterization of fibre waviness in sharply-curved tape laminates (Obj. I.iv-II.v)

A novel characterization approach is developed to investigate fibre waviness in tape corners based on the image analysis of optical micrographs and reconstructed micro-CT slices. Importantly, this approach introduces more computationally efficient means of re-orienting and warping scanned volumes in order to quantitively assess the magnitude of fibre misalignment with respect to pre-determined, curved reference planes. It is subsequently employed to investigate the extent, magnitude and morphology of fibre waviness in convex tape corners consisting of a UD layup, which proved the most affected of the sample configurations tested in this thesis. In-plane marcelling (locally-periodic waviness) is found to be the dominant regime of fibre waviness. It is stochastically-distributed in the corner region and clearly extends into adjacent flanges. In turn, the resulting property knockdown on the in-plane modulus of elasticity reaches nearly 30%, which drastically degrades the corner specimen's flexural stiffness.

An additional, noteworthy finding is the effect that semipreg design appears to have on the fibre waviness' morphology. Marcelling is found to prevail in the resin-free, mid-plane of tape plies designed to improve air evacuation. Dry fibres are free to undulate due to compaction-induced buckling during layup and intermediary debulking insofar as they can overcome adjacent fibres. Meanwhile, the cured laminate consists of stochastically-distributed, and overlapping bands of marcelling fibres with varying widths ranging from a single fibre diameter to the macroscale. These insights indicate that fibre waviness is additionally influenced by semipreg architecture and, notably, the presence of air evacuation channels. As such, it may be regarded as an irregularity rather than a defect given that it cannot be remedied by a stricter adherence to robust processing.

6.2 Future work

The research presented in this thesis highlights opportunities for future work. To this end, a number of candidate topics are proposed and listed below to further the understanding and robustness of VBO semipreg processing *vis-à-vis* complex-shape laminates.

Refinement and standardization of the stiffening sleeve modification. The modelling and validation presented in this thesis considers the specimen configuration prescribed in the ASTM D6415 standard, i.e. tape corner with a UD layup. It is will be important to extend the FEM work to alternate stacking sequences and woven reinforcements and validate the new FEM results with additional mechanical tests and fractographic inspections of failed sections. Ultimately, it is in the interest of standardization that the use of stiffening sleeves be reproduced in other research settings to confirm its attributes.

Adaptation of the digital image analysis methods to more complex-shape laminates. Both the corner thickness profiling method and the corner fibre waviness characterization approach are currently adapted to the L-shape corner specimen geometry and its cylindrical inner corner surface, resp. However, complex-shape laminates can include multiple corners in close proximity and more rarely, doubly-curved features. The digital image analysis methods developed in this thesis ought to be generally adapted to more complex geometries, and, specifically, the thickness profiling method ought to be adapted to 3D scanning data. This work should be relatively straightforward given that these methods are based on effectively flattening a complex-shape laminate cross-section based on a reference geometry, i.e. the tool-side edge or surface (2D or 3D scanning data, resp.).

Effect of semipreg T-T air evacuation strategies on corner laminate quality. It is not yet clear based on evidence in this thesis that semipregs with T-T air evacuation channels are ideally suited for sharply-curved tool features. A more extensive experimental matrix would be desirable that additionally varies stacking sequence in establishing the effect of novel T-T air evacuation strategies on laminate quality and, in turn, the reliability of next-generation semipregs.

Effect of semipreg design on fibre waviness in corners. In the same vein as novel T-T air evacuation strategies, the effect of air evacuation channels on in-plane waviness is investigated in this thesis in the case of a current-generation tape semipreg. It would be desirable to extend this work to semipregs with alternate reinforcement types, stacking sequences and air evacuation strategies to assess their effect on fibre waviness. In turn, a micro-CT approach such as that developed by Centea and Hubert [173] to measure the impregnation of flat laminates would be beneficial in establishing fibre waviness formation during ply collation and curing.

Stochastic modelling of laminate quality in VBO corners. VBO semipregs and cured corner laminates exhibit a high degree of variability in terms of the local degree of resin impregnation and local thickness deviations, resp.—amongst other important properties. Current analytical models that aim to predict laminate quality are best suited to illustrate extreme cases and generate conservative upper and lower bounds; however, they fail to adequately capture variability and thus make accurate predictions. The development of stochastic approaches such as those developed by Helmus *et al.* [123, 129] via first 2D and eventually 3D FEM is most likely to succeed in capturing the intricate phenomenological state of corners and improve predictions.

Fatigue life of VBO corners. Large, integrated parts such as ones featured in primary aerospace structures must be designed to endure various load cases during their service life including cyclical loading. As is demonstrated in this thesis, sharply-curved details represent some of the most critical features, wherefrom delaminations may form, spread and eventually lead to overall failure. It is consequently important to characterize the effect of increased variability and defect levels in sharply-curved details on the fatigue life of such features starting with corners.

Parametrized design and processing guidelines. Guidelines and best practices are currently itemized. As the effect of design considerations, processing parameters and other notable factors becomes better understood through experimental and modelling work, it will be important to translate these findings into parametric design and processing tools such as visual maps to rapidly refine part designs and aid in their manufacturing.

A Nomenclature

The following appendix defines the acronyms, units and symbols appearing on more than one occasion throughout this thesis.

A.1 Acronyms

17-4PH	Grade of martensitic-precipitation-hardening stainless-steel
4PB-CBS	Curved beam strength via four-point bending
8HS	Eight-harness satin weave
a.k.a.	“Also known as”
ADK	Anderson-Darling k-sample statistical test
ANOVA	Analysis of variance
ASTM	American Society for Testing and Materials
ATL/AFP	Automated tape laying / automated fibre placement
B	Baseline (sample processing conditions)
C3D20	Continuum quadratic brick element with reduced integration (Abaqus/Standard)
CFRP	Carbon fibre-reinforced polymer
DIC	Digital image correlation
DOF	Degree of freedom
ECC	Enhanced correlation coefficient
e.g.	“For example” (Latin: *exempli gratia*)
ESR	Externally (deleted) studentized residual
F	“Female” or concave tool (specimen naming scheme, figures and tables only)
FE-SEM	Field-emissions scanning electron microscopy or microscope
FE-[term]	Finite element-[term]
FEM	Finite element modelling
GFRP	Glass fibre-reinforced polymer
HLM	Hinged-loading mechanism (referring to NASA method)

i.e.	"That is" (Latin: *id est*)
ILS	Inter-laboratory study or interlaminar shear—depending on context
ILT	Interlaminar tension/tensile
L1	10% consolidation pressure loss (sample processing condition)
L2	20% consolidation pressure loss (sample processing condition)
L3	30% consolidation pressure loss (sample processing condition)
LCM	Liquid composite moulding
LVDT	Linear variable differential transformer (displacement sensor)
M	"Male" or convex tool (specimen naming scheme, figures and tables only)
MAD	Median absolute deviation method for detecting outliers
MDPR	Material data property report
Micro-CT	Computed X-ray micro-tomography
n/a	"Not applicable"
NCAMP	National Center for Advanced Materials Performance (part of NIAR)
ND	No-intermediary debulking (sample processing condition)
NDI/NDE	Non-destructive inspection / non-destructive evaluation
NIAR	National Institute for Aviation Research, Wichita State University, USA
OOA	Out-of-autoclave
P-P	Probability-probability (plot)
PMC	Polymer matrix composite
PW	Plain-weave
QI	Quasi-isotropic (stacking sequence, e.g. $[45°/0°/\text{-}45°/90°]_{ns}$)
R	Restricted air evacuation (sample processing condition)
resp.	"Respectively"
RH	Relative humidity
RT-	Room-temperature
RTD	Room-temperature dry
RTM	Resin transfer moulding
SBS	Short beam strength (i.e. "apparent" ILSS)
SEM	Scanning electron microscope
SR	Slow thermal ramp (sample processing condition)

T-	Tape (specimen naming scheme, figures and tables only)
T-T	“Though-[the]-thickness”
u.o.s.	“Unless otherwise specified”
UD	Unidirectional (stacking sequence, i.e. $[0°]_{ns}$)
VBO	Vacuum-bag-only
vs.	“Versus”
XP	Cross-ply (stacking sequence, i.e. $[0°/90°]_{ns}$)

A.2 Units

-k	Thousands ($\times 10^3$)
-M	Millions ($\times 10^6$)
%	Percentage
°C	Degree Celsius
c-	Centi-[unit] ($\times 10^{-2}$)
dpi	Dots-per-inch
g	gram
G-	Giga-[unit] ($\times 10^9$)
h	Hour
J	Joule
k-	Kilo-[unit] ($\times 10^9$)
M-	Mega-[unit] ($\times 10^6$)
m	Meter
m-	Milli-[unit] ($\times 10^{-3}$)
min	Minute
N	Newton
n-	Nano-[unit] ($\times 10^{-9}$)
Pa	Pascal
px	Pixel
rpm	Rotations-per-minute
s	Second

vol.%	Percentage by volume
wt.%	Percentage by weight
μ-	Micro-[unit] ($\times 10^{-6}$)

A.3 Latin symbols [units]

$-r$	Radial direction in corner regions (cylindrical coordinates)
$-\theta$	Tangential direction in corner regions (cylindrical coordinates)
$-xyz$	Cartesian coordinates
ALLIE	Total strain energy in FE model (Abaqus/Standard variable)
ALLSD	Viscous dissipated energy in FE model (Abaqus/Standard variable)
CBS	Curved beam strength [kN]
CPL	Consolidation pressure level relative to atmospheric pressure [%]
CTE	Coefficient of thermal expansion [°C^{-1}]
$cv_{W,B}$	Intra/inter-sample coefficient of variation (within/between; [%])
E	Young's elasticity modulus [GPa]
E_f	Energy-to-failure [J]
G	Shear elasticity modulus [GPa]
$ILSS$	Interlaminar shear strength [MPa] ($S_{13} \approx F_{sbs}$)
$ILTS$	Interlaminar tensile strength [MPa] ($F_{33,tu} = \sigma_{r,max}$)
k	Degree of anisotropy [-]
K	Laminate in-plane air permeability coefficient [m^2]
M	Applied bending moment [kN·mm]
N_{TT}	Number of through-thickness finite elements [-]
P	Applied load [kN]
RD	Relative difference [%]
R^2	Coefficient of determination [%]
r_i	Inner corner radius [mm]
$r_{i,o}'$	Corrected inner/outer corner radius [mm]
r_m	Mean corner radius [mm]
r_o	Outer corner radius [mm]

$s_{W,B}$	Intra/inter-sample standard deviation (within/between)
S11	In-plane/tangential stress [MPa] (σ_{11} / σ_{θ} ; Abaqus/Standard variable; 2D model)
S12	Interlaminar shear stress [MPa] ($\tau_{\theta r}$; Abaqus/Standard variable; 2D model)
S22	Out-of-plane/radial stress [MPa] (σ_{22} / σ_r ; Abaqus/Standard variable; 2D model)
s_{off}	Stiffening-sleeve offset distance [mm]
t	Laminate thickness [mm]; time [h:min:s] (§ 2.2.2)
T	Part temperature [°C]
t_A	Thickness of stiffening-sleeve-specimen assembly [mm]
T_g	Glass transition temperature [°C]
t_{hold}	Duration of RT-vacuum-hold during the air evacuation processing stage [h:min]
w	Corner specimen width [mm]
$\bar{\bar{x}}$	Grand (pooled) mean

A.4 Greek symbols [units]

α	Resin degree-of-cure [%] (Ch. 2); statistical significance [%] (Ch. 4); in-plane angular component of fibre misalignment and first Euler angle [°] (Ch. 5)
α_{gel}	Resin degree-of-cure at gelation [%]
β	Second Euler angle [°]
Δ	Machine displacement [mm]
η	Resin viscosity [Pa·s]
σ_r	Radial (T-T) stress in the corner [MPa]
$\sigma_{r,max}$	Maximum radial (T-T) stress in the corner [MPa] (see *ILTS*)
σ_{θ}	Tangential (circumferential or hoop) stress in the corner [MPa]
$\tau_{\theta r}$	Interlaminar shear stress in the corner [MPa]
υ	Poisson's ratio [-]
ϕ	Mean, absolute, out-of-plane angular component of fibre misalignment [°]

B Technical drawings

The following appendix contains technical drawings utilized to machine the experimental fixtures and define fixture dimensions for the FE modelling work and experimental data reduction. Fig. B-1 and B-2 detail the machining features and dimensions of the curved beam tool utilized to process corner beams (§ 2.3.2). Fig. B-3 and B-4 detail the machining feature and dimensions of the proposed stiffening-sleeve design (§ 3.3.1). Lastly, Fig. B-5 defines the key dimensions of the CBS-4PB fixture that are utilized in the FEM and experimental data reduction (§ 3.3.2).

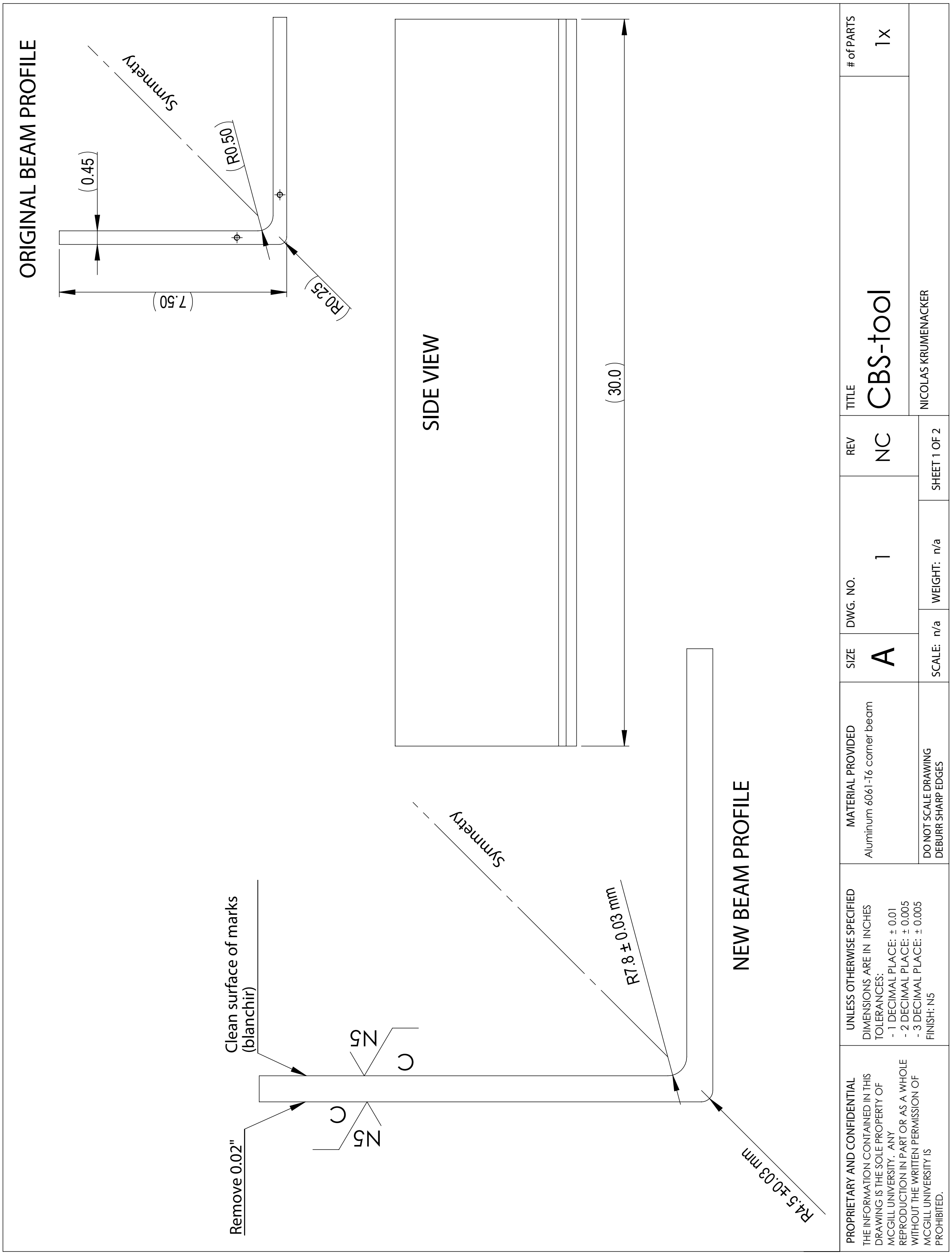

Fig. B-1. Technical drawing of curved beam tool machined surfaces.

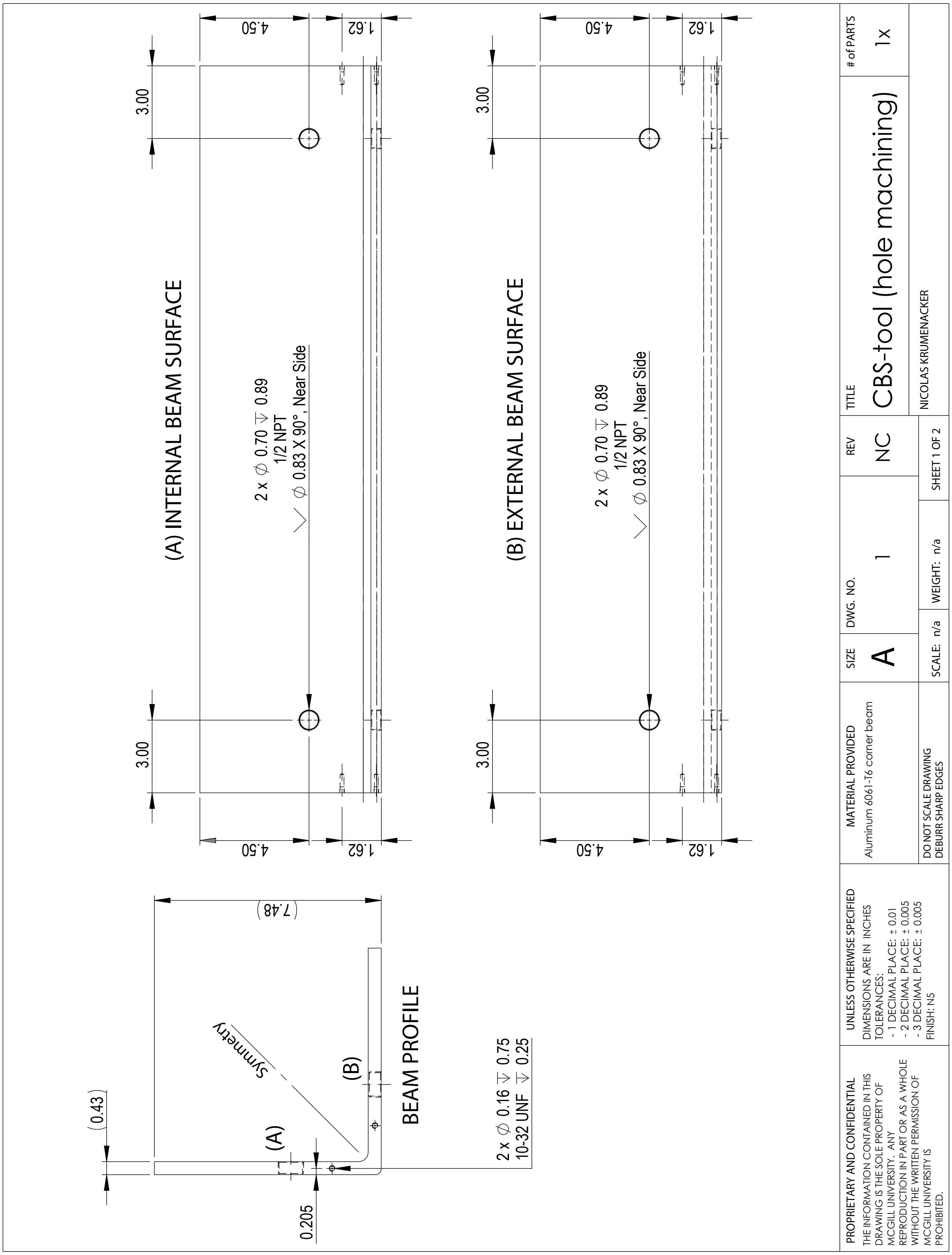

Fig. B-2. Technical drawing of curved beam tool machined holes.

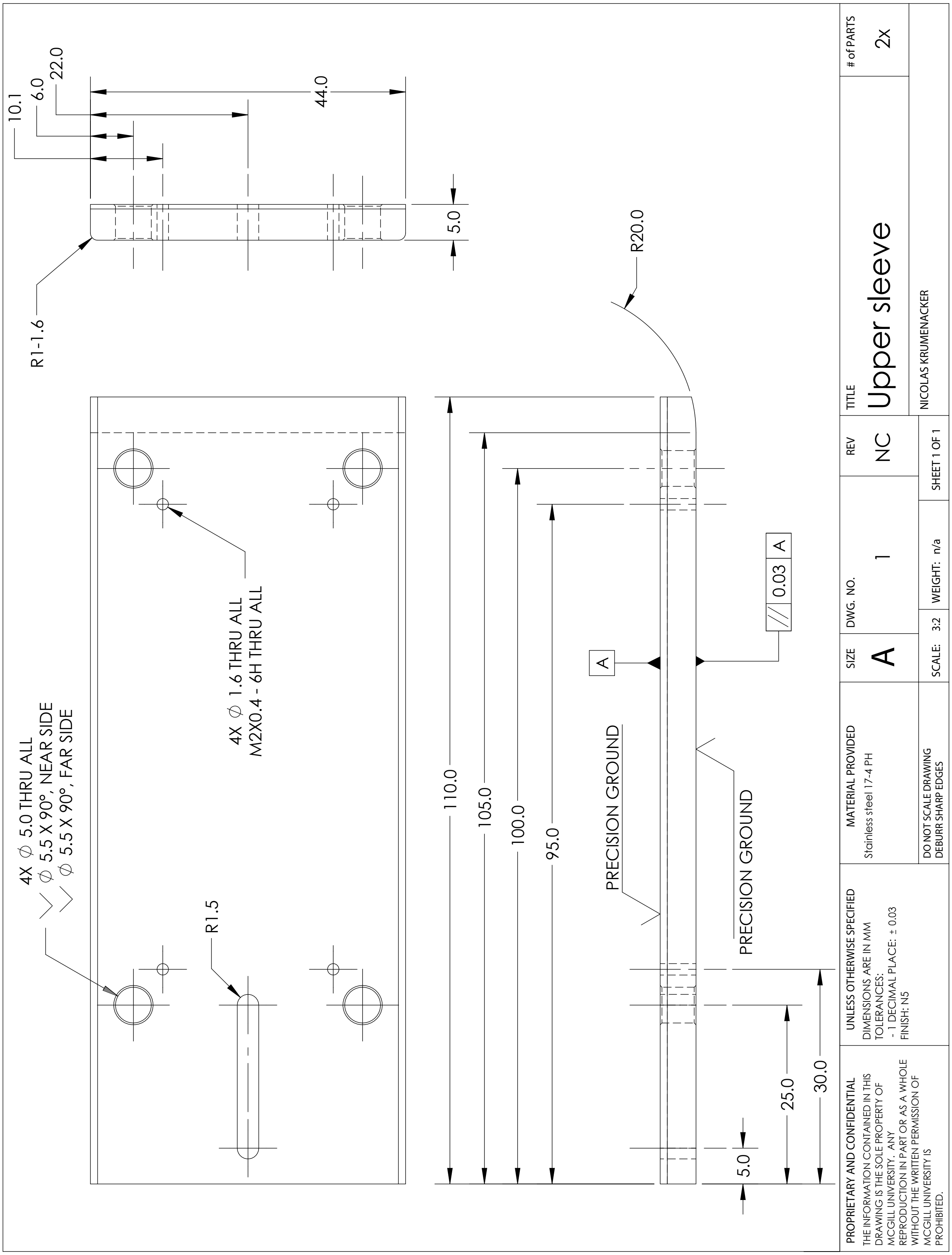

Fig. B-3. Technical drawing of upper stiffener.

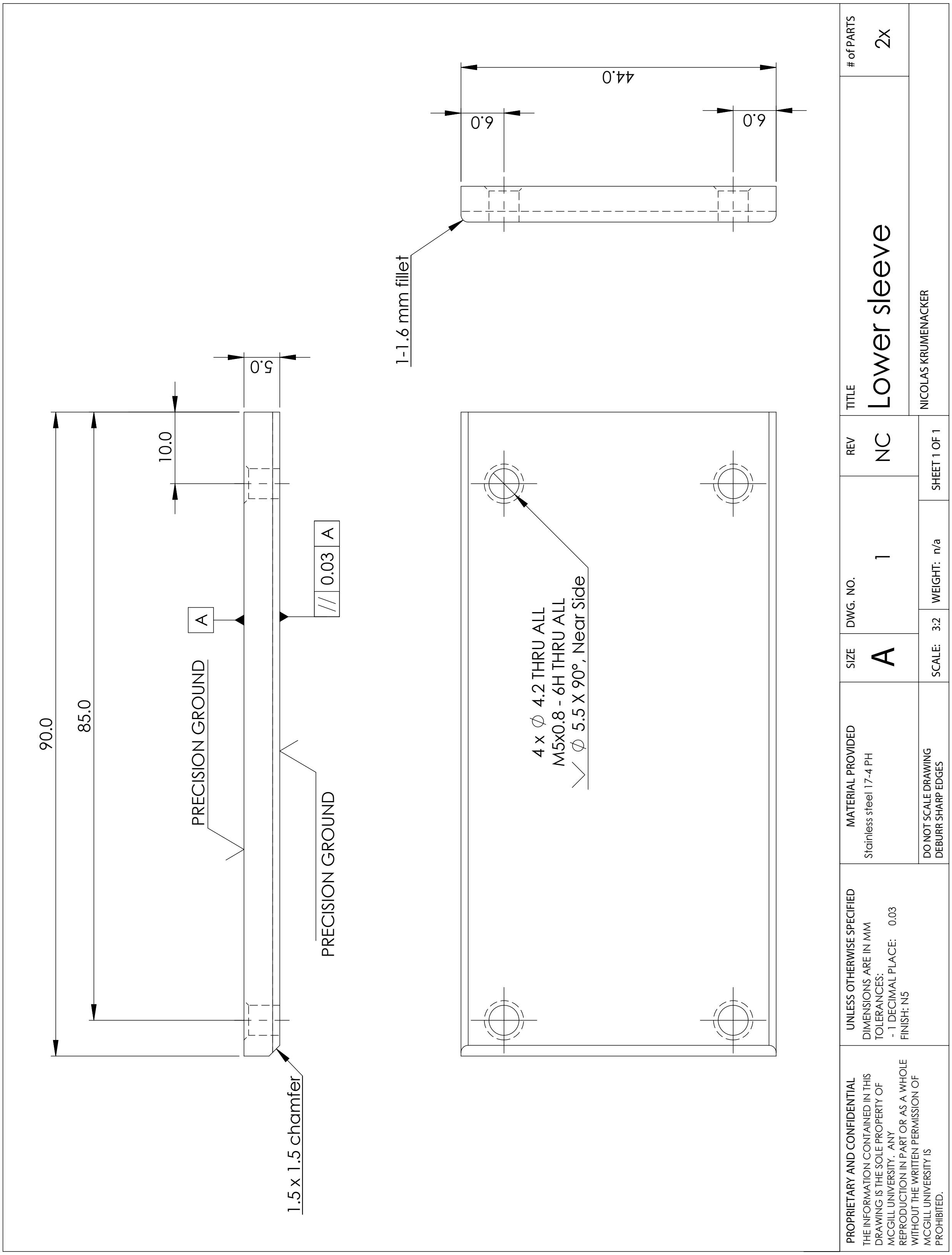

Fig. B-4. Technical drawing of lower stiffener.

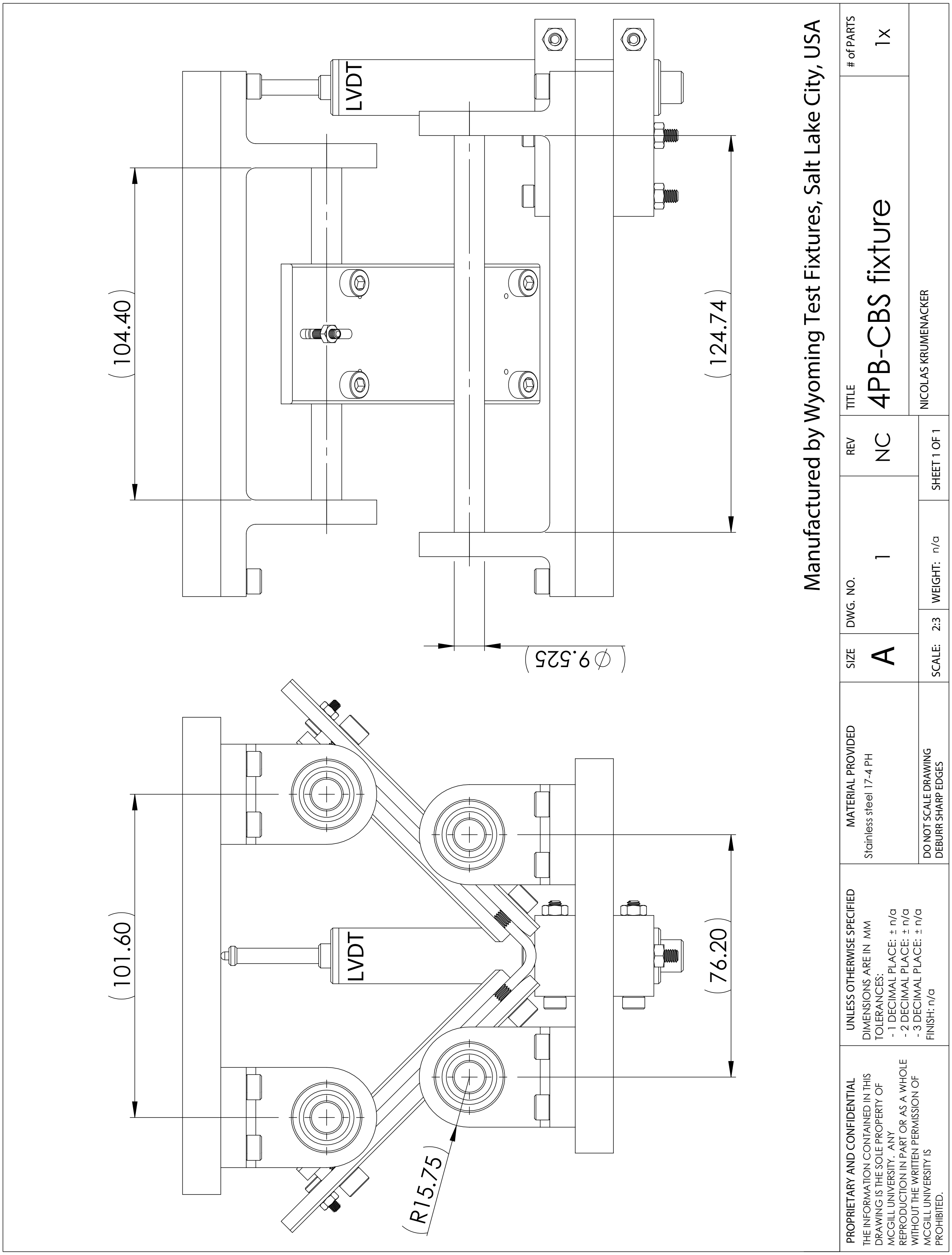

Fig. B-5. Technical drawing of 4PB-CBS fixture.

C Computational scripts

The following appendix contains a selection of custom m-scripts implemented in MathWorks Matlab (R2015b) and written to handle the various computational tasks of the presented research. The other scripts developed for this thesis are not included on account of their length, namely the *Corner sample thickness profiling* script and the *Curved beam strength testing data reduction* script discussed in §§ 2.4.3 and 3.3.2, resp.

C.1 Baselines repeatability study statistical analysis (m-script)

```
%%%%%%%%%%%%%%%%%%%%%%%%%%%%%%%%%%%%%%%%%%%%%%%%%%%%%%%%%%%%%%%%%%%%%%%%%%%
%%%                                                                     %%%
%%%   BASELINES REPEATABILITY SIDE_STUDY STATISTICAL ANALYSIS           %%%
%%%   (MathWorks Matlab R2015b)                                         %%%
%%%   NICOLAS KRUMENACKER (NOV-2017)                                    %%%
%%%                                                                     %%%
%%%%%%%%%%%%%%%%%%%%%%%%%%%%%%%%%%%%%%%%%%%%%%%%%%%%%%%%%%%%%%%%%%%%%%%%%%%

% OBJECTIVES: 1) Determine if dataset sample belong to single population
%             2) Determine inter- and intra-sample repeatability statistics

%% PREPARE WORKSPACE ======================================================
clear all; close all; clc; format shortG; disp('START RUN')
addpath(sprintf('%s/Functions',pwd))  % Add subdirectory to path

%% SCRIPT INPUTS ==========================================================
alpha = 0.05; % set significance level
fmt = '%.5g'; % set default number format for workspace outputs
% Enter data set
    prompt = 'Enter sample data in column form (do NOT forget [#]!):\n\n';
    datam = input(prompt); clc % workspace prompt
% Data parameters
    [n, k] = size(datam); % n = nominal sample size & k = number of samples
    for i = 1:k; ni(i) = n-sum(isnan(datam(:,i))); % actual sample sizes
    end
    N = sum(isnan(datam(:))==0); % pooled population size (no NaN values)
    nef = (N - sum(ni.^2./N))/(k-1); % effective sample size
% Sort data columns in ascending order (keep NaN values)
    sdatam = sort(datam,1);
    in = any(isnan(sdatam),2);
    sdatam = [sdatam(~in,:); sdatam(in,:)];
% Create data vector and corresponding sample index vector
    datav = sdatam(:);
    datav(find(isnan(datam))) = []; % remove NaN elements
    sampIndm = repmat((1:1:k),n,1); sampIndv = sampIndm(:);
```

```
    sampIndv(find(isnan(datam))) = [];
% Output inputs and sorted data matrix and data parameters to workspace
    % fprintf('INPUTS\n')
    % fprintf(['alpha: ',fmt,'\n\n'],alpha)
    fprintf('SORTED_COLUMNS\n')
    fmt2 = strjoin({repmat([fmt,' '],1,k),'\n'});
    fprintf([fmt2],sdatam') % sdatam must be transposed
    fprintf('\nDATA_PARAMETERS\n'); fprintf(['k: ',fmt,'\n'],k)
    fprintf(['nef: ',fmt,'\n'],nef); fprintf(['N: ',fmt,'\n'],N)

%% DESCIPTIVE STATS =======================================================
    for i = 1:k
        ni(:,i) = sum(isnan(datam(:,i))==0); % individual sample size
        mi(:,i) = nanmean(datam(:,i)); % mean (no NaN values)
        si(:,i) = nanstd(datam(:,i)); % standard deviation (no NaN values)
        cvi(:,i) = si(:,i)/mi(:,i) *100; % coefficient of variation
        medi(:,i) = nanmedian(datam(:,i)); % median (no NaN values)
    end
    GM = sum(ni.*mi)/N; % grand mean
% Output descriptive stats to workspace
    fprintf('\nSAMPLE_STATS\n')
    fmt3 = strjoin({repmat([fmt,' '],1,k),'\n'});
    fprintf(['n_i: ',fmt3],ni); fprintf(['m_i: ',fmt3],mi)
    fprintf(['s_i: ',fmt3],si); fprintf(['cv_i_(%%): ',fmt3],cvi)
    fprintf(['med_i: ',fmt3],medi)

%% K-SAMPLE ANDERSON-DARLING TEST (sample difference?) ====================
    ADKstats = ADKtest([datav,sampIndv],alpha);
    ADKstat = ADKstats.ADKn; % AD rank stat
    ADKststat = ADKstats.ADKsn; % standardized AD rank stat
    ADKp = ADKstats.pADK; % p-value
    if   ADKp >= alpha; ADKh = 0; % Unstructured data
    else ADKh = 1; % Structured data
    end
% Output test results to workspace
    fprintf('\nADK_TEST\n'); fprintf(['stat: ',fmt,'\n'],ADKstat)
    fprintf(['p: ',fmt,'\n'],ADKp); fprintf(['h0: ',fmt,'\n'],ADKh)

%% OUTLIER(S) DETECTION ===================================================
% Median Absolute Deviation method (MAD) for univariate data
    % REF: 1. Leys C, Ley C, Klein O, Bernard P, Licata L. Detecting
    % outliers: Do not use standard deviation around the mean, use absolute
    % deviation around the median. Journal of Experimental Social
    % Psychology. 2013;49(4):764-6.
% STRUCTURED or UNSTRUCTURED data set
% Outlier(s) within each sample
outlierData = []; % create variable
for i = 1:k
    sdatav = sdatam(:,i); % create temporary sample data vector
    % b = 1/Q3 of assumed distribution; b = 1.4826 for normality
    MAD = 1.4826 * nanmedian(abs(sdatav-medi(:,i)));
    thresh = 2.5; % 2.5 = moderately conservative criteria
    LB = medi(:,i)-thresh*MAD; % lower bound
    UB = medi(:,i)+thresh*MAD; % upper bound
    outlierGroup = find(sdatav < LB | sdatav > UB); % index(ices)
    % Find outlier values and position in original data matrix
    if  isempty(outlierGroup) == 0
```

```
        goutlier = sdatav(outlierGroup); % outlier value
        gref = repmat(i,length(goutlier),1); % create group ref vector
        outlierData = vertcat(outlierData,[goutlier,gref,outlierGroup]);
    end
end
% Output sample outliers to workspace
    fprintf('\nSAMPLE_OUTLIER(S)\n')
    fprintf('total: %d\n', size(outlierData,1));
    if isempty(outlierData) == 0
        fprintf([strjoin({'value','sample/column','row_(sorted)'}),'\n'])
        fmt4 = strjoin({repmat([fmt,' '],1,3),'\n'});
        fprintf(['',fmt4,''],outlierData')
    end
if ADKh == 0 % UNSTRUCTURED data ONLY -------------------------------------
    Gmed = median(datav); % combined data median
    % b = 1/Q3 of assumed normal distribution, i.e. 1.4826 for normality
    MAD = 1.4826*median(abs(datav-Gmed));
    thresh = 2.5; % 2.5 = moderately conservative criteria
    LB = Gmed-thresh*MAD; UB = Gmed+thresh*MAD; % lower/upper bound
    outlierIndex = find(datav < LB | datav > UB); % index(ices)
    % Find outlier values and position in original data matrix
    if  isempty(outlierIndex) == 0
        outlier = datav(outlierIndex); % outlier value
        [~,position] = ismember(outlier,datam); % position in data matrix
    end
    % Output outliers to workspace
        fprintf('\nOVERALL_OUTLIER(S)\n')
        fprintf('total: %d\n', size(outlierIndex,1));
        if isempty(outlierIndex) == 0
            fprintf([strjoin({'value','data_position'}),'\n'])
            fmt5 = strjoin({repmat([fmt,' '],1,2),'\n'});
            fprintf(['',fmt5,''],[outlier,position]')
        end
end

%%%%%%%%%%%%%%%%%%%%%%%%%%%%%%%%%%%%%%%%%%%%%%%%%%%%%%%%%%%%%%%%%%%%%%%%%%%%%%
%%%          CORRECT OUTLIERS IF APPLICABLE AND RERUN SCRIPT             %%%
%%%                    DO NOT DISCARD OUTLIERS!                          %%%
%%%%%%%%%%%%%%%%%%%%%%%%%%%%%%%%%%%%%%%%%%%%%%%%%%%%%%%%%%%%%%%%%%%%%%%%%%%%%%

%% EXTERNALLY STUDENTIZED RESIDUALS (excl. ith observation) ===============
    pnum = 2; % number of parameters in one-way ANOVA model
    fittedVals = mi(sampIndv).';
    r = (datav-fittedVals); % raw residuals
    sN = std(datav); % standard deviation of unstructured data (all)
    se = sqrt(sum(r.^2)/(n-pnum)); % stand. dev. of residuals
    for i = 1:numel(datav)
        hii(i) = 1/N+1/(N-1)*((datav(i)-GM)/sN)^2; % leverage
        hiinorm(i) = hii(i)*N/pnum; % normalized leverage
        isr(i) = r(i)/se/sqrt(1-hii(i)); % internally studentized r
        esr(i) = isr(i)*sqrt((N-pnum-1)/(N-pnum-isr(i)^2)); % externally...
        % D(i) = isr(i)^2*hii(i)/pnum/(1-hii(i)); % Cook's distance
    end
    esr = esr'; % D = D'; % transpose horizontal vectors
```

```
%% NORMALITY CHECK ==========================================================
% Shape parameters >> Skewness & Kurtosis (i.e. pointiness)
    Gs = skewness(esr,0); % Adjusted Fisher-Pearson
    SES = sqrt((6*n*(n-1))/((n-2)*(n+1)*(n+3))); % Stand. error (Cramer'97)
    Zs = Gs/SES; % Two-tailed test of skewness @ a = 0.05
    Gk = kurtosis(esr,0); % Adjusted
    SEK = 2*SES*sqrt((n^2-1)/((n-3)*(n+5))); % Standard error (Cramer'97)
    Zk = Gk/SEK; % Two-tailed test of kurtosis @ a = 0.05
    % REF: Cramer, D. 1997. Basic statistics for social research. Routledge.
% Shapiro-Wilk test (function available from MathWorks File Exchange)
    [SWh,SWp,SWstat] = swtest(esr,alpha);
% Output to workspace
    fprintf('\nSHAPE_PARAMETERS\n')
    fprintf('Z_skewness: %.5g\n',Zs); fprintf('Z_kurtosis: %.5g\n',Zk)
    % if N > 29
        fprintf('\nSW-TEST\n'); fprintf(['stat: ',fmt,'\n'],SWstat)
        fprintf(['p: ',fmt,'\n'],SWp); fprintf(['h0: ' fmt '\n'],SWh)
    % end
% P-P plot data ------------------------------------------------------------
% CALCULATE cumulative probability values for "esr"
    pd = fitdist(esr,'Normal');
    rescdf = cdf(pd,esr);
% Determine theoretical Z-scores
    percentiles = ((1:N)'-0.5)./N;
    Zthe = norminv(percentiles,0,1);
    pthe = normcdf(Zthe);
% Determine actual Z-scores
    sesr = sort(esr)';
    Zact = (sesr-mean(sesr))./std(sesr);
    pact = normcdf(Zact)';

%% EQUALITY OF VARIANCE =====================================================
% Brown-Forsythe test
    [BFp,stats] =
vartestn(datam,'Display','off','TestType','BrownForsythe');
    BFstat = stats.fstat;
    if   BFp < alpha; BFh = 1;
    else BFh = 0;
    end
% Output BF-test results to workspace
    fprintf('\nBF_TEST\n')
    fprintf(['stat: ',fmt,'\n'], BFstat)
    fprintf(['p: ',fmt,'\n'], BFp)
    fprintf(['h0: ',fmt,'\n'], BFh)
%% ONE-WAY ANOVA ============================================================
% Fisher (classic) one-way ANOVA >> homogeneous variance case
[Ap,Atbl,Astats] = anova1(datav,sampIndv,'off');
statA = Atbl{2,5}; % same for Welch ANOVA
sW = Astats.s; % pooled standard deviation (MSE)
Rsq = Atbl{3,2}/Atbl{4,2}; % same for Welch ANOVA
MSB = Atbl{2,4}; MSW = Atbl{3,4};
%if h0_BF == 0
    dfb = Atbl{2,3}; dfe = Atbl{3,3};
    if Ap < alpha; h0_A = 1;
    else h0_A = 0;
    end
```

```
    % Output results to workspace
        fprintf('\nClassic_1-WAY_ANOVA\n'); fprintf(['dfb: ',fmt,'\n'],dfb)
        fprintf(['dfe: ',fmt,'\n'],dfe); fprintf(['stat: ',fmt,'\n'],statA)
        fprintf(['p: ',fmt,'\n'],Ap); fprintf(['h0: ',fmt,'\n'],h0_A)
        fprintf(['s_within: ',fmt,'\n'],sW);fprintf(['R^2: ',fmt,'\n'],Rsq)
% Welch one-way ANOVA >> heterogeneous variance case ---------------------
% (function available from MathWorks File Exchange)
% else
    [WAstats] = welchanova([datav,sampIndv],alpha);
    df1 = WAstats.df1; df2 = WAstats.df2;
    WAstat = WAstats.Wstat;
    WAp = WAstats.p;
    if WAp < alpha; WAh = 1;
    else WAh = 0;
    end
    % Output results to workspace
        fprintf('\nWELCH_1-WAY_ANOVA\n'); fprintf(['df1: ',fmt,'\n'],df1)
        fprintf(['df2: ',fmt,'\n'],df2);fprintf(['stat: ',fmt,'\n'],WAstat)
        fprintf(['p: ',fmt,'\n'],WAp); fprintf(['h0: ',fmt,'\n'],WAh)
        fprintf(['s_within: ',fmt,'\n'],sW);fprintf(['R^2: ',fmt,'\n'],Rsq)
% end

%% INTER/INTRA-VARIABILITY (BETWEEN/WITHIN) ================================
% Intra-sample (pooled) statistics
    sP = sW; % already calculated in ANOVA: sP = sqrt(MSB)
    cvW = abs(sP/GM*100); % pooled coefficient of variation
% Inter-sample statistics
    sm = std(mi); % sample deviation of sample means
    % sB = sqrt(Atbl{2,4}); % variance already calculated in ANOVA: MSB
    sB = sqrt((sm^2+sW^2*(nef-1)/nef)/(k-1));
    cvB = abs(sB/GM*100); % coefficient of variation
% Output variability stats to workspace
    fprintf('\nVARIABILITY_STATS\n'); fprintf(['GM: ',fmt,'\n'],GM)
    fprintf(['s_B: ',fmt,'\n'],sB); fprintf(['cv_B_(%%): ',fmt,'\n'],cvB)
    fprintf(['s_W: ',fmt,'\n'],sW); fprintf(['cv_W_(%%): ',fmt,'\n'],cvW)

%% DIAGNOSTICS CHECKING PLOTS ==============================================
% Sort vectors -> Residuals vs fits plot
    [esr_temp,sortInd2] = sort(esr);
    fittedVals_temp = fittedVals(sortInd2);
    [sorted_fittedVals, sortInd3] = sort(fittedVals_temp);
    sorted_esr = esr_temp(sortInd3);
% Output plotting data to workspace
    fprintf('\nSTATISTICS\n')
    fprintf([strjoin({'RESIDUALS_vs_FITS_PLOT','...','PP-PLOT','...',...
        '\n'})])
    fprintf(strjoin({'fitted_values','esr','p_theoretical','p_actual',...
        '\n'}))
    fmt6 = strjoin({repmat([fmt,' '],1,4),'\n'}); % formatting
    fprintf(['' fmt6 ''],[sorted_fittedVals,sorted_esr,pthe,pact]')
% PLOTTING ----------------------------------------------------------------
figure('units','normalized','outerposition',[0 .1 1 .8])
subplot(1,2,1) % Residuals vs fitted values plot >> homogeneity of variance
    hold on, xmin = min(fittedVals); xmax = max(fittedVals);
    plot(fittedVals(:),esr(:),'bo',[xmin,xmax],[0,0],'r-')
    title('Residuals vs. Fits Plot')
    xlabel('fitted values (group means)')
```

```
    ylabel('externally studentized residuals')
    pbaspect([1 1 1]), hold off
subplot(1,2,2) % Normality P-P plot >> normality + platykurtosis
    hold on, plot(pthe,pact,'bo',[0,1],[0,1],'r')
    title('Normality PP-Plot')
    xlabel('Theoretical probabilities')
    ylabel('Observed probabilities')
    pbaspect([1 1 1]), hold off

%%%%%%%%%%%%%%%%%%%%%%%%%%%%%%%%%%%%%%%%%%%%%%%%%%%%%%%%%%%%%%%%%%%%%%%%%%%
%%%                                                                     %%%
%%%   END OF SCRIPT                                                     %%%
%%%                                                                     %%%
%%%%%%%%%%%%%%%%%%%%%%%%%%%%%%%%%%%%%%%%%%%%%%%%%%%%%%%%%%%%%%%%%%%%%%%%%%%
```

C.2 Determination of fibre waviness extent (m-script)

```
%%%%%%%%%%%%%%%%%%%%%%%%%%%%%%%%%%%%%%%%%%%%%%%%%%%%%%%%%%%%%%%%%%%%%%%%%%%
%%%                                                                     %%%
%%%   DETERMINATION OF FIBRE WAVINESS EXTENT                            %%%
%%%   (MathWorks Matlab R2015b)                                         %%%
%%%   NICOLAS KRUMENACKER (JAN-2018)                                    %%%
%%%                                                                     %%%
%%%%%%%%%%%%%%%%%%%%%%%%%%%%%%%%%%%%%%%%%%%%%%%%%%%%%%%%%%%%%%%%%%%%%%%%%%%

% OBJECTIVE: determine the extent of fibre waviness in corner laminates
% from cross-sectional micrographs of the flanges-only in the frontal plane

%% PREPARE WORKSPACE ======================================================
clear; close all; clc; format shortg; warning off; disp('START RUN')

%% OPEN IMAGE (one per run) ===============================================
filename = 'Specimen A'; filetype = '.tif';
%I = input('Input image name with file extension: 's');
I = imread(strcat(filename,filetype));

%% IMAGE MANIPULATION =====================================================
if  size(I,3) == 3; I = rgb2gray(I); end % Convert to grayscale if RGB
foregroundidx = find(I ~= 0); % Isolate laminate pizel indices
I = imadjust(I); % Boost contrast

% Threshold gray image based on Otsu's algorithm
thresh_v = multithresh(I,20); % Limit of 20

% Create fibre mask: fibres = 1 (white), rest = 0 (black)
level = round(mean(thresh_v(19:20)))/255; % Normalize threshold: 0-1
BW = im2bw(I,level); % Create binary image

% Erode to improve object separation
BW = imerode(BW,strel('line',5,0));
% Clean up image
```

```
BW = bwareaopen(BW,100); % Remove small foreground objects
BW = ~bwareaopen(~BW,100); % Remove small background objects

%% FIND CONNECTED OBJECTS + REGIONS PROPERTIES ============================
CC = bwconncomp(BW,8); % label image

% Call out regions (selected objects) properties
stats = regionprops(CC,'PixelIdxList','PixelList','Area',...
    'MajorAxisLength','MinorAxisLength','Orientation');
numobjects = CC.NumObjects;
refs = 1:numobjects;
areas = cat(1,stats.Area);
majors = cat(1,stats.MajorAxisLength);
minors = cat(1,stats.MinorAxisLength);
aspects = majors./minors;

%% FILTER OBJECTS =========================================================
fibredia = 6/0.581; % Nominal fibre dia. / image res.: 6(um)/0.581(um/px)
offangle = 5; % Equivalent off-axis angle floor (deg);
              % it should be noted that it is impossible to accurately
              % estimate fibre angle in the case of non-ciruclar fibre
              % cross-sections.
maxminor = 2*fibredia; maxmajor = fibredia/sind(offangle);

% Determine the vector indices of selected objects
idf = minors <= maxminor & majors <= maxmajor; % Restrict minor/major axes

% Create new region property vectors
minors2 = minors(idf);
numobjects2 = numel(nonzeros(idf));
refs2 = refs(idf); areas2 = areas(idf,:);
majors2 = majors(idf); minors2 = minors(idf); aspects2 = aspects(idf);

%% CREATE BINARY RESULT IMAGE =============================================
if  isempty(refs2) == 0; % Find selected object pixel indices
    for i = 1:length(refs2); list{i} = stats(refs2(i)).PixelIdxList; end
end
fullList = cat(1, list{:});

% Create result matrix/image (R)
R = zeros(size(BW,1),size(BW,2)); % Set background to 0 (black)
R(fullList) = 1; % Set fibres to 1 (white)

%% CREATE RGB RESULT IMAGE ================================================
D = imdilate(R,strel('disk',20,8)); % Dilate critical fibres for clarity
Didx = find(D == 1); % Find corresponding indices

% Create output image
Iout = ones(size(BW,1),size(BW,2)); % Background
Iout(foregroundidx) = 2; % Laminate
Iout(Didx) = 3; % Dilated critcal zones

% Create custom colormap
cmap = [1,1,1;          % Background: white
        0.8,0.8,0.8;    % Laminate: light grey
```

```
        0.6,0,0];       % Dilated critical fibres: dark red
f = figure(2); image(Iout); daspect([1 1 1]); box off; axis off;
colormap(f,cmap);

% Save results image
filename2 = strcat(filename,' - result.tif');
imwrite(Iout,cmap,filename2)

%% COUNT NUMBER OF T-T CRICTICAL PIXELS ===================================
for i = 1:length(R);
yTTdata(i) = nnz(R(:,i))/size(R,1)*100; % Percent
end
xTTdata = 1:length(R); % Define x-positon

% Remove zero data points
id0 = find(yTTdata ~= 0); % Find indices
xTTdata = xTTdata(id0); yTTdata = yTTdata(id0); % Remove datapoints

% Downsample for data smoothing and fitting
n = 100; xTTdata2 = downsample(xTTdata,n); yTTdata2 = downsample(yTTdata,n);

%% COUNT NUMBER OF LENGTHWISE CRICTICAL PIXELS ============================
for i = 1:size(R,2); yTTdata(i) = nnz(R(:,i))/size(R,1); end
xTTdata = 1:length(R); % Define x-positon

% Remove zero data points
id0 = find(yTTdata ~= 0); % Find indices
xTTdata = xTTdata(id0); yTTdata = yTTdata(id0); % Remove datapoints

% Downsample for data smoothing and fitting
n =100; xTTdata2 = downsample(xTTdata,n); yTTdata2 = downsample(yTTdata,n);

%% SMOOTH + FIT DATA ======================================================
ysTTdata2 = smooth(xTTdata2,yTTdata2,0.5,'rloess'); % Smooth data
% Bilinear piecewise function (broken-stick method)
% From: https://stackoverflow.com/questions/43602835/how-to-fit-data-with-
%       piecewise-linear-function-in-matlab-with-some-constraints-o
myfxn = @(coeffs, xdata2) coeffs(1) + ...
        (xdata2 <= coeffs(2)) .* coeffs(3) .* xdata2 + ...
        (xdata2 > coeffs(2)) .* (coeffs(3) * coeffs(2) + ...
        (coeffs(3) + coeffs(4)) .* (xdata2 - coeffs(2)));
guess = [0.3; 20000; -1e-7; 0]; % start point / initial guess
lb = [-Inf, -Inf, -Inf, -Inf]; ub = [+Inf, +Inf, +Inf, +Inf];
coeffs = lsqcurvefit(myfxn,guess,xTTdata2,yTTdata2,lb,ub);
xplot = [xTTdata2(1),coeffs(2),xTTdata2(end)];
figure(2); plot(xTTdata2,yTTdata2,'.c',xTTdata2,ysTTdata2,'-m',...
    xplot,myfxn(coeffs,xplot),'--ok')

%% COUNT NUMBER OF LENGTHWISE CRICTICAL PIXELS ============================
% Crop R to a 5mm width
width = 5; imres = 0.581; pxwidth = width*1000/imres;
Rcrop = imcrop(R,[0,0,pxwidth,size(R,2)]);
```

```
% Count
for j = 1:size(Rcrop,1);
xLdata(j) = nnz(Rcrop (j,:))/size(Rcrop,2)*100; % Percent
end
yLdata = 1:size(Rcrop,1); % Define x-positon
yLdata = yLdata./size(R,1);

% Remove zero data points
id0 = find(xLdata ~= 0); % Find indices
yLdata = yLdata(id0); xLdata = xLdata(id0); % Remove datapoints

% Downsample for data smoothing and fitting
n = 10; xLdata2 = downsample(xLdata,n); yLdata2 = downsample(yLdata,n);

% Plot
figure(3); plot(xLdata2,yLdata2,'*c'); hold on
nplies = 24; yplies = 0 : 1/nplies : 1;
for k = 2:nplies; plot([0,1.1*max(xLdata)],[yplies(k),yplies(k)],'-r'); end
hold off

%% OUTPUT RESULTS TO WORKSPACE ============================================
fprintf('\nDownsampled T-T data [xTTdata2; yTTdata2; ysTTdata2]:\n\n')
disp([xTTdata2',yTTdata2',ysTTdata2])
tempmsg = strcat('\nBilinear fit coefficients ',...
    '[y-intercept; x-transition; slope 1; slope 2]:\n\n');
fprintf(tempmsg); disp(coeffs)
fprintf('Bilenar fit plotting points:\n\n')
disp([xplot',myfxn(coeffs,xplot)'])
fprintf('\nDownsampled lengthwise data [xLdata2; yLdata2]:\n\n')
disp([xLdata2',yLdata2'])

%%%%%%%%%%%%%%%%%%%%%%%%%%%%%%%%%%%%%%%%%%%%%%%%%%%%%%%%%%%%%%%%%%%%%%%%%%%
%%%                                                                     %%%
%%%   END OF SCRIPT                                                     %%%
%%%                                                                     %%%
%%%%%%%%%%%%%%%%%%%%%%%%%%%%%%%%%%%%%%%%%%%%%%%%%%%%%%%%%%%%%%%%%%%%%%%%%%%
```

C.3 3D Euler angle transformation of compliance matrix (m-script)

```
%%%%%%%%%%%%%%%%%%%%%%%%%%%%%%%%%%%%%%%%%%%%%%%%%%%%%%%%%%%%%%%%%%%%%%%%%%%
%%%                                                                     %%%
%%%   3D EULER ANGLE TRANSFORMATION OF COMPLIANCE MATRIX                %%%
%%%   (MathWorks Matlab R2015b)                                         %%%
%%%   Nicolas Krumenacker (1-MAR-2018)                                  %%%
%%%                                                                     %%%
%%%%%%%%%%%%%%%%%%%%%%%%%%%%%%%%%%%%%%%%%%%%%%%%%%%%%%%%%%%%%%%%%%%%%%%%%%%
% OBJECTIVE: given mean, absolute in-plane and out-of-plane fibre
%            misalignment angles (alpha and phi, resp., determined from
%            micro-CT), transform the on-axis compliance matrix to
%            estimate the degraded off-axis engineering constants.
```

```
% Defining the fames:
% On-axis  --> 123-coordinates defined by unit vectors (ABC)
% Off-axis --> xyz-coordinates defined by unit vectors (XYZ)

%% INITIATE WORKSPACE =====================================================
clear all; close all; clc; warning off; format longg; disp('START RUN')

%% SCRIPT INPUTS ==========================================================
% Input misalignemnt angles in degrees relative to off-axis frame
alpha = 10; % in-plane angle (from x-axis in xy-plane)
phi = 2; % out-of-plane angle (from x-axis in xz-plane)

% Input engineering constants in MPa (assuming transverse isotropy)
E11 = 134000;   E22 = 9930;     E33 = E22;
nu12 = 0.33;    nu13 = nu12;    nu23 = 0.5;
G12 = 5410;     G13 = G12;      G23 = E33/(2*(1+nu23));

%% CALCULATIONS ===========================================================

% Calculate Euler angles based on ZYZ convention (alpha is already defined)
beta = atand(cosd(alpha)*tand(phi)); gamma = 0;

% Define shorthand for trigonometry functions
c1 = cosd(alpha);   c2 = cosd(beta);    c3 = 1; % cosd(gamma);
s1 = sind(alpha);   s2 = sind(beta);    s3 = 0; % sind(gamma);

% Compile strain transformation matrix [Te] using ZYZ convention
l1 = -s1*s3 + c1*c2*c3;      m1 = c1*s3 + s1*c2*c3;     n1 = -s2*c3;
l2 = -s1*c3 - c1*c2*s3;      m2 = c1*c3 - s1*c2*s3;     n2 = s1*s3;
l3 = c1*s2;                  m3 = s1*s2;                n3 = c2;
%%%T = [l1, m1, n1; l2, m2, n2; l3, m3, n3];
T11 = [l1^2, m1^2, n1^2;
       l2^2, m2^2, n2^2;
       l3^2, m3^2, n3^2];
T12 = [m1*n1, n1*l1, l1*m1;
       m2*n2, n2*l2, l2*m2;
       m3*n3, n3*l3, l3*m3];
T21 = [2*l2*l3, 2*m2*m3, 2*n2*n3;
       2*l3*l1, 2*m3*m1, 2*n3*n1;
       2*l1*l2, 2*m1*m2, 2*n1*n2];
T22 = [m2*n3+m3*n2, n2*l3+n3*l2, l2*m3+l3*m2;
       m3*n1+m1*n3, n3*l1+n1*l3, l3*m1+l1*m3;
       m1*n2+m2*n1, n1*l2+n2*l1, l1*m2+l2*m1];
Te = [T11, T12;
      T21, T22];

% Obtain stress transformation matrix [Ts]
Ts = inv(transpose(Te));

% Compile compliance matrix S
S11 = 1/E11;
S22 = 1/E22; % = S33
S12 = -nu12/E11; % = S13 = S21 = S31
S23 = -nu23/E22;
S44 = 2*(S22-S23);
```

```
S55 = 1/G12; % = S66
Son = [S11, S12, S12, 0,   0,   0;
       S12, S22, S23, 0,   0    0;
       S12, S23, S22, 0,   0,   0;
       0,   0,   0,   S44, 0,   0;
       0,   0,   0,   0,   S55, 0;
       0,   0,   0,   0,   0,   S55];

% Transform compliance matrix from on-axis to off-axis
Soff = inv(transpose(Ts)) * Son * inv(Ts);
% Soff = Sxyz and Son = S123

% Extract transformed engineering constants
Exx = 1/Soff(1,1); KnockD = (E11-Exx)/E11*100;
Eyy = 1/Soff(2,2);
Ezz = 1/Soff(3,3);
nuxy = -Soff(1,2)/Soff(1,1);
nuxz = -Soff(1,3)/Soff(1,1);
nuyz = -Soff(2,3)/Soff(2,2);
Gxy = 1/Soff(6,6);
Gxz = 1/Soff(5,5);
Gyz = 1/Soff(4,4);

%% OUTPUT TO WORKSPACE =================================================
fprintf('\nAngles in degrees:',alpha)
fprintf('\t alpha = %d\n',alpha)
fprintf('\t\t\t phi = %d\n',phi)
fprintf('\t\t\t beta = %.2f\n',beta)
fprintf('\nLamina (on-axis) engineering constants in MPa:\n\n')
fprintf('\t E11 = %.f\n',E11)
fprintf('\t E22 = %.f\n',E22)
fprintf('\t E33 = %.f\n',E33)
fprintf('\t nu12 = %.3f\n',nu12)
fprintf('\t nu13 = %.3f\n',nu13)
fprintf('\t nu23 = %.3f\n',nu23)
fprintf('\t G12 = %.f\n',G12)
fprintf('\t G13 = %.f\n',G13)
fprintf('\t G23 = %.f\n',G23)
fprintf('\nTransformed (off-axis) engineering constants in MPa:\n\n')
fprintf('\t Exx'' = %.f\n',Exx)
fprintf('\t Eyy'' = %.f\n',Eyy)
fprintf('\t Ezz'' = %.f\n',Ezz)
fprintf('\t nuxy'' = %.3f\n',nuxy)
fprintf('\t nuxz'' = %.3f\n',nuxz)
fprintf('\t nuyz'' = %.3f\n',nuyz)
fprintf('\t Gxy'' = %.f\n',Gxy)
fprintf('\t Gxz'' = %.f\n',Gxz)
fprintf('\t Gyz'' = %.f\n',Gyz)

%% PLOT ON- AND OFF-AXIS CARTESIAN FRAMES ==================================
% Projections of unit vectors defining the on-axis Cartesian frame
A1 = cosd(beta)*cosd(alpha);
A2 = cosd(beta)*sind(alpha);
A3 = sind(beta);
B1 = -sind(alpha);
B2 = cosd(alpha);
```

```
B3 = 0;
C1 = -sind(beta)*cosd(alpha);
C2 = -sind(beta)*sind(alpha);
C3 = cosd(beta);
%U = [A1, A2, A3; B1, B2, B3; C1, C2, C3];

% Plot on- and off-axis Cartesian frames
fig1 = figure('Name','On- and off-axis frames');
font = 'helvetica'; fsize = 14;
% Plot
plot3([-1,1],[0,0],[0,0],'b','LineWidth',1)
hold on
plot3([0,0],[-1,1],[0,0],'b','LineWidth',1)
plot3([0,0],[0,0],[-1,1],'b','LineWidth',1)
plot3([0,A1],[0,A2],[0,A3],'r','LineWidth',3)
plot3([0,B1],[0,B2],[0,B3],'r','LineWidth',3)
plot3([0,C1],[0,C2],[0,C3],'r','LineWidth',3)
if alpha ~= 0 || phi ~= 0; text(1,0,0,'X','FontSize',fsize); end
if alpha ~= 0; text(0,1,0,'Y','FontName',font,'FontSize',fsize); end
if phi ~= 0; text(0,0,1,'Z','FontName',font,'FontSize',fsize); end
text(A1,A2,A3,'A','FontName',font,'FontSize',fsize)
text(B1,B2,B3,'B','FontName',font,'FontSize',fsize)
text(C1,C2,C3,'C','FontName',font,'FontSize',fsize)
hold off
% Settings
view(115,20); daspect([1,1,1]); grid on; box on
xlim([-1,1]); ylim([-1,1]); zlim([-1,1])
% Labels
xlabel('1-axis'); ylabel('2-axis'); zlabel('3-axis')
close all

%% CREATE CONTOUR PLOTS OF ENGINEERING CONSTANTS
min1 = 0; max1 = 90; k1 = 1; %(max1-min1)/10;
alpha2s = min1 : k1 : max1;
min2 = 0; max2 = 90; k2 = 1; %(max2-min2)/10;
phi2s = min2 : k2 : max2;
for i = 1:length(phi2s)
for j = 1:length(alpha2s)
    % Define input angles
    alpha2 = alpha2s(j);
    phi2 = phi2s(i);
    % Populate angle vectors
    alphav(i,j) = alpha2;
    phiv(i,j) = phi2;
    % Calculate 2nd Euler angle: beta
    beta2 = atand(cosd(alpha2)*tand(phi2));
    % Define shorthand for trigonometry functions
    c1 = cosd(alpha2);   c2 = cosd(beta2);    c3 = 1;
    s1 = sind(alpha2);   s2 = sind(beta2);    s3 = 0;
    % Compile strain transformation matrix [Te2] using ZYZ convention
    l1 = -s1*s3 + c1*c2*c3;      m1 = c1*s3 + s1*c2*c3;     n1 = -s2*c3;
    l2 = -s1*c3 - c1*c2*s3;      m2 = c1*c3 - s1*c2*s3;     n2 = s1*s3;
    l3 = c1*s2;                  m3 = s1*s2;                n3 = c2;
    T11 = [l1^2, m1^2, n1^2; l2^2, m2^2, n2^2; l3^2, m3^2, n3^2];
    T12 = [m1*n1, n1*l1, l1*m1; m2*n2, n2*l2, l2*m2; m3*n3, n3*l3, l3*m3];
```

```
    T21 = [2*l2*l3, 2*m2*m3, 2*n2*n3;
           2*l3*l1, 2*m3*m1, 2*n3*n1;
           2*l1*l2, 2*m1*m2, 2*n1*n2];
    T22 = [m2*n3+m3*n2, n2*l3+n3*l2, l2*m3+l3*m2;
           m3*n1+m1*n3, n3*l1+n1*l3, l3*m1+l1*m3;
           m1*n2+m2*n1, n1*l2+n2*l1, l1*m2+l2*m1];
    Te2 = [T11, T12; T21, T22];
    % Obtain stress transformation matrix [Ts2]
    Ts2 = inv(transpose(Te2));
    % Transform compliance matrix from on-axis to off-axis
    Soff2 = inv(transpose(Ts2)) * Son * inv(Ts2);
    % Extract transformed engineering constants and populate matrices
    Exxv(i,j) = 1/Soff2(1,1); KnockDv(i,j) = (E11-Exxv(i,j))/E11*100;
    Eyyv(i,j) = 1/Soff2(2,2);
    Ezzv(i,j) = 1/Soff2(3,3);
    nuxyv(i,j) = -Soff2(1,2)/Soff2(1,1);
    nuxzv(i,j) = -Soff2(1,3)/Soff2(1,1);
    nuyxv(i,j) = -Soff2(2,3)/Soff2(2,2);
    Gxuv(i,j) = 1/Soff2(6,6);
    Gxzv(i,j) = 1/Soff2(5,5);
    Gyzv(i,j) = 1/Soff2(4,4);
end
end

% SURFACE PLOT OF ENGINEERING CONSTANT ====================================
% Parameters
var1 = Exxv; var1name = 'E_x_x (MPa)'; var2 = Exx;
zlow = 0; zhigh = 140000;
fig2 = figure('Name','Surfact plot');
font = 'helvetica'; fsize = 10;
% Plot
s1 = surf(alphav,phiv,var1); s1.FaceAlpha = 0.7;
hold on
p1 = plot3(abs(alpha),abs(phi),var2);
hold off
% Settings
colormap(cool); grid off; box on; shading flat %faceted % interp % flat
p1.LineWidth = 2; p1.Color = 'k';
p1.Marker = 'o'; p1.MarkerSize = 12; p1.MarkerFaceColor = 'r';
view(115,10); pbaspect([max1/min(max1,max2),max2/min(max1,max2),1]);
% Labels
xlim([min1,max1]); ylim([min2,max2]); zlim([zlow,zhigh])
xlabel('\alpha ({\circ})','FontName',font,'FontSize',fsize);
ylabel('\phi ({\circ})','FontName',font,'FontSize',fsize);
zlabel(var1name,'FontName',font,'FontSize',fsize);
% Colorbar
cb = colorbar('AxisLocation','out'); %caxis([var1(i,i),Inf])
ylabel(cb, var1name,'FontName',font,'FontSize',fsize)

%%%%%%%%%%%%%%%%%%%%%%%%%%%%%%%%%%%%%%%%%%%%%%%%%%%%%%%%%%%%%%%%%%%%%%%%%%%
%%%                                                                     %%%
%%%   END OF SCRIPT                                                     %%%
%%%                                                                     %%%
%%%%%%%%%%%%%%%%%%%%%%%%%%%%%%%%%%%%%%%%%%%%%%%%%%%%%%%%%%%%%%%%%%%%%%%%%%%
```

References

1. Gannon J.A., ‘History and development of epoxy resins’, in *High performance polymers: their origin and development*, Kirshenbaum G.S., Editor; 1986, Springer: New York, NY, USA; pp. 299-307.

2. Soutis C., ‘Carbon fiber reinforced plastics in aircraft construction’, *Materials Science and Engineering: A*; 2005, **412**(1-2): pp. 171-6.

3. Matthews F.L. and Rawlings R.D., *Composite materials: engineering and science*; 1999, Woodhead Publishing: Cambridge, UK.

4. Campbell F.C., *Manufacturing technology for aerospace structural materials*; 2006, Elsevier: UK.

5. Mazumdar S. *et al.*, ‘2018 state of the industry report – A global outlook at materials and markets for composites’, *Composites Manufacturing*; American Composites Manufacturing Association: 2018, Jan.-Feb. issue, pp. 18-23.

6. Stewart R., ‘Carbon fibre market poised for expansion’, *Reinforced Plastics*; 2011, **55**(2): pp. 26-31.

7. Roeseler W.G. *et al.*, ‘Composite structures: the first 100 years’, in *Proceedings of 16th International Conference on Composite Materials (ICCM-16)*, 8-13 Jul. 2007, Kyoto, Japan.

8. Hull D. and Clyne T.W., *An introduction to composite materials*, 2nd ed.; 1996, Cambridge University Press: Cambridge, UK.

9. Ilcewicz L. and Ashforth C., ‘Scaling crucial to integrated product development of composite airframe structures’, ch. 2 in *Comprehensive composite materials II* (vol. 3), 2nd ed., Zweben C.H. and Beaumont P.W.R., Editors; 2018, Elsevier: Cambridge, UK; pp. 26-90.

10. Lu K., ‘The future of metals’, *Science*; 2010, **328**(5976): pp. 319-20.

11. Warren A.S., ‘Developments and challenges for aluminum – A boeing perspective’, *Materials Forum*; 2004, **28**: pp. 24-31.

12. Boyer R., ‘Attributes, characteristics, and applications of titanium and its alloys’, *Journal of The Minerals, Metals & Materials Society (TMS)*; 2010, **62**(5): pp. 21-4.

13. Quilter A., ‘Composites in aerospace applications’, *IHS White Paper*; 2001, **444**(1).

14. Lowe J., 'Aerospace applications', ch. 11 in *Design and manufacture of textile composites*, Long A.C., Editor; 2005, Woodhead Publishing: Cambridge, USA; pp. 405-23.

15. Campbell F.C., *Structural composite materials*; 2010, ASM International: Materials Park, OH, USA.

16. Ashby M.F., *Materials selection in mechanical design*, 3rd ed.; 2005, Butterworth-Heinemann: Oxford, UK.

17. Greenhalgh E.S., 'Introduction to failure analysis and fractography of polymer composites', ch. 1 in *Failure analysis and fractography of polymer composites*; 2009, Woodhead Publishing: Cambridge, UK; pp. 1-21.

18. Airbus S.A.S., 'The A350 XWB "MSN1" forward fuselage takes shape'; 2011 (accessed 3 Apr. 2018), available from: www.airbus.com/newsroom.

19. Hemmerdinger J., 'Production of Sikorsky's S-97 Raider continues on track'; 2014 (accessed 3 Apr. 2018), available from: www.flightglobal.com.

20. NASA, 'NASA team builds composite space capsule with future in mind'; 2008 (accessed 3 Apr. 2018), available from: www.nasa.gov/exploration/csd/composite_capsule.html.

21. NASA, 'Composite Cryotank Technologies and Demonstration (CCTD)'; 2014 (accessed 3 Apr. 2018), available from: https://gameon.nasa.gov/projects-2/archived-projects-2/composite-cryogenic-propellant-tank/.

22. Gardiner G., Gardiner, G, 'Aircraft composites repair moves toward maturity', in *Composites World*; 2016 (accessed 3 Apr. 2018), available from: www.compositesworld.com/articles/aircraft-composites-repair-moves-toward-maturity.

23. Hale J., 'Boeing 787 from the ground up', *Aero*; 2006, **4**(24): pp. 7.

24. Marsh G., 'Airbus takes on Boeing with reinforced plastic A350 XWB', *Reinforced plastics*; 2007, **51**(11): pp. 26-9.

25. Marsh G., 'Airbus A350 XWB update', *Reinforced plastics*; 2010, **54**(6): pp. 20-4.

26. Timmis A.J. *et al.*, 'Environmental impact assessment of aviation emission reduction through the implementation of composite materials', *The International Journal of Life Cycle Assessment*; 2015, **20**(2): pp. 233-43.

27. Jacob A., 'Carbon fibre and cars–2013 in review', *Reinforced Plastics*; 2014, **58**(1): pp. 18-9.

28. Stewart R., 'Better boat building—trend to closed-mould processingcontinues', *Reinforced Plastics*; 2011, **55**(6): pp. 30-6.

29. Bodjona K. and Lessard L., 'Hybrid bonded-fastened joints and their application in composite structures: A general review', *Journal of Reinforced Plastics and Composites*; 2016, **35**(9): pp. 764-81.

30. Russell J.D., 'The impact of large integrated and bonded composite sturctures on future military transport aircraft', ch. 3 in *Comprehensive composite materials II* (vol. 3), 2nd ed., Zweben C.H. and Beaumont P.W.R., Editors; 2018, Elsevier: Cambridge, UK; pp. 92-130.

31. Visweswaraiah S.B. *et al.*, 'Mechanical characterisation and modelling of randomly oriented strand architecture and their hybrids–A general review', *Journal of Reinforced Plastics and Composites*; 2018.

32. Olsson R., 'A survey of test methods for multiaxial and out-of-plane strength of composite laminates', *Composites Science and Technology*; 2011, **71**(6): pp. 773-83.

33. Greenhalgh E.S., 'Delamination dominated failures in polymer composites', ch. 4 in *Failure analysis and fractography of polymer composites*; 2009, Woodhead Publishing: Cambridge, UK; pp. 164-237.

34. Greenhalgh E.S., 'Fiber-dominated failures in polymer composites', ch. 3 in *Failure analysis and fractography of polymer composites*; 2009, Woodhead Publishing: Cambridge, UK; pp. 107-59.

35. Garg A.C., 'Failure mechanisms in toughened epoxy resins—A review', *Composite Science and Technology*; 1988, **31**(3): pp. 179-223.

36. Broughton W.R., 'Through-thickness testing', ch. 8 in *Mechanical testing of advanced fibre composites*, Hodgkinson J.M., Editor; 2000, Woodhead Publishing: Cambridge, UK; pp. 143-68.

37. Schultheisz C.R. and Waas A.M., 'Compressive failure of composites, part I: Testing and micromechanical theories', *Prog. Aerospace Sci.*; 1996, **32**(1): pp. 1-42.

38. Tong L., Mouritz A.P. and Bannister M., 'Introduction', ch. 1 in *3D fibre reinforced polymer composites*; 2002, Elsevier: Oxford, UK; pp. 1-12.

39. Garg A.C., 'Fracture behavior of cross-ply graphite/epoxy laminates', *Engineering Fracture Mechanics*; 1985, **22**(6): pp. 1035-48.

40. Bekyarova E. *et al.*, 'Multiscale carbon nanotube-carbon fiber reinforcement for advanced epoxy composites', *Langmuir*; 2007, **23**(7): pp. 3970-4.

41. Kedward K.T., Wilson R.S. and McLean S.K., 'Flexure of simply curved composite shapes', *Composites*; 1989, **20**(6): pp. 527-36.

42. Greenhalgh E.S., 'Case studies failures due to overload and design deficiencies', ch. 8 in *Failure analysis and fractography of polymer composites*; 2009, Woodhead Publishing: Cambridge, UK; pp. 441-503.

43. Hubert P., Fernlund G. and Poursartip A., 'Autoclave processing for composites', ch. 13 in *Manufacturing techniques for polymer matrix composites (PMCs)*, Advani S.G. and Hsiao K.-T., Editors; 2012, Woodhead Publishing: Cambridge, UK; pp. 414-34.

44. Fernlund G., Mobuchon C. and Zobeiry N., 'Autocalve processing', ch. 3 in *Comprehensive composite materials II* (vol. 2), 2nd ed., Zweben C.H. and Beaumont P.W.R., Editors; 2018, Elsevier: Cambridge, UK; pp. 42-62.

45. Seferis J.C., Hillermeier R.W. and Buehler F.U., 'Prepregging and autoclaving of thermoset composites', ch. 20 in *Comprehensive Composite Materials* (vol. 2), Kelly A. and Zweben C.H., Editors; 2000, Elsevier: Cambridge, UK; pp. 1-36.

46. Campbell F.C., Mallow A.R. and Browning C.E., 'Porosity in carbon fiber composites an overview of causes', *Journal of advanced materials*; 1995, **26**(4): pp. 18-33.

47. Gardiner G., 'Out-of-autoclave prepregs: Hype or revolution', *High-Performance Composites*; 2011, **19**: pp. 32-9.

48. Schlimbach J. and Ogale A., 'Out-of-autoclave curing process in polymer matrix composites', in *Manufacturing techniques for polymer matrix composites (PMCs)*, Advani S.G. and Hsiao K.-T., Editors; 2012, Woohead Publishing: Cambridge, UK; pp. 435-81.

49. Centea T., Grunenfelder L.K. and Nutt S.R., 'A review of out-of-autoclave prepregs– Material properties, process phenomena, and manufacturing considerations', *Composites Part A: Applied Science and Manufacturing*; 2015, **70**: pp. 132-54.

50. CFK Valley, 'Airbus Operations GmbH Stade'; (accessed 3 Apr. 2018), available from: https://cfk-valley.com/en/members/a/airbus-operations-gmbh-stade/.

51. Hartley Corp., 'Composite curing oven'; 2011 (accessed 3 Apr. 2018), available from: http://hartleycorp.com/?p=86.

52. Hubert P. *et al.*, 'Out-of-autocalve prepreg processing', ch. 4 in *Comprehensive composite materials II* (vol. 2), 2nd ed., Zweben C.H. and Beaumont P.W.R., Editors; 2018, Elsevier: Cambridge, UK; pp. 63-94.

53. Repecka L. and Boyd J., 'Vacuum-bag-only-curable prepregs that produce void-free parts', in *Proceedings of the 47th International Symposium and Exhibition of the Society for the Advancement of Materials and Process Engineering (SAMPE 2002)*, Rasmussen B.M., Pilato L. and Kliger H.S., Editors, 12-16 May 2002, Long Beach, CA, USA pp. 1862-74.

54. Mortimer S., Smith M.J. and Olk E., 'Product development for out-of-autoclave (OOA) manufacture of aerospace structure', in *Proceedings of the 2010 Spring Symposium & Exhibition of the Society for the Advancement of Materials and Process Engineering (SAMPE Spring 2010)*, Albers R., Hubert P. and Beckwith S.W., Editors, 17-20 May 2010, Seattle, WA, USA.

55. Ridgard C., 'Next generation out of autoclave systems', in *Proceedings of the 2010 Spring Symposium & Exhibition of the Society for the Advancement of Materials and Process Engineering (SAMPE Spring 2010)*, Albers R., Hubert P. and Beckwith S.W., Editors, 17-20 May 2010, Seattle, WA, USA.

56. Ridgard C., 'Out of autoclave composite technology for aerospace, defense and space structures', in *Proceedings of the 2009 Spring Symposium of the Society for the Advancement of Materials and Process Engineering (SAMPE 2009)*, Fielding J.C. *et al.*, Editors, 18-21 May 2009, Baltimore, MD, USA.

57. Stewart R., 'New prepreg materials offer versatility, top performance', *Reinforced Plastics*; 2009, **53**(5): pp. 28-33.

58. Lucas S., Howard S. and Senger J., 'Vacuum bag only processing: Improving prepreg out-time and porosity for large composite structure', in *Proceedings of the 2010 Spring Symposium & Exhibition of the Society for the Advancement of Materials and Process Engineering (SAMPE Spring 2010)*, 17-20 May 2010, Seattle, WA, USA.

59. Gardiner G., 'Resin-infused MS-21 wings and wingbox', *High Performance Composites*; 2014, **22**(1): pp. 29.

60. McCarville D.A. *et al.*, 'Design, manufacture and test of cryotank components', ch. 5 in *Comprehensive composite materials II* (vol. 3), 2nd ed., Zweben C.H. and Beaumont P.W.R., Editors; 2018, Elsevier: Cambridge, UK; pp. 154-79.

61. Stavana J. *et al.*, 'Large scale composite manufacturing for heavy lift launch vehicles', in *Proceedings of the 2012 Conference & Exhibition of the Society for the Advancement of Materials and Process Engineering (SAMPE 2012)*, 21-24 May 2012, Baltimore, MD, USA.

62. Molyneux M., Murray P. and Murray B.P., 'Prepreg, tape and fabric technology for advanced composites', *Composites*; 1983, **14**(2): pp. 87-91.

63. Centea T., *Material - processing - quality relationships during the consolidation of out-of-autoclave prepregs*, Ph.D. Thesis; Mar. 2013, McGill University: Montreal, QC, Canada.

64. Dirk H.-J.L., Ward C. and Potter K.D., 'The engineering aspects of automated prepreg layup: History, present and future', *Composites Part B: Engineering*; 2012, **43**(3): pp. 997-1009.

65. Mathews F.L., 'Specimen preparation', ch. 3 in *Mechanical testing of advanced fibre composites*, Hodgkinson J.M., Editor; 2000, Woodhead Publishing: Cambridge, UK; pp. 36-42.

66. ASTM D5687 / D5687M-95(2015), *Standard guide for preparation of flat composite panels with processing guidelines for specimen preparation*; 2015, ASTM International: West Conshohocken, PA, USA.

67. Hickey C., *The influence of variation in process parameters on the manufacturing of advanced fibre composites*, Ph.D. Thesis; Jan. 2014, University of Auckland: Auckland, New Zealand.

68. *HexPly® 8552, Mid-Toughened, High Strength, Damage-Resistant, Structural Epoxy Matrix*, Technical data sheet; Hexcel: 2016 (reviewed 8 Feb. 2017).

69. Brillant M., *Out-of-autoclave manufacturing of complex-shape composite laminates*, M.Eng. Thesis; Dec. 2010, McGill University: Montreal, QC, Canada.

70. Arafath A.R.A., Fernlund G. and Poursartip A., 'Gas transport in prepregs: model and permeability experiments', in *Proceedings of the 17th International Conference on Composite Materials (ICCM-17)*, 27-31 Jul. 2009, Edinburgh, Scotland.

71. Grunenfelder L. *et al.*, 'Effect of prepreg format on defect control in out-of-autoclave processing', *Composites Part A: Applied Science and Manufacturing*; 2017, **93**: pp. 88-99.

72. Roman M., Howard S.J. and Jack D.B., *Curable prepregs with surface openings*; 2014, U.S. Patent No. 20140174632 A1.

73. Kellas S., Lerch B. and Wilmoth N., 'Mechanical characterization of in- and out-of-autoclave cured composite panels for large launch vehicles', in *Proceedings of the 2012 Conference & Exhibition of the Society for the Advancement of Materials and Process Engineering (SAMPE 2012)*, 21-24 May 2012, Baltimore, MD, USA.

74. Palardy-Sim M. and Hubert P., 'Characterization of the degree of impregnation of out-of-autoclave prepreg', in *Proceedings of the 20th International Conference on Composite Materials (ICCM-20)*, 19-24 Jul. 2015, Copenhagen, Denmark.

75. Smith R.A. *et al.*, 'Automated analysis and advanced defect characterisation from ultrasonic scans of composites', *Insight-Non-Destructive Testing and Condition Monitoring*; 2009, **51**(2): pp. 82-7.

76. National Institure for Aviation Research (NIAR), 'National Center for Advanced Materials Performance (NCAMP)'; (accessed 3 Apr. 2018), available from: www.niar.wichita.edu/coe/ncamp.asp.

77. Wisnom M., 'The challenge of predicting failure in composites', in *Proceedings of 19th International Conference on Composite Materials (ICCM 19)*, 28 Jul.-2 Aug. 2014, Monreal, QC, Canada.

78. Cui W. *et al.*, 'Interlaminar tensile strength (ILTS) measurement of woven glass/polyester laminates using four-point curved beam specimen', *Composites Part A: Applied Science and Manufacturing*; 1996, **27**(11): pp. 1097-105.

79. Lagace P.A. and Weems D.B., ‘A through-the-thickness strength specimen for composites’, in *Test methods and design allowables for fibrous composites: 2nd volume* (vol. 2), Chamis C.C., Editor; 1989, ASTM International: Philadelphia, PA, USA; pp. 197-207.

80. Martin R.H. and Jackson W.C., ‘Damage prediction in cross-plied curved composite laminates’, in *Composite materials: fatigue and fracture* (vol. 4), Stinchcomb W.W. and Ashbaugh N.E., Editors; 1993, ASTM International: Philadelphia, PA, USA.

81. Jackson W.C. and Martin R.H., ‘An interlaminar tensile strength specimen’, in *Composite materials: testing and design* (vol. 11), Camponeschi E.T., Editor; 1993, ASTM International: West Conshohocken, PA, USA.

82. Hiel C.C., Sumich M. and Chappell D.P., ‘A curved beam test specimen for determining the interlaminar tensile strength of a laminated composite’, *Journal of Composite Materials*; 1991, **25**(7): pp. 854-68.

83. Jackson W.C. and Ifju P.G., ‘Through-the-thickness tensile strength of textile composites’, in *Composite materials: testing and design* (vol. 12), Deo R.B. and Saff C.R., Editors; 1996, ASTM International: West Conshohocken, PA, USA; pp. 218–38.

84. Ferguson R.F., Hinton M.J. and Hiley M.J., ‘Determining the through-thickness properties of FRP materials’, *Composites Science and Technology*; 1998, **58**(9): pp. 1411-20.

85. Koudela K.L. *et al.*, ‘Static and fatigue interlaminar tensile characterization of laminated composites’, in *Composite materials: fatigue and fracture* (vol. 6), Armanios E.A., Editor; 1997, ASTM International: Philadelphia, PA, USA; pp. 516-30.

86. Mespoulet S. *et al.*, ‘Design, development, and implementation of test methods for determination of through thickness properties of laminated composites’, *Plastics, Rubber and Composites*; 2000, **29**(9): pp. 496-502.

87. ASTM D7291 / D7291M-15, *Standard test method for through-thickness flatwise tensile strength and elastic modulus of a fiber-reinforced polymer matrix composite material*; 2015, ASTM International: West Conshohocken, PA, USA.

88. Wisnom M.R. and Jones M., ‘Size effects in interlaminar tensile and shear strength of unidirectional glass fibre/epoxy’, *Journal of Reinforced Plastics and Composites*; 1996, **15**(1): pp. 2-15.

89. Ige D. and Sargent P., ‘An apparatus for determining the interlaminar tensile strength of laminated composites using the curved specimen geometry’, in *European Conference on Composites Testing and Standardisation (ECCM-CTS 1992)*, Hogg P.J., Editor, 1992, Amsterdam, Netherlands pp. 267-76).

90. ASTM D6415 / D6415M-06a(2013), *Standard test method for measuring the curved beam strength of a fiber-reinforced polymer-matrix composite*; 2013, ASTM International: West Conshohocken, PA, USA.

91. AITM1-0069 Issue 2, *Determination of curved-beam failure load*; 2011, Airbus S.A.S, Engineering Directorate: Blagnac, France.

92. Fletcher T.A. *et al.*, ‘Resin treatment of free edges to aid certification of through thickness laminate strength’, *Composite Structures*; 2016, **146**: pp. 26-33.

93. Makeev A. *et al.*, ‘A method for measurement of multiple constitutive properties for composite materials’, *Composites Part A: Applied Science and Manufacturing*; 2012, **43**(12): pp. 2199-210.

94. Seon G. *et al.*, ‘Effects of defects on interlaminar tensile fatigue behavior of carbon/epoxy composites’, *Composites Science and Technology*; 2013, **89**: pp. 194-201.

95. Blanchfield J.P. and Allegri G., ‘Delamination initiation due to interlaminar tension in fiber reinforced plastics’, in *Proceedings of the 19th International Conference on Composite Materials (ICCM-19)*, 28 Jul.-2 Aug. 2013, Montreal, QC, Canada.

96. Hao W. *et al.*, ‘Experimental investigation on deformation and strength of carbon/epoxy laminated curved beams’, *Polymer Testing*; 2012, **31**(4): pp. 520-6.

97. Avalon S.C. and Donaldson S.L., ‘Strength of composite angle brackets with multiple geometries and nanofiber-enhanced resins’, *Journal of Composite Materials*; 2011, **45**(9): pp. 1017-30.

98. Ranz D. *et al.*, ‘Experimental research into interlaminar tensile strength of carbon/epoxy laminated curved beams’, *Composite Structures*; 2017, **164**: pp. 189-97.

99. Krumenacker N. and Hubert P., ‘Effect of processing deficiencies on vacuum-bag-only complex-shape prepreg laminate consolidation and interlaminar tensile behaviour’, in *Proceedings of the 20th International Conference on Composite Materials (ICCM-20)*, 19-24 Jul. 2015, Copenhagen, Denmark.

100. Matsuo T., Goto T. and Takahashi J., ‘Investigation about the fracture behavior and strength in a curved section of CF/PP composite by a thin-curved beam specimen’, *Advanced Composite Materials*; 2015, **24**(3): pp. 249-68.

101. Lekhnitskii S.G., ‘Bending of plane anisotropic bars and curved beams’, ch. 3 in *Anisotropic plates*, 3rd ed., Tsai S.W. and Cheron T., Translators; 1968, Gordon & Breach Science Publishers: New York, NY, USA; pp. 95-8.

102. Ko W.L., *Delamination stresses in semicircular laminated composite bars*; 1988. [Report No. NASA-TM-4026]

103. Mabson G. and NEALL III E.P., ‘Analysis and testing of composite aircraft frames for interlaminar tension failure’, in *NAtional specialists meeting on toraty wing test technology of the American Helicopter Society*, 15-16 Mar. 1988, Bridgeport, CT, USA pp. 1988.

104. Most J., Stegmair D. and Petry D., 'Error estimation between simple, closed-form analytical formulae and full-scale FEM for interlaminar stress prediction in curved laminates', *Composite Structures*; 2015, **131**: pp. 72-81.

105. Chapelle D., Ferent A. and Bathe K., '3D-shell elements and their underlying mathematical model', *Mathematical Models and Methods in Applied Sciences*; 2004, **14**(01): pp. 105-42.

106. Bodjona K. *et al.*, 'Load sharing in single-lap bonded/bolted composite joints. Part I: Model development and validation', *Composite Structures*; 2015, **129**: pp. 268-75.

107. Weber J.P.H., *Through-the-Thickness Stresses and Failure in the Corner Radius of a Laminated Composite Section*; 1994, IHS ESDU. [Report No. ESDU 94019]

108. Airbus UK Ltd, *A400M spar development: inter-laminar shear and through-thickness direct stresses in laminated composites (internal document)*; 2004.

109. Jones R.M., 'Macromechanical behavior of a laminate', ch. 4 in *Mechanics of composite materials*, 2nd ed.; 1999, Taylor & Francis Group: New York, NY, USA; pp. 187-276.

110. Fletcher T.A., *Certification and design for manufacture of curved and tapered laminates*, Ph.D. Thesis; Nov. 2016, Bath University: Bath, UK.

111. Hinton M., Kaddour A. and Soden P., 'Predicting failure in fibre composites: Lessons learned from the World-Wide Failure Exercise', *Technical papers of the Society of Manufacturing Engineers*; 2002.

112. Sun C.T., *Comparative evaluation of failure evaluation of failure analysis methods for composite laminates*; 1996, Alexandria, VA, USA. [Report No. DOT/FAA/AR-95/109]

113. Wisnom M.R., Petrossian Z. and Jones M., 'Interlaminar failure of unidirectional glass/epoxy due to combined through thickness shear and tension', *Composites Part A: Applied Science and Manufacturing*; 1996, **27**(10): pp. 921-9.

114. Centea T. and Hubert P., 'Out-of-autoclave prepreg consolidation under deficient pressure conditions', *Journal of Composite Materials*; 2014, **48**(16): pp. 2033-45.

115. Loos A.C. and Springer G.S., 'Curing of epoxy matrix composites', *Journal of composite materials*; 1983, **17**(2): pp. 135-69.

116. Kardos J.L., 'Void growth and dissolution', ch. 6 in *Processing of composites*, Davé R.S. and Loos A.C., Editors; 2000, Hanser/Gardner Publications: Cincinnati, OH, USA; pp. 182-207.

117. Grunenfelder L. and Nutt S., 'Void formation in composite prepregs–Effect of dissolved moisture', *Composites Science and Technology*; 2010, **70**(16): pp. 2304-9.

118. Hsiao K., Kay J. and Fernlund G., ‘Gas transport and water evaporation in out-of-autoclave prepregs’, in *Proceedinds of the 26th Annual Technical Conference of the American Society for Composites (the 2nd Joint US-Canada Conference on Composites)*, 26-28 Sep. 2011, Montreal, QC, Canada.

119. Kay J. and Fernlund G., ‘Processing conditions and voids in out of autoclave prepregs’, in *Proceedings of the 2012 Conference of the Society for the Advancement of Materials and Process Engineering (SAMPE 2012)*, 21-24 May 2012, Baltimore, MD, USA.

120. Centea T., Preau M. and Hubert P., ‘Effect of layup and ply morphology on void formation in out-of-autoclave prepregs’, in *Proceedings of the 19th International Conference on Composite Materials (ICCM-19)*, 28 Jul.-2 Aug. 2013, Montreal, QC, Canada pp. 1-9.

121. Ma Y., Centea T. and Nutt S.R., ‘Defect reduction strategies for the manufacture of contoured laminates using vacuum BAG-only prepregs’, *Polymer Composites*; 2015, **38**(9): pp. 2016–25.

122. Hamill L., Centea T. and Nutt S., ‘Surface porosity during vacuum bag-only prepreg processing: Causes and mitigation strategies’, *Composites Part A: Applied Science and Manufacturing*; 2015, **75**: pp. 1-10.

123. Helmus R. *et al.*, ‘An experimental technique to characterize interply void formation in unidirectional prepregs’, *Journal of Composite Materials*; 2017, **51**(5): pp. 579-91.

124. Grunenfelder L.K. *et al.*, ‘Effect of room-temperature out-time on tow impregnation in an out-of-autoclave prepreg’, *Composites Part A: Applied Science and Manufacturing*; 2013, **45**: pp. 119-26.

125. Kim D., Centea T. and Nutt S., ‘Out-time effects on cure kinetics and viscosity for an out-of-autoclave (OOA) prepreg: Modelling and monitoring’, *Composites Science and Technology*; 2014, **100**: pp. 63-9.

126. Centea T., Kratz J. and Hubert P., ‘The effect of out-time and cure cycle on the consolidation of out-of-autoclave prepregs’, in *Proceedings of the 11th International Conference on Flow Processes in Compososite Materials*, 9-12 Jul. 2012, Auckland, New Zealand.

127. Hughes S., Krumenacker N. and Hubert P., ‘Out-of-autoclave prepreg processing: Thermally assisted compaction of complex laminates’, in *Proceedings of the 2015 Canadian International Conference on Composite Materials (CANCOM 2015)*, 18-20 Aug. 2015, Edmonton, AB, Canada.

128. Centea T. and Hubert P., ‘Modelling the effect of material properties and process parameters on tow impregnation in out-of-autoclave prepregs’, *Composites Part A: Applied Science and Manufacturing*; 2012, **43**(9): pp. 1505-13.

129. Helmus R. *et al.*, 'Modelling void formation in corners during out-of-autoclave prepreg processing', in *Proceedings of the 2016 Conference of the Society for the Advancement of Material and Process Engineering (SAMPE 2016)*, 23-26 May 2016, Long Beach, CA, USA.

130. Hubert P. and Poursartip A., 'Aspects of the compaction of composite angle laminates: an experimental investigation', *Journal of Composite Materials*; 2001, **35**(1): pp. 2-26.

131. Li Y. *et al.*, 'Numerical and experimental study on the effect of lay-up type and structural elements on thickness uniformity of L-shaped laminates', *Applied Composite Materials*; 2009, **16**(2): pp. 101-15.

132. Wang X. *et al.*, 'Correlated rules between complex structure of composite components and manufacturing defects in autoclave molding technology', *Journal of Reinforced Plastics and Composites*; 2009, **28**(22): pp. 2791-803.

133. Eom Y. *et al.*, 'A structure and property based process window for void free thermoset composites', *Polymer composites*; 2001, **22**(1): pp. 22-31.

134. Fernlund G. *et al.*, 'Experimental and numerical study of the effect of caul-sheets on corner thinning of composite laminates', *Composites Part A: Applied Science and Manufacturing*; 2002, **33**(3): pp. 411-26.

135. Li M. and Tucker C.L., 'Modeling and simulation of two-dimensional consolidation for thermoset matrix composites', *Composites Part A: Applied Science and Manufacturing*; 2002, **33**(6): pp. 877-92.

136. Hubert P., Vaziri R. and Poursartip A., 'A two-dimensional flow model for the process simulation of complex shape composite laminates', *International Journal for Numerical Methods in Engineering*; 1999, **44**(1): pp. 1-26.

137. Levy A., Stadlin J. and Hubert P., 'Corner consolidation in vacuum bag only processing of out-of-autoclave composite prepregs laminates', in *Proceedings of the 2014 Technical Conference of the Society for the Advancement of Materials and Process Engineering (SAMPE Tech 2014)*, 2-5 Jun. 2014, Seattle, WA, United States.

138. Cauberghs J., *Out-of-autoclave manufacturing of aerospace representative parts*, M.Eng. Thesis; Jul. 2012, McGill University: Montreal, QC, Canada.

139. Brillant M. and Hubert P., 'Modelling and characterization of thickness variations in L-shape out-of-autoclave laminates', in *Proceedings of the 18th International Conference of Composite Materials (ICCM-18)*, 21-26 Aug. 2011, Jeju, South Korea.

140. *Polymer matrix composite guidelines for characterization of structural materials*, vol. 1 of *Composites materials handbook*; 2002, US Department of Defense: Washington, DC, USA. [Document code: MIL-HDBK-17-1F]

141. Potter K. *et al.*, ‘Variability, fibre waviness and misalignment in the determination of the properties of composite materials and structures’, *Composites Part A: Applied Science and Manufacturing*; 2008, **39**(9): pp. 1343-54.

142. Piggott M.R., ‘The effect of fibre waviness on the mechanical properties of unidirectional fibre composites: a review’, *Composites science and technology*; 1995, **53**(2): pp. 201-5.

143. Wisnom M.R. and Atkinson J., ‘Fibre waviness generation and measurement and its effect on compressive strength’, *Journal of Reinforced Plastics and Composites*; 2000, **19**(2): pp. 96-110.

144. Hsiao H. and Daniel I., ‘Effect of fiber waviness on stiffness and strength reduction of unidirectional composites under compressive loading’, *Composites science and technology*; 1996, **56**(5): pp. 581-93.

145. Potter K. *et al.*, ‘Sources of variability in uncured aerospace grade unidirectional carbon fibre epoxy preimpregnate’, *Composites Part A: Applied Science and Manufacturing*; 2007, **38**(3): pp. 905-16.

146. Lightfoot J.S., Wisnom M.R. and Potter K., ‘A new mechanism for the formation of ply wrinkles due to shear between plies’, *Composites Part A: Applied Science and Manufacturing*; 2013, **49**: pp. 139-47.

147. Wang J. *et al.*, ‘Experimental fabrication and characterization of out-of-plane fiber waviness in continuous fiber-reinforced composites’, *Journal of Composite Materials*; 2012, **46**(17): pp. 2041-53.

148. Kugler D. and Moon T.J., ‘The effects of Mandrel material and tow tension on defects and compressive strength of hoop-wound, on-line consolidated, composite rings’, *Composites Part A: Applied Science and Manufacturing*; 2002, **33**(6): pp. 861-76.

149. Hoa S.V., ‘Manufacturing of composites – An overview’, ch. 4 in *Comprehensive composite materials II* (vol. 2), 2nd ed., Zweben C.H. and Beaumont P.W.R., Editors; 2018, Elsevier: Cambridge, UK; pp. 1-23.

150. Kugler D. and Moon T.J., ‘Identification of the most significant processing parameters on the development of fiber waviness in thin laminates’, *Journal of composite Materials*; 2002, **36**(12): pp. 1451-79.

151. Mandell J., Samborsky D. and Wang L., ‘Effects of fiber waviness on composites for wind turbine blades’, in *Proceedings of the 48th International Symposium and Exhibition of the Society for the Advancement of Materials and Process Engineering*, Cohen L.J., Ong C.-L. and Arendt C., Editors, 11-15 May 2003, Long Beach, CA, USA.

152. Veers P.S. *et al.*, ‘Trends in the design, manufacture and evaluation of wind turbine blades’, *Wind Energy*; 2003, **6**(3): pp. 245-59.

153. Farnand K. *et al.*, 'Micro-level mechanisms of fiber waviness and wrinkling during hot drape forming of unidirectional prepreg composites', *Composites Part A: Applied Science and Manufacturing*; 2017, **103**: pp. 168-77.

154. Yurgartis S., 'Measurement of small angle fiber misalignments in continuous fiber composites', *Composites Science and Technology*; 1987, **30**(4): pp. 279-93.

155. Clarke A., Archenhold G. and Davidson N., 'A novel technique for determining the 3D spatial distribution of glass fibres in polymer composites', *Composites science and technology*; 1995, **55**(1): pp. 75-91.

156. Sutcliffe M.P.F., Lemanski S.L. and Scott A.E., 'Measurement of fibre waviness in industrial composite components', *Composites Science and Technology*; 2012, **72**(16): pp. 2016-23.

157. Creighton C., Sutcliffe M. and Clyne T., 'A multiple field image analysis procedure for characterisation of fibre alignment in composites', *Composites Part A: Applied Science and Manufacturing*; 2001, **32**(2): pp. 221-9.

158. Soltani S.A. *et al.*, 'Effect of Fabric Weave Type on Distortion of Flat Panels Made of Out–Of–Autoclave Carbon-Fiber Epoxy Prepreg', in *Proceedings of the 2013 Fall Technical Conference of the Society for the Advancement of Materials and Process Engineering (SAMPE Fall 2013)*, 21-24 Oct. 2013, Wichita, KS, USA.

159. Soltani S.A. *et al.*, 'Effect of nonwoven fabric type and stacking sequence on distortion of flat panels made of out-of-autoclave carbon-fiber epoxy prepreg', in *Proceedings of the 2014 Technical Conference of the Society for the Advancement of Materials and Process Engineering (SAMPE Tech 2014)*, 2-5 Jun. 2014, Seattle, WA, USA.

160. Luner J.J. and Bond G.G., 'Producibility and variation of non-autoclave composite angles evaluated via design of experiments', in *Proceedings of the 2012 Conference & Exhibition of the Society for the Advancement of Materials and Process Engineering (SAMPE 2012)*, 21-24 May 2012, Baltimore, MD, USA.

161. Sim G.D., 'Development and use of standard test methods', ch. 15 in *Mechanical testing of advanced fibre composites*, Hodgkinson J.M., Editor; 2000, Woodhead Publishing: Cambridge, UK; pp. 340-57.

162. *CYCOM® 5320-1 Epoxy Resin System*, Technical data sheet; Cytec Industries: 2015 (reviewed Oct. 2015).

163. Man M., *Solvay Cytec Cycom 5320-1 T650 Unitape Qualification Material Property Data Report*, Lovingfoss R., Lian E. and Hooper E., Editors; 2017, National Center for Advanced Materials Performance: Wichita, KS, USA. [Report No. CAM-RP-2013-002 Rev A]

164. Man M., *Cytec Cycom 5320-1 T650 3k-PW Fabric Qualification Material Property Data Report*, Lovingfoss R. *et al.*, Editors; 2015, National Center for Advanced Materials Performance: Wichita, KS, USA. [Report No. CAM-RP-2012-017 Rev NC]

165. Marlett K., *Hexcel 8552 AS4 Unidirectional Prepreg at 190 gsm & 35% RC Qualification Material Property Data Report*, Ng Y., Tomblin J. and Hooper E., Editors; 2011, National Center for Advanced Materials Performance: Wichita, KS, USA. [Report No. CAM-RP-2010-002 Rev A]

166. Marlett K., *Hexcel 8552S AS4 Plain Weave Fabric Prepreg 193 gsm & 38% RC Qualification Material Property Data Report*, Ng Y. and Tomblin J., Editors; 2011, National Center for Advanced Materials Performance: Wichita, KS, USA. [Report No. CAM-RP-2010-006 N/C]

167. Sutter J.K. *et al.*, 'Comparison of autoclave and out-of-autoclave composites', in *Proceedings of the 42nd International Technical Conference of the Society for the Advancement of Materials and Process Engineering (SAMPE 2010)*, 11-14 Oct. 2010, Salt Lake City, UT, USA.

168. Vo T. *et al.*, 'Effect of post cure temperature variation on compressive properties of an out-of-autoclave prepreg composite', in *Proceedings of the 2011 Spring Technical Conference and Exhibitionof the Society for the Advancement of Materials and Process Engineering (SAMPE Spring 2011)*, 23-26 May 2011, Long Beach, CA, USA.

169. Kratz J. *et al.*, 'Thermal models for MTM45-1 and Cycom 5320 out-of-autoclave prepreg resins', *Journal of Composite Materials*; 2012, **43**(3): pp. 341-52.

170. *CYCOM 5320 toughened epoxy for structural applications, out-of-autoclave manufacturing*, Technical data sheet; Cytec Engineered Materials: 2009 (reviewed 18 Mar. 2009).

171. *Thornel T650/35 pan-based fiber*, Technical data sheet; Cytec Engineered Materials: 2012 (reviewed 21 May 2012).

172. Préau M., *Defect management in vacuum-bag-only semipreg processing of co-bonded composite repairs*, Ph.D. Thesis; Jul. 2016, McGill University: Montreal, QC, Canada.

173. Centea T. and Hubert P., 'Measuring the impregnation of an out-of-autoclave prepreg by micro-CT', *Composites Science and Technology*; 2011, **71**(5): pp. 593-9.

174. ASTM D5229 / D5229M-14, *Standard test method for moisture absorption properties and equilibrium conditioning of polymer matrix composite materials*; 2014, ASTM International: West Conshohocken, PA, USA.

175. Levy A., Kratz J. and Hubert P., 'Air evacuation during vacuum bag only prepreg processing of honeycomb sandwich structures: In-plane air extraction prior to cure', *Composites Part A: Applied Science and Manufacturing*; 2015, **68**: pp. 365-76.

176. Louis B.M., Hsiao K. and Fernlund G., 'Gas permeability measurements of out of autoclave prepreg MTM45-1 / CF2426A', in *Proceedings of the 2010 Spring Symposium & Exhibition of the Society for the Advancement of Materials and Process Engineering (SAMPE Spring 2010)*, 17-20 May 2010, Seatlle, WA, USA pp. 17-20.

177. Khoun L., Centea T. and Hubert P., 'Characterization methodology of thermoset resins for the processing of composite materials - Case study: CYCOM 890RTM epoxy resin', *Journal of Composite Materials*; 2010, **44**(11): pp. 1397-415.

178. Wimmer G. *et al.*, 'Computational and experimental investigation of delamination in L-shaped laminated composite components', *Engineering Fracture Mechanics*; 2009, **76**(18): pp. 2810-20.

179. Greenhalgh E.S., 'Methodology and tools for failure analysis of polymer composites', ch. 2 in *Failure analysis and fractography of polymer composites*; 2009, Woodhead Publishing: Cambridge, UK; pp. 23-105.

180. Hayes B.S. and Gammon L.M., *Optical microscopy of fiber-reinforced composites*; 2010, ASM International: Materials Park, OH, USA.

181. Davidson N., Clarke A. and Archenhold G., 'Large-area, high-resolution image analysis of composite materials', *Journal of Microscopy*; 1997, **185**(2): pp. 233-42.

182. Otsu N., 'A threshold selection method from gray-level histograms', *IEEE Transactions on Systems, Man, and Cybernetics*; 1979, **9**(1): pp. 62-6.

183. Waterbury M.C. and Drzal L.T., 'Determination of fiber volume fractions by optical numeric volume fraction analysis', *Journal of Reinforced Plastics and Composites*; 1989, **8**(6): pp. 627-36.

184. Madra A., El Hajj N. and Benzeggagh M., 'X-ray microtomography applications for quantitative and qualitative analysis of porosity in woven glass fiber reinforced thermoplastic', *Composites Science and Technology*; 2014, **95**: pp. 50-8.

185. Hodgkinson J.M., 'Flexure', ch. 7 in *Mechanical testing of advanced fibre composites*, Hodgkinson J.M., Editor; 2000, Woodhead Publishing: Cambridge, UK; pp. 124-42.

186. Inc. W.T.F., Wyoming Test Fixtures Inc., 'General information'; 2017 (accessed 25 Oct. 2017), available from: www.wyomingtestfixtures.com.

187. *17-4 PH® stainless steel*, Technical data sheet; AK Steel: 2014 (reviewed 22 Apr. 2014).

188. Bodjona K. and Lessard L., 'Load sharing in single-lap bonded/bolted composite joints. Part II: Global sensitivity analysis', *Composite Structures*; 2015, **129**: pp. 276-83.

189. Barbero E.J., *Finite element analysis of composite materials using Abaqus*; 2013, CRC Press: Boca Raton, FL, USA.

190. Dassault Systèmes Simulia Corp., ‘Abaqus 2016 documentation’; 2015 (accessed 25 Oct. 2017), available from: http://50.16.225.63/v2016/.

191. ‘Thick composite cylinder subjected to internal pressure’, sect. 1.1.4 in *Abaqus 6.12 benchmarks manual*; 2012, Dassault Systèmes Simulia: Providence, RI, USA; pp. 1-8.

192. Kim J., Yoon J.-C. and Kang B.-S., ‘Finite element analysis and modeling of structure with bolted joints’, *Applied Mathematical Modelling*; 2007, **31**(5): pp. 895-911.

193. Brodusch N. *et al.*, ‘Efficient cross-section preparation method for high-resolution imaging of hard polymer composites with a scanning electron microscope’, *Journal of Microscopy*; 2015, **260**(2): pp. 117-24.

194. Sawyer L., Grubb D. and Meyers G.F., *Polymer microscopy*, 3rd ed.; 2008, Springer: New York, NY, USA.

195. Krumenacker N. and Hubert P., ‘Development of mechanical stiffening-sleeves for curved beam strength testing (ASTM D6415)’; Technical presentation given to ASTM International Technical Committee Meeting on Interlaminar Properties (D30.36), 12 Oct. 2017, New Orleans, LA, United States.

196. Buckheit J.B. and Donoho D.L., ‘Wavelab and reproducible research’, in *Lecture notes in statistics: wavelets and statistics* (vol. 103), Antoniadis A. and Oppenheim G., Editors; 1995, Springer: New York, NY, USA; pp. 55-81.

197. Stodden V., ‘Reproducible research for scientific computing: Tools and strategies for changing the culture’, *Computing in Science & Engineering*; 2012, **14**(4): pp. 13-7.

198. ‘The Yale Law School Round Table on Data and Core Sharing: "Reproducible Research"’, *Computing in Science and Engineering*; 2010, **12**(5): pp. 8–12.

199. ASTM E691-16, *Standard practice for conducting an interlaboratory study to determine the precision of a rest method*; 2016, ASTM International: West Conshohocken, PA, USA.

200. Wolstenholme L.C., ‘Statistical modelling and testing of data variability’, ch. 14 in *Mechanical testing of advanced fibre composites*, Hodgkinson J.M., Editor; 2000, Woodhead Publishing: Cambridge, UK; pp. 314-39.

201. Nieuwenhuis S., Forstmann B.U. and Wagenmakers E.-J., ‘Erroneous analyses of interactions in neuroscience: a problem of significance’, *Nature Neuroscience*; 2011, **14**(9): pp. 1105-7.

202. Veldkamp C.L. *et al.*, ‘Statistical reporting errors and collaboration on statistical analyses in psychological science’, *PLoS ONE*; 2014, **9**(12).

203. *HexTow® AS4 Carbon Fiber*, Technical data sheet; Hexcel: 2016 (reviewed Feb. 2016).

204. Buxman A. *et al.*, *Fabrication of NMS 532 Qualification, Equivalency, and Acceptance Test Panels (Cytec Cycom 5320-1)*, Daggett S. *et al.*, Editors; 2014, National Center for Advanced Materials Performance: Wichita, KS, USA. [Report No. NPS 85321 Rev B]

205. Ng Y. and Tomblin J., *Fabrication of NMS 128 Qualification, Equivalency, and Acceptance Test Panels (for Hexcel 8552 and 8552S prepregs)*, Boll D. *et al.*, Editors; 2011, National Center for Advanced Materials Performance: Wichita, KS, USA. [Report No. NPS 81228 Rev B]

206. ASTM D2344 / D2344M-16, *Standard test method for short-beam strength of polymer matrix composite materials and their laminates*; 2016, ASTM International: West Conshohocken, PA, USA.

207. ASTM D3171-15, *Standard test methods for constituent content of composite materials*; 2015, ASTM International: West Conshohocken, PA, USA.

208. ASTM D2734-16, *Standard test methods for void content of reinforced plastics*; 2016, ASTM International: West Conshohocken, PA, USA.

209. Leys C. *et al.*, 'Detecting outliers: Do not use standard deviation around the mean, use absolute deviation around the median', *Journal of Experimental Social Psychology*; 2013, **49**(4): pp. 764-6.

210. Scholz F.W. and Stephens M.A., 'K-sample Anderson–Darling tests', *Journal of the American Statistical Association*; 1987, **82**(399): pp. 918-24.

211. Cook R.D. and Weisberg S., *Residuals and influence in regression*; 1982, Chapman & Hall: New York, NY, USA.

212. Ghasemi A. and Zahediasl S., 'Normality tests for statistical analysis: a guide for non-statisticians', *International Journal of Endocrinology and Metabolism*; 2012, **10**(2): pp. 486.

213. Razali N.M. and Wah Y.B., 'Power comparisons of Shapiro-Wilk, Kolmogorov-Smirnov, Lilliefors and Anderson-Darling tests', *Journal of Statistical Modeling and Analytics*; 2011, **2**(1): pp. 21-33.

214. Kelly R. and Colvin J., 'One-way ANOVA', in *Minitab Inc. technical papers*; 2013 (accessed 29 Nov. 2017), available from: http://support.minitab.com/en-us/minitab/17/technical-papers/.

215. Brown M.B. and Forsythe A.B., 'Robust tests for the equality of variances', *Journal of the American Statistical Association*; 1974, **69**(346): pp. 364-7.

216. Moder K., 'Alternatives to F-test in one way ANOVA in case of heterogeneity of variances (a simulation study)', *Psychological Test and Assessment Modeling*; 2010, **52**(4): pp. 343-53.

217. Welch B.L., ‘On the comparison of several mean values: an alternative approach’, *Biometrika*; 1951, **38**(3/4): pp. 330-6.

218. Glass G.V., Peckham P.D. and Sanders J.R., ‘Consequences of failure to meet assumptions underlying the fixed effects analyses of variance and covariance’, *Review of Educational Research*; 1972, **42**(3): pp. 237-88.

219. Lix L.M., Keselman J.C. and Keselman H.J., ‘Consequences of assumption violations revisited: A quantitative review of alternatives to the one-way analysis of variance F test’, *Review of Educational Research*; 1996, **66**(4): pp. 579-619.

220. Nikishkov G., Nikishkov Y. and Makeev A., ‘Finite element mesh generation for composites with ply waviness based on X-ray computed tomography’, *Advances in Engineering Software*; 2013, **58**: pp. 35-44.

221. Wisnom M.R., Reynolds T. and Gwilliam N., ‘Reduction in interlaminar shear strength by discrete and distributed voids’, *Composites Science and Technology*; 1996, **56**(1): pp. 93-101.

222. Charrier J.-S. *et al.*, ‘Determination of the out-of-plane tensile strength using four-point bending tests on laminated L-angle specimens with different stacking sequences and total thicknesses’, *Composites Part A: Applied Science and Manufacturing*; 2016, **81**: pp. 243-53.

223. Borg R., Nilsson L. and Simonsson K., ‘Simulation of low velocity impact on fiber laminates using a cohesive zone based delamination model’, *Composites Science and Technology*; 2004, **64**(2): pp. 279-88.

224. Breiman L., ‘Random forests’, *Machine learning*; 2001, **45**(1): pp. 5-32.

225. Peng B., Zhang L. and Zhang D., ‘Automatic image segmentation by dynamic region merging’, *IEEE Transactions on image processing*; 2011, **20**(12): pp. 3592-605.

226. Nayroles B., Touzot G. and Villon P., ‘Generalizing the finite element method: diffuse approximation and diffuse elements’, *Computational mechanics*; 1992, **10**(5): pp. 307-18.

227. Goldstein H., Poole C.P. and Safko J.L., *Classical Mechanics*, 3rd ed.; 2000, Pearson: Harlow, UK.

228. Herakovich C.T., ‘3-D constitutive equations’, ch. 3 in *Mechanics of fibrous composites*; 1998, John Wiley & Sons: New York, NY, US; pp. 47-76.